2022

Numerical Performance Prediction of a Composite Automotive Suspension Lower Arm

Zhe Ma
University of Windsor

Numerical Performance Prediction of a Composite Automotive Suspension Lower Arm

By

Zhe Ma

A Dissertation
Submitted to the Faculty of Graduates Studies
Through the Department of Mechanical, Automotive, & Materials Engineering
in Partial Fulfillment of the Requirements for
the Degree of Doctor of Philosophy
at the University of Windsor

Windsor, Ontario, Canada

2022

Numerical Performance Prediction of a Composite Automotive Suspension Lower Arm

by

Zhe Ma

APPROVED BY

G. Montesano, External Examiner
University of Waterloo

A. Alpas
Department of Mechanical, Automotive, & Materials Engineering

---

C. Novak
Department of Mechanical, Automotive, & Materials Engineering

---

B. Altenhof
Department of Mechanical, Automotive, & Materials Engineering

---

J. Johrendt, Co-Advisor
Department of Mechanical, Automotive, & Materials Engineering

---

B. Minaker, Co-Advisor
Department of Mechanical, Automotive, & Materials Engineering

September 6, 2022

Declaration of Originality

I hereby certify that I am the sole author of this thesis and that no part of this thesis has been published or submitted for publication.

I certify that, to the best of my knowledge, my thesis does not infringe upon anyone's copyright nor violate any proprietary rights and that any ideas, techniques, quotations, or any other material from the work of other people included in my thesis, published or otherwise, are fully acknowledged in accordance with the standard referencing practices. Furthermore, to the extent that I have included copyrighted material that surpasses the bounds of fair dealing within the meaning of the Canada Copyright Act, I certify that I have obtained a written permission from the copyright owner(s) to include such material(s) in my thesis and have included copies of such copyright clearances to my appendix.

I declare that this is a true copy of my thesis, including any final revisions, as approved by my thesis committee and the Graduate Studies office, and that this thesis has not been submitted for a higher degree to any other University or Institution.

Abstract

Using the lower arm from the front suspension of a typical passenger sedan as an example, this research explores the possibility of replacing automotive load bearing metal components with fibre reinforced plastic equivalents that could be manufactured using the injection moulding process.

To begin the study, the vehicle motion was modelled using a high fidelity multibody dynamics motion solver, under multiple different driving scenarios and road roughness levels. The time history of the suspension loads were recorded, and maximum load cases were identified and classified.

The injection moulding process was modelled using a sophisticated in-mould flow simulation software. The resulting fibre orientation distribution results have been studied and imported into a finite element model, in order to account for the anisotropic material behaviour during the stress analysis. A benchmark process was used to verify the simulation results on typical test specimens using data from the literature.

A series of static finite element analyses were conducted using the force combinations and fibre orientation results described above. The failure and plastic behaviour state is shown in the final finite element analysis results for different road levels and driving scenarios. The resulting performance of the composite lower arm is summarized and discussed as a guideline for future study and research. As a brief conclusion, the composite lower arm resulting from the injection moulding process studied in this research was predicted to have insufficient strength to safely replace the conventional aluminum lower arm, unless a dramatic geometry change or different manufacturing method is proposed.

I lovingly dedicate this dissertation to my wife: Kaiti
to my parents: Jianmin & Ping
to my parents-in-law: Qiuzhi & Jinmei
for their marvellous love and support.

谨以此篇论文献给我的妻子：李恺悌
父亲：马建民　　母亲：哈平
岳父：李求知　　岳母：李金美
感谢他们无微不至的关怀与支持。

Acknowledgements

I would like to express my deepest appreciation to my supervisor Dr. Bruce Minaker, and co-supervisor Dr. Jennifer Johrendt. Their positive attitude and intellectual thinking always inspired me during the journey of my graduate studies. The support, guidance, and ideas they have offered to me made this thesis and research become professional and meaningful. I owe much of my personal enrichment to them.

I owe a debt of gratitude to my committee members Dr. Giovanni Montesano, Dr. Ahmet Alpas, Dr. Colin Novak, and Dr. Bill Altenhof. Thanks to them for giving valuable comments and useful advice.

Finally, I must thank my wife, Kaiti, for her endless care and understanding during this endeavour. She has provided me with comfort, solace, and marvellous love during the most challenging time.

Content

List of Figures

List of Tables

Abbreviations

All abbreviations used in this paper are described in this section.

Abbreviation	Meaning
AME	Advanced Material Exchange®
ARD	Anisotropic Rotary Diffusion
CAD	Computer Aided Design
CAFE	Corporate Average Fuel Economy
CFD	Computational Fluid Dynamics
CG	Centre of Gravity
DAE	Differential-Algebraic Equation
EBOF	Eigenvalue-Based Optimal Fitting Closure Approximation
EMTA	Eshelby–Mori–Tanaka Approach
FEA	Finite Element Analysis
FEM	Finite Element Method
FOD	Fibre Orientation Distribution
FRP	Fibre Reinforced Plastic
FT	Folgar-Tucker
HD	Hydrodynamics
HYB	Hybrid Closure Approximation
IRD	Isotropic Rotary Diffusion
ISO	International Organization for Standardization
LIN	Linear Closure Approximation
MCT	Multi Continuum Theory
ORF	Orthotropic Fitted Closure
ORL	Orthotropic Fitted Closure For Low C_I
PSD	Power Spectral Density
QUA	Quadratic Closure Approximation
RSC	Reduced-strain Closure
SDV	Dependent State Variable

Notation

Mathematical notation throughout this paper is listed below, separated by the chapter in which it appears.

Introduction

Notation	Description	Used On Page:
$\mathbf{A}$	Second-order Orientation Tensor	12–14, 54–59
a	Orientation Tensors Notation	14, 56, 57, 59, 60, 66
a_{11}	Fibre Orientation Tensor's Entry in X Direction	xii, xiii, 13, 60, 62, 63, 82–84, 86–88, 201, 203, 205
a_{12}	Fibre Orientation Tensor's Entry for 45° and −45° in XY Plane	xii–xiv, 82, 85, 87, 91, 202, 204, 206
a_{13}	Fibre Orientation Tensor's Entry for 45° and −45° in XZ Plane	82
a_{22}	Fibre Orientation Tensor's Entry in Y Direction	xii, xiii, 13, 60, 62, 63, 82–84, 86, 87, 89, 201, 203, 205
a_{23}	Fibre Orientation Tensor's Entry for 45° and −45° in YZ Plane	82
a_{33}	Fibre Orientation Tensor's Entry in Z Direction	xii, xiii, 13, 60, 62, 63, 82, 83, 85, 86, 90, 202, 204, 206
$\mathbb{A}$	Fourth-order Orientation Tensor	xxiv, 12, 54–60
a_{ij}	Second-order Orientation Tensor	12, 14
a_{ijkl}	Fourth-order Orientation Tensor	12, 14, 66, 67

a_j	Gear Algorithm Parameter($j = 0, 1, 2...(k-1)$)	6
b_{-1}	Gear Algorithm Parameter	6, 7
B_a	Differential Operator with Shape Function	20
B_b	Differential Operator with Shape Function for The Total Strain	20
$\tilde{\mathbf{u}}_b$	Nodal Displacement for The Total Strain	20
$\mathbf{E}$	Strain Rate Tensor	14
$\boldsymbol{b}$	Body Forces Vector	17, 19, 20
$\bar{\mathbf{D}}$	Elasticity Matrix of Moduli	18–20
$\boldsymbol{t}$	Traction field	17, 19, 20
$\boldsymbol{u}$	The Displacement field	16, 17, 19–21, 95
b_x	Body Force in X Direction	17
b_y	Body Force in Y Direction	17
b_z	Body Force in Z Direction	17
$\mathbf{C}$	Constraint Conditions	5
$\mathcal{S}$	Differential Operator	16, 17
$\mathbf{C}_{\boldsymbol{q}}$	Constraint Jacobian Matrix	6
$\delta\boldsymbol{\varepsilon}$	Virtual Strain	19
$\delta\boldsymbol{u}$	Virtual Displacement	19
D_r	Rotary Diffusion Coefficient	14, 55
x_i	x_i direction	14
x_j	x_j direction	14, 53
x_k	x_k direction	14
E	Young's Modulus of Elasticity	18
$\boldsymbol{\varepsilon}$	Strain of The Body	16, 18–20
$\boldsymbol{\varepsilon}_0$	Initial Strain	18–20
ε_x	Strain of The Body in X Direction	16, 18, 19
γ_{xy}	Shear Strain of The Body in X-Y plane	16, 18, 19
ε_y	Strain of The Body in Y Direction	16, 18, 19
γ_{yz}	Shear Strain of The Body in Y-Z plane	16, 18, 19
ε_z	Strain of The Body in Z Direction	16, 18, 19
γ_{zx}	Shear Strain of The Body in Z-X plane	16, 18, 19
f_a	System Load Matrices	20
$\mathscr{G}$	Direction Cosines Matrix	17
$\boldsymbol{g}$	Function of System Equation Mixed Algebraic and Differential Equation	6, 7
Γ	External Boundary Surface of The Solid	19, 20
Γ_t	Boundary for Traction Condition	17, 19, 20

Γ_u	Boundary for Displacement Condition	17, 19
G	Shear Modulus	18
H	Initial Element Height	96
h	Time Step Size	6, 7
$\mathbf{I}$	Unit Tensor	13, 14, 54–57, 66, 69
i	The i th Time Step	6
j	The Time Step Before i^{th}	6
K	Bulk Modulus	18
k	The order of Gear Algorithm	6
K_{ab}	System Stiffness Matrices	20
l	Iteration Number	6, 7
λ	Lamé's First Parameter	18
$\boldsymbol{\lambda}$	The Vector of Lagrange Multipliers	6
$\mathbf{M}$	Mass Matrix of The System	5, 6
μ	Shear Modulus	18
N_a	Shape Function	20
ν	Poisson's Ratio	18, 19, 105
n_x	X Direction Cosine for Outward Pointing Normal to The Traction Boundary Γ_t	17
n_y	Y Direction Cosine for Outward Pointing Normal to The Traction Boundary Γ_t	17
n_z	Z Direction Cosine for Outward Pointing Normal to The Traction Boundary Γ_t	17
Ω	Problem Domain Volume	19, 20
$\boldsymbol{\omega}$	Vorticity Tensor	14
P	Unit Vector of Single Fibre	11, 12
ϕ	Out of Plane Angle of Single Fibre	11, 12
ψ	The Orientation Distribution Function	11, 12, 54, 59
$\boldsymbol{q}$	Vector of The System Coordinates	5, 6
$\boldsymbol{Q}_{\text{c}}$	Vector of Constraint Forces	5, 6
$\boldsymbol{Q}_{\text{e}}$	Vector of Applied Forces	5, 6
$\boldsymbol{Q}_{\text{v}}$	Vector of Centrifugal Forces	5
$\boldsymbol{\sigma}_0$	Initial Stress	18–20
$\boldsymbol{\sigma}$	Stress on The Body	17–19
σ_x	Stress on The Body in X Direction	17–19
σ_y	Stress on The Body in Y Direction	17–19
τ_{yz}	Shear Stress on The Body in Y-Z Plane	17–19

σ_z	Stress on The Body in Z Direction	17–19
τ_{xy}	Shear Stress on The Body in X-Y Plane	17–19
τ_{zx}	Shear Stress on The Body in Z-X Plane	17–19
t	Time	5
θ	In Plane Angle of Single Fibre	11, 12
u	Displacement Vector u	16
$\tilde{\boldsymbol{u}}_a$	Nodal Displacement	20
u_x	Displacement in X direction for arbitrary point inside element	96
${u_x}^{(a)}$	Displacement in X direction for Node a	96, 97
${u_x}^{(b)}$	Displacement in X direction for Node b	96, 97
${u_x}^{(c)}$	Displacement in X direction for Node c	96, 97
${u_x}^{(d)}$	Displacement in X direction for Node d	96, 97
u_y	Displacement in Y direction for arbitrary point inside element	96
${u_y}^{(a)}$	Displacement in Y direction for Node a	96, 97
${u_y}^{(b)}$	Displacement in Y direction for Node b	96, 97
${u_y}^{(c)}$	Displacement in Y direction for Node c	96, 97
${u_y}^{(d)}$	Displacement in Y direction for Node d	96, 97
v	Displacement Vector v	16
v_i	the component of the velocity in the x_i direction	14, 53
v_j	the component of the velocity in the x_j direction	14
v_k	the component of the velocity in the x_k direction	14
W	Initial Element Width	96
w	Displacement Vector w	16
X	Coordinate X for arbitrary point inside element	96
x	Cartesian Coordinates x	16, 20
ξ	Fibre Shape Factor	14, 53, 54, 56, 59
Y	Coordinate Y for arbitrary point inside element	96
$\boldsymbol{y}$	System Coordinates for Integration Method	6, 7
y	Cartesian Coordinates y	16, 20
z	Cartesian Coordinates z	16, 20

Dynamics Simulation

Notation	Description	Used On Page:
i	Notation of Indivadual Point in Road Profile	33

x	Road Profile Longitudinal Coordinate	33, 34
y	Road Profile Lateral Coordinate	33, 34
z	Road Profile Vertical Coordinate	33, 34
g	Gravitational Constant	40
a	Length from Vehicle Centre of Mass to Front Alxe	42
a_c	Centripetal Acceleration	41, 42
A_i	Amplitude of The Harmonic Function	31, 32
B	The Sampling Interval of Road Profile	31, 32
b	Length from Vehicle Centre of Mass to Rear Alxe	42
B_f	Front Braking propertion	40
C_f	Lumped Front Two Tire Cornering Stiffness	42
C_r	Lumped Rear Two Tire Cornering Stiffness	42
δ	Front Wheel Steering Angle	42
D_g	Desired Deceleration (proportion to gravity constant)	40
G_d	PSD of Vertical Displacement	xv, 30–32
L	The Length of Road Profile	31, 32
m	Vehicle Mass	42
M_{total}	Total Mass of The Vehicle	40
N	Number of Samples	31, 32
n	Spatial Frequency	30–32
n_0	Conventional Values of Spatial Frequency	xv, 30–32, 34, 35, 37
n_i	Discretised Spatial Frequency Values	31, 32
φ_i	A Random Phase Angle of The Harmonic Function	31, 32
ψ_x	The Mean Square Value of The Component of The Signal	31
R	Cornering Radius	41, 42
R_0	kinematic cornering radius	42
h	Harmonic Function	31, 32
k	Random Road Level(varing from 3 to 9)	32
φ	Phase Angle of The Harmonic Function	31
$\tilde{x}$	Longitudinal Coordinate in Harmonic Function	31, 32
R_w	Radius of wheel	40
T_{bc}	Braking Torque Control Function Coefficient	40, 41
T_d	Desired Driving Torque	39

T_{front}	Braking Torque on Front Wheel	40
T_{rear}	Braking Torque on Rear Wheel	40
V	Vehicle Longitudinal Velocity	41
V_d	Vehicle Desired Constant Speed	39
x_{bt}	Braking Torque Control Function Input	40, 41
x_{dt}	Driving Torque Control Function Input	39
y_{bt}	Braking Torque Control Function Output	40, 41
y_{dt}	Driving Torque Control Function Output	39

Manufacturing Process Simulation

Notation	Description	Used On Page:
A_1^m	Adjustable Coefficients of Matrix Failure Criteria	71, 72, 74, 76
A_2^m	Adjustable Coefficients of Matrix Failure Criteria	71, 72, 74, 76
A_4^m	Adjustable Coefficients of Matrix Failure Criteria	71, 72, 74, 76
$\mathbf{A}_f$	Fibre Strain Concentration Tensor	xxiii, 65, 66, 69
α	The Weighting Coefficient That Describe The Impact of Stress Component in The Average Fibre Direction	xxiii, xxvi, 70, 72, 74, 76
α_o	Optimized Value Of α For Perfect Aligned Material With Largest Eienvalue $\lambda_{o,l}$	70
$\mathbf{A}_m$	Matrix Strain Concentration Tensor	69
a_r	Aspect Ratio of Particle	54
B_1	The First Coefficient For Orientation Averaging Function	66, 67
B_2	The Second Coefficient For Orientation Averaging Function	66, 67
B_3	The Third Coefficient For Orientation Averaging Function	66, 67
B_4	The Fourth Coefficient For Orientation Averaging Function	66, 67
B_5	The Fifth Coefficient For Orientation Averaging Function	66, 67
$\bar{\mathbf{A}}_f$	The Orientation Average of $\mathbf{A}_f$	69

$\bar{\mathbf{C}}$	Stiffness Tensor of Actual Composite Material With A Particular FOD	66
$\bar{\mathbf{C}}^t$	Tangent Stiffness Tensor of Actual Composite Material With A Particular FOD	71
$\bar{\varepsilon}_m$	Equivalent Matrix Strain	69
$\bar{\varepsilon}_m^e$	Equivalent Matrix Elastic Strain	69
$\bar{\varepsilon}_m^p$	Equivalent Matrix Plastic Strain	69–71
$\bar{\sigma}_m$	Equivalent Matrix Stress	69–71
$\mathbf{C}^*$	The Stiffness Tensor of Unidirectional Composite Material	65–67
$\mathbf{C}_f$	Stiffness Tensor of Fibre Material	65, 66
$\mathbf{C}_m$	Stiffness Tensor of Matrix Material	65, 66, 69, 71
$\mathbf{C}_m^t$	The Tangent Stiffness Tensor of Matrix	69–71
β	The Weighting Coefficient That Describe The Impact of Stress Component Normal to The Average Fibre Direction	xxiv, xxvi, 70, 72, 74, 76
β_o	Optimized Value Of β For Perfect Aligned Material With Largest Eienvalue $\lambda_{o,l}$	70
$\mathbf{L}$	Velocity Gradient Tensor	53
$\mathbf{p}$	Unit Vector Represent Particle in 3 Dimensional Space	53, 54, 59
$\mathbf{R}$	The Transform Matrix Which ith column Is The Eigenvector $\mathbf{e}_i$	58
$\mathbf{W}$	Vorticity Tensor	53, 54, 56
C_I	Empirical Factor of Fibre-Fibre Interactions	54–56, 59–62, 64, 82
C_i^1	The First Coefficient of The Fitting Function For $\hat{\mathbb{A}}_{ii}$	59
C_i^2	The Second Coefficient of The Fitting Function For $\hat{\mathbb{A}}_{ii}$	59
C_i^3	The Third Coefficient of The Fitting Function For $\hat{\mathbb{A}}_{ii}$	59
C_i^4	The Fourth Coefficient of The Fitting Function For $\hat{\mathbb{A}}_{ii}$	59
C_i^5	The Fifth Coefficient of The Fitting Function For $\hat{\mathbb{A}}_{ii}$	59
C_i^6	The Sixth Coefficient of The Fitting Function For $\hat{\mathbb{A}}_{ii}$	59

$\mathbf{D}$	Rate of Deformation Tensor	53, 54, 56
$\Delta\bar{\sigma}_m$	Equivalent Matrix Stress Increment	71
$\Delta\varepsilon$	The Total Composite Material Strain Increment	69, 71
$\Delta\varepsilon_f$	The Average Strain Increment in The Fibre Material	69
$\Delta\varepsilon_m$	The Average Strain Increment in The Matrix Material	69, 71
$\dot{\gamma}$	The Magnitude of the rate of Deformation Tensor	54–56
$\Delta\sigma$	Total Cmposite Material Stress Increment	71
$\mathbf{e}_1$	The Eigenvector of Second-order Orientation Tensor in First Direction	58
$\mathbf{e}_2$	The Eigenvector of Second-order Orientation Tensor in Second Direction	58
$\mathbf{e}_3$	The Eigenvector of Second-order Orientation Tensor in Third Direction	58
E_f	Fibre Elastic Modulus	72, 74, 76
$\mathbf{e}_i$	The ith Eigenvector of Second-order Orientation Tensor ($i = 1, 2, 3$)	55, 56
E_m	Matrix Elastic Modulus	69, 70, 72, 74, 76
E_m^p	The Plastic Modulus of Matrix	69, 70
E_m^t	The Tangent Modulus of Matrix	70
f	The Scalar Function of Orientation	58
I_1^m	Invariants of The Matrix Average Stress State	71
I_2^m	Invariants of The Matrix Average Stress State	71
I_4^m	Invariants of The Matrix Average Stress State	71
κ	The Empirical factor of Reduce-strain Closure Model	55, 56, 61, 64, 82
$\mathbb{L}$	The Auxiliary Fourth-order Tensor As The Function of The Eigenvalues and Eigenvectors of The Second-order Tensor	56
$\mathbb{M}$	The Auxiliary Fourth-order Tensor As The Function of The Eigenvectors of The Second-order Tensor	56
λ_1	The First Eigenvalue of Second-order Orientation Tensor	58, 59, 70
λ_2	The Second Eigenvalue of Second-order Orientation Tensor	58, 59, 70

λ_3	The Third Eigenvalue of Second-order Orientation Tensor	58, 59
λ_i	The ith Eigenvalue of Second-order Orientation Tensor ($i = 1, 2, 3$)	55, 56
λ_l	Largest Eigenvalue of Second-order Fibre Orientation Tensor	70, 72, 74, 76
$\lambda_{o,l}$	The Largest Eienvalue Value Of Perfect Aligned Material	xxiii, xxiv, 70
ν_f	Fibre Poisson's Ratio	72, 74, 76
ν_m	Matrix Poisson's Ratio	72, 74, 76
ϕ_f	Fibre Content of Volume Fraction	54, 65, 66, 69
$\mathbf{S}$	Fouth-order Eshelby's Tensor	66
σ_{11}	Stress Component σ_{11} in Stress Tensor	70–72
σ_{12}	Stress Component σ_{12} in Stress Tensor	70–72
σ_{13}	Stress Component σ_{13} in Stress Tensor	71
σ_{22}	Stress Component σ_{22} in Stress Tensor	70–72
σ_{23}	Stress Component σ_{23} in Stress Tensor	70, 72
σ_{31}	Stress Component σ_{31} in Stress Tensor	70, 72
σ_{33}	Stress Component σ_{33} in Stress Tensor	70–72
σ_{max}	Maximum Von Mises Stress At Rupture	71, 72
σ_Y	The Yield Stress of Composite Material	69, 72, 74, 76
$\mathbf{T}$	The Exact Concentration Tensor For A Single Inhomogeneity In An Infinite Matrix	66
θ_r	The Value For α and β When The Fibre Orientation Becomes Random	70

Finite Element Analysis

Notation	Description	Used On Page:
$\bar{I}_1$	First Invariant of The Deviatoric Strain Tensor	106, 107
$\bar{I}_2$	Second Invariant of The Deviatoric Strain Tensor	106
C_{ij}	Strain Energy Potential Parameter For First and Second Invariant of The Deviatoric Strain Tensor	106
D_i	Strain Energy Potential Parameter For Elastic Volume Strain	106, 107

ε_{th}	Linear Thermal Expansion	106
J	The Total Volume Strain	106
J_{el}	The Elastic Volume Strain	106, 107
J_{th}	The Thermal Volume Strain	106
K_0	Initial Bulk Modulus	105, 106
μ_0	Initial Shear Modulus	105, 106
U	strain energy potential	106, 107

Chapter 1

Introduction

1.1 Motivation

The automotive industry has been pushed to achieve higher fuel economy according to the Corporate Average Fuel Economy (CAFE) standard in the next decade[1]. A great deal of research has been ongoing to facilitate this goal. Lightweight design and application is one of the major ways among recent studies. Replacement of conventional metal components with those made from composite materials such as Fibre Reinforced Plastic (FRP) has become more and more popular. The global automotive composite materials market was estimated to be approximately USD 9.4 billion in 2020, and is predicted to reach around USD 19.4 billion by 2027[2]. This reflects a large and recent trend of applying composite materials in the automotive industry. Carbon and glass fibre composites are the most popular FRP, and can potentially achieve weight reduction of 40–70% and 25–35%, respectively[3]. More importantly, the automotive industry has continued shifting toward electric vehicle development. Great benefits are also shown when applying lightweight composite material to electric vehicles. However, many applications have been focused on lightly loaded exterior parts, such as body panels, roofs, and doors[4]. More research is needed on parts that sustain a heavy load during driving. In author's opinion, there are several reasons that lead to this situation:

1. Uncertainty on material properties, such as tensile strength, as affected by the manufacturing process.
2. High material/manufacturing costs and long cycle times during processing prevent adoption on certain applications.
3. Lack of testing on the material behaviour, caused by the cost and concerns relating to mass production.
4. Lack of experience on verifying the strength of components made with composite materials.

According to these reasons, the application of composite materials to structural components is not easy to achieve. A systematic process of numerical performance prediction on related components is necessary and useful to achieve good design outcomes.

1.2 Objective

The objective of this research is to explore the possibility of weight savings through replacement of metal with composite material on automobile structural components, and to propose a systematic method for the assessment of the strength of the replacement component using modern computer simulations. In this work, a specific target component was identified (a suspension lower arm) although the method should be equally applicable to other similar components. The specific objectives of each individual simulation process are stated as follows:

1. Obtain maximum force combinations under different road roughness and driving scenarios through a full car multibody dynamic analysis.
2. Simulate the injection moulding process of a fibre reinforced plastic lower arm, in order to get the proper anisotropic material properties for FEA.
3. Build a high fidelity FEA model to predict the strength of a composite lower arm under maximum force combinations through a static analysis.
4. According to the performance, summarize any potential improvements in the manufacturing process and geometric design.

Through this process, the feasibility of expanding the use of composite materials in automotive components can be more fully explored. The entire process can serve as a guideline for future study on a similar topic.

1.3 Research Scope

A series of full car dynamic simulations will be conducted with different levels of 3D random roads and different driving scenario implementations. The maximum force combinations on the lower arm ball joint will be found and summarized. The corresponding forces and moments acting on the lower arm bracket will be extracted.

The injection moulding process simulations using the proposed fibre and matrix material with four different injection locations will be conducted. The predicted fibre orientation distribution results will be mapped into a FEA model to define the anisotropic composite material properties.

Several static finite element analyses will be conducted using the appropriate boundary conditions and corresponding composite material properties obtained from varying injection point

locations. The loads from the dynamic simulations will be used to predict the strength of a composite lower arm under different road conditions and different driving manoeuvres. The flowchart related to the models and simulations that are involved in this research is shown in Figure 1.1.

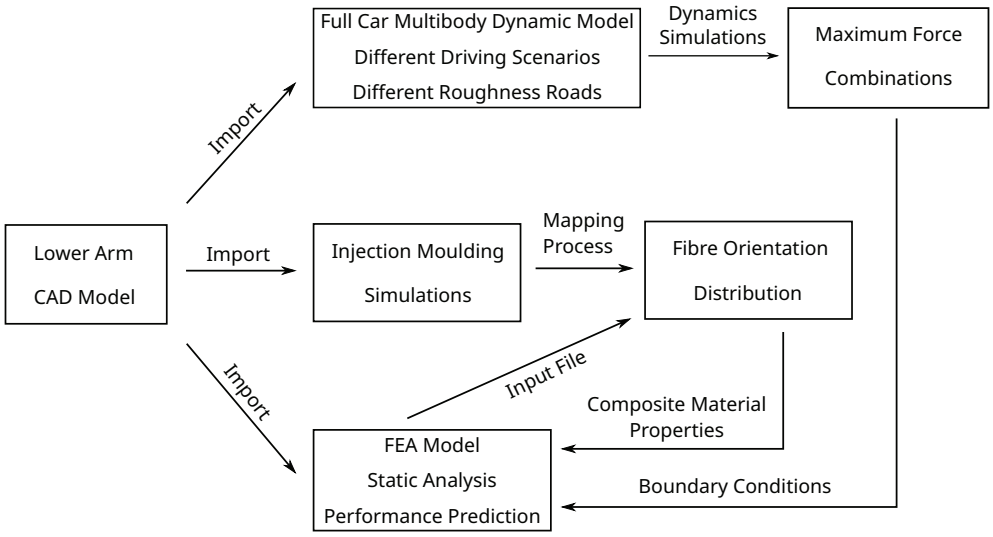

Figure 1.1: Simulation Process in This Research

In a general sense, a fatigue analysis is needed for a proper study of automotive suspension component durability, due to the cyclic loading that is inherent in this type of application, and especially so for a composite material. However, the goal of this research is to explore the possibility of composite materials passing the static or instantaneous load conditions that would be a minimum requirement before any fatigue study was relevant. So, fatigue analysis is considered as beyond the scope of this study, and it will not be considered in the simulations. However, it surely will be major consideration for future works in this area.

1.4 Multi-body Dynamics

1.4.1 Suspension System

The suspension system is a very important part in the vehicle. Basically, it is a system containing springs, shock absorbers and linkages that connects the vehicle body to its wheels, and allows a relative motion between the wheels and the chassis. The main purpose of the suspension is to achieve good road handling in order to offer safety and comfort for the driver. It offers good isolation for the vehicle from road noise, bumps, and vibrations. There are two popular types of independent suspension systems that are used in most modern passenger vehicles. They are the *double control arm* system and *MacPherson strut* system. As shown in Figure 1.2, the double control arm system, while offering better performance, is more complicated and needs more space for installation. It is generally not ideal for small economical vehicles. The structure of the MacPherson strut system is relatively simple. It is a compact system with fewer design parameters to consider.

For both systems, the anti-roll bar is another necessary part, to decrease the body roll when the vehicle is cornering.

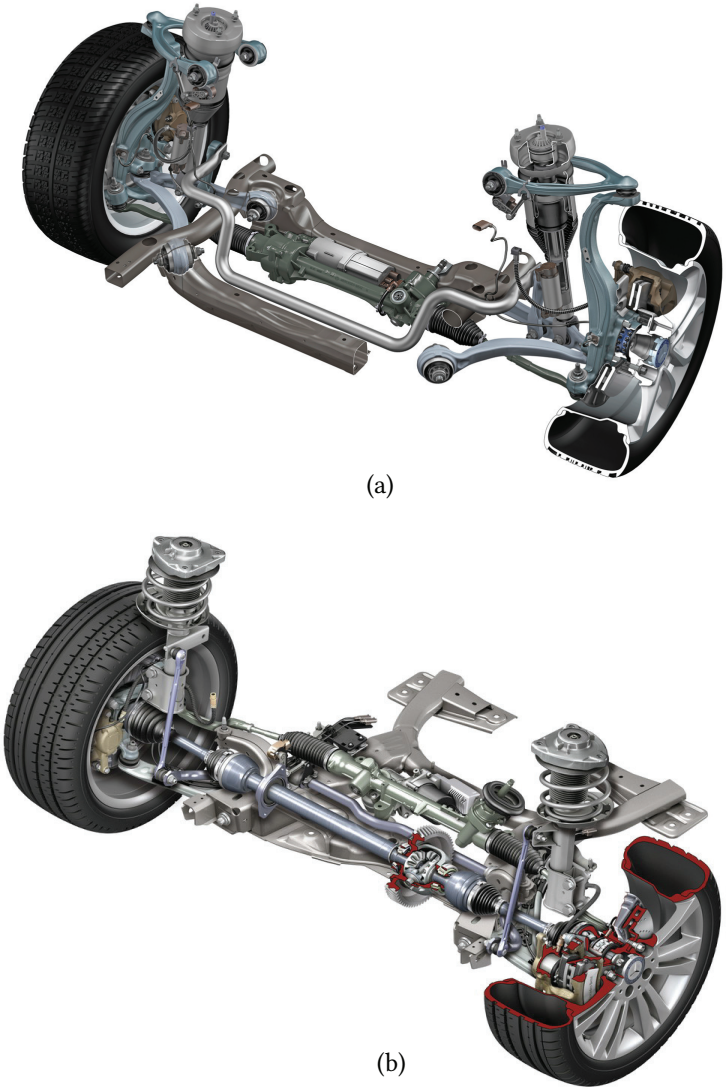

(a)

(b)

Figure 1.2: Suspension System: (a) Double Control Arm System and (b) Macpherson Strut System (Reproduced from https://www.caricos.com)

The part that has the major focus in this research is the lower control arm in a Macpherson type suspension. Generally, the lower control arm is treated as a linkage to connect the wheel and chassis. On the wheel side, it is connected by a ball joint that offers three rotational degrees of freedom. On the chassis side, it connected by two rubber bushing joints which offer six degrees of freedom, but limits relative motion using the rubber bushing stiffness. The rubber bushing provides an interface between the chassis and the lower arm, damping the energy transmitted through the bushing. Based on the connecting direction of the rubber bushing: the major stiffness

of the front bushing is the torsional stiffness, and the major stiffness of the rear bushing is the conical stiffness. The rubber bushing offers good isolation to minimize the noise and vibrations when the vehicle is in motion. The anti-roll bar mounts to the chassis, and connects to the lower control arms on either side of the vehicle through a revolute joint and a short lever arm, and behaves as a torsional spring. Depending on the different motions of vehicle, such as acceleration, braking, cornering, and bumps, the lower control arm may experience tension, compression, torsion or bending loads. In order to analyze the force on the lower control arm, a comprehensive multi-body dynamics system, including all the effects from the bushing, the anti-roll bar, and the road condition will be necessary. Different road conditions and driving scenarios also should be considered during the simulation, in order to compare and cover different cases.

1.4.2 Multi-body Dynamics Simulation

In order to analyze to the behaviour of a suspension system, a multi-body dynamics simulation is necessary. In this section, a brief introduction about multi-body dynamics will be provided. A multi-body dynamics system is formed by a series of interconnected rigid or flexible bodies. Each individual body may undergo large translation and/or rotational displacements. In this research, the dynamics simulation that assumes rigid multi-body systems only is considered. Generally, an unconstrained rigid body has six degrees of freedom in space, three translational degrees of freedom and three rotational degrees of freedom. Between each body, there may be a joint or force element to limit the motion of the whole system. Force elements such as springs, dampers, and bushings do not completely prevent motion in any particular direction, but they significantly affect the motion of the bodies in one or more directions based on their stiffness properties. As a result, a force element does not reduce the degrees of freedom of the system. In contrast, mechanical joints, such as spherical joints, will entirely prevent motion in certain directions and therefore reduce the degrees of freedom of the system. Thus, the number of degrees of freedom depends on the number of bodies and the number of joints in the system. One can derive the equations of motion of a multi-body system using either the Newton-Euler equations or Lagrange's equations. The equations of motion are used to describe the dynamic behaviour of a multi-body system. The general equation of motion of a multi-body system is shown in the following matrix form:

$$\mathbf{M}\ddot{\boldsymbol{q}} = \boldsymbol{Q}_{\mathrm{e}} + \boldsymbol{Q}_{\mathrm{c}} + \boldsymbol{Q}_{\mathrm{v}} \tag{1.1}$$

In this equation, $\mathbf{M}$ is the mass matrix of the system, $\boldsymbol{q}$ is the vector of the system coordinates, $\boldsymbol{Q}_{\mathrm{e}}$ is the vector of applied forces, $\boldsymbol{Q}_{\mathrm{c}}$ is the vector of constraint forces, and $\boldsymbol{Q}_{\mathrm{v}}$ is the vector of centrifugal forces and gyroscopic moments. The number of independent constraint forces is equal to the number of the algebraic constraint equations, which are defined in following form:

$$\mathrm{C}(\boldsymbol{q}, t) = 0 \tag{1.2}$$

It was shown by Ahmed[5] that the vector $\boldsymbol{Q}_c$ of the constraint forces can be written in terms of the system constraint Jacobian matrix $\mathbf{C}_{\boldsymbol{q}}$ and the vector of Lagrange multipliers $\boldsymbol{\lambda}$ as:

$$\boldsymbol{Q}_c = -\mathbf{C}_{\boldsymbol{q}}{}^{\mathrm{T}}\boldsymbol{\lambda} \tag{1.3}$$

Substituting Eqn. 1.3 into Eqn. 1.1, and by setting the reference points to be the centres of mass of each body, which means $Q_v = 0$, one can obtain:

$$\mathbf{M}\ddot{\boldsymbol{q}} + \mathbf{C}_{\boldsymbol{q}}{}^{\mathrm{T}}\boldsymbol{\lambda} = \boldsymbol{Q}_e \tag{1.4}$$

This is the general form of the equations of motion of a constrained multi-body dynamic system. In general, this class of problem is known as a Differential-Algebraic Equation (DAE). In order to get the solution of this type of equation, many special numerical integration algorithms have been developed to obtain the state over a specified period of simulation time. In this research, the software Motionview® has been used for multi-body dynamics simulation. The integration algorithm used by this software is called a *stiff differential equation* method. This method considers the algebraic constraint equation to be a special form of differential equation in which the time derivatives of the variables do not appear. This assumption has proved to cause the system equations to become *numerically* stiff (i.e., distinct from physical stiffness, but describing a system in which any drift from the true solution causes that drift to increase). Assume one has a system with mixed algebraic and differential equations in the following form:

$$\boldsymbol{g}(\boldsymbol{y}, \dot{\boldsymbol{y}}, t) = 0 \tag{1.5}$$

The Newton-Raphson formula for this system equation is:

$$\boldsymbol{g}_{\boldsymbol{y}}{}^{(l)}\Delta\boldsymbol{y}^{(l)} + \boldsymbol{g}_{\dot{\boldsymbol{y}}}{}^{(l)}\Delta\dot{\boldsymbol{y}}^{(l)} = -\boldsymbol{g}^{(l)} \tag{1.6}$$

where l represents the iteration number in a recursive solution. For the l^{th} and $l+1^{\text{th}}$ Newton-Raphson iterations, one has:

$$(\boldsymbol{y}^{i+1})^{(l)} - hb_{-1}(\dot{\boldsymbol{y}}^{i+1})^{(l)} - \sum_{j=0}^{k-1}(a_j\boldsymbol{y}^{i-j}) = 0 \tag{1.7}$$

$$(\boldsymbol{y}^{i+1})^{(l+1)} - hb_{-1}(\dot{\boldsymbol{y}}^{i+1})^{(l+1)} - \sum_{j=0}^{k-1}(a_j\boldsymbol{y}^{i-j}) = 0 \tag{1.8}$$

where h is the time step size. The $k+1$ coefficients $a_0, \ldots, a_{k-1}$ and b_{-1} are determined by the choice of solution algorithm, e.g., the k^{th} order Gear algorithm. The non-zero b_{-1} term indicates

that the method is an implicit method. Note that the summation terms in these equations are not a function of the iteration number. They are a function of the information from the i^{th} and previous j^{th} time steps, so they remain constant at each iteration. Subtracting Eqn. 1.7 from Eqn. 1.8 yields:

$$\Delta \dot{\boldsymbol{y}}^{(l)} = \frac{1}{hb_{-1}} \Delta \boldsymbol{y}^{(l)} \tag{1.9}$$

By substitution of Eqn. 1.9 into Eqn. 1.6, one can get the corrector formula:

$$\left(\boldsymbol{g}_{\boldsymbol{y}}{}^{(l)} + \frac{1}{hb_{-1}} \boldsymbol{g}_{\dot{\boldsymbol{y}}}{}^{(l)} \right) \Delta \boldsymbol{y}^{(l)} = -\boldsymbol{g}^{(l)} \tag{1.10}$$

At each time step, the iterative corrector process of Eqn. 1.10 is continued until all the Newton differences $\Delta \boldsymbol{y}^{(l)}$ are below a specified value. At each Newton-Raphson iteration, vectors $\boldsymbol{y}$ and $\dot{\boldsymbol{y}}$ are updated using following equations:

$$\boldsymbol{y}^{(l+1)} = \boldsymbol{y}^{(l)} + \Delta \boldsymbol{y}^{(l)} \tag{1.11}$$

$$\dot{\boldsymbol{y}}^{(l+1)} = \dot{\boldsymbol{y}}^{(l)} + \frac{1}{hb_{-1}} \Delta \boldsymbol{y}^{(l)} \tag{1.12}$$

It was noted previously that treating algebraic equations as special forms of differential equations makes the system numerically stiff. This brings artificial high frequency components into the solution. Because of the existence of high frequency components in the response, the time increment h must be chosen relatively small, making the term $1/h$ in the algorithm become very large. At certain points, due to the resulting numerical round-off error, the iterative process may not converge and no solution can be found. However, up until the failure to converge, the solutions will be very accurate.

1.5 Fibre Reinforced Plastic

FRP will be the primary composite material considered in this research. FRP is a combination of fibres in a polymeric matrix material. Generally, the fibres are treated as reinforcement to carry load or to control strain. The polymer matrix is regarded as a bonding medium to transfer the load and to provide the connection between fibres. FRP is well-known by its high specific modulus and strength, i.e., the modulus and strength per unit weight are typically higher when compared to conventional metals. It provides a huge potential to replace metals with FRP without any losses on strength.

The main feature of this type of material is that the properties are highly dependent on the choice of fibre, the polymer matrix, and manufacturing process. Each individual option will have a great effect on the final product. Also, every option will influence each other to limit the possibility

of choices. The general options for modern industry and production have been demonstrated in Owen's book[6] and Mallick's book[7]. A brief introduction on the featured fibre, polymer, manufacturing process and properties follows.

The most common fibres used in industry are glass and carbon. They are widely used in many fields such as aerospace, automotive, building structures, and sports products. Carbon fibre has higher strength when compared to glass fibre, but the cost is relatively high, limiting its use to certain fields, such as high performance racing cars, where cost effectiveness is less important. Glass fibre provides less strength when compared to carbon fibre. It is widely used in the automotive industry for common passenger vehicles. Some other types of fibre, such as aramid and Boron are also possible, but much less widely used, and won't be discussed in this research.

The commonly used polymer matrices are *thermoset* and *thermoplastic*. The major different is that thermoplastic polymers can be reshaped by a heating process after the composite material has been formed, providing more options for manufacturing process design. For example, processing the mixing of fibre and polymer with desired fibre distribution first, and then reshaping it into the final product using another forming process.

Besides the different kind of fibres that can be chosen, the most important factor that influences the manufacturing process is the fibre length. Depending on the final length of the fibres inside a composite material, it can be divided into two categories: short fibre and continuous fibre. Based on the current state of the art, it has been shown that longer fibres will result in better strength properties, but also more difficult and therefore expensive manufacturing processes. From recent studies on continuous fibre, laminate stacks are the most popular configuration for this type of FRP. The basic idea is making unidirectional fibre and polymer compounds in thin layers, and stacking them together at different angles to form the final product. In Table 1.1, the major properties of continuous fibre reinforced plastic are been compared to conventional metals such as aluminum and steel. The unidirectional configuration has stronger properties than metal, but only along the fibre direction. This is known as *anisotropic* behaviour, and is not good for use in complex load environments, as the strength will be weak when load is perpendicular to the fibre direction. For bi- or multi-directional configurations in continuous fibre plastic, the material is usually treated as quasi-isotropic or isotropic. Although the properties are much lower than the unidirectional composite, they still have a considerable advantage over common structural metals on a unit weight basis.

The manufacturing process for continuous fibre plastic is relatively new and complicated when compared to the short fibre plastic, so at present it is only suited for small or medium volume production. The most popular manufacturing process used in the automotive industry is injection or compression moulding, with short fibre plastic, because of the flexibility in product shape, the relatively low cost, and easy operation for mass production. For most cases, the material properties of short fibre plastic are determined by measurement of the final product. Alternatively, one can assume a transversely isotropic elastic behaviour, because of the three layer 'shell-core-shell'

Table 1.1: Properties of Some Metallic and Structural Composite Materials*

Material	Density [g/m^3]	Modulus [GPa]	Tensile Strength [MPa]
SAE 1010 steel (cold-worked)	7.87	207	365
AISI 4340 steel (quenched and tempered)	7.87	207	1,722
6061-T6 aluminum alloy	2.7	68.9	310
7178-T6 aluminum alloy	2.7	68.9	606
High-strength carbon fibre-epoxy matrix (unidirectional)†	1.55	137.8	1,550
High-modulus carbon fibre-epoxy matrix (unidirectional)	1.63	215	1,240
E-glass fibre-epoxy matrix (unidirectional)	1.85	39.3	965
Carbon fibre-epoxy matrix (quasi-isotropic)	1.55	45.5	579
Sheet-molding compound (SMC) composite (isotropic)	1.87	15.8	164

∗ Reproduced from [7]

† For unidirectional composites, the fibres are unidirectional and the reported modulus and tensile strength values are measured along the direction of fibres.

structure that often results when injection moulding components with thin walls. However, this approach will often lead an unsafe design when applied to relatively thick structural components.

As discussed above, the fibre orientation distribution of FRP is very important and has a substantial effect on the strength of the final product. In the next section, a detailed discussion will be made on injection moulding with short fibre reinforced thermoplastic, and how to predict the fibre orientation distribution.

1.6 Composite Manufacturing Process

1.6.1 Fibre Geometry

The most commonly used processing technology for short fibre FRP is injection moulding. Thermoplastic is usually chosen to be the polymer matrix in this process. The processing parameters, such as temperature, pressure, and pre-processing method largely depend on the type of thermoplastic reinforcement. There are two major thermoplastic reinforcements commonly used for injection moulding; one is short fibre granules, the other one is long fibre granules.

Short fibre granules are the most common reinforcement in injection moulding. They are manufactured by chopping fibre strands into the polymer matrix and mixing them in a compounding extruder. After the mixture is cooled, the granules are cut into 3-6 mm lengths and ready for feeding into the injection moulding. The final fibre length in the granules is usually less than 1 mm despite the initial length being around 4 mm. The process of manufacturing short fibre granules is continuous and automated, providing the ability for high-volume production.

When compared to short fibre granules, long fibre granules enhance the fibre length in the fibre and polymer compound. They are manufactured by impregnating a continuous fibre roving into a polymer matrix and then cutting into 5, 9 or 16 mm granules. In this way, the fibre length

is equal to the granule length. Hence, the mechanical properties can be improved by increasing the fibre length in the final product. This processing technology is still in its infancy and not yet suited for large-scale production.

After the fibre granules have been formed, they are fed from a hopper into a heated barrel equipped with a reciprocating screw, causing them to melt and be moved forwards to fill the injection chamber. As shown in Figure 1.3, the injection moulding machine is divided into two parts: the heating and mixing unit consisting of the hopper, screw and barrel, and the moulding unit that controls the mould operation. The process allows the production of components with a great variety in both size and shape. Even complicated three dimensional shapes such as holes, ribs, and slots can be moulded by using sliding or detachable cores. Typical fibre volume fractions employed are in the range 10–20%. Moulding conditions are usually specified depending on the polymer type, but in general are in the ranges given below:

- Barrel Temperature: 200-350 °C
- Mould Temperature: 20-120 °C
- Injection Pressure: 300-1500 bar
- Cycle Time: 20-180 mouldings/hour

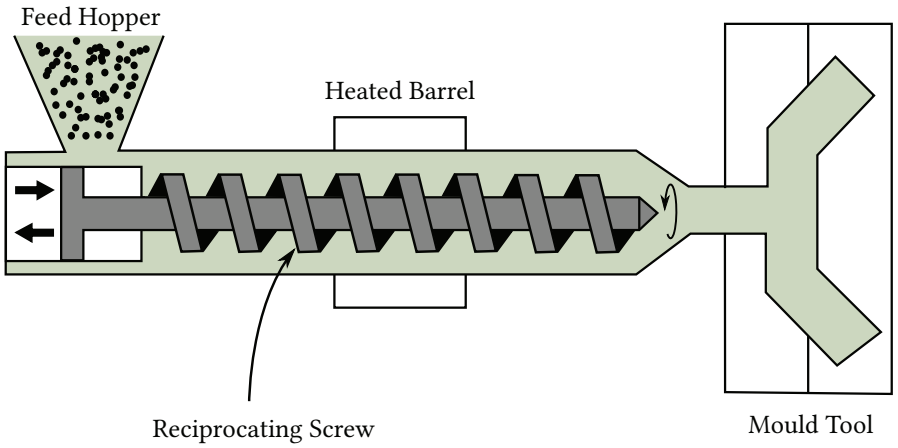

Figure 1.3: Injection Moulding

1.6.2 Fibre Orientation Tensor

Short fibre reinforced thermoplastics can be manufactured economically at high volume using standard injection moulding techniques. Because of this, there are many applications in the automotive industry. Although they have been used successfully in many areas, the design procedures are often based on past experience rather than a codified process. Importantly, the fibre

orientation and its effect on material properties is very often ignored during the design process. However, it is very important to account for this effect when designing a load bearing component. In order to understand the distribution of fibre orientation during an injection moulding process, some basic fundamental flow conditions should be discussed. There are three main types of flow affecting fibre orientation:

- In-plane shear flow
- In-plane tensile or compression flow
- Out-of-plane fountain flow

Different flow conditions are caused by the complex shape of the moulded part. They have combined effects on fibre orientation. The details about these effects are discussed in Owen's book[6]. Generally, these three types of flow form a three layer 'shell-core-shell' structure. The fibres in both side shell layers are highly aligned in the flow direction, while in the core layer, fibres are usually transversely oriented. Thus, for a moulded part with a thin wall structure, the fibre orientation is largely aligned in the flow direction, which depends on the injection location and the shape of the part. This assumption will not work for applications like the suspension lower arm in this research, because the geometry is not thin wall.

For a more accurate design, a quantitative description of the fibre orientation is necessary. A single fibre in 3D space can be described by a unit vector P. It has two orientation angles: the in plane angle ϕ and the out of plane angle θ. As shown in Figure 1.4, the components of P are related to θ and ϕ:

$$P_1 = \sin\theta \ \cos\phi \tag{1.13a}$$

$$P_2 = \sin\theta \ \sin\phi \tag{1.13b}$$

$$P_3 = \cos\theta \tag{1.13c}$$

The orientation state at a point inside the component can be described by a probability distribution function, $\psi(\theta, \phi)$. This function defines the probability of finding a fibre with orientation between the angles θ_1 and $(\theta_1 + d\theta)$, and ϕ_1 and $(\phi_1 + d\phi)$. When associating the unit vector P with the fibre, one can write the probability distribution function as $\psi(P)$. The integral over the surface of the unit sphere (or over all possible directions of P) is defined by:

$$\oint dP = \int_{\phi=0}^{2\pi} \int_{\theta=0}^{\pi} \sin\theta \, d\theta d\phi \tag{1.14}$$

The integral of function ψ over the surface of the unit sphere must be equal to 1, because every fibre must have some orientation. This is called the normalization condition:

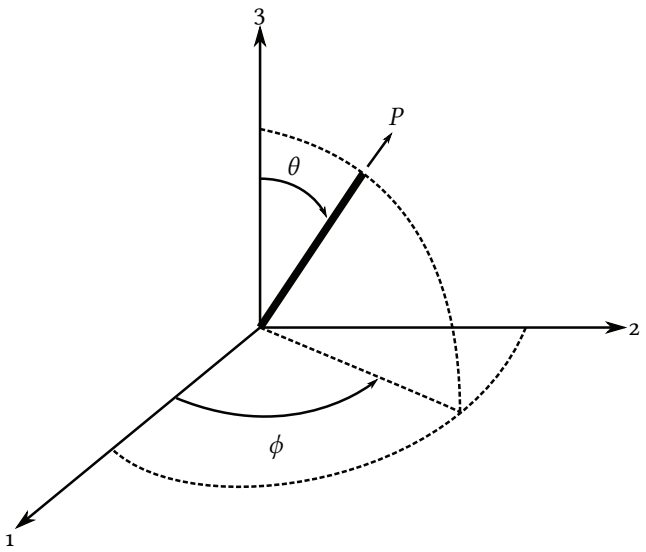

Figure 1.4: Coordinate System of Single Fibre

$$\int_{\phi=0}^{2\pi}\int_{\theta=0}^{\pi}\psi(\theta,\phi)\ \sin\theta\, d\theta d\phi = \oint\psi(P)dP = 1 \tag{1.15}$$

The orientation probability distribution function is complete but complicated. It would take a huge computation time when considering the large amount of fibres inside the three dimensional space that describes the component. A more concise method is necessary.

For a collection of fibres, orientation tensors can be defined by forming dyadic products of the vector P and then integrating the product of these tensors with the distribution function over all possible directions. The following equations define the second-order and fourth-order orientation tensors:

$$\mathbf{A} = a_{ij} = \oint P_i P_j \psi(P)\, dP \tag{1.16a}$$

$$\mathbb{A} = a_{ijkl} = \oint P_i P_j P_k P_l \psi(P)\, dP \tag{1.16b}$$

The second-order orientation tensor a_{ij} is usually sufficient for orientation prediction. Because of the symmetry, there are only five independent entries in the second-order tensors needed to describe the state of orientation at any point. They are a_{11}, a_{22}, a_{12}, a_{13} and a_{23}. The value of a_{11} indicate the possibility of fibre alignment in x direction. the value of a_{22} indicate the possibility of fibre alignment in y direction. Value closer to 1 indicate higher possibility. The out of plane orientation is given by the value of a_{33} which is derived from Equation 1.17.

$$a_{11} + a_{22} + a_{33} = 1 \tag{1.17}$$

Other entries such as a_{12}, a_{13} and a_{23} are necessary for a full description, but are less important for the actual state of orientation. The eigenvectors of $\mathbf{A}$ can be treated as the principal axes of the orientation state, and the eigenvalues of $\mathbf{A}$ indicate the probability that the fibres are distributed in each of these three principal directions. The totally random (and therefore isotropic) orientation state will have $\mathbf{A} = \mathbf{I}/3$, where $\mathbf{I}$ is the identity tensor:

$$\mathbf{I} = \begin{bmatrix} 1 & 0 & 0 \\ 0 & 1 & 0 \\ 0 & 0 & 1 \end{bmatrix} \tag{1.18}$$

Some featured fibre orientation states described using the orientation tensor are illustrated in Figure 1.5.

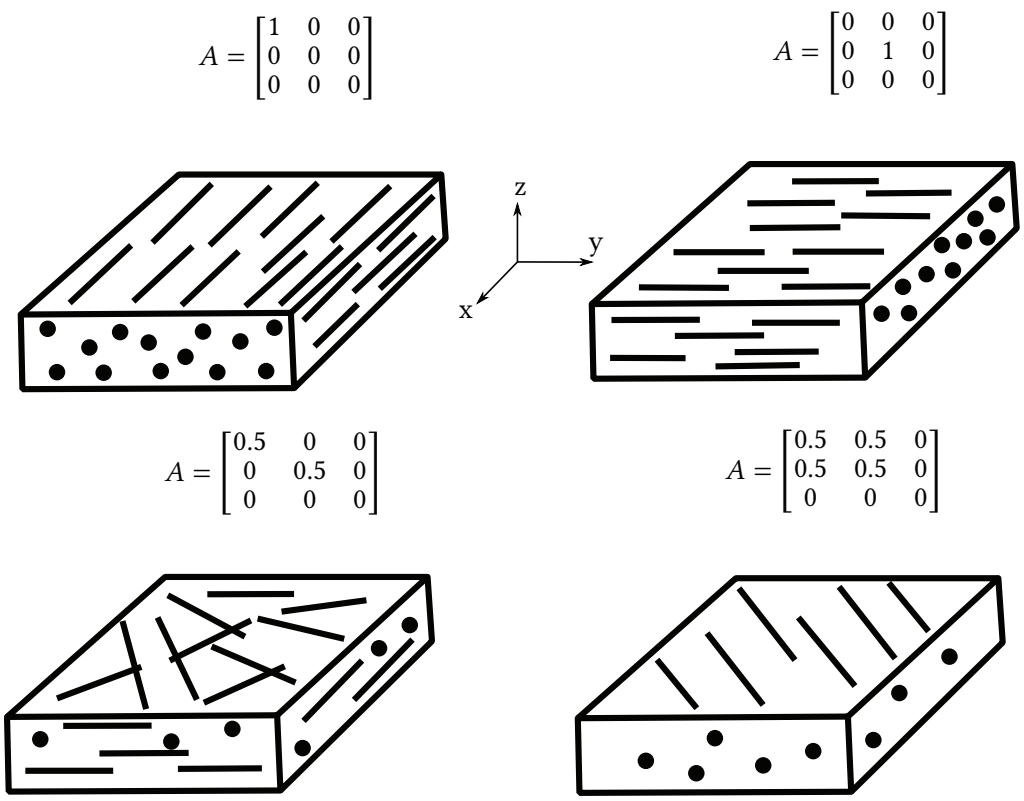

Figure 1.5: Examples of Fibre Orientation Tensor. Note the role of the off-diagonal elements in the tensor.

Fibre orientations have been measured and presented with the orientation tensor in the literature[6], showing that it is a useful and concise way to quantitatively describe the orientation state.

In order to predict the fibre orientation state during manufacturing process, an equation for the rate of change for the orientation tensor as a function of fluid deformation is needed. Advani and Tucker[8] have shown how to write the equation of change of the second-order orientation tensor as function of the fluid properties in a three-dimensional domain.

$$\begin{aligned}\dot{\mathbf{A}} = \frac{Da_{ij}}{Dt} &= \frac{\partial a_{ij}}{\partial t} + v_k \frac{\partial a_{ij}}{\partial x_k} \\ &= -\frac{1}{2}(\omega_{ik}a_{kj} - a_{ij}\omega_{kj}) + \frac{1}{2}\xi(\mathbf{E}_{ik}a_{kj} + a_{ik}\mathbf{E}_{kj} - 2\mathbf{E}_{kl}a_{ijkl}) + 2D_r(\mathbf{I} - 3a_{ij})\end{aligned} \tag{1.19}$$

$$\omega_{ij} = \frac{\partial v_j}{\partial x_i} - \frac{\partial v_i}{\partial x_j} \tag{1.20}$$

$$\mathbf{E}_{ij} = \frac{\partial v_j}{\partial x_i} + \frac{\partial v_i}{\partial x_j} \tag{1.21}$$

In this equation, $\dot{\mathbf{A}}$ is the *material derivative* of $\mathbf{A}$, which is also denoted as $\frac{D}{Dt}$, and includes two parts: changes over time due to the changes in the flow field, and changes over time due to a changing location inside the flow field. The terms $\mathbf{E}$ and $\boldsymbol{\omega}$ are the strain rate (rate of deformation) tensor and vorticity tensor, respectively, which are determined according to the velocity of fluid. The term ξ is a fibre shape factor that depends on the aspect ratio of fibres. Usually, it is set to a value of one, based on typical fibre aspect ratios. The term D_r is the rotary diffusion coefficient. Equation 1.19 shows that the rate of change of the orientation tensor depends on the current state of orientation, the velocity properties of the fluid and the rotary diffusivity of fluid. Although it is based on the second-order orientation tensor expression, it will introduce a term of fourth-order type orientation tensor. To calculate the results, a_{ijkl} can be replaced with a certain form of second order tensor by a closure approximation function. One of the earliest functions that covers a wide range of flow fields, called the Hybrid Closure Approximation (HYB), has been demonstrated by Advani and Tucker[8]. The HYB mixes the Linear Closure Approximation (LIN) and the Quadratic Closure Approximation (QUA) together, according to a scalar measure of orientation. However, it overpredicts the fibre orientation state in most flow situations. A more accurate and widespread closure approximation function is needed for general flow fields. More details will be discussed in Chapter 3.

1.7 Finite Element Method and Analysis

1.7.1 The concept of the Finite Element Method

The objective of this research is predicting the performance of a FRP suspension lower control arm. In order to achieve this goal, a complete and sufficient finite element model will be necessary. In this section, the basic concept of Finite Element Method (FEM) and fundamental knowledge regarding FEA software will be introduced.

Many problems in engineering are so complex that they cannot be solved in a single operation or calculation. In these cases, the process of subdividing a large system into individual components or 'elements', and then rebuilding the original system from such components to obtain the final solution may be the only effective way to proceed.

In many cases, a complete system can be modelled by using a finite number of components; one can describe such systems as *discrete*. In other cases, the subdivision extends to infinity and the problem can only be defined by a mathematical approximation. This will lead to differential equations, which imply an infinite number of elements. One can describe such systems as *continuous*. With the help of computer technology, discrete problems can be solved very quickly, even if the number of elements is very large. As the capacity of all computers is finite, continuous problems can only be solved exactly by mathematical manipulation. However, by subdivsion, an approximation can be found that is arbitrarily close to the true solution, and only limited by the computing resources available.

To overcome the difficulty of realistic types of continuum problems, various methods of discretization have been proposed both by engineers and mathematicians in the past century[9]. Based on all these methods, the unified treatment of 'standard discrete problems' leads to the first definition of the finite element process as a method of approximation to continuum problems such that:

- The continuum is divided into a finite number of parts (elements), the behaviour of which is specified by a finite number of parameters, and
- The solution of the complete system as an assembly of its elements follows precisely the same rules as those applicable to standard discrete problems.

This is the basic idea of the FEM and how it can be used to solve a complex problem. For more specific cases, for example in solid mechanics, one will analyze the problem in the following manner:

- The whole body is separated by imaginary lines, curves, or surfaces into a number of finite elements.
- The elements are assumed to be interconnected at a number of nodal points located on their boundaries or in their interior.

- A set of functions is chosen to define the state of displacement within each element and on its boundaries in terms of its nodal displacements.
- The displacement functions define the state of strain within an element in terms of the nodal displacements. By using these strains and the constitutive properties of the material, the state of stress throughout the element and on its boundaries will be defined.
- A system of forces applied at the nodes and balanced the boundary stresses and any distributed loads is determined, through a stiffness and displacement relationship.

In the next section, the fundamental theory of FEM applied in 3D solid mechanics will be demonstrated. The basic equation that needs to be solved during a FEA process will be discussed.

1.7.2 Theory

As an example, the theory of linear elastic problems will be discussed, beginning with the set of governing equations[9] that describe the state of a solid part, which must be solved through a FEA process.

Displacement Function

For a three-dimensional problem, the displacement field $\boldsymbol{u}$ is given by:

$$\boldsymbol{u} = \begin{Bmatrix} u(x,y,z) \\ v(x,y,z) \\ w(x,y,z) \end{Bmatrix} \tag{1.22}$$

Strain Matrix

The strain under small deformation is computed from the displacements:

$$\boldsymbol{\varepsilon} = \begin{Bmatrix} \varepsilon_x \\ \varepsilon_y \\ \varepsilon_z \\ \gamma_{xy} \\ \gamma_{yz} \\ \gamma_{zx} \end{Bmatrix} = \mathcal{S}\boldsymbol{u} = \begin{bmatrix} \frac{\partial}{\partial x} & 0 & 0 \\ 0 & \frac{\partial}{\partial y} & 0 \\ 0 & 0 & \frac{\partial}{\partial z} \\ \frac{\partial}{\partial y} & \frac{\partial}{\partial x} & 0 \\ 0 & \frac{\partial}{\partial z} & \frac{\partial}{\partial y} \\ \frac{\partial}{\partial z} & 0 & \frac{\partial}{\partial x} \end{bmatrix} \begin{Bmatrix} u \\ v \\ w \end{Bmatrix} \tag{1.23}$$

where $\mathcal{S}$ is a differential operator and the strain $\boldsymbol{\varepsilon}$ is written in six independent components.

Equilibrium equations

The equilibrium equations for the three-dimensional behaviour of a solid is shown as below matrix form:

$$\mathcal{S}^{\mathrm{T}}\boldsymbol{\sigma} + \boldsymbol{b} = 0 \tag{1.24}$$

where $\mathcal{S}$ is the same differential operator as that given in Eq. 1.23, and $\boldsymbol{\sigma}$ is the array of stresses, which are ordered as:

$$\boldsymbol{\sigma} = [\sigma_x, \sigma_y, \sigma_z, \tau_{xy}, \tau_{yz}, \tau_{zx}]^{\mathrm{T}} \tag{1.25}$$

and $\boldsymbol{b}$ is the vector of body forces given as:

$$\boldsymbol{b} = \begin{Bmatrix} b_x \\ b_y \\ b_z \end{Bmatrix} \tag{1.26}$$

Boundary Conditions

Boundary conditions must be specified for each point on the surface of the solid. There are two types of boundary conditions: (1) displacement boundary conditions and (2) traction boundary conditions. Thus, we separate the boundary into two parts, Γ_u for the displacement conditions and Γ_t for the traction conditions.

Displacement boundary conditions are specified at each point of the boundary Γ_u as:

$$\boldsymbol{u} = \bar{\boldsymbol{u}} \tag{1.27}$$

where $\bar{\boldsymbol{u}}$ are known values of displacement boundary condition. Traction boundary conditions are specified for each point of the boundary Γ_t and are given in terms of stresses as:

$$\boldsymbol{t} = \mathcal{G}^{\mathrm{T}}\boldsymbol{\sigma} = \bar{\boldsymbol{t}} \tag{1.28}$$

in which $\bar{\boldsymbol{t}}$ is the known values of the traction boundary condition, and $\mathcal{G}^{\mathrm{T}}$ is the matrix as:

$$\mathcal{G}^{\mathrm{T}} = \begin{bmatrix} n_x & 0 & 0 & n_y & 0 & n_z \\ 0 & n_y & 0 & n_x & n_z & 0 \\ 0 & 0 & n_z & 0 & n_y & n_x \end{bmatrix} \tag{1.29}$$

where n_x, n_y, n_z are the direction cosines for the outward pointing normal to the boundary Γ_t, and the matrices $\mathcal{G}$ and $\mathcal{S}$ have identical non-zero components in the structure.

Elasticity Matrix

The stress–strain equations, also known as constitutive relations, for a linear elastic material can be expressed as:

$$\boldsymbol{\sigma} = \bar{\mathbf{D}}(\boldsymbol{\varepsilon} - \boldsymbol{\varepsilon}_0) + \boldsymbol{\sigma}_0 \tag{1.30}$$

or, equivalently:

$$\boldsymbol{\varepsilon} = \bar{\mathbf{D}}^{-1}(\boldsymbol{\sigma} - \boldsymbol{\sigma}_0) + \boldsymbol{\varepsilon}_0 \tag{1.31}$$

where the $\bar{\mathbf{D}}$ is the elasticity matrix of moduli for the material, and $\boldsymbol{\sigma}_0$ and $\boldsymbol{\varepsilon}_0$ are the initial stress and initial strain, respectively.

Table 1.2: Relations Between Isotropic Elastic Constants*

Parameters	E, ν	K, G	λ, μ
$E =$	–	$9KG/(3K + 2G)$	$\mu(3\lambda) + 2\mu/(\lambda + \mu)$
$\nu =$	–	$(3K - 2G)/(6K + 2G)$	$\lambda/(\lambda + \nu)/2$
$K =$	$E/(1 - 2\nu)/3$	–	$\lambda + 2\nu/3$
$G = \mu =$	$E/(1 + \nu)/2$	G	μ
$\lambda =$	$\nu E/(1 + \nu)/(1 - 2\nu)$	$K - 2G/3$	–

∗ Reproduced from [9]

One can write a general stress-strain expression for isotropic materials in terms of the six stress and strain terms. Any two independent elastic constants can be used in this expression. Here, the Young's modulus of elasticity, E, and Poisson's ratio, ν were used. The relationship between E, ν and other parameters commonly used in the literature is shown in Table 1.2. Using Cartesian coordinates, the expression is given by:

$$\begin{Bmatrix} \varepsilon_x \\ \varepsilon_y \\ \varepsilon_z \\ \gamma_{xy} \\ \gamma_{yz} \\ \gamma_{zx} \end{Bmatrix} = \frac{1}{E} \begin{bmatrix} 1 & -\nu & -\nu & 0 & 0 & 0 \\ -\nu & 1 & -\nu & 0 & 0 & 0 \\ -\nu & -\nu & 1 & 0 & 0 & 0 \\ 0 & 0 & 0 & 2(1+\nu) & 0 & 0 \\ 0 & 0 & 0 & 0 & 2(1+\nu) & 0 \\ 0 & 0 & 0 & 0 & 0 & 2(1+\nu) \end{bmatrix} \begin{Bmatrix} \sigma_x \\ \sigma_y \\ \sigma_z \\ \tau_{xy} \\ \tau_{yz} \\ \tau_{zx} \end{Bmatrix} \tag{1.32}$$

Inverting to obtain the appropriate $\bar{\mathbf{D}}$ matrix as:

$$\begin{Bmatrix} \sigma_x \\ \sigma_y \\ \sigma_z \\ \tau_{xy} \\ \tau_{yz} \\ \tau_{zx} \end{Bmatrix} = \frac{E}{d} \begin{bmatrix} (1-\nu) & \nu & \nu & 0 & 0 & 0 \\ \nu & (1-\nu) & \nu & 0 & 0 & 0 \\ \nu & \nu & (1-\nu) & 0 & 0 & 0 \\ 0 & 0 & 0 & (1-2\nu)/2 & 0 & 0 \\ 0 & 0 & 0 & 0 & (1-2\nu)/2 & 0 \\ 0 & 0 & 0 & 0 & 0 & (1-2\nu)/2 \end{bmatrix} \begin{Bmatrix} \varepsilon_x \\ \varepsilon_y \\ \varepsilon_z \\ \gamma_{xy} \\ \gamma_{yz} \\ \gamma_{zx} \end{Bmatrix} \tag{1.33}$$

where $d = (1+\nu)(1-2\nu)$. The form of d limits the value of ν to keep the material parameters positive. So one can get:

$$-1 < \nu < \frac{1}{2}$$

The case of $\nu = \frac{1}{2}$ indicates the material is incompressible. Generally, no material can be incompressible and only the case where $\nu \to \frac{1}{2}$ is of interest. A good example is the rubber bushing modelling, which will be discussed in Chapter 4.

For anisotropic linear elastic materials, one may write a general stress and strain relationship as:

$$\begin{Bmatrix} \sigma_x \\ \sigma_y \\ \sigma_z \\ \tau_{xy} \\ \tau_{yz} \\ \tau_{zx} \end{Bmatrix} = \bar{\mathbf{D}} = \begin{bmatrix} D_{11} & D_{12} & D_{13} & D_{14} & D_{15} & D_{16} \\ D_{21} & D_{22} & D_{23} & D_{24} & D_{25} & D_{26} \\ D_{31} & D_{32} & D_{33} & D_{34} & D_{35} & D_{36} \\ D_{41} & D_{42} & D_{43} & D_{44} & D_{45} & D_{46} \\ D_{51} & D_{52} & D_{53} & D_{54} & D_{55} & D_{56} \\ D_{61} & D_{62} & D_{63} & D_{64} & D_{65} & D_{66} \end{bmatrix} \begin{Bmatrix} \varepsilon_x \\ \varepsilon_y \\ \varepsilon_z \\ \gamma_{xy} \\ \gamma_{yz} \\ \gamma_{zx} \end{Bmatrix} \tag{1.34}$$

For an elastic material, the $\bar{\mathbf{D}}$ matrix must be symmetric, meaning $\bar{D}_{ij} = \bar{D}_{ji}$. This will make a possibility of 21 individual elastic constants for a general anisotropic linear problem.

Virtual Work Expression

The previous content describes the governing equations for three-dimensional behaviour of solids. The next step is to do the finite element approximation in order to use all the governing equations to solve the problem. To illustrate the process, one should consider the virtual work expression given by:

$$\int_\Omega \delta\boldsymbol{\varepsilon}^{\mathrm{T}}\boldsymbol{\sigma}\, \mathrm{d}\Omega - \int_\Omega \delta\boldsymbol{u}^{\mathrm{T}}\boldsymbol{b}\, \mathrm{d}\Omega - \int_\Gamma \delta\boldsymbol{u}^{\mathrm{T}}\boldsymbol{t}\, \mathrm{d}\Gamma = 0 \tag{1.35}$$

where Ω is the solid volume in the problem domain, Γ is the external boundary surface of the solid, $\delta\boldsymbol{\varepsilon}$ and $\delta\boldsymbol{u}$ are the virtual strain and virtual displacement, respectively. To simplify the solution process, the boundary can be split into Γ_u and Γ_t, and the known traction boundary conditions can be introduced. Assuming the virtual displacement $\delta\boldsymbol{u}$ vanishes on Γ_u, and introducing the constitutive equation given by Eq. 1.30, simplifies the virtual work equation to:

$$\int_\Omega \delta\boldsymbol{\varepsilon}^{\mathrm{T}} \left[\bar{\mathbf{D}}(\boldsymbol{\varepsilon} - \boldsymbol{\varepsilon}_0) + \boldsymbol{\sigma}_0\right]\, \mathrm{d}\Omega - \int_\Omega \delta\boldsymbol{u}^{\mathrm{T}}\boldsymbol{b}\, \mathrm{d}\Omega - \int_{\Gamma_t} \delta\boldsymbol{u}^{\mathrm{T}}\bar{\boldsymbol{t}}\, \mathrm{d}\Gamma = 0 \tag{1.36}$$

with the constraint $\boldsymbol{u} = \bar{\boldsymbol{u}}$ on Γ_u.

In the finite element solution, the equation is divided into the sums of individual elements as an approximation, giving the 'weak' form of the equation:

$$\sum_e \int_{\Omega^e} \delta\boldsymbol{\varepsilon}^{\mathrm{T}} \left[\bar{\mathbf{D}}(\boldsymbol{\varepsilon} - \boldsymbol{\varepsilon}_0) + \boldsymbol{\sigma}_0\right]\, \mathrm{d}\Omega - \sum_e \int_{\Omega^e} \delta\boldsymbol{u}^{\mathrm{T}}\boldsymbol{b}\, \mathrm{d}\Omega - \sum_e \int_{\Gamma_t{}^e} \delta\boldsymbol{u}^{\mathrm{T}}\bar{\boldsymbol{t}}\, \mathrm{d}\Gamma = 0 \tag{1.37}$$

where Ω^e and ${\Gamma_t}^e$ denote the volume in element domains and traction boundaries of any element. The 'approximation' in this step results from two sources: the sum of element domains Ω^e is not always exactly equal to Ω, nor is the sum of ${\Gamma_t}^e$ exactly equal to Γ_t.

Displacement and Strain Approximation

To finish the displacement and strain approximation, the displacement expression can be written in terms of a shape function:

$$\boldsymbol{u} \approx \sum_a N_a \tilde{\boldsymbol{u}}_a \tag{1.38}$$

where $\tilde{\boldsymbol{u}}_a$ is the nodal value of the displacement, and N_a is the shape function. Different element shapes will have different shape functions N_a. More detail can be found in Zienkiewicz et al[9]. A similar expression can be written for $\boldsymbol{\varepsilon}$:

$$\boldsymbol{\varepsilon} \approx \sum_a \begin{bmatrix} \frac{\partial N_a}{\partial x} & 0 & 0 \\ 0 & \frac{\partial N_a}{\partial y} & 0 \\ 0 & 0 & \frac{\partial N_a}{\partial z} \\ \frac{\partial N_a}{\partial y} & \frac{\partial N_a}{\partial x} & 0 \\ 0 & \frac{\partial N_a}{\partial z} & \frac{\partial N_a}{\partial y} \\ \frac{\partial N_a}{\partial z} & 0 & \frac{\partial N_a}{\partial x} \end{bmatrix} \tilde{\boldsymbol{u}}_a = \sum_a B_a \tilde{\boldsymbol{u}}_a \tag{1.39}$$

Similar expressions may be written for virtual displacement and strain.

Stiffness and Load Matrices

Introducing the above approximation in the weak form Eq. 1.37, results in:

$$\sum_e \delta\tilde{\boldsymbol{u}}_a{}^{\mathrm{T}} \left[\int_{\Omega^e} B_a{}^{\mathrm{T}} [\bar{\mathbf{D}}(B_b \tilde{\mathbf{u}}_b - \boldsymbol{\varepsilon}_0) + \boldsymbol{\sigma}_0] \, \mathrm{d}\Omega - \int_{\Omega^e} N_a \boldsymbol{b} \, \mathrm{d}\Omega - \int_{{\Gamma_t}^e} N_a \bar{\boldsymbol{t}} \, \mathrm{d}\Gamma \right] = 0 \tag{1.40}$$

where $\delta\tilde{\boldsymbol{u}}_a$ is the nodal displacement for the virtual strain, B_a is the differential operator with the shape function for the virtual strain, $\tilde{\mathbf{u}}_b$ is the nodal displacement for the total strain, and B_b is the differential operator with the shape function for the total strain. Summing the element integrals, and recognizing that the result must hold for any an arbitrary value for $\delta\tilde{\boldsymbol{u}}_a$, gives the linear equation for the system:

$$K_{ab}\tilde{\mathbf{u}}_b + f_a = 0 \tag{1.41}$$

where:

$$K_{ab} = \sum_e \int_{\Omega^e} B_a{}^{\mathrm{T}} \bar{\mathbf{D}} B_b \, \mathrm{d}\Omega \tag{1.42}$$

and:

$$f_a = \sum_e \int_{\Omega^e} [B_a{}^{\mathrm{T}} (\boldsymbol{\sigma}_0 - \bar{\mathbf{D}}\boldsymbol{\varepsilon}_0) - N_a \boldsymbol{b}] \, \mathrm{d}\Omega - \sum_e \int_{{\Gamma_t}^e} N_a \bar{\boldsymbol{t}} \, \mathrm{d}\Gamma \tag{1.43}$$

By using a proper integration method, the system stiffness and load matrices can be evaluated. As a summary, the finite element solution should be solved by following steps:

- Use the virtual work (or weak form) equations for system equilibrium.
- Introduce an approximation for the displacement field $\boldsymbol{u}$ in terms of shape functions.
- Relate strains and stresses using the constitutive relationship.
- Perform the integration over each element.
- Assemble the element results to form the global stiffness and load matrices.
- Apply the known traction and displacement boundary conditions.
- Evaluate the resulting stiffness and load matrices.
- Solve the linear system for the nodal displacements.

1.8 Literature Review

Based on a search of the literature, the number of works that focus on the same suspension component using the same manufacturing method or materials that have been proposed in this research is very sparse. However, some similar topics of study can be presented.

Mahdi et al[10] tested a lightweight composite elliptic spring for a vehicle suspension based on an elliptical shape configuration. A FEA model was built using 36 constituent properties according to the chosen woven roving glass/epoxy material. Different spring rates corresponding to the ellipticity ratios were reported. A fatigue analysis was also conducted. The conclusion showed hybrid composite elliptical springs have better fatigue behaviour than the conventional and composite leaf and coil springs.

Davide[11] modelled a composite rear suspension cradle in Abaqus® based on the different directional constitutive properties in each lamina of the composite material. Different stacking angles and thicknesses of laminates were tested. The stiffness values in the different directions were reported and compared with the conventional aluminum cradle outputs. A 7.45% weight savings was stated in the conclusion.

In[12], Doody developed analytical laminated cylinder model through Matlab® code to evaluate the elastic response of a composite automotive anti-roll bar. Physical testing and finite element method were used to predict elastic response of an existing steel anti-roll bar. By comparing the results from computational predictions, it was expected to have a mass that is 63% less than the steel bar.

Honickman[13] proposed a novel hybrid composite co-pultruded structural member design that potentially offers a variety of benefits for applications in the aerospace and/or automotive

industries. An analytical model built in Matlab® was developed to improve the mechanical response prediction of targeted structural members. Some shortcomings in the current analytical models were stated. The designed model was computationally validated through coupled flexural-torsional-shear buckling analyses using the finite element method. An experimental program was also carried out to validate the analytical model.

Kim et al[14] designed a carbon fibre reinforced composite automotive lower arm with an optimized stacking sequence of the composite layers. Static and buckling analyses were conducted using the finite element method. A failure analysis using the Riks method and based on the Tsai-Wu failure criterion was performed according to the optimized stacking angles. By comparing failure prediction with the conventional steel lower arm analysis results, a 2.2 times higher failure load was found for composite lower arm, along with a 50% weight reduction.

Liu et al[15] designed a carbon twill weave fabric composite body structure for an electric vehicle. A finite element model of a representative volume element in a laminate composite was established to characterize the elastic properties of the targeted material using the homogenization technique. The geometric parameters of the representative volume element were measured from a T300 carbon twill weave fabric composite sample using optical microscopy. The numerical elastic properties were compared with those from uniaxial tensile and three point bending physical tests. Finally, the confirmed constitutive model of the composite material was applied to a crash and side pole impact analysis for an electric vehicle body structure. Results showed that the body structure made from the carbon fibre reinforced plastic provided a 28% weight saving compared with glass fibre reinforced plastic.

Chavhan and Wankhade[16] manufactured a leaf spring from a composite material (60% by weight of E-glass unidirectional fibre and 40% epoxy matrix) using a hand lay-up fabrication technique. Physical bending and hardness testing were conducted on the manufactured spring. After a bending test was done on the spring, a micro-structural analysis was completed using a scanning electron microscope. The results showed that the bonding between the fibre and the matrix was poor due to the low weight fraction of resin. Also, the fibre pullout and delamination could be observed due to the bending load. A potential 75% weight reduction was stated in the conclusion.

Anandakumar et al[17] developed an efficient short/continuous fibre thermoplastic composite automobile suspension upper control arm. During the study, a proposed improvement was applied to the short fibre injection moulded composite material by inserting the continuous fibre in the critical locations of the arm. The mechanical properties of the composite material were obtained from a physical tensile test. Then, the measured mechanical properties were used in a static finite element analysis of the arm. The testing loads were calculated through the dynamic simulation of an existing steel control arm according to the gross vehicle weight and 40:60 weight distribution. The results showed that the continuous fibre inserts with short fibre thermoplastic composites material has better performance compared to steel or short fibre composites. A maximum 67.86% weight reduction was achieved.

As stated previously, the studies on similar topics have mainly focused on composite materials with the configuration of unidirectional fibres or multiple unidirectional fibre/matrix laminar stacking. They rarely consider a systematic process of numerical modelling and testing using multiple different simulations. Plastic deformation and failure prediction are usually not deeply discussed or shown in the final results. These shortcomings in the studies indicatess that the proposed methodology and analysis of this research has value and will contribute to the body of knowledge in the area.

Some literature relevant to the methodology used in this research will be further discussed in each separate chapter.

1.9 Dissertation Structure

As discussed previously, the objective of this research is to obtain knowledge regarding the potential replacement of metal load-bearing vehicle components with composite material alternatives. In particular, the goal is to do a stress analysis of a FRP vehicle suspension lower arm under specific loading conditions that are defined by different driving scenarios from a dynamics simulation. Associated with this research, there are three different aspects of simulation or analysis that need to be done to achieve this goal.

- The multi-body dynamics simulation is used for determination of loads in FEA
- The manufacturing process simulation is using for definition of FRP material properties in FEA
- The FEA is used for the final stress analysis of FRP suspension lower arm in the appropriate loading case

These three types of simulation process and relevant related content will be divided into three chapters.

Chapter 2 describes the multi-body dynamics simulation. It describes the full-car simulation modelling, the random road implementation, the braking and cornering driver model, and provides a discussion of the force results from the suspension lower arm ball joint.

The manufacturing process simulation will be discussed in Chapter 3. The methodology of building a Moldflow® model will be introduced, and the concept of mapping fibre orientation results into FEA model will be shown. Finally, a summary of fibre orientation results will be made at the end of the chapter.

Chapter 4 will focus on the FEA. The process of building the lower arm model in the FEA software will be discussed. Many simulations will be shown, including the rubber bushing modelling, the tensile test simulation on the FRP material samples, and the FRP lower arm simulation using different loading cases. At the end, a brief discussion will be made about the simulation results.

In Chapter 5, the conclusions are stated based on the performance of the composite lower arm in each level of road. The limitations regarding each analysis are summarized. Several design recommendations are given based on the process of generating each numerical model. Finally, potential future works are summarized.

Chapter 2

Dynamics Simulation

As mentioned in Chapter 1, dynamic simulation is the key to determine the loads that are used in the associated FEA analysis. To ensure that the FEA results are reasonable, a more realistic and complete dynamics simulation model is necessary. The complete process of defining a dynamics simulation model will be discussed in this chapter. At the end of this chapter, the force results summary process from several simulation cases will discussed.

2.1 Motionview® Modelling

2.1.1 Full Car Model

A full car model has been built using the 'assembly wizard' tool in Altair's Motionview® multi-body dynamics software. In this program, one needs to specify the necessary information to build the full car model, including the configuration of the front and rear suspension systems, the type of steering system, the drive-line configuration and the tire model. The following configurations were chosen for the full car model: The front suspension configuration was a MacPherson strut type system with a wishbone lower control arm. A front wheel drive configuration was chosen in the model of the drive-line. The rear suspension configuration was also a MacPherson strut type system with two lower control links and a tension bar attached to the rear knuckle. The MF-Swift tire model was chosen to account for the complex force response between the tire and the road. A schematic of this tire model is shown in Figure 2.1. The rack and pinion type steering system was chosen, which included the steering wheel and steering column.

After all the settings were chosen, the software generated the multi-body full car system using default properties, including the inertia properties of each body, and the stiffness and damping values of the springs and rubber bushings. The inertia values of the vehicle body were redefined so that they were more representative of a small household passenger car; in this research, values from the 1992 Honda Accord LX are used. The inertial data of the Honda was measured and reported by Heydinger et al[18]. As shown in Table 2.1, the full car model was adjusted according to the second row parameters. The first row parameters represent the whole vehicle, including

the suspension, wheels, steering system and so on. But in the full car model, the suspension components, wheels, and steering system components have been defined as individual bodies in the model. The mass values for all the individual bodies are shown in Table 2.2. A simple calculation will give the fraction between total individual body mass and the whole vehicle mass. This fraction is equal to 0.127 in this case. The proportion factor is equal to $1 - 0.127 = 0.873$. So the mass of vehicle chassis body in the full car model was set to $1730.8 - 219.6 = 1511.2$ kg. The moment of inertia value also needed to be scaled by the proportion factor in order to be used in the full car model. This will be an approximation for the moment of inertia value. Because the total mass of the individual bodies is relatively small compared to the whole vehicle body, it was assumed that this choice will give reasonable values. The inertia values of other bodies except the lower control arm, have minimal effect on the outcome, so the default value were used. Similarly, the damping value of the rubber bushings will not have a substantial effects on the final force results, so again, the default values were used.

There were 53 individual rigid bodies included in the full car model. The full list, without the vehicle chassis body, is given in Table 2.2. The anti-roll bars in the full car model were modelled as 19 individual flexible bodies. There were two anti-roll bars, located in the front suspension and rear suspension, respectively. For the front and rear anti-roll bars alone, there were 38 bodies in total, adding significantly to the size of the model. Several of the joints between the various bodies were modelled as 'compliance joints', meaning that they are treated as a stiffness, rather than as a constraint. Using compliance joints tends to increase the number of degrees of freedom in the model. Without considering the tire model, running a linear analysis on the full car model, without either front or rear anti-roll bars, gave a total of 165 eigenvalues. When including both the front and rear anti-roll bars, the total eigenvalue count increases to 668. This means that the final full car model had the equivalent of 334 degrees of freedom.[1] The allowed motions of course include bounce, pitch, roll, yaw, etc., plus motion of the individual suspensions and wheel rotations, plus deflection of the individual suspension elements within the suspension mechanism. This is an indication that the generated full car system was a high fidelity model and was capable of providing reasonable results for the proposed simulations.

In the following sections, the more important modelling parameters will be discussed.

Table 2.1: Honda Accord LX Inertia Parameters

	Moments of Inertia[kg·m^2]			
	Pitch	Roll	Yaw	Mass[kg]
Original value	2,891	541	2,922	1,730.78
Adjusted value	2,524.13	472.35	2,551.2	1,511.21

[1]Each degree of freedom is generally modelled as a second order differential equation that has two eigenvalues, but in some cases, first order equations may also be included in the system, e.g., when a spring and damper act in series.

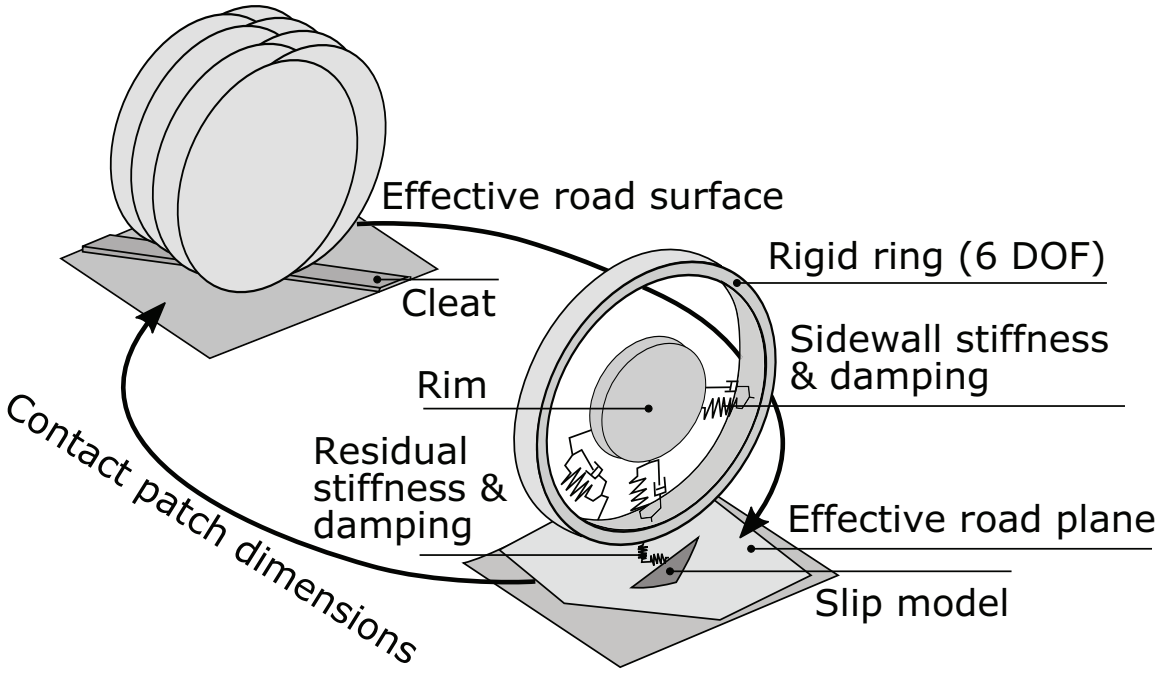

Figure 2.1: Schematic of Tire Model (Reproduced from [19])

2.1.2 Lower Control Arm Parameters

The lower control arm is the component with the main focus in this research. As shown in Figure 2.2, the Computer Aided Design (CAD) drawing is based on this actual lower control arm. A few small adjustments have been made during the CAD drawing to simplify the model and make the simulation less problematic. The inertial values and Centre of Gravity (CG) location of the lower control arm were obtained from the CAD model. By using the mass properties function in the CAD software, the mass properties were calculated and are shown in Table 2.3. The position of each connection point relative to the CG is measured in the software, as shown in Figure 2.3. The lower control arm parameters in the full car model were adjusted according to these values.

Figure 2.2: Actual lower control arm and CAD drawing

Table 2.2: Individual body mass value in full car model, excluding the vehicle chassis

Bodies	Mass[kg]	Bodies	Mass[kg]
Front knuckle ×2	6	Middle steering column internal Shaft	1
Front lower control arm ×2	3.87	Lower column internal Shaft	1
Front wheel ×2	40	Rear wheel ×2	40
Front wheel hub ×2	20	Rear wheel hub ×2	30
Front strut rod ×2	2	Rear knuckle ×2	18
Front strut tube ×2	2	Rear suspension front lower link ×2	8
Front anti-roll bar drop link ×2	0.6	Rear suspension rear lower link ×2	4
Steering tierod ×2	2	Rear suspension tension strut ×2	4
Steering rack	2	Rear strut rod ×2	2
Steering rack housing	8	Rear strut tube ×2	2
Steering connection Pinion	1	Rear anti-roll bar drop link ×2	0.6
Steering dummy body	5×10^{-3}	Drive-line halfshaft Plunge Body ×2	3
Steering wheel	5	Drive-line halfshaft ×2	7
Upper steering column Shaft	1	Drive-line differential	8.5
Lower steering column Shaft	1	Drive-line output shaft ×2	3
Upper steering column internal Shaft	1	Drive-line pinion	2
Total number of bodies	52		
Total mass	219.57		

2.1.3 Suspension Spring Stiffness and Damping Confirmation

The spring stiffness and damping of the suspension system is defined by a default value. Because the vehicle chassis body mass has been increased to 1.51 times the default value, the spring stiffness and damping value also need to be increased to be representative of a typical passenger car. After the change, the values need to be verified to ensure the results are reasonable. A linear analysis model was built to ensure the natural frequencies are in a reasonable range. In the linear analysis, the software will calculate the eigenvalues and normal modes of the equations of motion. The eigenvalues indicate the stability and natural frequencies of the vibrational modes. The normal modes describe the motion patterns of vibrating systems. For a typical vehicle model, one should expect the suspension bounce motion frequency is around 1 Hz and the wheel hop motion frequency is around 10 Hz, with damping ratios around 0.2[20]. As shown in Table 2.4, the results were in the typical range, meaning the spring stiffness and damping setting was acceptable for the full car model.

Table 2.3: Mass properties of lower control arm

		Moments of Inertia[kg·mm^2]					
Density[kg/mm^3]	Mass[kg]	Ixx	Iyy	Izz	Ixy	Ixz	Iyz
1.21×10^{-6}	1.93	32,212.05	22,255.26	54,157.14	−18,081.48	12.38	−62.64

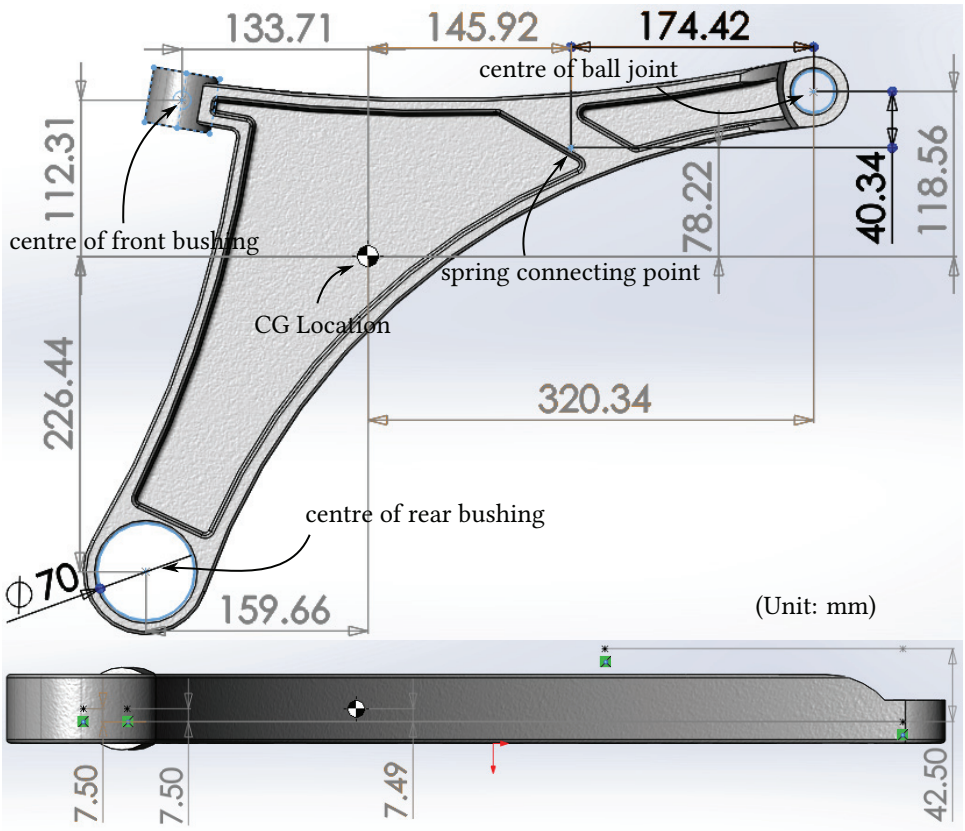

Figure 2.3: CAD drawing of lower control arm and relative position of connection point

2.1.4 Front Suspension Rubber Bushing Properties

The rubber bushing properties will have a smaller effect on the final force results of dynamics simulation, but they certainly have an influence on the stress analysis of the control arm, because the rubber bushing was modelled as a solid part in the FEA model. More details about the rubber bushing model will be discussed in Chapter 4. To ensure that the model properties were consistent between each software, the rubber bushing properties of the full car model in the front suspension were adjusted to an appropriate value, defined by a series of points on the force vs displacement relationship curves. These curves are obtained by related FEA simulations of the solid rubber bushing model. The rubber bushing properties in the rear suspension were left at the default values.

2.2 3D Random Road Implementation

Road unevenness generates vibration that increases the dynamic loading during the dynamics simulation, so it is important to count the road surface irregularities in the dynamic simulation. To make sure the multi-body dynamics model is realistic, a 3D random road surface should be used in the simulation. A 3D random road is a better way to describe the road condition when

Table 2.4: Full Car Model Linear Analysis Results

Normal Modes	Natural frequency[Hz]	Damping Ratio	Real[Hz]	Imaginary[Hz]
Front suspension bounce	1.4257×10^{0}	1.1976×10^{-1}	-1.7075×10^{-1}	$\pm 1.4155 \times 10^{0}$
Rear suspension bounce	1.7289×10^{0}	1.3725×10^{-1}	-2.3729×10^{-1}	$\pm 1.7126 \times 10^{0}$
Vehicle body rolling	2.2241×10^{0}	1.5289×10^{-1}	-3.4004×10^{-1}	$\pm 2.1979 \times 10^{0}$
Rear wheel bounce(in phase)	1.2586×10^{1}	2.2211×10^{-1}	-2.7956×10^{0}	$\pm 1.2272 \times 10^{1}$
Rear wheel bounce(out phase)	1.2812×10^{1}	2.2671×10^{-1}	-2.9046×10^{0}	$\pm 1.2478 \times 10^{1}$
Front wheel bounce(in phase)	1.3504×10^{1}	2.3011×10^{-1}	-3.1074×10^{0}	$\pm 1.3141 \times 10^{1}$
Front wheel bounce(out phase)	1.3757×10^{1}	2.4151×10^{-1}	-3.3224×10^{0}	$\pm 1.3349 \times 10^{1}$

compared to the 2D random road. For a 2D random road, when the vehicle movement direction has a component perpendicular to the road profile axis, the road elevation data may not change. In that case, the simulation will lose the random road effects, which is clearly not the actual situation. In this section, the definition of the 2D random road will be discussed, along with the method of creating a 3D random road from two 2D random road profiles.

2.2.1 2D Random Road

A 2D random road profile can be generated by summing a series of sine waves of increasing frequency and random phase angles, with amplitudes that decrease proportionally with the wavelength. The amplitude of these sine waves determine the road roughness level according to the Power Spectral Density (PSD) value of the vertical displacements G_d. The G_d is expressed as a function of spatial frequency n cycles/m. Based on the International Organization for Standardization (ISO) 8608, the road roughness classification is based on the PSD, calculated in correspondence with conventional values of spatial frequency n_0=0.1 cycles/m[21]. As shown in Table 2.5, 8 classes of roads are identified from class A to class H.

Table 2.5: ISO 8608 values of $G_d(n_0)$*

Road Class	$G_d(n_0)[10^{-6}\mathrm{m}^3]$	
	Lower limit	Upper limit
A	--	32
B	32	128
C	128	512
D	512	2048
E	2048	8192
F	8192	32768
G	32768	131072
H	131072	--
	n_0=0.1 cycles/m	

∗ Reproduced from [22]

At the same time, ISO 8608 provides that the roughness of a road profile can be defined using the equation:

$$G_d(n) = G_d(n_0) \cdot \left(\frac{n}{n_0}\right)^{-2} \tag{2.1}$$

where the value of $G_d(n_0)$ must be derived from Table 2.5, corresponding to different road class. For general use, base on the ISO road roughness classification, one can generate a random road profile through a harmonic function in terms of the function of PSD of vertical displacements obtained by the Fourier transform of the auto-correlation function.

Consider a continuous road profile, for defined values of spatial frequency n within an equally spaced interval Δn. The value of the PSD function is defined by the following expression[20]:

$$G_d(n) = \lim_{\Delta n \to 0} \frac{{\psi_x}^2}{\Delta n} \tag{2.2}$$

where ${\psi_x}^2$ is the mean square value of the component of the signal. If the length of road profile is L and the sampling interval is B, the maximum theoretical sampling spatial frequency is n_{max}=1/B, and within the frequency domain, discretized spatial frequency values n_i are equally spaced with an interval of Δn=1/L. The generic spatial frequency value n_i can be expressed as $i \cdot \Delta n$ and Eq. 2.2 can be written in the discrete form:

$$G_d(n_i) = \frac{{\psi_x}^2(n_i, \Delta n)}{\Delta n} = \frac{{\psi_x}^2(i \cdot \Delta n, \Delta n)}{\Delta n} \tag{2.3}$$

where i is varying from 0 to N=n_{max}/Δn. Now consider the road profile can be described by a simple harmonic function as:

$$h(\tilde{x}) = A_i \cos(2\pi n_i \tilde{x} + \varphi) = A_i cos(2\pi i \Delta n \tilde{x} + \varphi) \tag{2.4}$$

where A_i is the amplitude, n_i is the spatial frequency and φ is the phase angle. The mean square value of this harmonic signal is:

$${\psi_x}^2 = \frac{{A_i}^2}{2} \tag{2.5}$$

Substituting into Eq. 2.3 gives:

$$G_d(n_i) = \frac{{\psi_x}^2(n_i, \Delta n)}{\Delta n} = \frac{{A_i}^2}{2 \cdot \delta n} \tag{2.6}$$

If the PSD function of vertical displacements is known, one can generate a random road profile using Eq. 2.6 and assuming a random phase angle φ_i which varies within the $0 - 2\pi$ range. The random road profile can be described as:

$$h(\tilde{x}) = \sum_{i=0}^{N} A_i \cos(2\pi n_i \tilde{x} + \varphi_i) = \sum_{i=0}^{N} \sqrt{2\Delta n G_d(i\Delta n)} \cos(2\pi i \Delta n \tilde{x} + \varphi_i) \tag{2.7}$$

Substituting Eq. 2.7 into Eq. 2.1, a random road profile corresponding to an ISO classification can be generated by following equation:

$$h(\tilde{x}) = \sum_{i=0}^{N} \sqrt{\Delta n} 2^k 10^{-3} \left(\frac{n_0}{i\Delta n}\right) \cos(2\pi i \Delta n \tilde{x} + \varphi_i) \tag{2.8}$$

where $\tilde{x}$ is the longitudinal coordinate varying from 0 to L, Δn=1/L, N=L/B, and k is a constant value defined from ISO road profile classification. It is an integer changing from 3 to 9, corresponding to road roughness within the transition of class A to B, B to C, C to D, etc., as shown in Table 2.6.

Table 2.6: k values corresponding to ISO road roughness classification*

Road Class		k
Upper limit of	Lower limit of	
A	B	3
B	C	4
C	D	5
D	E	6
E	F	7
F	G	8
G	H	9

∗ Reproduced from [22]

The previous function can be coded in the MATLAB® environment to generate a random road with different k values. The specific MATLAB® codes that have been used in this research are listed in Appendix A.1. Figure 2.4 shows three curves of random road profiles generated by the codes with k values equal to 4, 6 and 8. As shown in the figure, the road is described as a two-dimensional profile that shows the vertical value of the road changing along with the longitudinal direction. The higher level of the road roughness results in more aggressive changes in the vertical value. Here, the level 4 road is a regular road as one might drive on daily, and the level 8 road is a extremely rough off-road style terrain.

2.2.2 3D Random Road

When considering the complex motion of a full car model during a simulation, a 2D random road does not represent the condition of a real road surface very well. A 3D random road will be a better representative of the real road, especially when the vehicle's moving direction is changing with time. The OpenCRG® library is an open source freely available tool-suite for the creation, modification and evaluation of 3D road surfaces. According to the definition of a 3D road in the

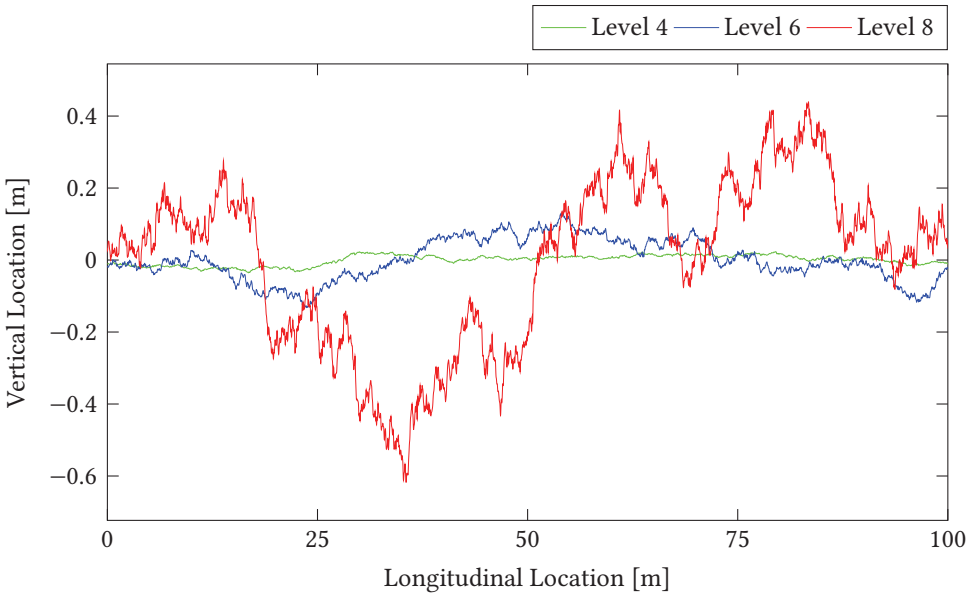

Figure 2.4: Sample Random Roads, level k=4, 6, 8, generated using the sum of sinusoids approach.

OpenCRG® user manual[23], there are two major data that need to be defined in a 3D road. One is the road reference line data which is complemented by slope values and defined by consecutive heading angles, and another one is the road elevation data in proximity of the reference line, which is defined by a matrix. By using some special purpose MATLAB® codes, the 3D random road elevation data can be defined by summing two 2D random road profiles in two perpendicular axes. In the following content, an example of this summing process will be demonstrated.

Suppose one has two 2D random road profiles. One is in the longitudinal direction, the other one is in the lateral direction. Both roads are 120 meters long, and the precision is 0.01 m, meaning each road profile will have 12000 points. These 2D random road profiles can expressed as:

$$z(x) = (x_i, z_{xi}) \quad (i = 1, 2, 3 \cdots 12000) \tag{2.9}$$

$$z(y) = (y_i, z_{yi}) \quad (i = 1, 2, 3 \cdots 12000) \tag{2.10}$$

In order to generate the 3D random road elevation data, one can sum each individual point in these two road profiles to form a gigantic matrix. In this case, a 12000 by 12000 points matrix was formed and expressed as:

$$z(x,y) = \begin{bmatrix} z_{x1}+z_{y1} & z_{x1}+z_{y2} & z_{x1}+z_{y3} & \cdots & z_{x1}+z_{y12000} \\ z_{x2}+z_{y1} & z_{x2}+z_{y2} & z_{x2}+z_{y3} & \cdots & z_{x2}+z_{y12000} \\ z_{x3}+z_{y1} & z_{x3}+z_{y2} & z_{x3}+z_{y3} & \cdots & z_{x3}+z_{y12000} \\ \vdots & \vdots & \vdots & \ddots & \vdots \\ z_{x12000}+z_{y1} & z_{x12000}+z_{y2} & z_{x12000}+z_{y3} & \cdots & z_{x12000}+z_{y12000} \end{bmatrix} \tag{2.11}$$

The previous matrix $z(x,y)$ represents the elevation data of a 120 meters by 120 meters road surface. After the elevation data has been defined, one can use some special purpose MATLAB® codes combined with the OpenCRG® tool-suite to implement these elevation data into a 3D road and define the reference line data of this 3D road. The detail of these MATLAB® codes can be found in Appendix A.2. As shown in Figure 2.5, the 3D random road surface is plotted in a local xyz coordinate and has its origin $(0,0,0)$ at the lower right corner. The lower right corner is chosen as the origin because the Motionview® software will treat this point as the road reference point when implementing this 3D road into a Motionview® simulation. In this way, the output of a Motionview® simulation and OpenCRG road will stay consistent. Also, by using this origin choice, one can easily adjust the location of the road reference point or rotate the direction of the road reference frame in Motionview® model in order to achieve different vehicle locations and initial motion directions.

After all the properties have been defined in an OpenCRG® road data set, one can write all the information into a $*$.crg file, which can be recognized by Motionview® tire models, or referenced by a Motionview® road data file ($*$.rdf). The difference between these two methods is whether the friction correction factor can be changed or not. Location dependant friction is not a key point in this research, so the default setting was chosen. After this $*$.crg file was referenced in the Motionview® tire modelling, this 3D random road surface has been used in the full car simulation. One can change the model parameters and the road reference point location in order to get different scenarios.

This 3D random road surface has been generated by summing two level 6 2D random roads. As mentioned in the previous section, the level of each individual 2D random road can be quantified by its PSD value at conventional values of spatial frequency n_0=0.1 cycles/m. Ideally, one should expect the final 3D random road will have same roughness level as each single 2D random road. However, the summing process may change road level to an unexpected value. So the final 3D random road still needs to be verified through a PSD calculation process. The details will be discussed in the next section.

2.2.3 3D Random Road Verification

There are two major points that need to be verified for a 3D random road:

- If the implementation in Motionview® is correct.
- If the roughness level is reasonable.

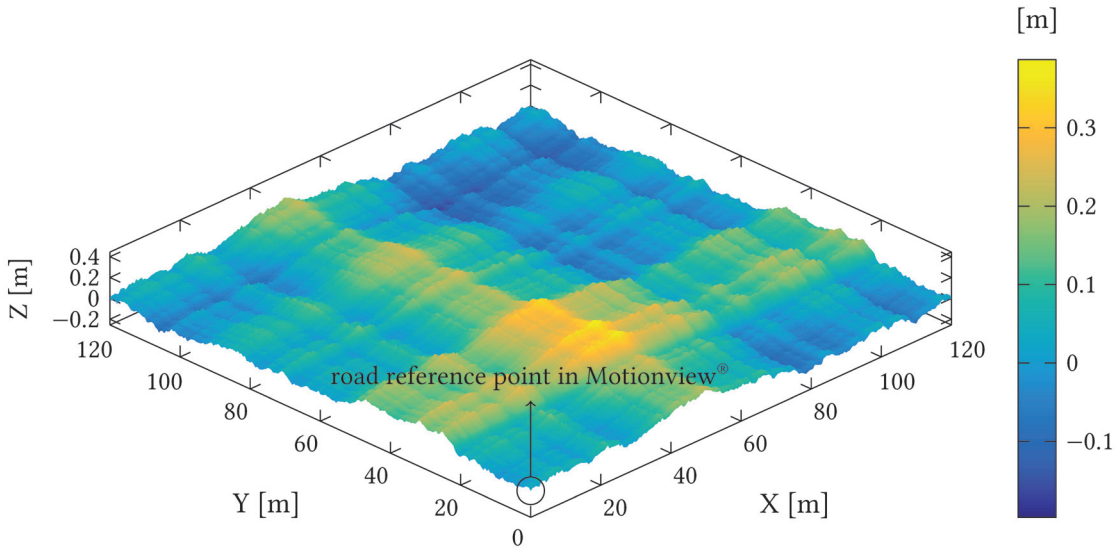

Figure 2.5: A 120 by 120 Meters 3D Random Road Surface Generated by OpenCRG® Tool-suite

One can verify these two points by using the Motionview® full car simulation and some specific MATLAB® codes. As mentioned in previous section, different vehicle motion scenarios can be created after the 3D road has been implemented. To confirm the result is as expected, four different vehicle motion scenarios have been generated. The first three scenarios are straight constant speed driving in a direction 30°, 45° and 60° from the origin of the 3D road surface. The last scenario is a circular motion with a constant radius around the centre of the 3D road surface. The four scenarios are illustrated in Figure 2.6. In the Motionview® full car simulation output, one can extract the (x, y, z) values of each wheel's contact patch location for each road profile. In order to verify that the implementation is correct, one can compare the z axis values with the OpenCRG ® road profile at the same x and y coordinate. This can be done by using an OpenCRG ® MATLAB® code named "`crg_eval_xy2z.m`". The code details can be found in Appendix A.3.

As shown in Figure 2.7, the compared z location values have been plotted in the 30° straight driving case. To simplify the results, only the results from the front-left wheel have been shown. The results on the front-left (and other wheels and other scenarios) shows a near perfect fitting between the two curves, meaning that the implementation of the 3D random road is successful. Next, the roughness level is verified by PSD calculation according to the contact patch z values.

In order to compare the results, the original 2D random road PSD plot is shown in Figure 2.8. The PSD value at conventional values of spatial frequency n_0=0.1 cycles/m (i.e., a 10 m wavelength) has been highlighted. The value is in the expected range. According to Table 2.5, the road class is in the middle of D to E range, which corresponds to a level 6 road. The PSD curve is a deceasing straight line along spatial frequency in logarithmic space. After the spatial frequency is beyond 10 cycles/m, the curve has a dramatic drop, because the shortest wavelength in the road has been set

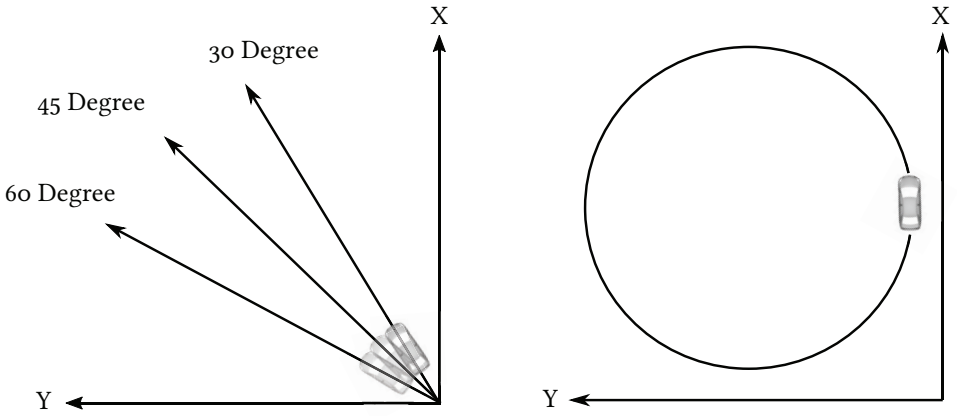

Figure 2.6: Four different driving scenarios were used to ensure the 3D random road surface was included into the Motionview® simulation as expected.

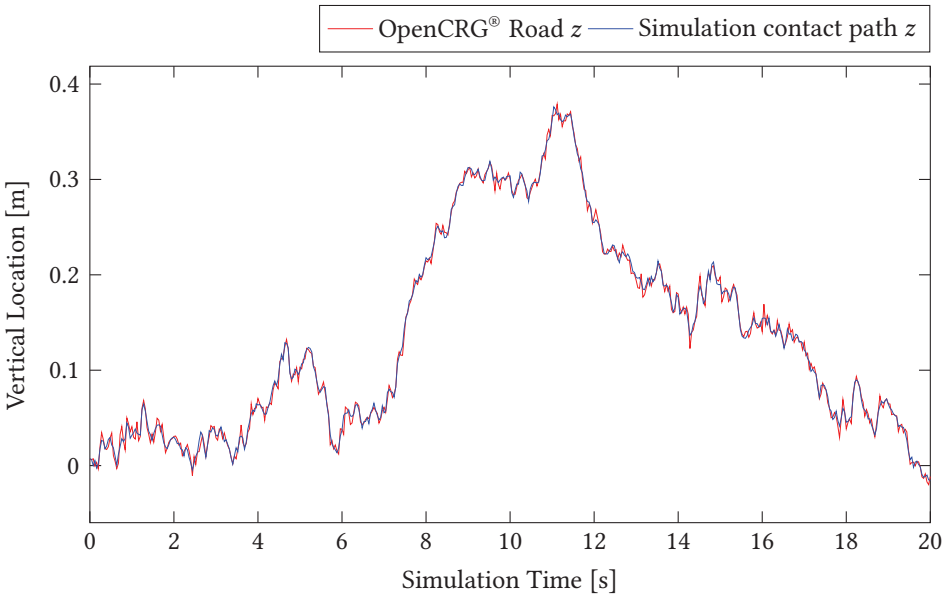

Figure 2.7: Road z Values Comparison for the Front-left Wheel in the 30° Straight Driving Case. Notice that the z value in the simulation corresponds almost exactly to the OpenCRG® value. Because the vehicle was moving, some small errors in the local area are apparent.

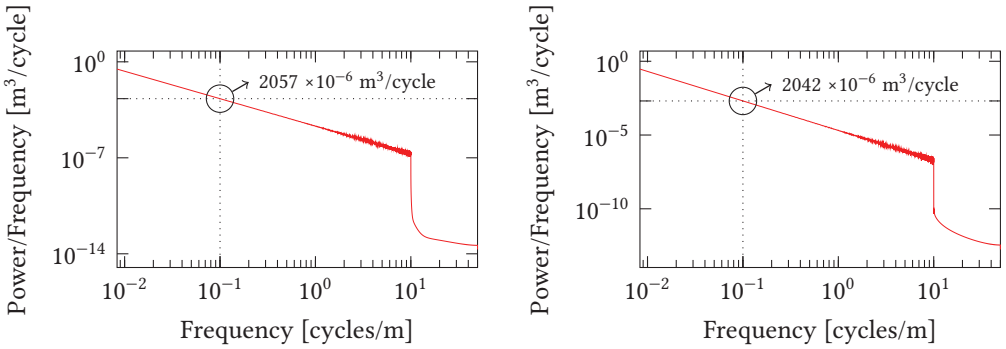

Figure 2.8: PSD of 2D Random Road in (left) Longitudinal Direction (right) Lateral Direction

to 0.1 m during the generation process. As there won't be any data captured beyond 10 cycles/m, the curve in this range can be ignored. The relevant MATLAB® codes used to ccompute this PSD curve can be found in Appendix A.4.

In any of the 3D scenarios, each wheel will have a different contact location in the z axis, so there will be four different contact patch locations for which a PSD value can be calculated for for each scenario. In order to simplify the presentation, only results from a specific wheel will be plotted. As shown in Figure 2.9, the PSD results from four different scenarios with four different wheels have been plotted. Also, the PSD value at the spatial frequency of n_0=0.1 cycles/m has been highlighted. By comparing these values with the values in Tables 2.5 and 2.6, one can estimate the road roughness level of this summed 3D random road surface. When comparing these PSD plots to the 2D random road PSD plots, one can see the results are no longer exactly a straight line in log-log space. In the 3D case, the data show some variation around around a linear trend that is decreasing with increasing spatial frequency. If one considers the summing process used to generate this 3D random road, this behaviour can be expected. The summing process is simply adding each single point in two 2D random road profiles. During this process, randomly, some points in each of the 2D road profiles will have out-of-phase values (i.e., one result will be positive, and the other negative). Summing these values will make the elevation data of the 3D random road level smaller than expected. On the other hand, some points will have in-phase values, making the sum larger than expected. This is the reason why the PSD curve has varying behaviour along the spatial frequency. But the mean values of this PSD curve are still based on a level 6 random road. As a result, there will be some uncertainty when defining the road roughness level of this 3D random road. Considering only the values at n_0=0.1 cycles/m does not show the level accurately. But by looking the value of each plot, one can see that they are all reasonably close to the expected value. In any case, a highly accurate measurement roughness level is not that important in this case. The level is close to a level 6, so the result is acceptable.

The 3D random road implementation has proved to be very successful. The results show the road roughness is close to the intended level and the behaviour is as expected. In the next section,

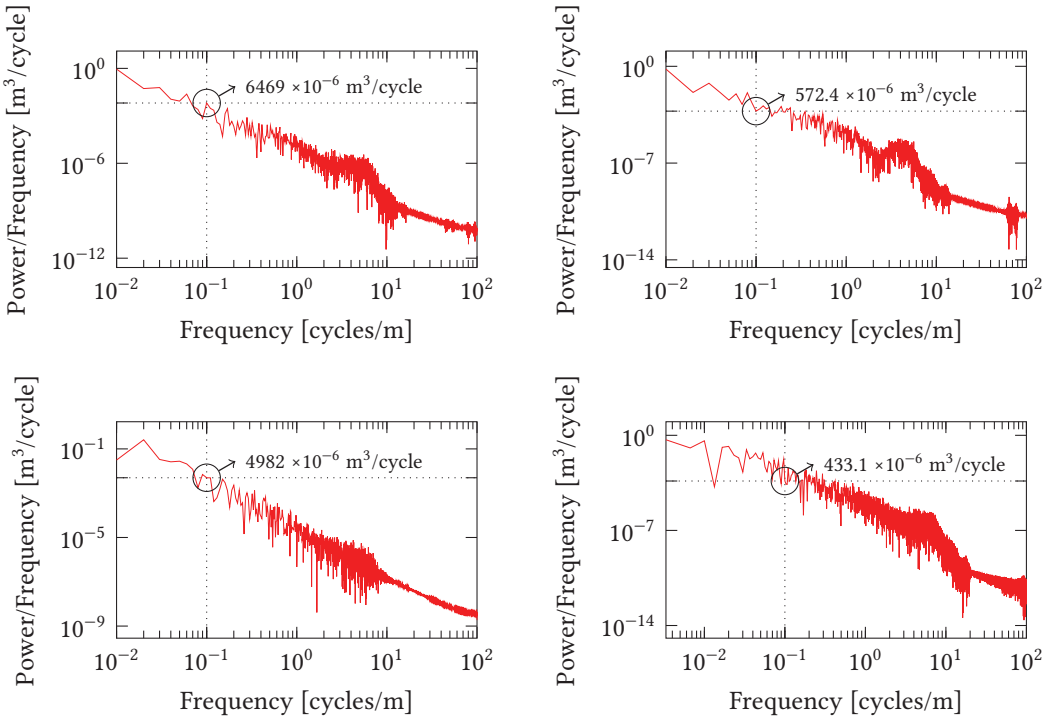

Figure 2.9: PSD of 3D Random Road data. Upper left: 30° path, front left wheel. Upper right: 45° path, front right wheel. Lower left: 60° path, rear left wheel. Lower right: Circular path, rear right wheel. Note that there is some expected variation away from a straight line, but the results are all close the expected range for a level 6 roughness

the different driving scenarios in the simulation will be be discussed.

2.3 Driving Scenario Implementation

Generally, it is expected that the lower control arm will carry more load when the vehicle is in a braking and cornering condition. However, to ensure that the force data from from the dynamics simulation is sufficient, many different vehicle handling scenarios should be included in the simulation. These scenario can first be separated into individual motions, such as constant speed, braking, and cornering, which can be studied separately. Combinations of these simple motions, such as cornering while braking, can be considered after. The details will be discussed in this section.

2.3.1 Constant Speed Motion

The complete scenario will be that the vehicle will start moving forward at constant speed for a certain length of time, and after that time will start braking at desired deceleration speed and

cornering at a constant radius. To make sure this scenario functions properly, the constant speed segment will be considered first. The constant speed motion can be achieved by:

- Creating a global dataset to define the initial speed for the vehicle body and wheel rotational speeds.
- Defining all the bodies in the model with correct initial speed according to the global dataset.
- Defining a proper drive torque value on the front axle.
- In order to keep the constant speed, using a control function to determine when to apply the drive torque.

The vehicle speed should be the input variables of the control function, and the output value should be the desired driving torque. The function relationship should be such that when the vehicle speed reaches or exceeds the desired value, the output value will be 0 (no driving torque applied); when the vehicle speed is smaller than the desire value, the output value should apply the desired drive torque value. Based on this relationship, the inverse tangent function is good choice to be the control function in this case. The inverse tangent function has a relationship where the output value changes from $-\frac{\pi}{2}$ to $\frac{\pi}{2}$ when the input value changes from $-\infty$ to ∞, and the curve is symmetric about the origin. To make the function relationship meet the requirement, one should shift the symmetric point from the origin to the desired vehicle speed value, increase the maximum output value from $\frac{\pi}{2}$ to the desired driving torque value and replace the negative output value with 0. Supposing the desired vehicle speed is V_d = 5 m/s (5000 mm/s), and the desired driving torque is T_d = 600000 N·mm, one can modify the inverse tangent function into:

$$y_{dt} = \max(0, T_d \frac{2}{\pi} \arctan(x_{dt} - V_d)) \tag{2.12}$$

The max() function will replace all the negative values in the inverse tangent function into 0. In this way, the control function will prevent reverse torque from being applied when the desired vehicle speed has been reached. This driving torque control function has been plotted in Figure 2.10. When this control function is applied in the Motionview® simulation, it should be combined with a step function with corresponding braking time, which will work as a trigger to tell the model to stop applying the driving torque and start to applying a braking torque. Based on this function, to achieve a constant acceleration motion is very simple. The V_d and T_d terms can easily be changed to give the desired velocity and desired acceleration values. In this way, the vehicle will accelerate from the initial speed to the desired speed at a constant acceleration speed, and keep a constant speed after the desired speed has been reached.

2.3.2 Braking at Desired Deceleration

The braking implementation is quite similar to the constant speed case. One can also use the inverse tangent function to control the braking torque in order to achieve the desired deceleration.

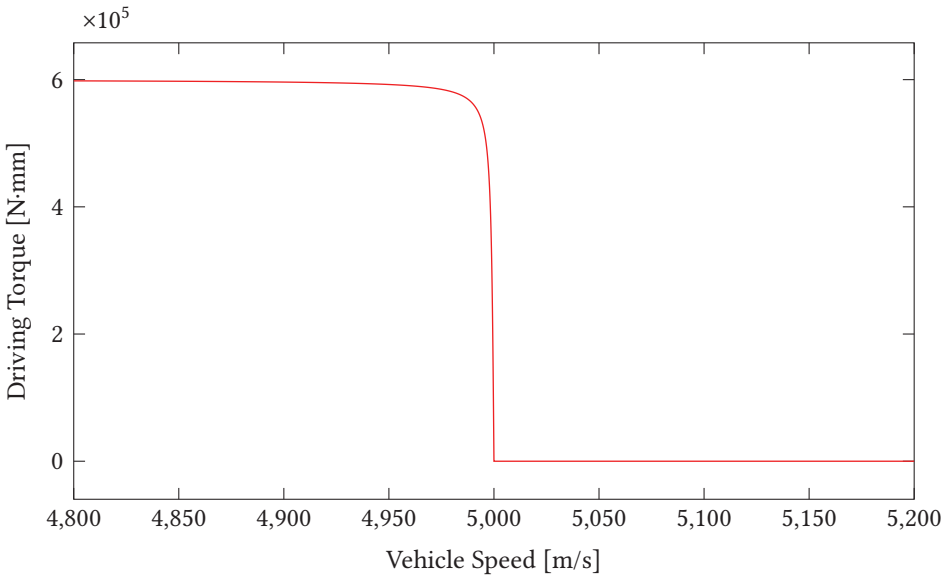

Figure 2.10: Driving Torque Control Function

To ensure the force on lower control arm is under the critical condition, the desired deceleration should be set to $\leq -0.5g$[24]. Here the g is the gravitational constant. This deceleration will be treated as 'hard' braking, which causes relatively high loads on the suspension components. The braking torque will acted on each individual wheel. Once the desired deceleration is chosen, the individual braking torque can be calculated for each wheel using the following equations:

$$T_{front} = \frac{M_{total} D_g g B_f}{2} R_w \tag{2.13}$$

$$T_{rear} = \frac{M_{total} D_g g (1 - B_f)}{2} R_w \tag{2.14}$$

Here, T_{front} and T_{rear} are the front and rear wheel braking torques, respectively. The total mass of the vehicle is M_{total}. The desired deceleration (proportion to the gravitational constant) is D_g; for all the simulations in this research, D_g is set to 0.65. The term B_f is the front braking proportion; for normal situations B_f=0.7. The radius of wheel is R_w.

After the braking torques have been found, one can use the modified inverse tangent function to control the braking torque according to wheel rotation speed. When the wheel has stopped rotating, the braking torque should not to be applied anymore. The function is shown in Eqn. 2.15. The input x_{bt} is the wheel rotation speed, the output y_{bt} will be the desired braking torque and T_{bc} is the calculated coefficient for control function. In order to ensure the braking torque value is correct under certain wheel rotation speeds, the correct coefficient can be calculated by substituting the wheel rotation speed and desired braking torque into the x_{bt} and y_{bt} term and calculate the corresponding coefficient T_{bc}. In this way, the braking torque and desired deceleration will be correct, independent of how fast the vehicle is moving. The max() function was not used in this

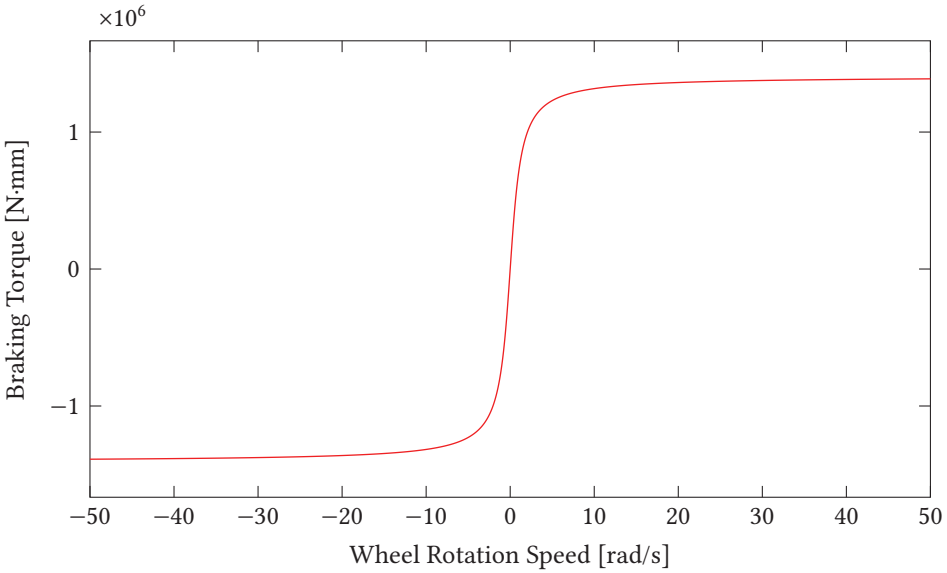

Figure 2.11: Braking Torque Control Function

case, which means the negative values will be allowed in the function. This is reasonable because the braking manner is always opposing the vehicle motion. For example, if the vehicle is moving backward, the braking force direction will be forward. The final braking control function has been plotted in Figure 2.11.

$$y_{bt} = T_{bc}\frac{2}{\pi}\arctan(x_{bt}) \tag{2.15}$$

2.3.3 Cornering at Desired Radius

Vehicle cornering can be a complex and detailed topic. In this research, only a brief discussion will be introduced. The cornering implementation will be considered to be a very simple function in this dynamics simulation. There are many parameters that influence the vehicle cornering behaviour, such as the mass of vehicle, the speed of vehicle, the lateral friction coefficient between the tires and the ground, the cornering radius, the centripetal acceleration, the maximum front wheel steering angle, the wheelbase, the location of centre of mass of vehicle, the tire cornering stiffness, and so on. There are several functions that will determine these parameters. The first one is the basic dynamic relationship of a particle with circular in-plane motion, which is expressed as:

$$a_c = \frac{V^2}{R} \tag{2.16}$$

If the centripetal acceleration and the desired cornering radius is known, the vehicle velocity can be easily calculated. The second relationship is a geometry relationship, which is shown in

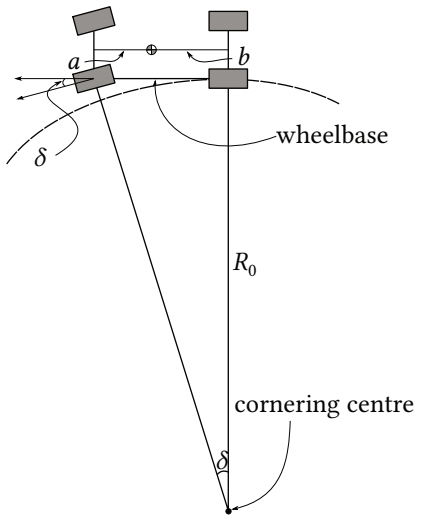

Figure 2.12: Vehicle Cornering Geometry Relationship. In most cases the steering angle will be small enough to allow a simple relationship between wheelbase, kinematic cornering radius, and steer angle.

Figure 2.12. From the figure, the kinematic cornering radius R_0 can be defined. In most cases, one can assume a small steering angle δ, allowing the simplified relationship: $\tan\delta \approx \delta$. This kinematic cornering radius will be considered when cornering at very low speed, where the lateral forces are low, and the tire slip angle is negligible.

$$R_0 = \frac{a+b}{\delta} \tag{2.17}$$

To consider the lateral force effect, tire slip angle will not be ignored. Under this situation, the direction of tire is travelling will be different than the direction the tire is pointing. The well known yaw plane model discussed in Minaker[20] is useful here. This model uses a linear tire model that treats the lateral force as proportional to the tire slip angle only. The steady state yaw rate gain equation can be manipulated to give a function showing the relationship between front wheel steering angle δ and the desired cornering radius R. This relationship is shown in Eq. 2.18.

$$\delta = \frac{(a+b)^2 C_f C_r - m(a_c R)^2 (aC_f - bC_r)}{(a+b)C_f C_r R} \tag{2.18}$$

In this equation, a is the length from centre of mass to the front axle, b is the length from centre of mass to the rear axle, a+b will be the wheelbase, C_f is the lumped front cornering stiffness, C_r is the lumped rear cornering stiffness. If the centripetal acceleration a_c and desired cornering radius R is provided, the required the front wheel steering angle can be calculated. By using this function and proper dataset, one can implement the desired steering motion into the dynamics simulation.

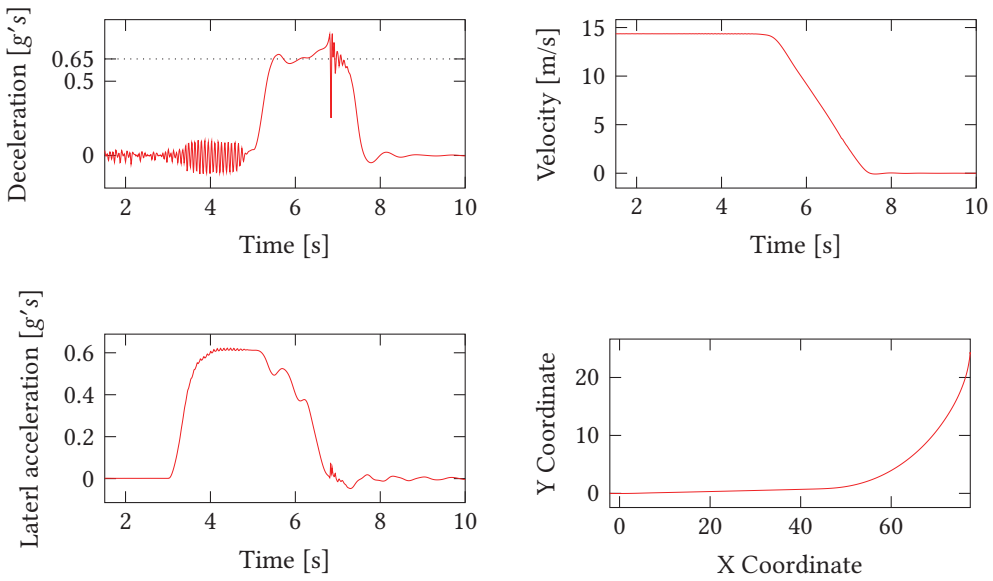

Figure 2.13: Simulation Results of The Implementation Example. upper-left: Vehicle Deceleration VS Time, upper-right: Vehicle Velocity VS Time, lower-left: lateral acceleration VS Time, lower-right: Travel Path

In this research, the focus will be strength of suspension lower arm, so the centripetal acceleration is chosen as relatively high during the cornering motion. The usual comfortable centripetal acceleration of average passenger car driver is $0.4g$[25]. For most racing or competition car this value will be much higher, even close to or beyond $1g$. For safety and performance consideration, in this research, the centripetal acceleration has been set to $0.7g$ for all simulations. This is a reasonable value for common passenger car design.

2.3.4 Implementation Example

Now that the implementation of constant speed driving, fixed deceleration braking, and desired radius cornering have been discussed, a simulation scenario with constant speed cornering combined with hard braking can be described. The total simulation time is set to be 10 s. The desired cornering radius is 30 m. The desired lateral acceleration is $0.7g$. The calculated vehicle speed is 51.671 km/h ($\approx$ 14.353 m/s). The vehicle is driving on a smooth road, and cornering starts at $t = 3$ s. The braking torque is applied after $t = 5$ s. Simulation results of vehicle velocity, deceleration, lateral acceleration and travel path have been plotted in Figure 2.13. It shows the driving torque, the steering angle, and the braking torque have been applied properly. The speed is keeping constant before $t = 5$ s. The deceleration is started from $t = 5$ s and the value is as expected ($\approx 0.65g$). The turning radius is close to 30 m. Because the tire properties are not fixed in the simulation (a fully nonlinear tire model is used), the lateral acceleration did not quite reach $0.7g$, but it is in a reasonable range. All control functions work well.

Table 2.7: Driving Scenarios Summary

Driving Scenarios	V [km/h]	a_x [g]	a_y [g]	Road Level
Straight Constant Speed	60, 80, 100	0	0	6, 7, 8
Straight-line Acceleration	From 0 to 80	0.4	0	6, 7
Straight Braking	From 80 to 0	-0.65	0	6, 7
Constant Speed Cornering	80	0	0.7	6, 7
Braking During Cornering	From 80 to 0	-0.65	0.7	6, 7
Straight-line Acceleration	From 0 to 60	0.4	0	8
Straight Braking	From 60 to 0	-0.65	0	8
Constant Speed Cornering	25	0	0.1	8
Braking During Cornering	From 25 to 0	-0.65	0.1	8

2.4 Force Results Summary and Discussion

In previous sections, the dynamic simulation parameters setting and scenario design have been explained and shown to be suitable according to the research objectives. Based on the FEA model requirement that will be discussed in Chapter 4, the most important results from the dynamics simulation will be the forces on lower control arm. All the forces should be treated in the same reference coordinate when building the FEA model, in order to keep the simulation parameters consistent between different software tools. In the FEA model, the forces on the ball joint will be treated as an applied external load, the forces on front and rear bushing point will be determined by a solid rubber model with corresponding hyper-elastic parameters, the forces on the anti-roll bar connecting point will be determined by a spring model with fixed stiffness value. As a result, the forces on the bushing point do not need to be extracted from the dynamics simulation. The forces will be consistent if the model has same hyper-elastic parameters to describe the bushing stiffness. The forces on the ball joint need to be discussed and summarized, in order to find the maximum loading case, which should be applied in the FEA model. The output forces and moments on the anti-roll bar connecting joint need to be extracted at the corresponding time step where maximum forces on the ball joint occurred. These summarized processes will be introduced in this section.

2.4.1 Lower Ball Joint Force Summary

The ball joint force that will be used in the FEA simulation needs to be summarized from the dynamics simulation results. Depending on the simulation running time, the force history results will have many of data points from either the left side or the right side ball joint. The first step is to confirm which scenarios should be used during the simulation. As mentioned in Section 2.3, in order to keep the force results sufficient, the simulation scenarios should cover all the basic driving situations such as acceleration, braking, cornering, and bumping. At the same time, all cases should be in a relatively critical status, such as high acceleration, hard braking, sharp cornering, and high level rough road. To compute the forces under these many different cases will increase the confidence in the safety of the lower arm design. According to these considerations, there are several simulations that have been implemented. The details are shown in Table 2.7.

As shown in the table, all cases have been run using three roads of different roughness. To ensure the road roughness is sufficiently aggressive, levels 6, 7, and 8 have been chosen. For the constant speed straight driving case, the simulations have been run with three different velocities of 60, 80, and 100 km/h, which cover the range from normal local road speed to the highway speed. For other cases on level 6 and level 7 roads, the velocity has been set to 80 km/h, which is used for the most common driving situation. All driving manoeuvres such as accelerating, braking, and cornering have been set to a relatively critical condition, except on the level 8 road. Because the level 8 road surface is so aggressive, the relatively low speed and mild driving manoeuvres have been applied to those cases, in order to finish the simulation without vehicle rollover. There are 21 cases in total. For each case, the force history results on the lower control arm ball joint on each of the left and right side of the vehicle will have thousands of data points. It is not necessary to verify all of these forces. A strategy was needed to pick the maximum or critical force cases among all force history results. There will be forces acting in each of the three different directions on the lower ball joint. According to the sign of these three forces, one can classify the forces into 8 different groups corresponding 8 octants in the Cartesian coordinate system, as shown in Figure 2.14. The maximum magnitude force combination can be chosen in each octant. By doing this, 8 maximum force combinations can be found for each simulation case. However, because it is unknown which force directions will contribute the most stress in the lower control arm, the maximum magnitude force combinations might not cover all critical cases. To account for this, there are 6 more force combinations that will be summarized; the maximum force case in each axis including both positive and negative directions. Altogether, there will be 14 maximum force combinations for each driving scenario. And for each road roughness level, there will be 7 different driving scenarios.

An additional summary process has been applied to pick the maximum force combination among the 7 driving scenarios for each road level. In the end, there will be 14 maximum force cases determined for each road level. This summary process will choose the most critical cases during all the dynamics simulations to simplify the the stress analysis procedure. In order to finish this summary process from the thousands of data points in the simulation output, two specially designed MATLAB® codes have been created. They will choose the correct force combinations by searching and comparing all data points and write the results into a table. The first MATLAB® code will be shown in Appendix A.5. This process will choose the maximum force combinations for each driving scenario. In the following, the summarized force results of the braking-during-cornering simulation on a level 6 roughness road will be shown and discussed as an example.

As shown in Table 2.8, 14 maximum force combinations have been found. The first column shows the octant or direction of the forces. As mentioned before, forces on both side's lower ball joints have been considered, so the second column shows which side carries that maximum force. In the third column, it tells the time that the forces have been applied during the simulation. Based on the simulation parameters, the vehicle is driving straight forward at a constant speed (80 km/h) in the first five seconds. Then it starts a constant radius cornering motion from $t = 5$ s to $t = 8$ s.

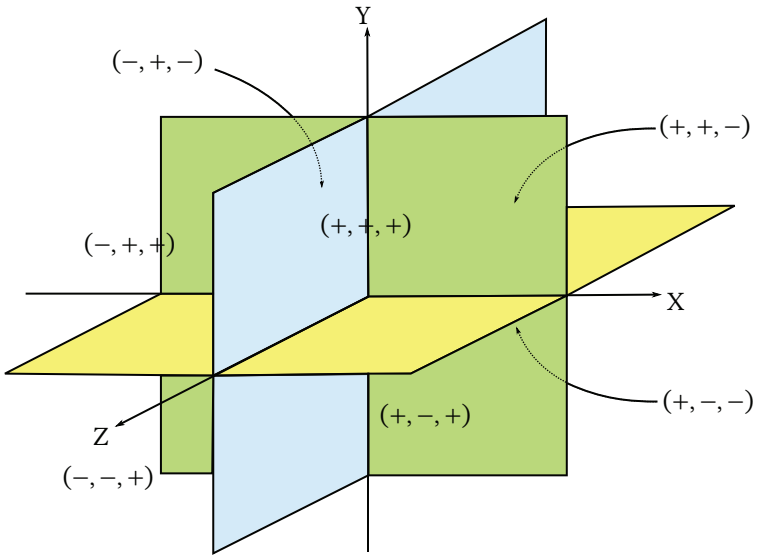

Figure 2.14: Cartesian Coordinate System with 8 Octants

At $t = 8$ s, a hard braking force (deceleration $\approx 0.65g$) will be applied until the vehicle comes to a stop. By examining the force summary results, one can tell that most of the maximum force combinations occur around the time that vehicle motion changed, which is reasonable because these driving manoeuvres will increase the load on the suspension lower arm through the ball joint. Also, some of the maximum force combinations are caused by the aggressive bumping road. In addition, by checking the details of these results, it is not hard to find that only one of the maximum magnitude cases is overlapping with the individual axis maximum force cases. This proves that all of the 14 cases are necessary to ensure the force summary results are complete. The details of the force summary results from other cases are shown in Appendix B.1. By checking and comparing all other results, it is seen that, as expected, a more aggressive road surface will cause larger loads on the ball joint, even though the speed of vehicle has been reduced in the level 8 road simulation. By viewing the animations of the simulation on the level 8 road, it can be seen that the vehicle has some dramatic motions caused by the huge change in road elevation value, especially during high speed straight driving. These motions are not normal during our regular driving. In these cases, even if the lower arm strength is strong enough to support the loads, the vehicle body may well suffer severe damage regardless. So the force results from the level 8 road simulation will represent an extreme load case.

After getting these maximum force combinations from every driving scenario, the MATLAB® code shown in Appendix A.6 will be used to choose the maximum force combination among every driving scenario for each road level. The final summary force results for each road level will be shown in Tables 2.10, 2.11, and 2.12. There will be 14 maximum force cases for each road level. For each case, it will show which driving scenario resulted in this force combination. By examining

these three tables, one can tell that following the increase of road level, the maximum force combination is increasingly concentrated in the high speed straight driving case. This is caused by the aggressive road elevation change in level 7 and level 8 roads, which generates larger forces on the ball joint than those resulting from the different driving manoeuvres. If the road roughness level is not too high, for example in the level 6 road case, the driving manoeuvre causes more forces on the ball joint in most of the cases. Also, the result shows that higher speed causes more forces in most cases. The exception happens in the level 8 road, where none of the 100 km/h cases causes more forces when compared to the 80 km/h case. One of the reasons for this could be that the road elevation data is quite random and during higher speed driving the vehicle may simply leave the surface during some of the more aggressive areas. In this way, the lower control arm may suffer smaller forces due to the bumping road compared to a relatively lower speed. This result also reinforces the need to run multiple different driving scenarios, in order to capture the most severe force combination.

When comparing the three different road roughness levels, the level 8 road is very aggressive. In normal operation, the vehicle won't be driven in such a bad condition under this relatively high speed. The level 6 road will be a good example for a general rough road and the level 7 road will be a good representation of a critical road condition. In Chapter 4, the lower arm strength will be tested in the FEA software using the force results from this chapter. The strategy will be to use the forces from the level 6 road case to verify the lower arm strength first. Depending on the performance of the lower arm on the level 6 road, the level 7 and level 8 road results might also be tested. It should not come as a surprise that the composite lower arm will fail when driving on the level 7 or level 8 road. In fact, the results will show that on a level 6 road, the composite lower arm already fails in some driving scenarios, so the level 5 roads have been considered to include in the simulation. The force summary results are shown in the Table 2.9. The force results from other driving scenarios are also added to Appendix B.

Table 2.8: Maximum Forces of Braking During Cornering on Level 6 Road

Direction	Side	Time [s]	F_x [N]	F_y [N]	F_z [N]
$(+,+,+)$	Left	10.23	7.19×10^3	4.00×10^3	7.54×10^0
$(-,-,-)$	Right	7.3	-1.40×10^3	-3.51×10^3	-9.38×10^1
$(-,+,+)$	Left	3.11	-1.21×10^2	4.09×10^3	1.17×10^2
$(+,-,-)$	Right	8.7	6.22×10^3	-1.06×10^3	-5.77×10^1
$(-,-,+)$	Right	6.74	-1.32×10^3	-4.80×10^3	5.63×10^2
$(+,+,-)$	Left	8.26	4.68×10^3	1.09×10^4	-4.04×10^2
$(+,-,+)$	Right	9.38	6.84×10^3	-1.50×10^3	2.34×10^1
$(-,+,-)$	Left	6.99	-7.06×10^2	4.70×10^3	-2.14×10^2
maximum $+x$	Left	10.22	7.47×10^3	4.52×10^3	-1.43×10^1
maximum $+y$	Left	8.26	4.68×10^3	1.09×10^4	-4.04×10^2
maximum $+z$	Right	6.29	-8.83×10^2	-2.41×10^3	9.56×10^2
maximum $-x$	Right	6.37	-2.33×10^3	-3.16×10^3	7.47×10^2
maximum $-y$	Right	8.06	2.75×10^2	-5.06×10^3	7.56×10^2
maximum $-z$	Left	6.28	-4.48×10^2	1.37×10^3	-9.27×10^2

Table 2.9: Maximum Forces of Level 5 Road

Direction	Scenario	F_x [N]	F_y [N]	F_z [N]
$(+,+,+)$	Straight Braking	6.57×10^3	4.26×10^3	1.54×10^1
$(-,-,-)$	Straight Accelerating	-4.99×10^3	-4.49×10^3	-2.83×10^1
$(-,+,+)$	Straight Constant Speed 100	-3.03×10^2	3.77×10^3	1.64×10^2
$(+,-,-)$	Constant Speed Cornering	2.92×10^0	-2.29×10^3	-7.35×10^1
$(-,-,+)$	Straight Accelerating	-5.13×10^3	-4.35×10^3	6.90×10^0
$(+,+,-)$	Cornering Braking	6.60×10^3	6.67×10^3	-2.71×10^2
$(+,-,+)$	Cornering Braking	6.16×10^3	-1.71×10^3	3.09×10^2
$(-,+,-)$	Constant Speed Cornering	-3.92×10^2	6.25×10^3	-2.62×10^2
maximum $+x$	Cornering Braking	7.01×10^3	3.99×10^3	-4.02×10^1
maximum $+y$	Cornering Braking	6.60×10^3	6.67×10^3	-2.71×10^2
maximum $+z$	Constant Speed Cornering	-1.97×10^3	-1.83×10^3	1.02×10^3
maximum $-x$	Straight Accelerating	-5.13×10^3	-4.35×10^3	6.90×10^0
maximum $-y$	Constant Speed Cornering	-1.02×10^3	-5.30×10^3	4.22×10^2
maximum $-z$	Constant Speed Cornering	-3.95×10^2	1.49×10^3	-8.45×10^2

Table 2.10: Maximum Forces of Level 6 Road

Direction	Scenario	F_x [N]	F_y [N]	F_z [N]
$(+,+,+)$	Straight Braking	7.67×10^3	7.69×10^3	6.64×10^0
$(-,-,-)$	Straight Accelerating	-3.51×10^3	-8.06×10^3	-5.57×10^1
$(-,+,+)$	Straight Constant Speed 100	-2.82×10^3	7.55×10^3	3.01×10^2
$(+,-,-)$	Straight Accelerating	3.91×10^2	-6.45×10^3	-1.64×10^2
$(-,-,+)$	Straight Accelerating	-3.03×10^3	-1.33×10^4	1.04×10^2
$(+,+,-)$	Cornering Braking	4.68×10^3	1.09×10^4	-4.04×10^2
$(+,-,+)$	Cornering Braking	6.84×10^3	-1.50×10^3	2.34×10^1
$(-,+,-)$	Straight Accelerating	-2.77×10^3	8.86×10^3	-2.40×10^2
maximum $+x$	Straight Braking	8.45×10^3	8.30×10^3	-2.80×10^1
maximum $+y$	Cornering Braking	4.68×10^3	1.09×10^4	-4.04×10^2
maximum $+z$	Constant Speed Cornering	-1.90×10^3	-1.34×10^3	1.41×10^3
maximum $-x$	Straight Braking	-6.71×10^3	-3.59×10^3	1.50×10^2
maximum $-y$	Straight Accelerating	-3.03×10^3	-1.33×10^4	1.04×10^2
maximum $-z$	Constant Speed Cornering	-1.27×10^2	6.18×10^2	-1.02×10^3

2.4.2 Anti-roll Bar Reaction Forces and Moments

After the maximum force combinations from ball joint were summarized, the corresponding forces and moments on the anti-roll bar connecting joint at same time step need to be extracted. As an example, the forces and moments values summary for level 5 road in each maximum force case are shown in Table 2.13. Notice that some maximum cases in individual axes are not listed here, because they are a duplicate with one of the maximum magnitude case. For example in level 5 road, the maximum $+y$ case is the same as the $(+,+,-)$ case and the maximum $-x$ case is the same as the $(-,-,+)$ case. The summary for other levels of road can be found in Appendix B.2. These forces and moments along with maximum forces from the ball joint will be applied as the load boundary conditions in the final FEA model to test the strength of the composite lower arm.

Table 2.11: Maximum Forces of Level 7 Road

Direction	Scenario	F_x [N]	F_y [N]	F_z [N]
$(+,+,+)$	Straight Braking	1.39×10^4	2.67×10^4	1.93×10^2
$(-,-,-)$	Straight Constant Speed 100	-9.01×10^1	-1.59×10^4	-2.34×10^2
$(-,+,+)$	Straight Constant Speed 100	-2.54×10^3	3.05×10^4	2.74×10^2
$(+,-,-)$	Straight Constant Speed 100	3.62×10^3	-2.50×10^4	-8.17×10^1
$(-,-,+)$	Straight Accelerating	-4.35×10^2	-4.34×10^4	1.38×10^3
$(+,+,-)$	Straight Constant Speed 100	1.78×10^4	3.27×10^4	-1.55×10^2
$(+,-,+)$	Straight Constant Speed 100	5.01×10^3	-3.57×10^4	5.35×10^2
$(-,+,-)$	Straight Constant Speed 100	-6.31×10^3	3.83×10^4	-1.19×10^3
maximum $+x$	Straight Constant Speed 100	1.87×10^4	2.01×10^4	1.90×10^1
maximum $+y$	Straight Constant Speed 100	-6.31×10^3	3.83×10^4	-1.19×10^3
maximum $+z$	Straight Constant Speed 100	5.00×10^3	3.21×10^3	1.97×10^3
maximum $-x$	Straight Constant Speed 80	-1.05×10^4	-6.12×10^2	6.95×10^2
maximum $-y$	Straight Accelerating	-4.35×10^2	-4.34×10^4	1.38×10^3
maximum $-z$	Straight Constant Speed 100	-1.59×10^3	1.17×10^4	-1.54×10^3

Table 2.12: Maximum Forces of Level 8 Road

Direction	Scenario	F_x [N]	F_y [N]	F_z [N]
$(+,+,+)$	Straight Constant Speed 80	1.76×10^5	1.59×10^5	1.78×10^1
$(-,-,-)$	Straight Constant Speed 80	-5.28×10^3	-3.24×10^4	-2.83×10^2
$(-,+,+)$	Straight Constant Speed 60	-6.22×10^3	6.28×10^4	1.05×10^2
$(+,-,-)$	Straight Constant Speed 60	6.46×10^3	-4.94×10^4	-2.40×10^1
$(-,-,+)$	Straight Constant Speed 60	-5.68×10^3	-1.36×10^5	3.71×10^3
$(+,+,-)$	Straight Constant Speed 80	1.98×10^5	9.83×10^4	-3.05×10^3
$(+,-,+)$	Straight Constant Speed 80	1.80×10^4	-1.43×10^5	2.44×10^3
$(-,+,-)$	Straight Constant Speed 80	-2.56×10^4	1.50×10^5	-4.15×10^3
maximum $+x$	Straight Constant Speed 80	1.98×10^5	9.83×10^4	-3.05×10^3
maximum $+y$	Straight Constant Speed 80	1.76×10^5	1.59×10^5	1.78×10^1
maximum $+z$	Straight Constant Speed 80	-6.38×10^3	-8.50×10^4	4.78×10^3
maximum $-x$	Straight Constant Speed 80	-2.99×10^4	9.93×10^4	-4.50×10^3
maximum $-y$	Straight Constant Speed 80	1.80×10^4	-1.43×10^5	2.44×10^3
maximum $-z$	Straight Constant Speed 80	9.54×10^4	1.21×10^5	-8.02×10^3

2.4.3 Dynamics Effect On Loads

In the following chapters, the previously summarized force combinations from the ball joint will be tested using FEM under static analysis. During the static analysis, the dynamic loading effect will be ignored. To prove this assumption does not significantly influence the stress analysis results, the dynamic loading effect in the multi-body dynamics simulations should be quantified. In order to achieve this, the time history results of the acceleration values of the centre of mass of the lower arm body are multiplied by the mass of the lower arm, and plotted as a function of time. These results are compared with the time history results of forces on the lower arm ball joint. In this way, the value of the dynamic forces compared to the ball joint forces in the three different directions can be visualized. Based on this approach, the comparison curves between mass × acceleration and ball joint forces in three different directions have been generated. The

Table 2.13: Anti-roll Bar Forces and Moments Summary of Level 5 Road

Case	F_x [N]	F_y [N]	F_z [N]	M_x [Nmm]	M_y [Nmm]	M_z [Nmm]
$(+,+,+)$	1.12×10^3	-2.94×10^2	-1.75×10^3	-4.80×10^4	5.30×10^3	-1.53×10^4
$(-,-,-)$	-7.85×10^2	3.19×10^2	1.17×10^3	-2.70×10^4	-8.54×10^3	-1.14×10^4
$(-,+,+)$	-6.99×10^1	-1.22×10^2	3.58×10^2	2.99×10^4	3.39×10^3	1.00×10^4
$(+,-,-)$	-2.36×10^2	1.19×10^2	3.07×10^2	-4.70×10^3	4.78×10^3	8.30×10^3
$(-,-,+)$	-7.50×10^2	2.79×10^2	1.15×10^3	-3.06×10^4	-6.58×10^3	-9.69×10^3
$(+,+,-)$	9.19×10^2	1.87×10^1	-1.72×10^3	5.27×10^4	-1.73×10^3	8.80×10^3
$(+,-,+)$	1.11×10^3	-5.86×10^2	-1.61×10^3	-4.64×10^4	5.36×10^3	-1.61×10^4
$(-,+,-)$	-9.28×10^1	3.18×10^2	-6.98×10^1	-4.75×10^3	4.03×10^2	1.11×10^3
maximum $+x$	1.16×10^3	-2.73×10^2	-1.91×10^3	5.47×10^4	-5.20×10^3	1.44×10^4
maximum $+z$	-1.51×10^2	-1.20×10^3	1.05×10^3	5.16×10^4	-6.31×10^3	-1.03×10^4
maximum $-y$	-1.63×10^1	-4.15×10^2	2.85×10^2	9.29×10^3	-6.33×10^2	-8.50×10^2
maximum $-z$	-6.39×10^2	1.18×10^3	3.39×10^2	4.74×10^3	-8.55×10^3	-1.25×10^4

straight acceleration driving scenario on a level 6 road has been chosen as an example. It is assumed that the similar results will be shown in other cases. As shown in Figures 2.15, 2.16, and 2.17, the comparison curves in the longitudinal, and lateral direction show a very small effect of dynamic loading on the ball joint forces. The influence is negligible in these two directions. For the vertical direction, the dynamic forces are larger in comparison to the ball joint force, but still relatively small during the majority of the time. In some rare instances, the effect may be significant. However, considering the overall effect is still quite small during most of time and the force magnitude in vertical direction is significantly smaller when compared to the other two directions, the dynamics effect on loads will be ignored in the following stress analysis. The static analysis will be used in the FEA simulation in this research.

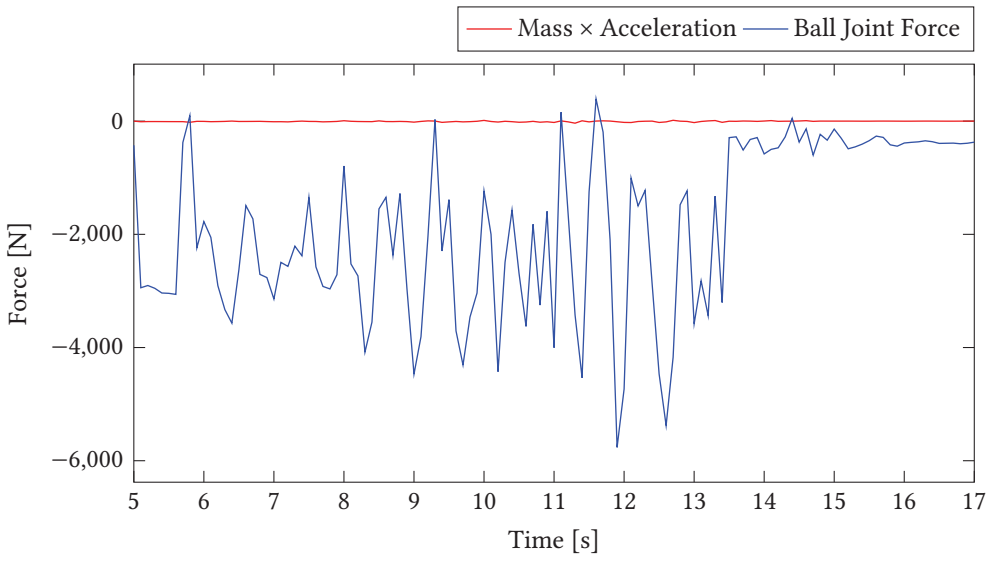

Figure 2.15: Dynamics Load Effect In Longitudinal Direction. Note that the mass × acceleration values are negligible compared to the lower arm force values in longitudinal direction.

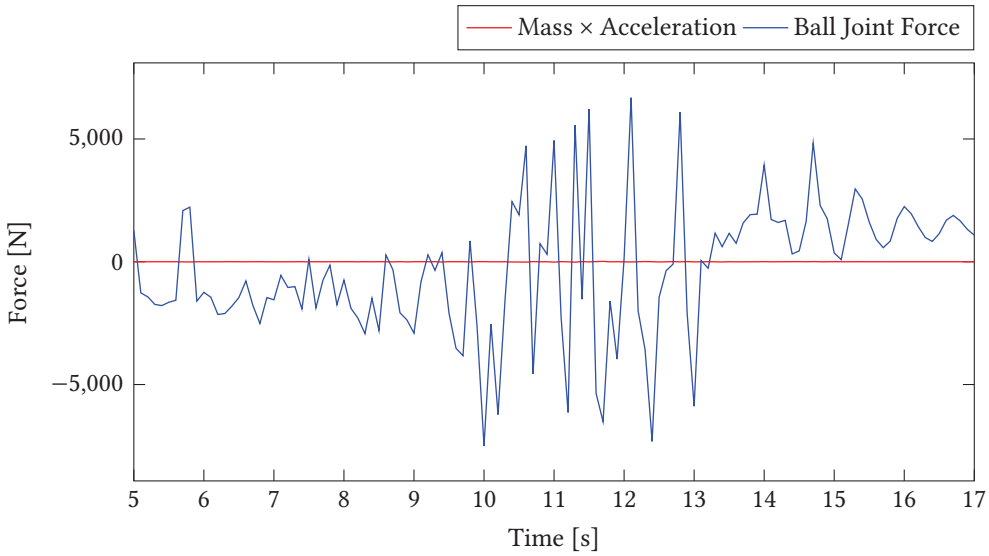

Figure 2.16: Dynamics Load Effect In Lateral Direction. Note that the mass × acceleration values are negligible compared to the lower arm force values in lateral direction.

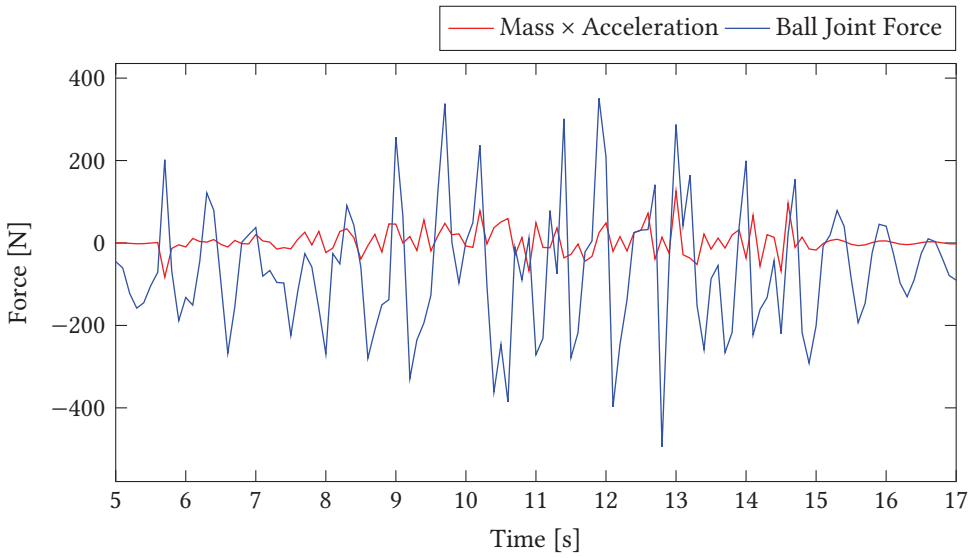

Figure 2.17: Dynamics Load Effect In Vertical Direction. Note that the mass × acceleration values are relatively small compared to the lower arm force values in vertical direction during the majority of the time.

Chapter 3

Manufacturing Process Simulation

Consider the characteristics of composite materials. The material properties are highly dependent on the manufacturing process. As mentioned in Chapter 1, there are many factors that will influence the final part properties, such as the shape of the part, the individual properties of the fibre and matrix, the injection location and direction, etc. All these factors will make the fibre orientation distribution (FOD) different in the final part. The strength of the final part will influenced by these factors as well. To better understand the strength of the composite lower suspension arm, a complete thermoplastic injection moulding process simulation will be introduced and discussed in this chapter. The simulation process will use a numerical FOD prediction model to predict the detail of the fibre orientation distribution in the final part. Then, another process will be introduced to transfer these distribution results into a FEA model. In this way, the manufacturing effects on the composite material properties can be considered in the stress analysis.

3.1 Moldflow® Software

Moldflow® is a manufacturing simulation software which has been used in many industry and academic fields. Moldflow® can be used to simulate a wide range of injection moulding processes to predict and avoid potential manufacturing defects. Several studies have used Moldflow® to simulate the injection moulding process[26][27][28]. Most of them are focused on the study of processing parameters such as injection pressures and temperature, filling rate, potential shrinkage, cooling issues, etc. When considering the features of FRP, the FOD prediction is another important function that can be achieved in Moldflow® simulation. As mentioned in Chapter 1, several FOD prediction models based on the equation of change of the second-order orientation tensor have been implemented in the Moldflow® 3D simulation solver. The details of these FOD prediction models will be introduced in the next section.

In order to use Moldflow® to build an injection moulding simulation model, several step must be followed:

1. Create a model of the geometry of the intended final part in a specialized CAD software, e.g., Solidworks®, and import this CAD model into Moldflow®.

2. Choose a suitable processing type for the manufacturing simulation, such as Thermoplastic Injection moulding.
3. Choose the desired processing sequence, such as 'fill+pack'.
4. Select the suitable materials from the material database. Usually the materials database will have all the needed material properties already included. Users can also define their own properties by changing the parameters in the material properties option.
5. Pick and define the injection location(s) on the part.
6. Mesh imported geometry either using the global meshing size setting, or using the automatic size calculation based on the dimensions and curvatures of the part. The minimum through-thickness element number is key to provide a good FOD prediction. The default option 'minimum 10 elements' or higher number is better. This will be discussed further in a later section.
7. Adjust the processing parameters if necessary. Usually the default settings will meet the majority of processing requirements. Apply any optimization process if appropriate.
8. Start the analysis.

After the simulation finishes, there are several results that can be checked. One can choose the corresponding results in the list to show by plot. The most important result will be the fibre orientation tensor, which can be used in the later structural analysis by a mapping process. Before making further discussion on this mapping process, the details of FOD prediction process and theory will be discussed in the following section.

3.2 Background Knowledge

3.2.1 Fibre Orientation Model

The fundamental fibre orientation prediction is based on the famous Jeffery's equation[29]. The equation analyzes the motion of a rigid ellipsoidal particle in a dilute viscous Newtonian fluid without Brownian movement. The general form of the equation is written as:

$$\dot{\mathbf{p}} = \mathbf{W} \cdot \mathbf{p} + \xi(\mathbf{D} \cdot \mathbf{p} - \mathbf{D} : \mathbf{ppp}) \tag{3.1}$$

The $\mathbf{p}$ is a unit vector representing the orientation of a particle or fibre in 3 dimensional space. The $\dot{\mathbf{p}}$ is the *material derivative* of $\mathbf{p}$, $\mathbf{W} = \frac{1}{2}(\mathbf{L} - \mathbf{L}^{\mathrm{T}})$ is the vorticity tensor and $\mathbf{D} = \frac{1}{2}(\mathbf{L} + \mathbf{L}^{\mathrm{T}})$ is rate of deformation tensor. Here, $\mathbf{L}$ is the velocity gradient tensor and $L_{ij} = \frac{\partial v_i}{\partial x_j}$, and the superscript T is the transpose operator of a matrix. The value ξ is the particle or fibre shape factor, as mentioned in Section 1.6.2, which is defined by:

$$\xi = \frac{{a_r}^2 - 1}{{a_r}^2 + 1} \tag{3.2}$$

where a_r is the aspect ratio of a particle. The aspect ratio of a fibre equals to the ratio of its length to its diameter. Considering common fibre as a long slender shape ($a_r \gg 1$), ξ will be assumed to be 1 in this research. Usually, Jeffery's equation is also called the Jeffery Hydrodynamics (HD) equation. It strictly applies to dilute suspensions without any fibre-fibre interaction. However, for common FRP material, the compound of fibre and polymer is treated as a concentrated suspension. The model of this type of suspension include two terms: the Hydrodynamics term from the Jeffery HD equation and a rotary diffusion term according to fibre-fibre interaction. Folgar and Tucker[30] introduced a rotary diffusion term to account the fibre-fibre interaction. The modified Jeffery's equation becomes:

$$\dot{\mathbf{p}} = \mathbf{W} \cdot \mathbf{p} + \xi(\mathbf{D} \cdot \mathbf{p} - \mathbf{D} : \mathbf{ppp}) - \frac{1}{\psi} C_I \dot{\gamma} \cdot \nabla_s \psi \tag{3.3}$$

where ψ is the orientation distribution function, introduced in Section 1.6.2. The C_I term is an empirical parameter of fibre-fibre interactions. Its typical value is in the range of $0.0001 - 0.02$. A higher value means more fibre-fibre interactions, which will decrease the alignment of fibre and randomize the fibre orientation. The C_I term is usually determined by matching numerical predictions with experiments in simple shear flow. There is no clear evidence to show dependency of C_I on a_r and ϕ_f, where ϕ_f is the fibre content of volume fraction. Contradictory results have been found in different literature[31][32]. The term $\dot{\gamma}$ is the magnitude of the rate of deformation tensor which is defined by: $\dot{\gamma} = \sqrt{2\mathbf{D} : \mathbf{D}}$. The ∇_s represents the gradient operator on the surface of the unit sphere.

As discussed in Section 1.6.2, Advani and Tucker[8] suggest replacing the orientation vector $\mathbf{p}$ with orientation tensor $\mathbf{A}$. According to the continuity condition of ψ:

$$\frac{D\psi}{Dt} = -\nabla_s \cdot (\psi \dot{\mathbf{p}}) \tag{3.4}$$

where $\frac{D}{Dt}$ is the material derivative operator. This continuity condition provides an equation for the evolution of ψ with time, once a proper value of $\dot{\mathbf{p}}$ is chosen. Using Equation 1.16a, 3.3 and 3.4, Advani and Tucker develop the time evolution equation for $\mathbf{A}$:

$$\dot{\mathbf{A}}^{\mathrm{FT}} = \dot{\mathbf{A}}^{\mathrm{HD}} + \dot{\mathbf{A}}^{\mathrm{IRD}} \tag{3.5}$$

$$\dot{\mathbf{A}}^{\mathrm{HD}} = (\mathbf{W} \cdot \mathbf{A} - \mathbf{A} \cdot \mathbf{W}) + \xi(\mathbf{D} \cdot \mathbf{A} + \mathbf{A} \cdot \mathbf{D} - 2\mathbb{A} : \mathbf{D}) \tag{3.6}$$

$$\dot{\mathbf{A}}^{\mathrm{IRD}} = 6C_I \dot{\gamma}(\mathbf{I}/3 - \mathbf{A}) \tag{3.7}$$

This is standard form of the well-known FT model or IRD model, where $\mathbb{A}$ in the HD term is the fourth-order fibre orientation tensor that is defined in Eqn. 1.16b. Note that a similar time evolution equation of $\mathbf{A}$ has been introduced in Eqn. 1.19. This standard form looks different, because different expressions of the vorticity tensor and rate of deformation tensor have been defined. Also, the D_r has been replaced by $C_I\dot{\gamma}$. And a small manipulation has been done on the coefficients of IRD term to make it easier to understand through its physical meaning. By looking at the IRD equation, the rotary diffusion term tries to orient the fibres into an isotropic state, $\mathbf{A} = \mathbf{I}/3$, at a rate proportional to $C_I\dot{\gamma}$. The steady state orientation in any steady flow is reached when the rotary diffusion term balances the HD term, which tries to align the fibres in single direction. Finding this proportional relationship between diffusion rate and the scalar deformation rate is a key contribution of FT model. The Jeffery HD equation will reach a steady state with all fibres aligned in the flow direction, $A_{11} = 1$. In fact, fibres in injection moulding are never perfectly aligned. The steady state orientation is typically in the range $A_{11} = 0.7 - 0.9$. When the FT model is used, the predicted orientation state can easily match the experimental values of A_{11} by using proper C_I values. Most of the models that have been implemented in popular commercial Computational Fluid Dynamics (CFD) software such as Moldflow®, Moldex3D®, is the improved or modified form of FT model.

The orientation model that is used in this research is called the Reduced-strain Closure (RSC) model. It was introduced by Wang, O'Gara and Tucker in 2008[33]. Based on experimental observation, the short fibre alignment is much slower in the injection moulding compared to the FT model prediction, so an objective model has been proposed to account for the slow orientation kinetics found in short fibre injection moulding. The main idea is to involve a scalar factor κ that reduces the growth rates of the eigenvalues of the second-order orientation tensor but to keep the rotation rate of the eigenvectors unchanged. For any second-order orientation tensor, it can be written as:

$$\mathbf{A} = \sum_{i=1}^{3} \lambda_i \mathbf{e}_i \mathbf{e}_i \tag{3.8}$$

Based on the essence of RSC model, one has:

$$\dot{\lambda}_i^{\text{RSC}} = \kappa \dot{\lambda}_i^{\text{std}} \tag{3.9a}$$

$$\dot{\mathbf{e}}_i^{\text{RSC}} = \dot{\mathbf{e}}_i^{\text{std}} \tag{3.9b}$$

The superscript 'std' represents the quantities in the standard FT model. So the time evolution equation for $\mathbf{A}$ in RSC model can be expressed as:

$$\dot{\mathbf{A}}^{\mathrm{RSC}} = \dot{\mathbf{A}}^{\mathrm{FT}} - (1-\kappa)\sum_{i=1}^{3} \dot{\lambda}_i^{\mathrm{std}} \mathbf{e}_i\mathbf{e}_i \tag{3.10}$$

Finally, by defining two fourth-order tensors:

$$\mathbb{L} = \sum_{i=1}^{3} \lambda_i \mathbf{e}_i\mathbf{e}_i\mathbf{e}_i\mathbf{e}_i \tag{3.11}$$

$$\mathbb{M} = \sum_{i=1}^{3} \mathbf{e}_i\mathbf{e}_i\mathbf{e}_i\mathbf{e}_i \tag{3.12}$$

the RSC model can be recast into following form:

$$\dot{\mathbf{A}}^{\mathrm{RSC}} = (\mathbf{W}\cdot\mathbf{A} - \mathbf{A}\cdot\mathbf{W}) + \xi\{\mathbf{D}\cdot\mathbf{A} + \mathbf{A}\cdot\mathbf{D} - 2[\mathbb{A} + (1-\kappa)(\mathbb{L} - \mathbb{M} : \mathbb{A})] : \mathbf{D}\} + 6\kappa C_I\dot{\gamma}(\mathbf{I}/3 - \mathbf{A}) \tag{3.13}$$

Compared to the FT model, there are two differences: (1) The diffusion term is multiplied by a factor κ. (2) The fourth-order orientation tensor $\mathbb{A}$ has been replaced by $[\mathbb{A} + (1-\kappa)(\mathbb{L} - \mathbb{M} : \mathbb{A})]$. This makes the implementation of the RSC model straightforward, based on the FT model. The κ value is varying between 0 and 1. The typical value is in the range between 0.05 and 0.2[34]. The smaller value of κ makes a wider core region in the orientation prediction, but keeps the steady state orientation unchanged.

For short FRP injection moulding, the RSC model will give a reasonable result of fibre orientation state. However, for long FRP case (usually fibre length $>$ 1 mm), one should use the Anisotropic Rotary Diffusion (ARD) model, which has been proved to match experimental results better during the long fibre process[35]. Several ARD models have been demonstrated by Favaloro and Tucker[36]. Since the focus of this research will be on the short fibre FRP injection moulding, the detail of ARD will not be discussed here. The available ARD models in the Moldflow® software can be found in [37] and [38].

3.2.2 Closure Approximation Function

As mentioned in Section 1.6.2, in order to solve the time evolution equation for $\mathbf{A}$, a closure approximation function is required to express $\mathbb{A}$ as function of $\mathbf{A}$. According to the definition of $\mathbb{A}$, it will have 81 components in total. To express every single term in this huge tensor is cumbersome. Based on the minor symmetry of $\mathbb{A}$:

$$a_{ijkl} = a_{jikl} = a_{ijlk} \tag{3.14}$$

So $\mathbb{A}$ can be expressed into the contracted form $\mathbb{A}_{mn}$ with 6×6 independent components, where m is related to ij and n is related to kl according to following relationship:

$$m \text{ or } n \; : \begin{cases} 1 \rightarrow 11 \\ 2 \rightarrow 22 \\ 3 \rightarrow 33 \\ 4 \rightarrow 23 \\ 5 \rightarrow 31 \\ 6 \rightarrow 12 \end{cases} \tag{3.15}$$

This contracted form is very useful to explain the orthotropic closure which will be introduced later. The $\mathbb{A}$ can be expressed as:

$$\mathbb{A} = \begin{bmatrix} \mathbb{A}_{11} & \mathbb{A}_{12} & \mathbb{A}_{13} & \mathbb{A}_{14} & \mathbb{A}_{15} & \mathbb{A}_{16} \\ \mathbb{A}_{21} & \mathbb{A}_{22} & \mathbb{A}_{23} & \mathbb{A}_{24} & \mathbb{A}_{25} & \mathbb{A}_{26} \\ \mathbb{A}_{31} & \mathbb{A}_{32} & \mathbb{A}_{33} & \mathbb{A}_{34} & \mathbb{A}_{35} & \mathbb{A}_{36} \\ \mathbb{A}_{41} & \mathbb{A}_{42} & \mathbb{A}_{43} & \mathbb{A}_{44} & \mathbb{A}_{45} & \mathbb{A}_{46} \\ \mathbb{A}_{51} & \mathbb{A}_{52} & \mathbb{A}_{53} & \mathbb{A}_{54} & \mathbb{A}_{55} & \mathbb{A}_{56} \\ \mathbb{A}_{61} & \mathbb{A}_{62} & \mathbb{A}_{63} & \mathbb{A}_{64} & \mathbb{A}_{65} & \mathbb{A}_{66} \end{bmatrix} \tag{3.16}$$

The earliest attempt is made by Hand[39] in 1962, which is denoted as LIN. It uses all the products of $\mathbf{A}$ and $\mathbf{I}$ to form a summation expression. After applying symmetry and normalization conditions, the linear approximation is expressed as:

$$\mathbb{A}^{LIN} = -\frac{1}{35}(\mathbf{I}_{ij}\mathbf{I}_{kl} + \mathbf{I}_{ik}\mathbf{I}_{jl} + \mathbf{I}_{il}\mathbf{I}_{jk}) + \frac{1}{7}(a_{ij}\mathbf{I}_{kl} + a_{ik}\mathbf{I}_{jl} + a_{il}\mathbf{I}_{jk} + a_{kl}\mathbf{I}_{ij} + a_{jl}\mathbf{I}_{ik} + a_{jk}\mathbf{I}_{il}) \tag{3.17}$$

However, LIN is only good for isotropic distribution of orientation. So Hinch and Leal[40] provide another type of closure called QUA that omits the linear terms and makes the dyadic product of two second-order tensors:

$$\mathbb{A}^{QUA} = a_{ij}a_{kl} \tag{3.18}$$

But QUA is only good for perfectly aligned fibre orientation. Advani and Tucker[8][41] reviewed all the available closure methods and offer a new strategy to form the closure function that mixes the LIN and QUA in a scalar measure of orientation. This type of closure is called HYB. It is the first closure approximation function that covers a wide range of flow fields, and it is still

implemented in modern commercial CFD software due to the simplicity and fast calculation time. The function is expressed as:

$$\mathbb{A}^{HYB} = (1 - f)\mathbb{A}^{LIN} + f\mathbb{A}^{QUA} \tag{3.19a}$$

$$f = 1 - 27 \cdot \det \mathbf{A} \tag{3.19b}$$

Since the HYB has been proved to show over prediction on fibre alignment in all flow fields, a more accurate closure method was introduced by Cintra and Tucker[42]. This type of new closure method is called Eigenvalue-Based Optimal Fitting Closure Approximation (EBOF). The main idea is to assume any approximate fourth-order tensor must be orthotropic, and the principle axes of the fourth-order tensor is the same as the second-order tensor. Finally, each component of the fourth-order tensor in the principal frame will be expressed as a function of two largest eigenvalues of the second-order tensor.

Consider any second-order fibre orientation tensor, which is symmetric. It will have 3 orthogonal eigenvectors $\mathbf{e}_1(i)$, $\mathbf{e}_2(i)$ and $\mathbf{e}_3(i)$, where $i = 1,\ 2,\ 3$, and 3 relative eigenvalues λ_1, λ_2 and λ_3. Similar to the equation 3.8, $\mathbf{A}$ can be transformed to its eigenspace representation $\hat{\mathbf{A}}$ that is expressed as:

$$\hat{\mathbf{A}} = \begin{bmatrix} \lambda_1 & 0 & 0 \\ 0 & \lambda_2 & 0 \\ 0 & 0 & \lambda_3 \end{bmatrix} = \mathbf{R}^{\mathrm{T}}\mathbf{A}\mathbf{R} \tag{3.20}$$

$$\mathbf{R} = \begin{bmatrix} \mathbf{e}_1(1) & \mathbf{e}_2(1) & \mathbf{e}_3(1) \\ \mathbf{e}_1(2) & \mathbf{e}_2(2) & \mathbf{e}_3(2) \\ \mathbf{e}_1(3) & \mathbf{e}_2(3) & \mathbf{e}_3(3) \end{bmatrix} \tag{3.21}$$

Also, assume $\hat{\mathbb{A}}$ is representation of $\mathbb{A}$ in its principle frame, which is same as the corresponding second-order tensor. If $\mathbb{A}$ is orthotropic, it will have following contracted form:

$$\hat{\mathbb{A}} = \begin{bmatrix} \hat{\mathbb{A}}_{11} & \hat{\mathbb{A}}_{12} & \hat{\mathbb{A}}_{13} & 0 & 0 & 0 \\ \hat{\mathbb{A}}_{21} & \hat{\mathbb{A}}_{22} & \hat{\mathbb{A}}_{23} & 0 & 0 & 0 \\ \hat{\mathbb{A}}_{31} & \hat{\mathbb{A}}_{32} & \hat{\mathbb{A}}_{33} & 0 & 0 & 0 \\ 0 & 0 & 0 & \hat{\mathbb{A}}_{44} & 0 & 0 \\ 0 & 0 & 0 & 0 & \hat{\mathbb{A}}_{55} & 0 \\ 0 & 0 & 0 & 0 & 0 & \hat{\mathbb{A}}_{66} \end{bmatrix} \tag{3.22}$$

According to the major and special symmetry of $\mathbb{A}$ and the normalization condition of $\mathbb{A}$:

$$\text{major: } a_{ijkl} = a_{klij} \tag{3.23a}$$

$$\text{special: } a_{ijkl} = a_{kjil} = a_{ljki} = a_{ikjl} = a_{ilkj} \tag{3.23b}$$

$$\text{normalization condition: } a_{ijkk} = a_{ij} \tag{3.23c}$$

where the repeated notation kk indicates a summation. All these properties will be also applied in the principal frame. So they will be expressed as:

$$\hat{\mathbb{A}}_{12} = \hat{\mathbb{A}}_{21} = \hat{\mathbb{A}}_{66} \tag{3.24a}$$

$$\hat{\mathbb{A}}_{23} = \hat{\mathbb{A}}_{32} = \hat{\mathbb{A}}_{44} \tag{3.24b}$$

$$\hat{\mathbb{A}}_{13} = \hat{\mathbb{A}}_{31} = \hat{\mathbb{A}}_{55} \tag{3.24c}$$

$$\hat{\mathbb{A}}_{11} + \hat{\mathbb{A}}_{55} + \hat{\mathbb{A}}_{66} = \lambda_1 \tag{3.24d}$$

$$\hat{\mathbb{A}}_{22} + \hat{\mathbb{A}}_{44} + \hat{\mathbb{A}}_{66} = \lambda_2 \tag{3.24e}$$

$$\hat{\mathbb{A}}_{33} + \hat{\mathbb{A}}_{44} + \hat{\mathbb{A}}_{55} = \lambda_3 \tag{3.24f}$$

This will reduce the independent components down to 3 in the principal frame of the fourth-order tensor. The task of finding the closure approximation is simplified to select the proper function of $\hat{\mathbb{A}}_{11}$, $\hat{\mathbb{A}}_{22}$ and $\hat{\mathbb{A}}_{33}$ in terms of λ_1 and λ_2. The function is denoted as:

$$\hat{\mathbb{A}}_{11} = f_1(\lambda_1, \lambda_2) \tag{3.25a}$$

$$\hat{\mathbb{A}}_{22} = f_2(\lambda_1, \lambda_2) \tag{3.25b}$$

$$\hat{\mathbb{A}}_{33} = f_3(\lambda_1, \lambda_2) \tag{3.25c}$$

Then, a series flow fields have been used to get the exact value of $\mathbf{A}$ and $\mathbb{A}$ according to the probability density function $\psi(\mathbf{p},t)$ at each time step. Finally, a least-squares algorithm has been used to fit an arbitrary function to the data set in order to find the proper expression of three independent components of $\hat{\mathbb{A}}$. There are two fitted closures that have been introduced. One is choosing $\xi = 1$ and $C_I = 0.01$ to generate the data set. This closure is denoted as Orthotropic Fitted Closure (ORF). The ORF show a great agreement compared to the results calculated from $\psi(\mathbf{p},t)$. However, it will show non-physical oscillations on orientation components when $C_I = 0.001$. So another closure was created by setting $\xi = 1$ and $C_I = 0.001$, which is called Orthotropic Fitted Closure For Low C_I (ORL). For both closures, a complete second-order polynomial has been selected as the fitting function:

$$\hat{\mathbb{A}}_{ii}^{\text{closure}} = C_i^1 + C_i^2\lambda_1 + C_i^3{\lambda_1}^2 + C_i^4\lambda_2 + C_i^5{\lambda_2}^2 + C_i^6\lambda_1\lambda_2 \qquad i = 1\ ,\ 2,\ 3\ ;\ \text{no sum on } i \tag{3.26}$$

Once the components of $\hat{\mathbb{A}}$ is determined, one can transform the $\hat{\mathbb{A}}$ back to $\mathbb{A}$. The details can be found in[43]. It has been proved that different closure approximation will influence the value of steady state orientation tensor component a_{33} and the choice of C_I value. It is very important to use more accurate closure approximation function and to illustrate the type of closure approximation function that is used for any fibre orientation prediction. Both orthotropic fitted closures (ORF, ORL) and HYB have been implemented in the Moldflow® software. In this research the closure approximation function used is called Moldflow bi-quadratic model, which is a modified version based on the EBOF[44].

3.3 Fibre Orientation Result Confirmation

3.3.1 Reference Material and Data

Based on the knowledge of fibre orientation prediction, the better way to get a reasonable prediction of injection moulding simulation is using physical injection moulding orientation results and a proper orientation model to fit the physical data. The physical orientation results used in this confirmation process come from Holmström et al[45]. In this paper, the authors chose polyamide-6 as the matrix material and combined it with 15% and 30% weight fraction of short glass fibre. A rectangular plate with dimension 200 mm × 140 mm × 3 mm (long, wide and thick) was manufactured using injection moulding. The FOD data was investigated through an X-ray computed tomography. The relative location of the scanned sample in the plate can be found in the reference paper. The FOD data was shown as the variation of the second-order fibre orientation tensor components a_{11}, a_{22} and a_{33} through the part thickness. The orientation data of 30% fibre weight fraction sample will be selected for the confirmation process because of the relatively higher tensile stress, and are shown in Figure 3.1.

A physical tensile test have been reported in the reference paper as well. The stress-strain data can be used in the mapping process to transfer the FOD data and material properties into a FEA model, and the stress analysis on this type of composite material can be implemented using this FEA model. In this way, the tensile test data can be confirmed through a numerical tensile test using the FEA model. This will be demonstrated in the next section.

3.3.2 Simulation Setting

In order to compare and confirm the results between numerical prediction and physical measurement, a same dimension plate has been created in Solidworks®. As shown in Figure 3.2, an extra sector area in the front section has been added to the geometry, to get more uniform and stable flow in the main area of the part. The injection location is picked on the sector area which is shown in the figure as well. A similar polyamide-6 matrix material has been chosen from the database according to the properties described in the reference paper. The short glass fibre with

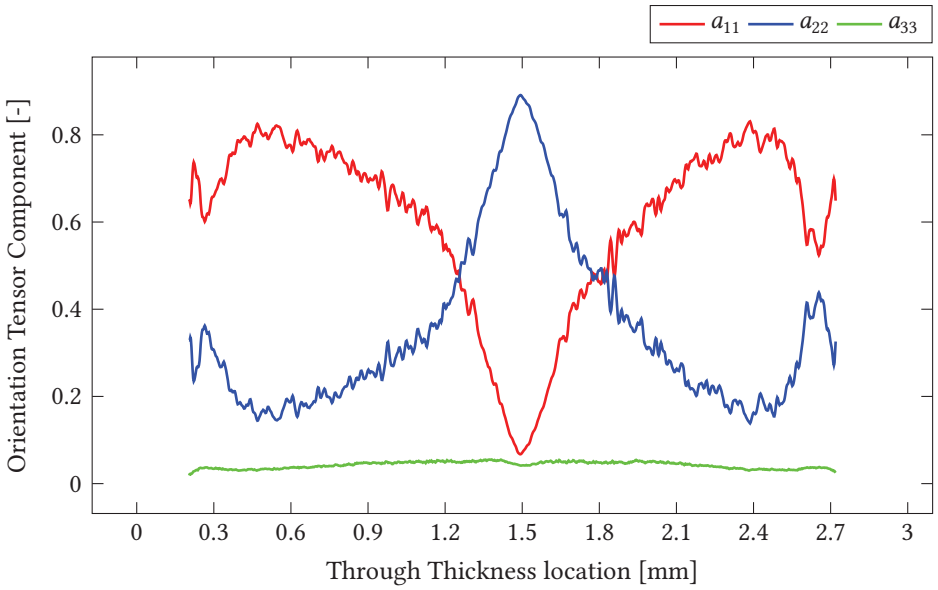

Figure 3.1: FOD Data From Experiment Measurement For 30% Fibre Weight Fraction (reproduced from[45])

29.04% weight fraction is chosen as the reinforced filler. The aspect ratio (fibre length/fibre diameter) is set to 29 according to the measurement in the reference paper. The processing parameters have been set to the default value recommended by the material manufacturer. The RSC fibre orientation prediction model is chosen according the background knowledge. The RSC was proven to be the most suitable model for short fibre injection moulding. There are two parameters, κ and C_I, that can be adjusted in the RSC model. They are empirical coefficients that will influence the speed of alignment and fibre-fibre interaction, respectively. The automatic calculation option will be used for C_I according to an empirical function based on the material property[46]. The automatically calculated value of C_I is 0.0041. The default value $\kappa = 0.05$ is used. The closure approximation function used in this study is the modified version of EBOF as mentioned in previous section. The inlet initial fibre orientation state is set to 'Fibre aligned at skin/random at core'. This option may influence the final orientation state because the slow kinetic model (RSC) and relative short cavity. This setting was chosen for initial tests with the option to change latter to better fit the experimental measurement.

Only one type of element can be chosen for the 3D mesh, a 4 nodes tetrahedral element. The remaining factor that can influence the final fibre orientation results is the mesh refinement. There are two ways to refine the mesh in Moldflow®. One is the global meshing size setting, which can be defined to automatic calculation or to the users choice. The other option is the through thickness element number setting, which will refine the inside 3D mesh regardless of the surface meshing. This choice will usually improve the accuracy of orientation prediction. To study the mesh sensitivity and its effect on the orientation prediction, different sets of global meshing size and through thickness element number have been attempted in the confirmation process. The

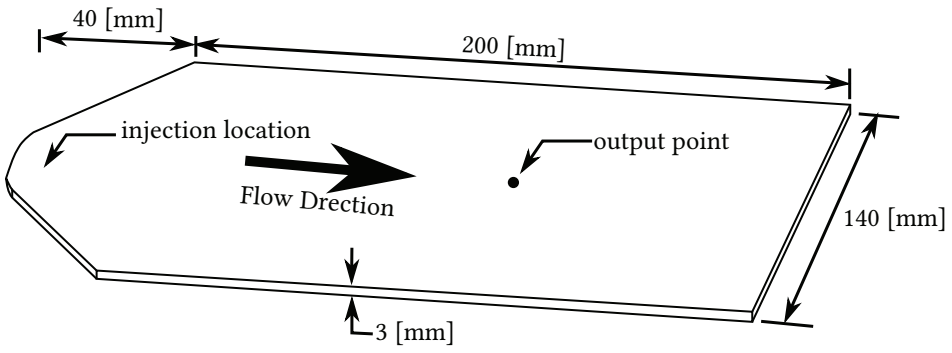

Figure 3.2: Sample Plate Dimensions. The geometry of the sample plate for the simulations was chosen to match the physical specimen used in the reference paper[45].

strategy used was to change one setting at a time and fix the other one, and run the simulation to compare the difference with physical measurement. Thus, the effect of each refinement can be investigated, and a proper setting can be found that will fit the experimental results best. The simulation prediction results of fibre orientation tensor components a_{11}, a_{22} and a_{33} are plotted as a function of the through thickness distance as well. The selected output point is as close as possible to the location where the scanned sample in the paper was taken. The approximate location is shown in Figure 3.2.

3.3.3 Results Comparison

First, the global mesh size was set to automatic calculation based on the geometry and curvature. Three different through-thickness element numbers have been defined for each simulation, which are 6, 10, and 20. The results for a_{11}, a_{22} and a_{33} are shown in Figures 3.3, 3.4, and 3.5 respectively. According to each plot, the RSC model gives quite a reason prediction for each second-order tensor component. All the simulation results show the three layers 'shell-core-shell' structure with reasonable accuracy. Increasing of the through-thickness element number improves the prediction accuracy in the core region dramatically, but it doesn't substantially influence the accuracy in the shell region. The difference from 10 elements to 20 elements is less when compared to the difference from 6 elements to 10 elements. Considering the simulation running time for both 10 elements and 20 elements case, the 10 elements will be a better choice for shorter simulation time without significantly losing accuracy. For both the 10 and 20 elements cases, the simulation would either slightly overestimate the a_{11} component in the shell region or slightly underestimate the a_{22} component in the shell region. This may indicate a different C_I value could improve the

simulation. The worst prediction was found in the core region for the a_{33} component. There are no peak values at all in the core region for a_{33} from the physical measurement, but the numerical prediction gives a relatively large peak range in the a_{33} plot. This may indicate a shortfall in the RSC model that it cannot predict the a_{33} component properly, or possibly a physical measurement error. Considering that the overall values for a_{33} is quite small, the prediction result is still in a reasonable range and very close to the physical measurement. The a_{22} component in the core region was slightly underestimated. These may be improved by setting a different inlet initial orientation state. Based on the current results, the through thickness element number was set to 10 for the remainder of the simulations.

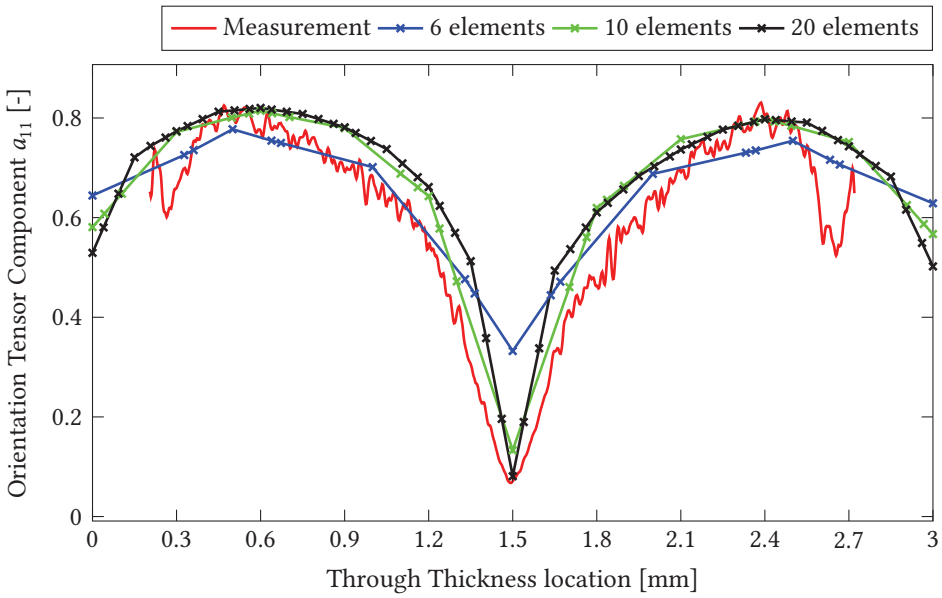

Figure 3.3: Comparison Between Experimental Measurement and Simulation Prediction for Different Through Thickness Element Number for Tensor Component a_{11}. Note that using either 10 or 20 elements provides a substantial improvement over 6 elements.

Then, after the through thickness element number was fixed at 10, the global mesh size was changed to 3 mm, 2 mm and 1 mm for each simulation. This value defines the longest element edge that can be generated during the mesh process. The comparison is shown in Figures 3.6, 3.7, and 3.8 for a_{11}, a_{22}, and a_{33} respectively. The results show that the global element size has a minor influence in the shell region but a major influence in the core region. The prediction accuracy has an outstanding improvement when changing from a mesh size of 3 mm to a size of 2 mm. Both the size 2 mm and size 1 mm cases fit the physical measurement values very well for both the shell and core regions. An obvious improvement can be found for the a_{33} component as well, especially the core region peak values that shrank with reduced global element size. For every tensor component, the size 2 mm and size 1 mm cases are almost identical. Comparing the simulation time for these two cases, the size 2 mm case was three times faster than the size 1 mm case. A global element

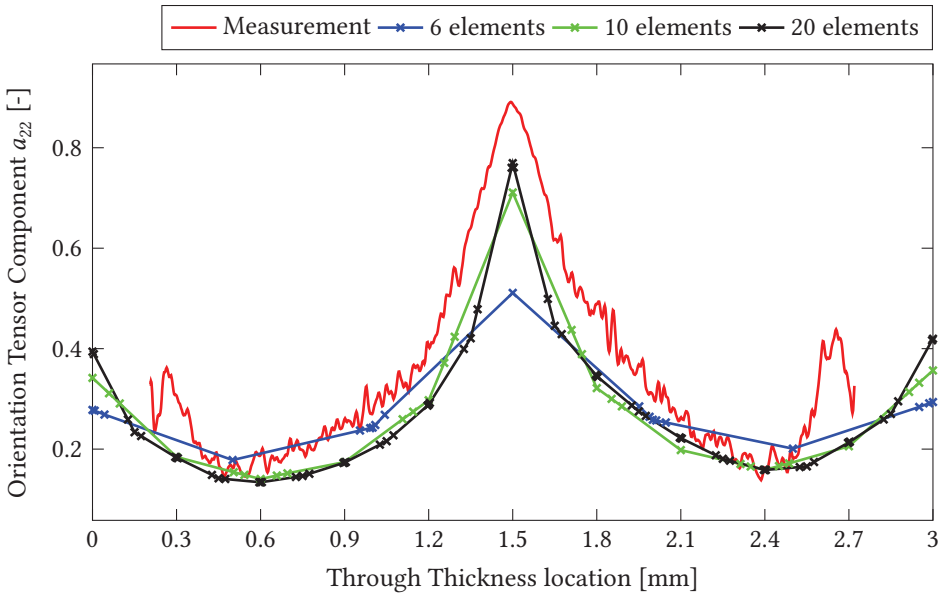

Figure 3.4: Comparison Between Experimental Measurement and Simulation Prediction for Different Through Thickness Element Number for Tensor Component a_{22}. As in the a_{11} result, note that using either 10 or 20 elements provides a substantial improvement over 6 elements.

size of 2 mm will have an advantage if a large scale project was involved. The size of 2 mm setting was chosen for best accuracy and efficiency for this research.

According to all the simulation results, the RSC model has been shown to fit the experimental measurement very well using the automatically calculated C_I value and the default κ value. Mesh refinement is the key to obtain better results. The shortage of this numerical prediction is that only a single location and geometry can be verified because of the lack of physical measurements for other cases. The effect of different thickness and complex shapes is unknown. Considering that the essence of any fibre orientation prediction model is to build an objective method based on confirmation through experimental observation, for higher accuracy and more confident design, the actual composite lower arm could be manufactured as a sample to validate the numerical prediction. This could be future work if suitable injection moulding equipment can be located, but the expense of producing a mould makes this a challenge. For this research, the orientation prediction was assumed to be sufficiently accurate for this particular fibre and matrix combination, and the confirmed parameters were used in the lower arm study.

3.4 Connection to Stress Analysis

3.4.1 Background Theory

One objective of this research is to predict the strength of composite lower arm using FEA. The predicted orientation results should be connected to the stress analysis as a contribution to

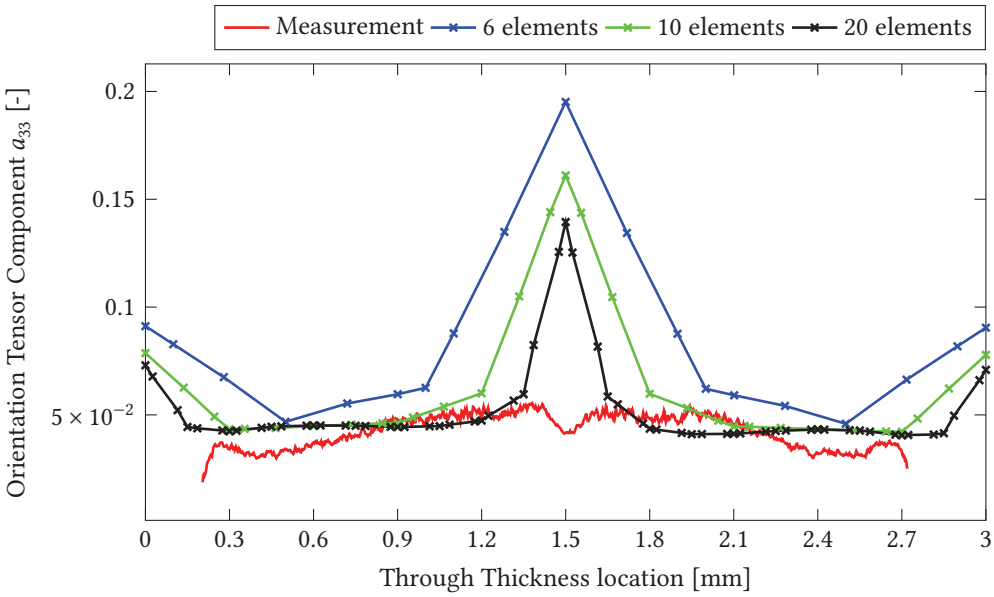

Figure 3.5: Comparison Between Experimental Measurement and Simulation Prediction for Different Through Thickness Element Number for Tensor Component a_{33}. Notice that the trends for a_{33} prediction do not match as well as those for a_{11} or a_{22}, but also that the range of values is also significantly smaller.

anisotropic stiffness properties in FEA model. This connection process is achieved through another software from AutoDesk® called AME. The AME software has two major functions:

1. Map orientation results from an Autodesk Moldflow® analysis mesh into a structural finite element analysis mesh.
2. Offer a fitting process on non-linear stress-strain data to get the coefficients of a multi-scale material model, which characterize the elastic-plastic response of the target material for structural analysis.

In this section, the background theory of this multi-scale material model will be introduced.

Based on many previous studies, e.g.,[8][47], a fibre orientation averaging process is a reliable way to calculate the composite material stiffness matrix according to the fibre orientation tensor of actual composite material and a reference composite material with unidirectional fibre alignment. First, the stiffness of the unidirectional fibre reinforced composite material was evaluated using the following equation:

$$\mathbf{C}^* = \mathbf{C}_m + \phi_f(\mathbf{C}_f - \mathbf{C}_m) : \mathbf{A}_f \tag{3.27}$$

where $\mathbf{C}^*$ is the stiffness tensor of the unidirectional composite material, also called reference material. The ϕ_f is the fibre volume fraction. The $\mathbf{C}_m$ and $\mathbf{C}_f$ are the stiffness tensors of the

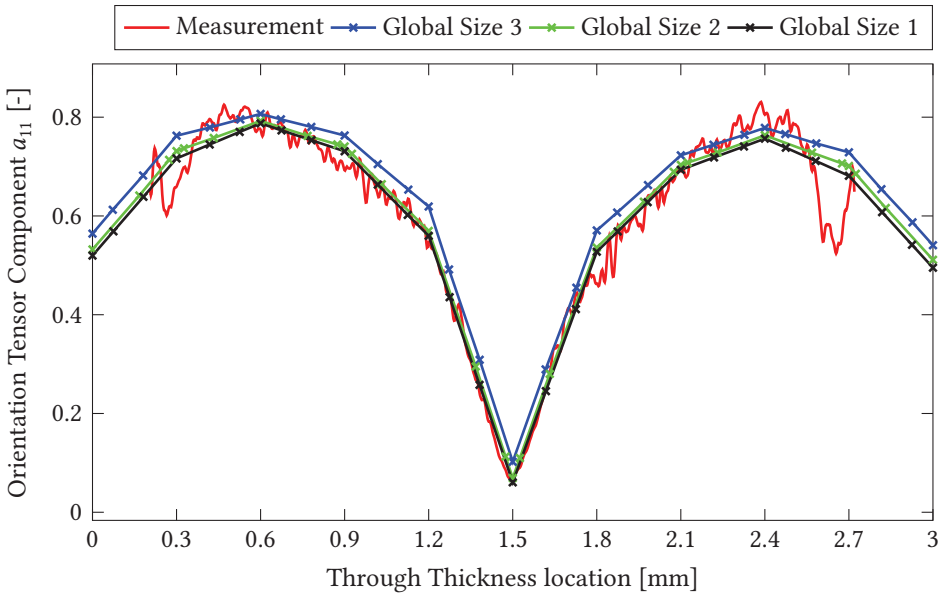

Figure 3.6: Comparison Between Experimental Measurement and Simulation Prediction For Different Global Element Size for Tensor Component a_{11}. Note that all three choices show good agreement.

individual matrix and fibre materials, respectively. The $\mathbf{A}_f$ is the fibre strain concentration tensor, which is defined by:

$$\mathbf{A}_f = \mathbf{T} : [(1-\phi_f)\mathbf{I} + \phi_f \mathbf{T}]^{-1} \tag{3.28}$$

$$\mathbf{T} = [\mathbf{I} + \mathbf{S} : {\mathbf{C}_m}^{-1} : (\mathbf{C}_f - \mathbf{C}_m)]^{-1} \tag{3.29}$$

where $\mathbf{S}$ is Eshelby's tensor. Based on Eqns. 3.27, 3.28, and 3.29, the $\mathbf{C}^*$ can be calculated. This process is called Eshelby–Mori–Tanaka Approach (EMTA)[48]. After the $\mathbf{C}^*$ is known, the orientation averaging process can be applied to get the stiffness tensor $\bar{\mathbf{C}}$ of the actual composite material with a predicted FOD. The function of the averaging method is expressed as:

$$\bar{\mathbf{C}} = B_1 a_{ijkl} + B_2(a_{ij}\mathbf{I}_{kl} + a_{kl}\mathbf{I}_{ij}) + B_3(a_{ik}\mathbf{I}_{jl} + a_{il}\mathbf{I}_{jk} + a_{jk}\mathbf{I}_{il}) + B_4\mathbf{I}_{ij}\mathbf{I}_{kl} + B_5(\mathbf{I}_{ik}\mathbf{I}_{jl} + \mathbf{I}_{ij}\mathbf{I}_{jk}) \tag{3.30}$$

where B_i $(i = 1, \ldots, 5)$ are the coefficients that are defined by the invariants of the $\mathbf{C}^*$. The expression of each coefficient is given in[8][47] and expressed as:

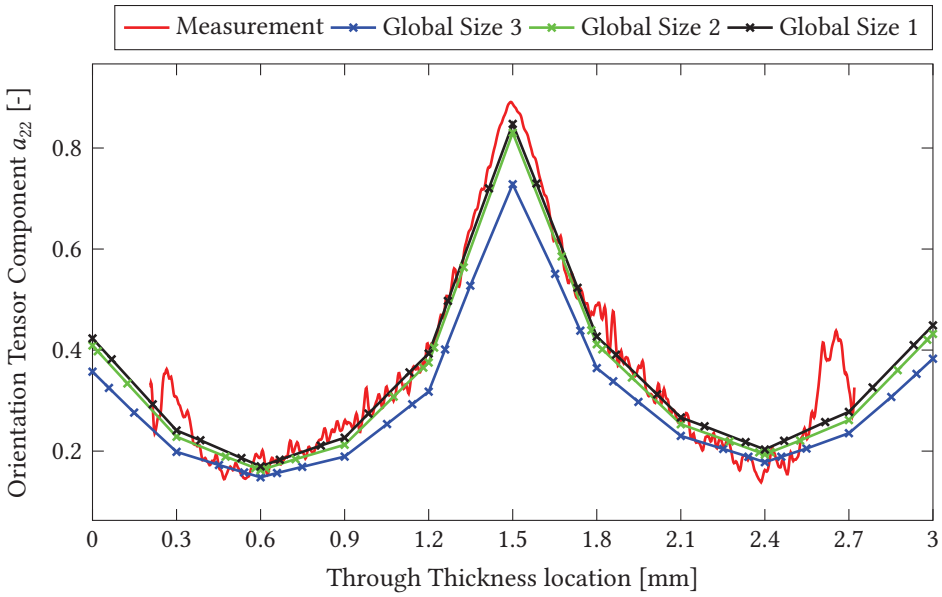

Figure 3.7: Comparison Between Experimental Measurement and Simulation Prediction For Different Global Element Size for Tensor Component a_{22}. Note that the 1 mm and 2 mm size shows improvements over the 3 mm size.

$$B_1 = \mathbf{C}^*{}_{11} + \mathbf{C}^*{}_{22} - 2\mathbf{C}^*{}_{12} - 4\mathbf{C}^*{}_{66} \tag{3.31}$$

$$B_2 = \mathbf{C}^*{}_{12} - \mathbf{C}^*{}_{23} \tag{3.32}$$

$$B_3 = \mathbf{C}^*{}_{66} + \frac{1}{2}(\mathbf{C}^*{}_{23} - \mathbf{C}^*{}_{22}) \tag{3.33}$$

$$B_4 = \mathbf{C}^*{}_{23} \tag{3.34}$$

$$B_5 = \frac{1}{2}(\mathbf{C}^*{}_{22} - \mathbf{C}^*{}_{23}) \tag{3.35}$$

For convenience, the fourth-order tensor $\mathbf{C}^*{}_{ijkl}$ is expressed with the contracted index notation, following the rule in Eqn. 3.15. Also, the fourth-order orientation tensor a_{ijkl} needs to be approximated by a closure function as described in Section 3.2.2. Following this sequence, the predicted fibre orientation state can be used to model the stiffness properties of composite materials in the FEA model. The previous procedure is only good in describing linear material behaviours. Considering that most FRP material will experience some degree of plasticity depending on the degree of fibre alignment and the direction of loading, relative to the fibre-aligned direction, a plasticity and rupture model is also used in the AME software to predict the non-linear behaviours of composite materials according to the predicted fibre orientation state[49].

Based on a previous damage behaviour study[50], since the fibre length is relatively short in the polymer material, most ruptures happen without actually breaking the fibre in common short

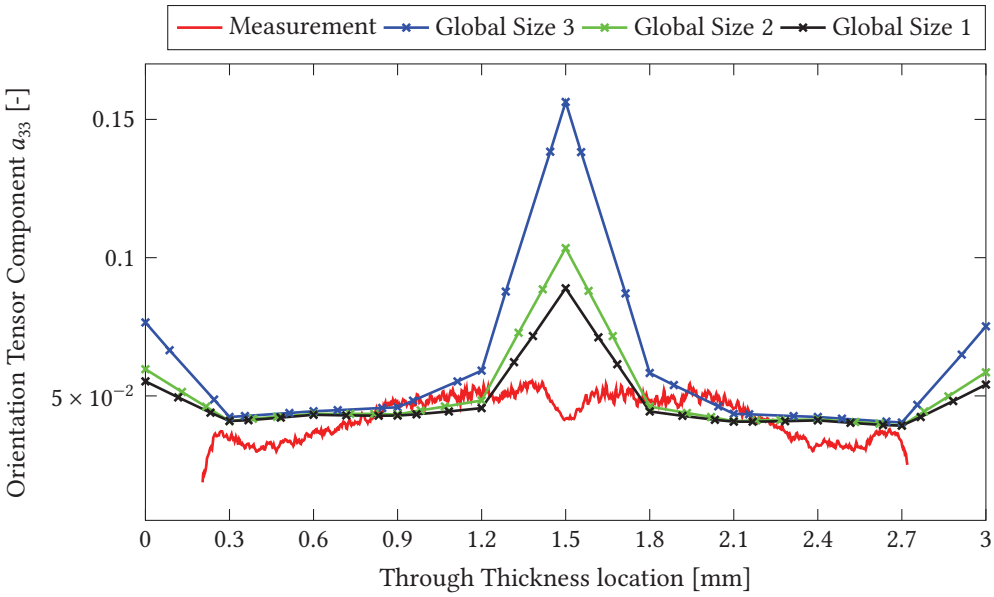

Figure 3.8: Comparison Between Experimental Measurement and Simulation Prediction For Different Global Element Size for Tensor Component a_{33}. Note that the predicted peak value in the core is reduced with shrinking element size.

FRP material. The major failure is caused by micro-cracking in the matrix and interfacial decohesion between the fibre and the matrix. According to the characteristics of plasticity and damage behaviours, a multi-scale material model has been built based on the following assumptions:

1. The fibres won't have any plastic or rupture behaviours, only simple linear elastic behaviour. The matrix material will show both plastic and rupture response under loading.
2. The intended plasticity and rupture model are designed to include the debonding between fibre and matrix that happens in the composite material.
3. All non-linear (plasticity and rupture) behaviour is caused by the matrix material. The non-linearity is driven by the stress in the matrix constituent material, not the homogenized stress in the composite material.
4. The non-linear responses of the matrix material are strongly dependent on the alignment of the fibre orientation. If the degree of fibre alignment is high, the plasticity and rupture responses will be strongly dependent on the direction of loading relative to alignment direction.

To build the multi-scale material model, two steps must be followed: The homogenization process and the decomposition process[51]. In the homogenization process, individual fibre and matrix material properties are used by the EMTA to generate the stiffness properties of a perfectly aligned unidirectional composite material. These properties are then used to produce the actual

composite material stiffness properties by a fibre orientation averaging method, based on the predicted FOD from the Moldflow® software. The details of this process were introduced in previous content. The homogenization process primarily accounts for the linear behaviour of the composite material. In the decomposition process, the first step is to decompose the homogenized strain from the composite material into the average strain in the matrix constituent material, and the second step is to use the average strain of the matrix to account for the matrix plastic response. The first step is achieved by following equations:

$$\Delta\varepsilon_f = \bar{\mathbf{A}}_f \,:\, \Delta\varepsilon \tag{3.36}$$

$$\Delta\varepsilon_m = \mathbf{A}_m \,:\, \Delta\varepsilon \tag{3.37}$$

where $\Delta\varepsilon$ is the total composite material strain increment, and $\Delta\varepsilon_f$ and $\Delta\varepsilon_m$ are the decomposed average strain increment in the fibre and the matrix, respectively. The $\bar{\mathbf{A}}_f$ is the orientation average of $\mathbf{A}_f$, which is calculated by using the orientation averaging method in Eqn. 3.30. The matrix strain concentration tensor $\mathbf{A}_m$ is expressed as function of $\bar{\mathbf{A}}_f$:

$$\mathbf{A}_m = \frac{\mathbf{I} - \phi_f \bar{\mathbf{A}}_f}{1 - \phi_f} \tag{3.38}$$

Based on the assumptions, all the plastic response comes from the matrix material. So the main idea of the second step is to replace the elastic stiffness tensor of the matrix $\mathbf{C}_m$ in Eqns. 3.27, 3.28, and 3.29 with the tangent stiffness tensor of matrix $\mathbf{C}_m^t$. The $\mathbf{C}_m^t$ is calculated based on the Ramberg-Osgood plasticity model[52] through an iterative process. The elastic-plastic behaviour of the matrix constituent material is expressed as:

$$\bar{\varepsilon}_m = \bar{\varepsilon}_m^e + \bar{\varepsilon}_m^p = \frac{\bar{\sigma}_m}{E_m} + (\frac{\sigma_Y}{E_m})(\frac{\bar{\sigma}_m}{\sigma_Y})^n \tag{3.39}$$

The relationship shows the total strain of the matrix $\bar{\varepsilon}_m$ can be divided into two parts: the equivalent matrix elastic strain $\bar{\varepsilon}_m^e$ and the equivalent matrix plastic strain $\bar{\varepsilon}_m^p$, where σ_Y and n are the constant material coefficients, which are known as the yield stress and the power-law index. The E_m is the matrix elastic modulus. The $\bar{\sigma}_m$ is the equivalent matrix stress. The plastic modulus E_m^p is calculated based on the Ramberg-Osgood relationship:

$$E_m^p = \frac{d\bar{\sigma}_m}{d\bar{\varepsilon}_m^p} = \frac{(E_m)^{1/n}(\sigma_Y)^{(n-1)/n}(\bar{\varepsilon}_m^p)^{(1-n)/n}}{n} \tag{3.40}$$

Then, the current tangent modulus of the matrix is defined by:

$$E_m^t = \frac{E_m E_m^p}{E_m + E_m^p} \tag{3.41}$$

As shown in Eqns. 3.39 and 3.40, in order to calculate the tangent modulus E_m^t, the equivalent matrix stress $\bar{\sigma}_m$ needs to be defined at current state, so the $\bar{\sigma}_m$ is expressed by an enhanced version of von Mises stress:

$$\bar{\sigma}_m = \sqrt{\frac{(\alpha\sigma_{11} - \beta\sigma_{22})^2 + (\beta\sigma_{22} - \beta\sigma_{33})^2 + (\beta\sigma_{33} - \alpha\sigma_{11})^2 + 6[(\sigma_{12})^2 + (\sigma_{23})^2 + (\sigma_{31})^2]}{2}} \tag{3.42}$$

Note that the stress components here represent the average stress in the matrix constituent material, where the α and β are the weighting coefficients for the impact of stress components in the average fibre direction and normal to the average fibre direction, respectively. By adding these two coefficients in the standard von Mises stress expression, the calculated equivalent matrix stress $\bar{\sigma}_m$ accounts for the strong directional dependency behaviours in the matrix plastic response. This directional dependency phenomenon is only obvious when the fibre alignment is relatively high, so α and β cannot be constant for all cases. Instead, they are a function of the largest eigenvalue λ_l of the fibre orientation tensor. Based on the knowledge of the second-order orientation tensor, λ_l quantifies the degree of fibre alignment, so α and β are a linear function of λ_l and expressed as:

$$\alpha(\lambda_l) = \theta_r + [\frac{(\alpha_o - \theta_r)}{(\lambda_{o,l} - 1/2)}](\lambda_l - 1/2) \tag{3.43}$$

$$\beta(\lambda_l) = \theta_r + [\frac{(\beta_o - \theta_r)}{(\lambda_{o,l} - 1/2)}](\lambda_l - 1/2) \tag{3.44}$$

where the α_o and β_o are the values of α and β, respectively, that are obtained by using an optimization fitting process on the highly aligned material that has the largest fibre orientation eigenvalue of $\lambda_{o,l}$. The θ_r is the value that both α and β should become when a random fibre orientation is formed. In most cases, a completely 3D random distribution of fibres will not happen for injection moulding material. Instead, the injection moulding material will most likely form an in-plane random fibre orientation (i.e., $\lambda_1 = \lambda_2 = 1/2$). In order to account for this common in-plane isotropic behaviour, the term $(\lambda_l - 1/2)$ is added to the equation to ensure that when $\lambda_l = 1/2$, α and β become the same value θ_r and there is no strong directional dependency on the stress components of the von Mises stress calculation.

After the $\bar{\sigma}_m$ has been defined, the current equivalent matrix plastic strain $\bar{\varepsilon}_m^p$ can be calculated using Eqn. 3.39, and the tangent modulus E_m^t can be calculated using Eqns. 3.40 and 3.41. Using the calculated tangent modulus result, the calculation of the current tangent stiffness tensor $\mathbf{C}_m^t$

can be achieved. By replacing the $\mathbf{C}_m$ with $\mathbf{C}_m^t$ in Eqns. 3.27, 3.28, and 3.29, and applying Eqn. 3.30, the current overall tangent stiffness tensor of the composite material $\bar{\mathbf{C}}^t$ can be determined. Then, the equivalent matrix stress increment and the total composite stress increment can be calculated using:

$$\Delta\bar{\sigma}_m = \mathbf{C}_m^t \,:\, \Delta\varepsilon_m \tag{3.45}$$

$$\Delta\sigma = \bar{\mathbf{C}}^t \,:\, \Delta\varepsilon \tag{3.46}$$

Thus, the equivalent matrix stress and overall composite stress are updated. The new $\bar{\sigma}_m$ is used to calculate the equivalent matrix plastic strain $\bar{\varepsilon}_m^p$ for next increment of the loading process. Through this iterative process, the plastic evolution of a composite material with a particular FOD under a total strain increment can be evaluated.

The next step is to utilize a rupture criterion to identify the failure state of this composite material. There are two failure criteria in the AME software. The default setting is the Multi Continuum Theory (MCT) failure criterion. According to this criterion, the rupture state is defined by a quadratic function of the matrix average stress components:

$$A_1^m(\mathrm{I}_1^m)^2 + A_2^m(\mathrm{I}_2^m)^2 + A_4^m\mathrm{I}_4^m \geq 1 \tag{3.47}$$

where I_1^m, I_2^m and I_4^m are the transversely isotropic invariants of the matrix average stress state. They are expressed as:

$$\mathrm{I}_1^m = \sigma_{11} \tag{3.48a}$$

$$\mathrm{I}_2^m = \sigma_{22} + \sigma_{33} \tag{3.48b}$$

$$\mathrm{I}_4^m = (\sigma_{12})^2 + (\sigma_{13})^2 \tag{3.48c}$$

where A_1^m, A_2^m and A_4^m are the adjustable coefficients of the matrix failure criteria that are defined through the curve fitting process in the AME software. These parameters influence the failure behaviours dramatically. It is necessary to adjust them to get better fitting results from the experimental tensile test data.

The other choice is the maximum effective stress failure criterion. This criterion assumes the weighted von Mises stress expression is good enough to account for the directional dependency of the composite material rupture. Based on this assumption, the rule of this failure criteria is simply defining an upper limit value σ_{max} for enhanced von Mises stress. So the rupture condition is expressed as:

$$\sqrt{\frac{(\alpha\sigma_{11}-\beta\sigma_{22})^2+(\beta\sigma_{22}-\beta\sigma_{33})^2+(\beta\sigma_{33}-\alpha\sigma_{11})^2+6[(\sigma_{12})^2+(\sigma_{23})^2+(\sigma_{31})^2]}{2}} \geq \sigma_{max} \quad (3.49)$$

In this research, the MCT failure criterion has been used, because it shows more directional dependency on the failure results, which is similar to the experimental tensile test observation. After the rupture condition is reached, there were several changes made to the constitutive relations of the failed material.

1. The composite stress and strain did not need to be decomposed into matrix stress and strain any more.
2. The constitutive relations of the homogenized composite material were used.
3. The stiffness of the failed material reduced to a fraction of the original elastic stiffness of the composite material. This was controlled by the degradation parameter in the FEA model.
4. The tangent formulation changed to a secant formulation, because the integration process does not contribute any non-linear solution.

According to all the previous processes, the multi-scale material model has been built and implemented in the AME software. In order to use this model on the Moldflow® simulation results, several coefficients needed to be determined. They are σ_Y, n, α, β and λ_l for plastic response; E_f, ν_f, E_m and ν_m for linear response; A_1^m, A_2^m and A_4^m for rupture identification. These coefficients were defined by fitting the curve to a collection of tensile experimental data for the target material in MoldFlow®. The tensile test data is offered in the reference paper[45]. The confirmation process on the stress-strain response prediction will be shown in the next section.

3.4.2 Confirmation On Stress-strain Response Prediction

To achieve the confirmation process, a tensile test specimen of the same dimensions as those in the reference has been modelled using Abaqus® FEA software. The dimensions of the specimen are shown in Figure 3.9. The chosen coordinate system is shown in the figure as well. The positive x direction is pointing to the right. The positive y direction is pointing up. The positive z direction is pointing out of the page. The holes on both sides of the sample are omitted in the FEA because the pin support is not suitable for the numerical test. The pin support has been evaluated in the Abaqus® model, and it causes numerical difficulties and complexity in the boundary conditions and makes the results difficult to compare to the traditional clamp support. For the physical tensile test, the specimen was cut from the manufactured composite plate at angles of 0°, 15°, 30°, 45°, 60°, 75°, and 90° relative to the flow direction. A similar approach can be achieved using the mapping function in AME software. As shown in Figure 3.10, by changing the location and direction of the specimen relative to the manufactured composite plate during the mapping process, different

distributions of fibre alignment can be obtained in the mapped specimen for the structural analysis. This makes the numerical test setting mimic the physical test case.

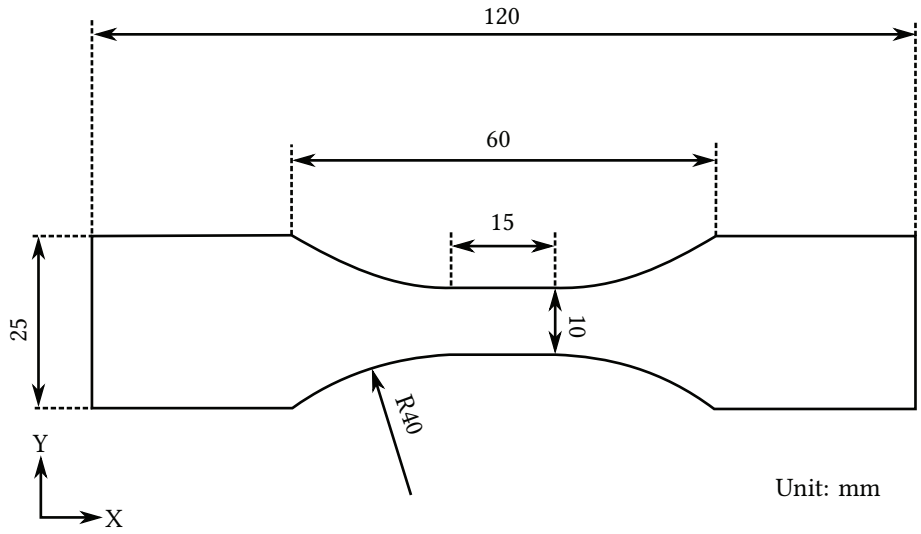

Figure 3.9: Tensile Test Specimen Measurement

Meshing size is another important effect to achieve a good simulation result. According to the mapping suitability plot in the AME software, at least 20 elements are necessary through the specimen thickness. In the Abaqus®, the mesh size can be controlled by setting corresponding element number on each edge of the specimen to achieve a different meshing size case. For all the cases, the edges on the thickness were defined to have 20 elements based on the mapping suitability. For the standard case, to ensure the gauge section had a relatively finer mesh, based on the dimensions of the gauge section (10 mm × 15 mm in the width and length), the edges on the width were defined to have 10 elements and the edges on the length were defined to have 12 elements. The fillet edges were set to have 19 elements. For the grip section, the dimension is 25 mm × 30 mm in the width and length. The same '10 elements × 12 elements setting on the width and length edges' was selected. The grip section was allowed to have a coarse mesh, because most of the strain occurs in the gauge section. To achieve a meshing sensitivity study, the other cases defined the mesh according to the standard setup. Double and triple element number were set on the edges according to the standard setting. This setting resulted in two refined meshing cases: one with 1/2 the standard meshing size; the other with 1/3 the standard meshing size. The C3D8R 8-node linear reduced integration brick element was chosen for the simulation. The total element number with the standard element size was 59200.

The right face, which points in the positive x direction, was chosen as the moving side of the specimen. The other end was the fixed side. Three constraint boundary conditions were set on the left face of the specimen: 1. The whole surface was constrained in the x direction; 2. The middle point of the bottom edge was fixed in both y and z directions; 3. The middle point of the top edge

was fixed only in the y direction. On the moving side of the specimen, a total 3 mm displacement boundary condition was defined to achieve the tensile behaviours and to ensure the specimen broke under this displacement. These boundary conditions were properly designed to allow the specimen to strain in both y and z directions when a displacement was applied to the moving end. The static load step was created in the model using a total 72 second period and minimum 1 second increment. This resulted in a strain rate close to the rate in the physical test. An empty material property definition was set in the model. The material properties were defined by several parameters that were confirmed through the mapping process. After all the properties had been defined in the Abaqus® input file (∗.inp), this input file was imported into the AME software as a source for the mapping process. The other source was the study results file (∗.sdy) from Moldflow®, which contains the fibre orientation results.

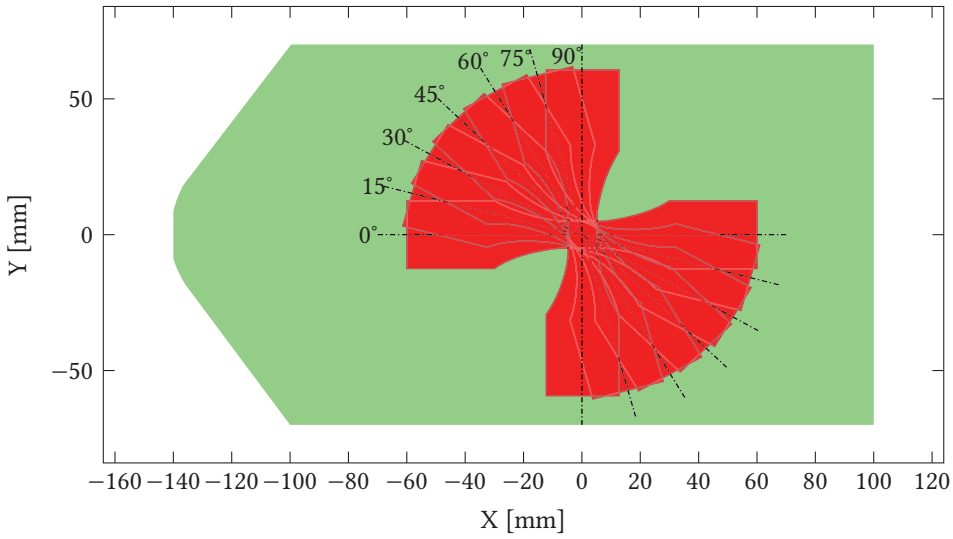

Figure 3.10: Specimen Mapping Location For Numerical Tensile Test

During the mapping process, the material parameters were defined by the curve fitting method. There are two methods of curve fitting in AME software. Multi-layer curve fitting was chosen in this research, because it is described to be more accurate according to the user manual. The 0°, 45° and 90° tensile test stress-strain data are used in curve fitting process. The ideal fitting results are shown in Figure 3.11. The parameters defined during the curve fitting process are: $\sigma_Y = 73.9869$ MPa, $n = 14.2918$, $\alpha = 2.01682$, $\beta = 1.07911$ and $\lambda_l = 0.85$ for plastic response; $E_f = 38716.5$ MPa, $\nu_f = 0.222148$, $E_m = 3567.6$ MPa and $\nu_m = 0.448913$ for linear response; $A_1^m = 0.000946617$ MPa^{-1}, $A_2^m = 0.0000518264$ MPa^{-1} and $A_4^m = 0.0000089634$ MPa^{-1} for rupture identification. There are three files generated by the mapping process: 1. The modified Abaqus® input file that contains the material definition; 2. The structural interface file (∗.sif) which stores all the above material parameters and the fibre orientation mapping results; 3. The helius input file (∗.hin) which contains the keywords that can change the above parameters to influence the analysis. All three files can be exported after the mapping process is complete. These three files must be in the same path when

the simulation is running.

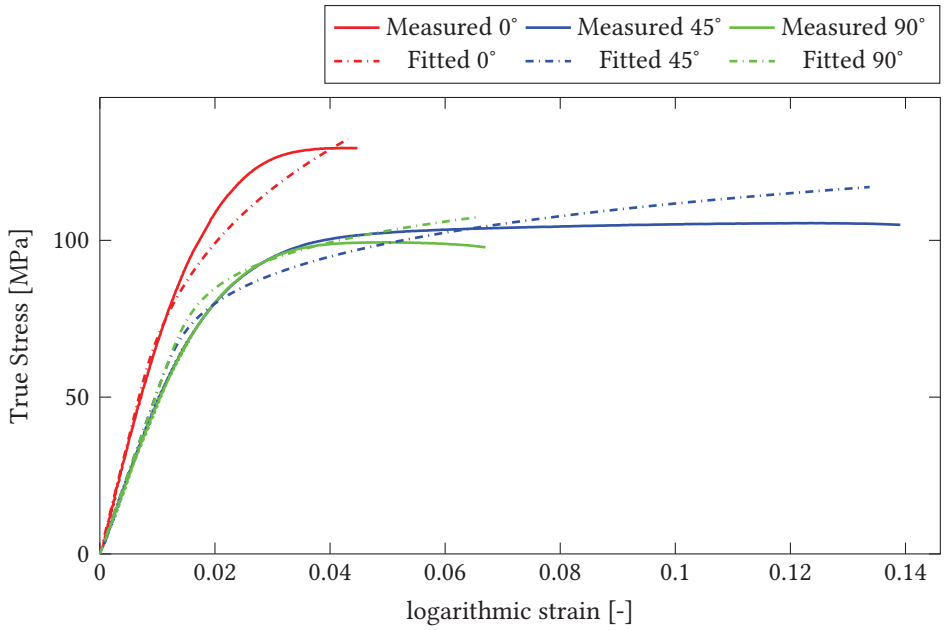

Figure 3.11: AME Stress-strain Curve Fitting For Physical Tensile Test (Multi-layer)

After the simulation has finished, a way to compare the results between the numerical and physical tests is needed. From the reference paper, the physical test results are shown in a true stress vs true strain curve. To obtain the same curve from the FEA simulation results, a proper python script has been developed to extract the true stress and true strain data from the output database file (*.obd). The python script file for standard element size can be found in Appendix A.7. By using this python script, the true stress vs true strain data was written into a text file for each fibre orientation alignment case. The comparison of the results obtained using the default curve-fitting parameters is shown in Figure 3.12. The numerical tensile test results show a substantial difference compared to the physical test in both linear and non-linear behaviours. When considering the linear behaviour, the simulation shows that the difference in stiffness between the 0° and 90° cases is almost negligible. The degree of fibre alignment appears to have very little influence on the material strength. This behaviour does not agree with the actual physical observation. It appears that in the material properties from the Moldflow® database, the stiffness of the fibre is too low and the stiffness of the matrix is too high. This is one of most important reasons that the numerical linear behaviour shows so much difference compared to the physical test. When considering the non-linear behaviour, the result shows that the yield strength of 0° case is much lower and the yield strength of 45° case is much higher when compared to the physical test. This leads the stress-strain curve in plastic range to have a large difference. All the results show that the numerical FEA model with the default material parameters are not capable of accurately predicting the physical stress-strain response. A modification on the material parameters was needed

to manually fit the numerical model to become close to the physical case.

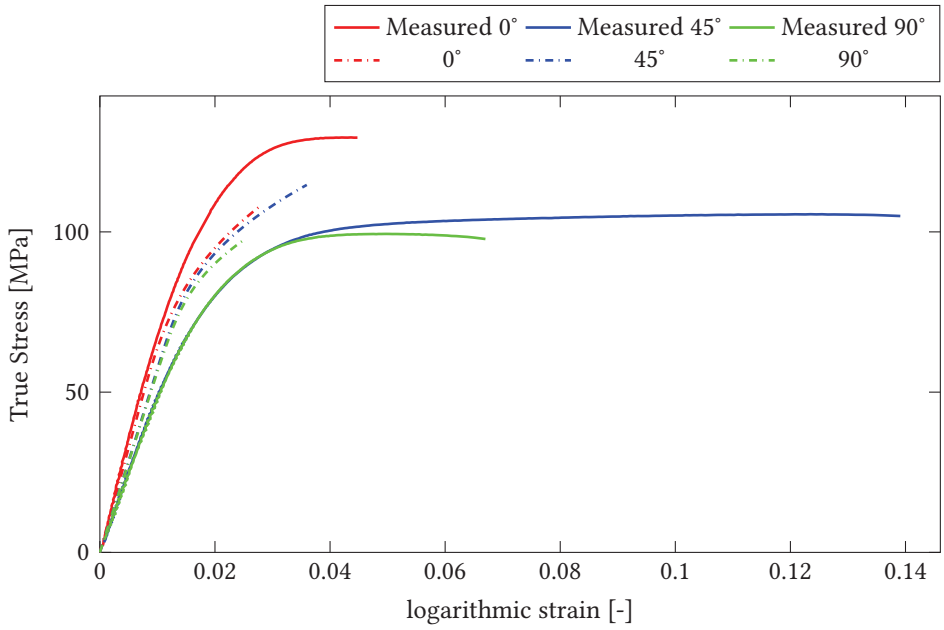

Figure 3.12: Numerical Test With Standard Meshing Size (default material parameters) vs Physical Test in 0°, 45°, 90°. The standard material properties in the database do not give an acceptable predition of specimen behaviour.

The strategy used was to change the linear properties incrementally to make the stiffness close to the physical case in three major fibre-aligned directions (0°, 45°, 90°). The stiffness of the fibre was adjusted to a higher value step-by-step, while the stiffness of matrix was adjusted to a lower value accordingly. After the stiffness had been confirmed and fitted to the physical case, the next goal was changing the non-linear parameters to ensure the plastic behaviour and failure point are similar to the physical case. It is important to mention that the non-linear behaviour could not be perfectly fitted to match the physical case, for two reasons. First is the issue that the plasticity model in the AME software is only good for predicting the behaviour of relatively brittle material. Accurate large strain behaviour cannot be achieved using this plasticity model. The other reason is that the failure detection in the FEA model has been defined based on a single element failure, instead of the actual breaking of the specimen, so the rupture point arrives relatively early in the stress-strain curve when compared to the physical case. Based on the above strategies, 90 different trials have been conducted in the numerical tensile test. The final parameter set made the numerical stress-strain curve fit much better to the measured curve.

The adjusted material parameters are: $\sigma_Y = 37.5869$ MPa, $n = 14.2918$, $\alpha = 2.01682$, $\beta = 0.75$ and $\lambda_l = 1$ for plastic response; $E_f = 108716.5$ MPa, $\nu_f = 0.222148$, $E_m = 1567.6$ MPa and $\nu_m = 0.328913$ for linear response; $A_1^m = 0.001966617$ MPa^{-1}, $A_2^m = 0.0000518264$ MPa^{-1} and $A_4^m = 0.0007689634$ MPa^{-1} for rupture identification. There are noticeable changes that have been

found in the mechanical properties for both the fibre and matrix material. These changes are unexpected in the real world, because these values should be relatively constant or within a small range. This indicates a shortcoming of the numerical composite material model in properly representing the actual physical behaviours in the tensile test. There could be two reasons for this. First, the confirmed material constants used in the Ramberg-Osgood model during the mapping process were not accurate at representing the fibre directional dependency behaviour that occurred in the physical tensile test. Second, the failure definition in the numerical tensile test depends on any individual element failure which is not same as the physical case. These are main reasons that some unrealistic values are shown when the mapping process is used to fit the numerical model to represent the actual physical case. Considering that the final numerical model should predict the tensile behaviours of the physical case, these large changes in the material constants could be tolerated. The final stress analysis on the composite lower arm should result in a reasonable performance prediction. However, more accurate composite material models will are recommended for further studies.

The comparison between the numerical and physical tests using the adjusted parameters is shown in Figure 3.13. It shows that in the linear range, the numerical results fit very well in all three angle cases. The non-linear behaviour in 0° and 90° case are an acceptable approximation to the physical measurement. A relatively large over-estimate in the non-linear behaviour has been shown in the 45° case. This is the best fitting result that can be obtained using the current plasticity model. A relatively high ultimate strength is shown on the 45° case. Additional changes of the parameters were also tested, but no significant influence on the non-linear range for the 45° case was found. In total, the overall fitting results are very reasonable, with especially good results in the linear behaviour prediction. This is significant because the lower arm performance assessment was focused on the linear range. Some inaccuracy in the plastic behaviour in the 45° load case using the adjusted material parameters is tolerated.

Figure 3.13 only shows the comparison of the 0°, 45° and 90° cases. The reference paper offers the stress-strain data in the 15°, 30°, 60° and 75° cases as well. To make the confirmation process complete, these four cases were also conducted in the FEA model. The comparison results are shown in Appendix C.

To study the meshing size effect on the stress-strain prediction, double and triple element numbers for the meshing procedure were applied on the FEA model. In other words, 1/2 and 1/3 meshing size, compared to the standard element size, have been tested in the FEA simulation. The stress-strain curve comparison under 1/2 meshing size is shown in Figure 3.14. The three major directions of fibre alignment have been compared in the figure. It shows that the meshing size did have an influence on the stress-strain response, but only in the non-linear range. The linear behaviour does not change significantly for all three cases. The notable difference is that the rupture happens at a smaller strain. The trend of plastic hardening behaviour does not change either. This result is predictable because the rupture definition in the numerical model is based

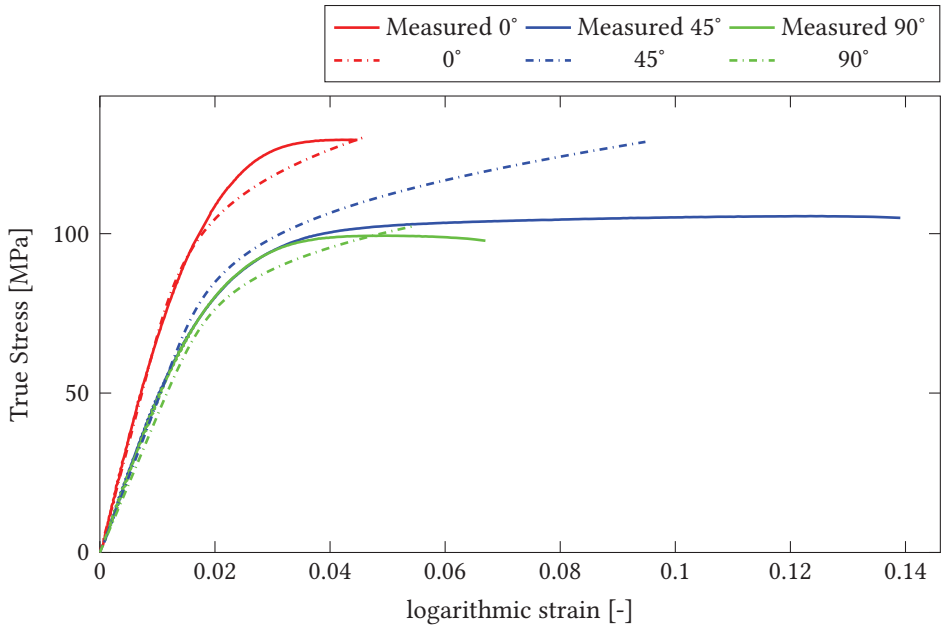

Figure 3.13: Numerical Test With Standard Meshing Size (adjusted material parameters) vs Physical Test in 0°, 45°, 90°. Notice that the adjusted material properties provide a substantial improvement in the model prediction.

on a single element failure. A more refined mesh size will encourage an earlier rupture detection during the simulation. Considering that the linear behaviour is the main focus in the later lower arm simulations, a smaller meshing size will not have significant influence on the material strength analysis. This could be one of the considerations in a future study, as a finer meshing size will offer more conservative prediction and safer design for the numerical structure analysis. The comparison of other four direction cases have been plotted in Appendix C in Figure C.2. The result shows the same behaviour as the three major directions. There is one exception in the 60° case, where the first rupture occurred at a larger strain when smaller element size was used, but the increase in strain was not significant. It is hard to explain the reason for this result. It may be caused by the relatively large time step, result in an error in the element failure detection. Additional refinement on the element size was needed to check the consistency of the meshing size effect. To make a more obvious illustration, the comparison plot for the stress-strain curves of the standard and 1/2 size element is shown in Figure 3.15. It is quite apparent that the total trend of each curve does not change significantly. The only difference is the rupture occurred at lower strain. A comparison plot of the other four cases can also be found in Appendix C, in Figure C.3. In this figure, it shows an obvious exception in the 60° case.

To further test the mesh size effect, an additional refinement was applied in the FEA model. An element size of 1/3 of the standard element size was also tested. To avoid showing redundant figures, the stress-strain curve comparison results between the numerical model and the physical test are presented in Appendix C. The key point with this test is to compare the difference between

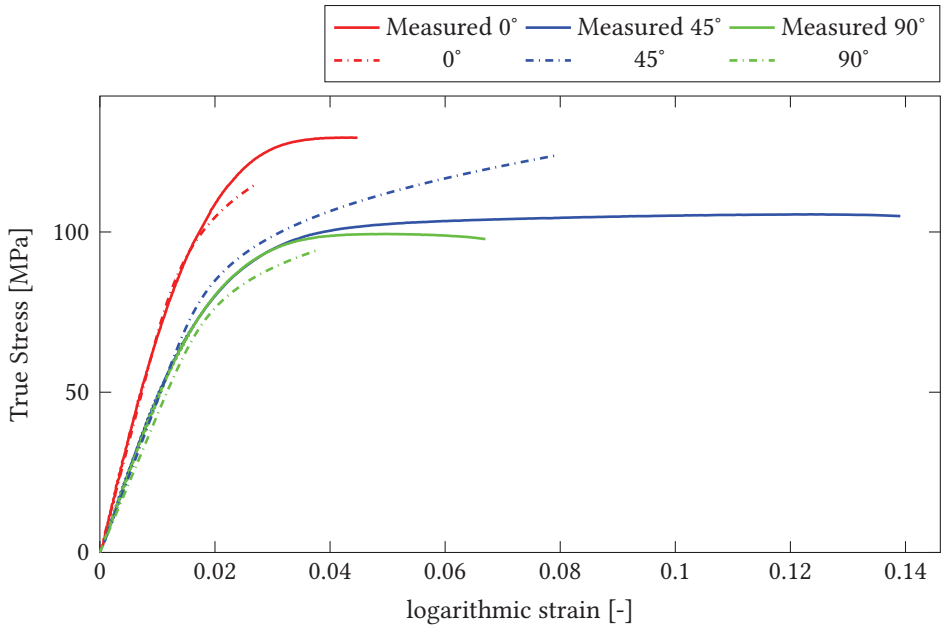

Figure 3.14: Numerical Test With 1/2 Meshing Size (adjusted material parameters) vs Physical Test in 0°, 45°, 90°. The reduced meshing size has limited influence the linear range prediction, but shortened curves in the non-linear range are observed.

the 1/2 size case and the 1/3 size case. The results have been plotted in Figure 3.16. As expected, the three major direction cases show a similar result as when the size changed from the standard to 1/2. A more refined mesh predicted that rupture happened at even smaller strain during the simulation, but the amount of difference was smaller when compared to the previous refinement. The other four direction cases have been plotted in Appendix C in Figure C.6. As in the previous refinement, all the other cases, except for the 60° case, show behaviour consistent with the three major direction cases. For the 60° case, the rupture occurred at the same strain as predicted by the 1/2 element size case. For some reason, the 60° case is less sensitive to the element size. This may be caused by the fact that as the fibre alignment changed from 45° to 60°, the initial rupture location on the specimen also changed from the other cases. Fortunately, the rupture strain was not larger than the previous mesh size, indicating that the mesh refinement is affecting the model in the expected way.

Because the strain change at the failure point is not too significant, and the change happened only at the very end of the plastic range, this exception on the 60° case can be ignored. Also, it is not expected that the lower arm will experience such a large strain during the stress analysis. The behaviour of most importance should be in the linear range in this research, as the intent is that the lower arm will not plastically deform under normal, or even severe use. Even though the plastic behaviour is not the focus of this study, it is still worthwhile to show the comparison between the physical and numerical case during plastic behaviour. This is another way to verify

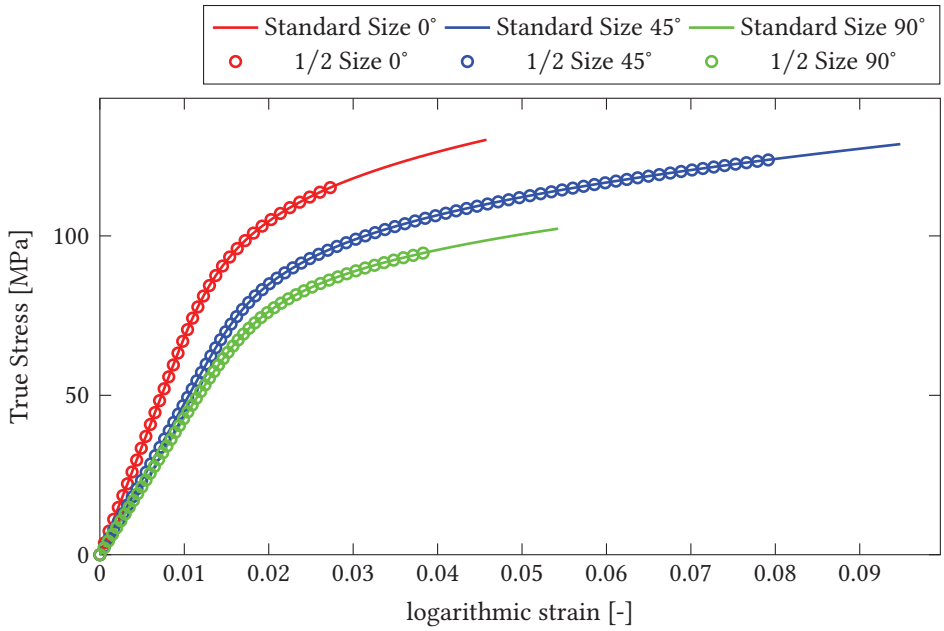

Figure 3.15: 1/2 Meshing Size vs Standard Meshing Size in 0°, 45°, 90°. Notice that the reduced mesh size has relatively little effect on the behaviour, other than the strain at rupture.

the accuracy of the numerical model prediction. In the reference paper, there are several strain contour plots to show the strain states at the very end of the tensile test just before the failure occurred. By checking these plots, an indication of the failure location can be predicted, and the region that has the largest strain can also be visualized. Similar contour plots can be obtained in the numerical simulation as well. One can compare the strain distribution in these contour plots with those obtained from the physical test. The strain contour plots from the numerical simulation are shown in Appendix C.2. The strain contour plots from the physical tensile test can be checked in Fig.13 of Holmström et al[45]. The contour plots have been shown for each of the seven different angle cases.

The presentation of the plots makes it somewhat challenging to compare them using the colours assigned for the various strain values. The plots from the physical test use a single colour legend to cover the range of strains of all seven cases at once, while instead, the numerical tests use a different legend for each case, depending on the individual strain ranges. Also, the total strain in the numerical test is much smaller when compared to the physical test, because the numerical test terminates as soon as any failure is detected. Nevertheless, a careful inspection of these plots reveals the pattern and trend of the strain distribution in each direction case. Even if the largest strain value is much smaller when compared to the physical case, the numerical simulation results show a similar strain distribution pattern relative, especially in the 15° to 75° cases. The special slanted shape of the strain concentration in the gauge section is shown as well, which is quite similar to the physical case. These strain concentration areas indicate that the chance of failure

happening in these locations was very high. The overall accuracy of the prediction on the plastic and failure behaviours is in the reasonable range. The numerical results show underestimation on the plastic strain values at failure in every case, which could be a positive outcome when considering a conservative design in the suspension lower arm or any similar component.

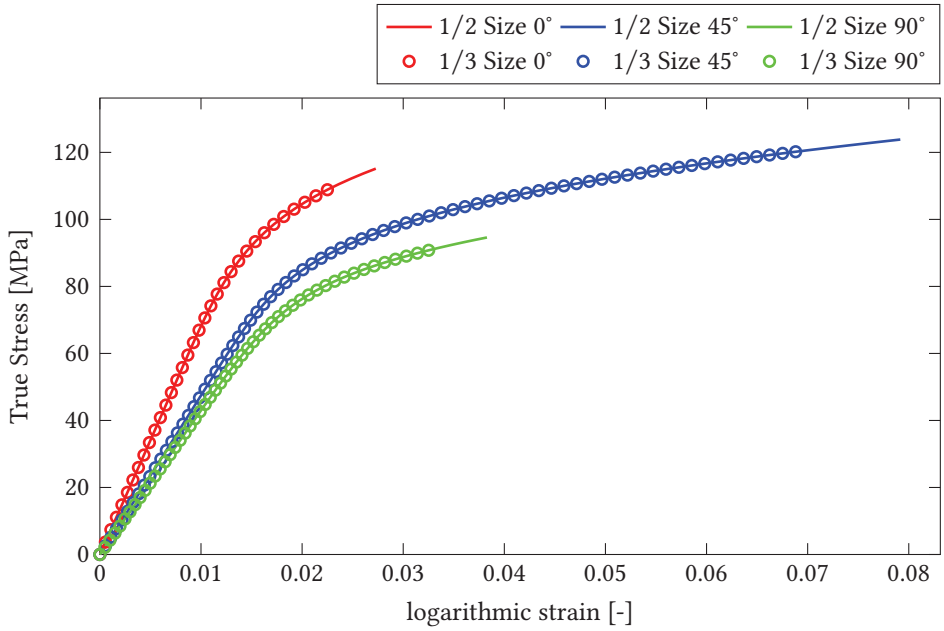

Figure 3.16: 1/3 Meshing Size vs 1/2 Meshing Size in 0°, 45°, 90°. Note that the trend from the first mesh refinement continues in the further refinement, but with a smaller effect.

3.5 Manufacturing Process Simulation on the Lower Arm

After the parameters of the manufacturing process simulation were confirmed, the injection moulding simulation on the lower arm component could be attempted using the settings and parameters from Section 3.3. In this section, the injection moulded lower arm will be discussed in two parts. The first part will discuss items that are related to model settings, processing parameters, and the final part situation. The second part will be the major discussion, which relates to the predicted fibre orientation distribution.

3.5.1 Injection Moulding Process

As mentioned earlier, the basic processing parameters were set to the default values. These values are recommended by the software according to the material properties. The polymer material 'Ultramid B3WG6 GIT BK807', which is manufactured by BASF Engineering Plastics company, was selected from the database. It is a PA6 thermoplastic polymer material with 30% glass fibre as reinforcement in the default setting. According to the confirmation process based on the reference material, there are a few material properties that needed to be changed in the settings. The

fibre orientation calculation model was set to RSC with an automatically calculated C_I value of $C_I = 0.0041$. The κ value was set to 0.05. The weight fraction of fibre was set to 29.04%, and the fibre aspect ratio was set to 29. The 'fibre aligned at skin/random at core' was chosen as the fibre inlet condition.

3.5.2 Fibre Orientation Result of the Lower Arm

Because the injection location can influence the final fibre distribution quite dramatically, the selections of the injection location will be very important. The resulting stress analysis will be influenced by these selections as well. Considering the motion and mechanism of the lower control arm in a McPherson strut suspension system, the direction of the major forces that act on the control arm are in the longitudinal and lateral direction. So in-plane strength was the first concern during the simulation. To achieve a better in-plane strength during the injection moulding process, side injection locations are preferred. Any injection locations that lie on the top surface of the lower arm were not considered in this study. Additionally, because it was unknown which in-plane direction force would be more critical during the stress analysis, four different injection locations were chosen during the injection moulding simulation. Three typical locations at each end of the lower arm body were chosen: the ball joint side, the front bushing side and the rear bushing side. One special location was chosen in the middle region of the arm where the flow will change direction rapidly after injection. Different injection locations form different flow directions based on the geometry of lower arm. The flow direction has a huge effect on the fibre alignment in any particular direction. In addition to this, the varying thickness of the arm influence the fibre alignment as well.

The fibre orientation distribution results can be checked as a contour plot in the Moldflow® software. The contour plots are shown using four different fibre orientation tensor components (a_{11}, a_{22}, a_{33} and a_{12}) as variables. According to the results, overall low a_{33} values show in all the cases. This indicates a very low degree of fibre alignment in any out-of-plane (xy plane) direction. The in-plane term a_{13} for xz plane and a_{23} for yz plane provide less valuable information in this case. Only the a_{12} off-diagonal values are of interest to check, because shows the additional information about the characteristics of the fibre alignment in the xy plane. The plots from the rear bushing injection location case are shown as examples in Figures 3.17, 3.18, 3.19, and 3.20. The Cartesian coordinate system used in these plots is shown in the lower right corner. The legend on the left side shows the colour changing from blue to red, indicating the value of the relevant tensor component a_{11}, a_{22} and a_{33}, which must have a range between 0 and 1. The bigger value indicates a higher degree of fibre alignment in the corresponding direction. The a_{11} corresponds to the direction along the x axis, the a_{22} corresponds to the direction along the y axis, and the a_{33} corresponds the direction along the z axis. For the a_{12} plot, the legend value changes to range from -0.5 to 0.5 corresponding the colour from blue to red. The a_{12} value indicates the degree of fibre alignment in the 45° and -45° directions in the xy plane. A more positive value shows a higher degree of alignment in the 45° direction and a more negative value shows a higher degree

of alignment in the -45° direction. A value close to 0 could indicate two different situations: 1. If either a_{11} or a_{22} have relatively large values, the small off-diagonal indicates a higher probability of fibre alignment along either the x or y axes, respectively; or 2. if a_{11} and a_{22} are both close to 0.5, the small off-diagonal indicates an in-plane random distribution. The small yellow triangle in the figure is pointing to the injection location. The plots from other three injection location cases are shown in Appendix C.3.

For all four injections locations, the values a_{33} are relatively small. This means the out-of-plane fibre alignment is really rare for all the cases. Some bigger a_{33} values can be noticed in the region where the flow front hits the thicker wall on the upper and left side of the arm. The influence of this could be ignored because of the relatively small a_{33} values compared to the a_{11} and a_{22} values, but some potential improvements could be realized by changing the cross section thickness to be uniform in the lower arm (this ignores the potentially negative effects on the bending stiffness in the longitudinal direction). According to the low a_{33} value, most of the fibres are aligned along the directions within the xy plane. This is the common situation in an injection moulded part, especially when the injection locations are chosen on the sides of a mostly planar party. Considering that the out-of-plane forces acting on the lower arm were lower than the in-plane forces during the vehicle motion, these low a_{33} values might be accepted and will not overly influence the lower arm strength. On the other hand, according to Eqn. 1.17, the low a_{33} value offers an easy judgment on the value of a_{11} and a_{22}. A small a_{11} value indicates a relatively large a_{22} value at the same location. Based on the observations of these contour plots in the four different injection cases, they can be grouped into three categories:

1. A consistently aligned configuration where the fibres generally follow the main shape of the lower arm.
2. A better alignment in the ball joint area and random distribution in the rest of the lower arm.
3. A random distribution configuration in most parts of the lower arm.

The first situation, a better fibre alignment, in which the fibres generally follow the shape of the arm, can be found in the rear bushing injection case and the ball joint injection case. These two cases have a similar feature that the fibre alignment away from the injection point is slightly better than near the flow start area. The overall fibre distribution is quite similar in these two cases. Most of the fibres are aligned along the main shape of the lower arm.

In the front bushing injection case, a better aligned fibre orientation, which is along the x axis, is showing near the ball joint. Near the front and rear bushings, an almost random distribution can be found.

In the middle region injection case, an overall in-plane random fibre distribution can be found in the majority of the lower arm body.

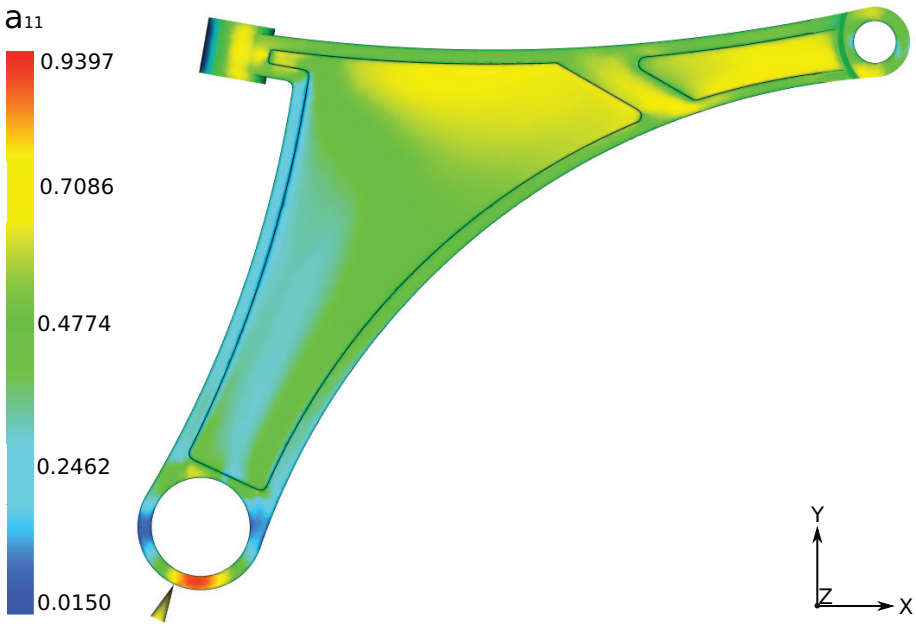

Figure 3.17: Fibre Orientation Result a_{11} with Injection Point Location at Rear Bushing Side. Note that the fibres become more aligned in the x direction near the ball joint.

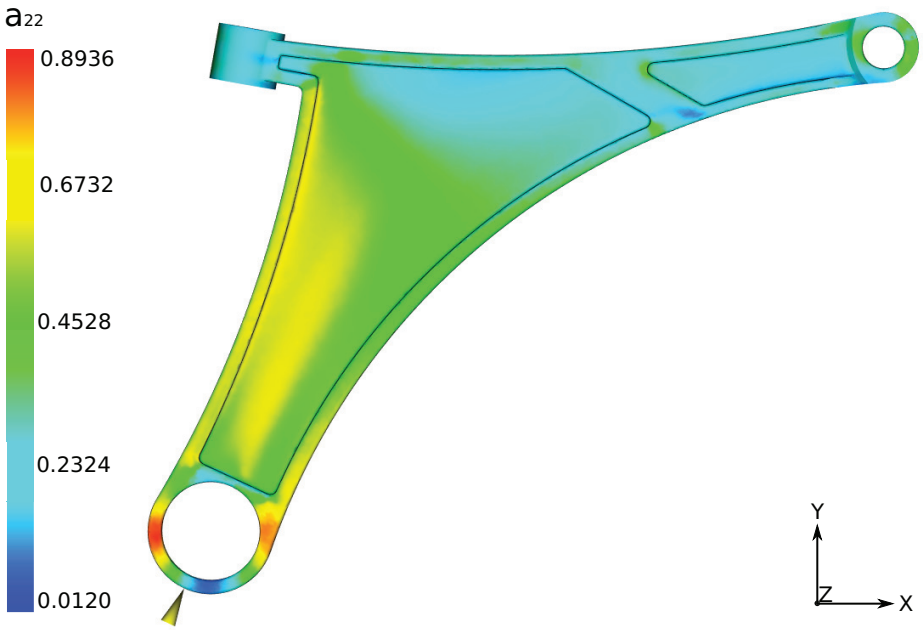

Figure 3.18: Fibre Orientation Result a_{22} with Injection Point Location at Rear Bushing Side. Note that the fibres become more aligned in the y direction near the inner edge of the arm.

Figure 3.19: Fibre Orientation Result a_{33} with Injection Point Location at Rear Bushing Side. Note that the small a_{33} value throughout the part indicates a nearly planar fibres orientation.

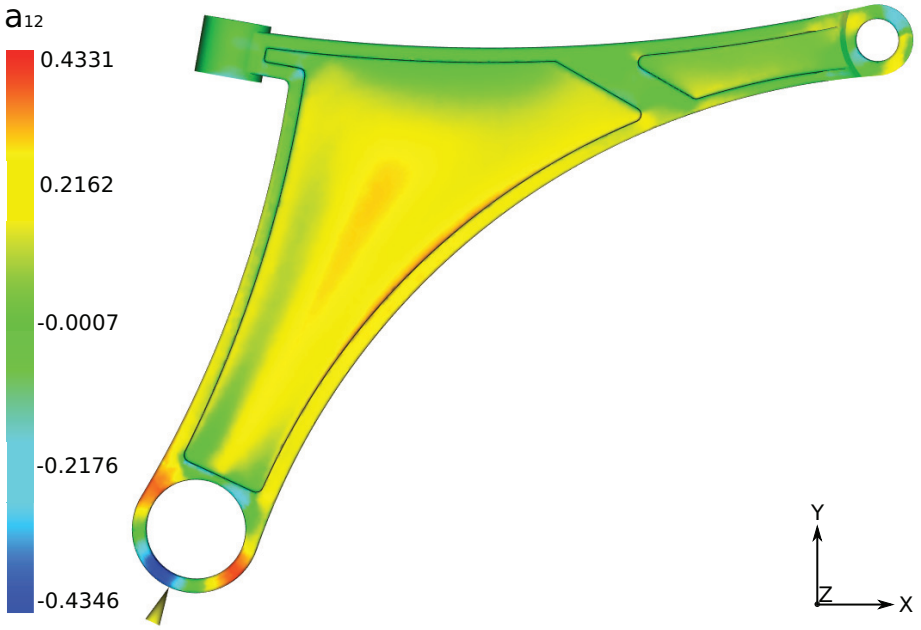

Figure 3.20: Fibre Orientation Result a_{12} Injection Point Locate at Rear Bushing Side. Note that the small off-diagonal value near the ball joint shows a nearly unidirectional fibre orientation in the x direction, but the larger value on the outer edge indicates a uniform flow closer to 45°.

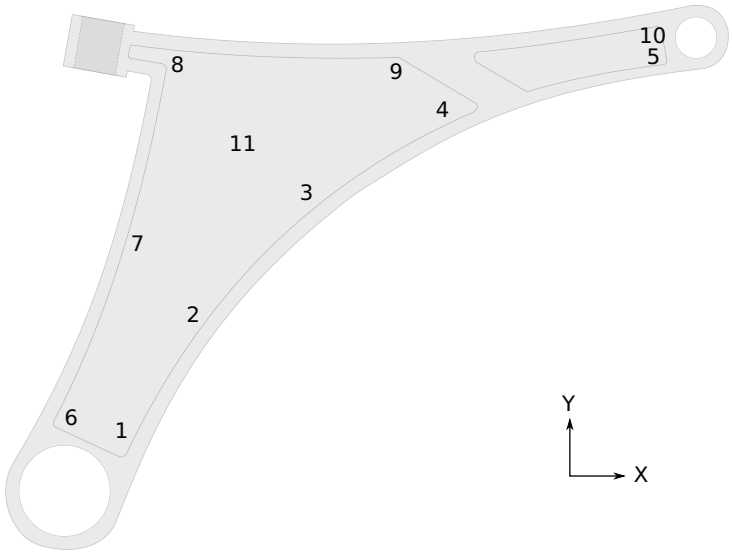

Figure 3.21: Approximate Locations for Through-Thickness Probe xy Plot Generation. Eleven locations were chosen to obtain a more complete picture of how the fibre orientation changes through the thickness of the arm.

As mentioned in the stress-strain confirmation process, sometimes a through-thickness fibre orientation change can be noticeable, even in a really thin plate. It is worthwhile to check the fibre orientation change through the thickness in the lower arm. A distribution contour plot is not good choice to the show the through thickness results, because it does not present the situation in more than one plane inside the lower arm. One is able to request a probe xy plot in the Moldflow® software by picking different locations on the top surface of the lower arm. In this way, the change in the different tensor component values through the thickness can be investigated. Eleven different locations were chosen in this process, to cover the majority of the lower arm body. The approximate positions of these locations have been labelled in Figure 3.21. At all of these positions, the probe xy plots were generated for all four of the injection location cases. In these plots, the x axis value is the through thickness distance and y axis shows the relevant fibre orientation tensor component value.

As an example, the probe xy plot from the rear bushing injection case is shown in Figure 3.22 to figure 3.29. Based on these plots, the details of the fibre orientation distribution through the thickness of the lower arm can be illustrated clearly. First, the results from these plots agree with the conclusions that have been found in the previous contour plots. The a_{33} values for all locations are quite small compared to a_{11} and a_{22}, and the a_{33} through-thickness value change can be neglected in this case. At the same time, the a_{11} and a_{22} plot are mirrors of each other due to the low a_{33} value.

The trend of the fibre alignment, which is following the shape of lower arm, can also be seen

from these plots. For example, the plots from locations 1-5 show increasing a_{11} values and decreasing a_{22} values as the location changes from 1 to 5. This means that the alignment direction changes from y to x due to the flow direction change caused by the curved shape of the arm. A similar situation can be found in the plots of points 6-11; locations 6 and 7 have a relatively high a_{22} value and locations 9 and 10 have a relative high a_{11} value.

Locations 8 and 11 are special among these locations. They are the points where the flow starts to diverge into different directions due to the shape of the arm. At location 8, a relatively large through-thickness value change is shown in both the a_{11} and a_{22} plots. This is caused by the flow front hitting the upper wall of the arm, which leads to a significant fibre alignment change in the core region of the arm. For location 11, the flow direction is even more complex in this region. Both the a_{11} and a_{22} values are close to 0.5 here. By checking the a_{12} value at location 11, a higher positive value around 0.3 has been found at the top and bottom layer of the arm and lower positive values are shown in the centre region of the arm. This indicate a slightly higher chance of fibre alignment along the +45° in the top and bottom layer of the arm and more random distribution in the centre region of the arm.

Based on all the plots, the thickness effect is stronger at the locations where the flow direction changes due to changes in the shape. For example, in the those plots for locations 1-5, the locations 1, 2, and 3 show a stronger through-thickness effect than locations 4 and 5. Similar results are also found among the locations 6-11. Locations 7, 9, and 10 have mild thickness effect compared to 6, 8, and 11. Overall, in most of the locations, the through-thickness tensor component value changes are relatively small compared to the thin plate case. This could be caused by the smaller top and bottom wall influence on the flow due to the thicker cross section. However, in some particular locations where the flow direction changes, it does show a certain influence from the change in thickness. There may be some effect on the strength of the composite lower arm if any stress concentrations happen to occur in these particular locations.

Overall, it appears that results from the injection moulding process simulation on the lower control arm are reasonable and in the expected range. The fibre orientation definitely changes throughout the part in a complex fashion due to the part geometry, but the effect of injection location on the FOD can be observed. The plan of this numerical performance prediction is to keep the composite lower arm geometry the same as the sample aluminum lower arm. In this way, because the geometry of the arm is fixed, the only factor that may lead a different performance is the injection location. At this point, it is difficult to judge which injection location is better, because the loading direction will vary according to the motion of vehicle. This is the reason that FEA simulation is needed for all the injection cases, in order to test and check the influence from different injection locations on the strength of the arm. More details on this will be discussed in Chapter 4.

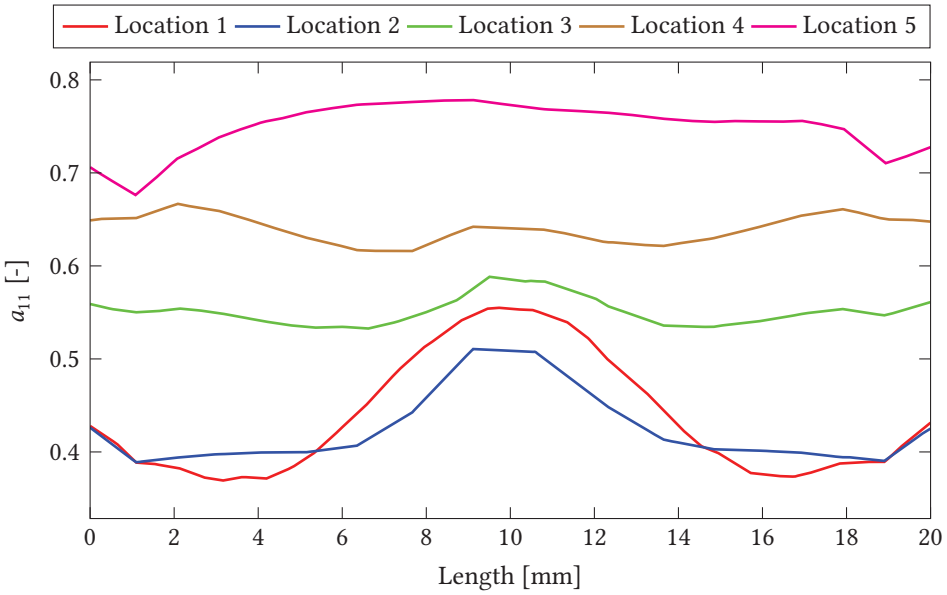

Figure 3.22: Tensor Component a_{11} Through Thickness at Location 1-5. Notice that the trend is in increasing values as the flow moves along the curve of the arm.

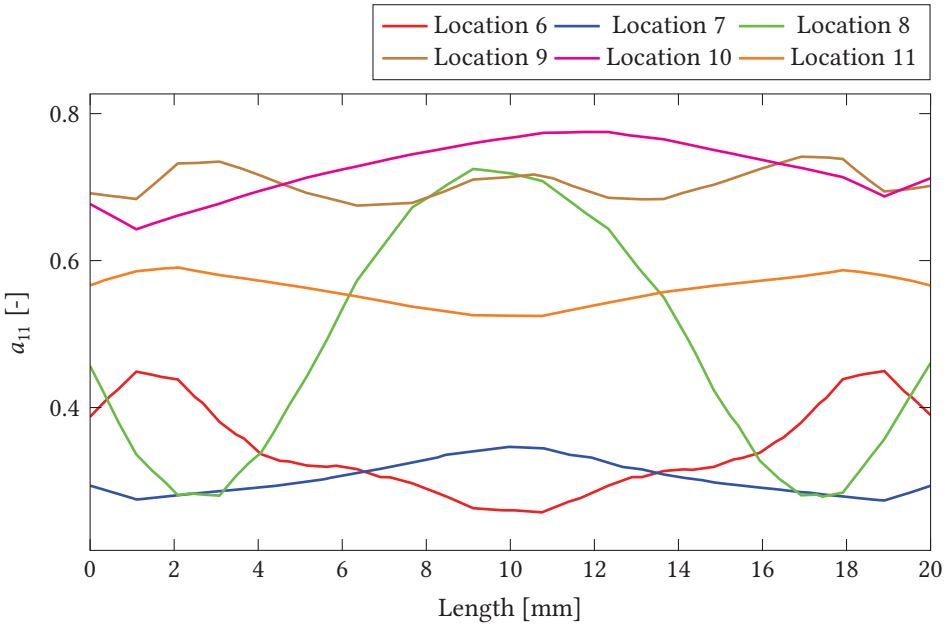

Figure 3.23: Tensor Component a_{11} Through Thickness at Location 6-11

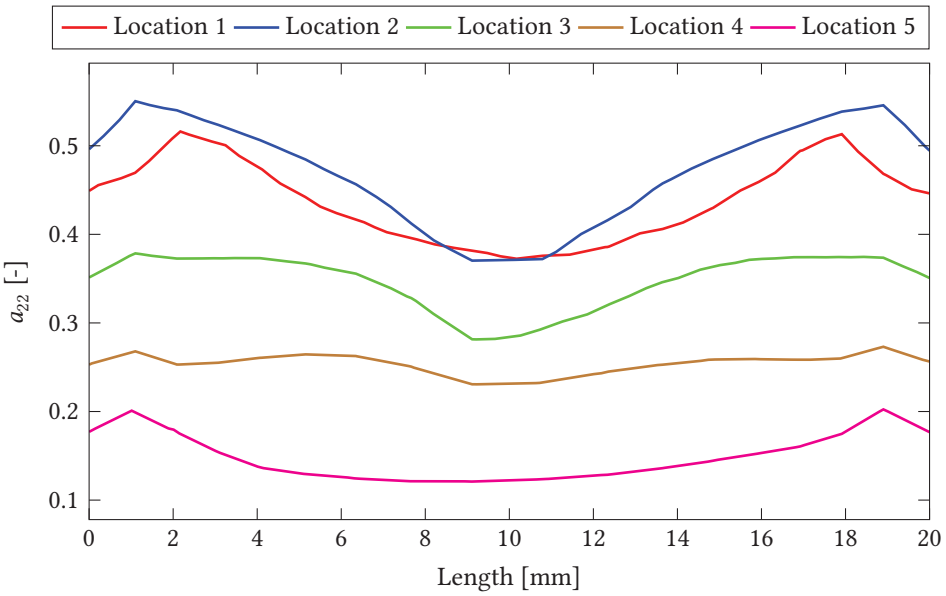

Figure 3.24: Tensor Component a_{22} Through Thickness at Location 1-5

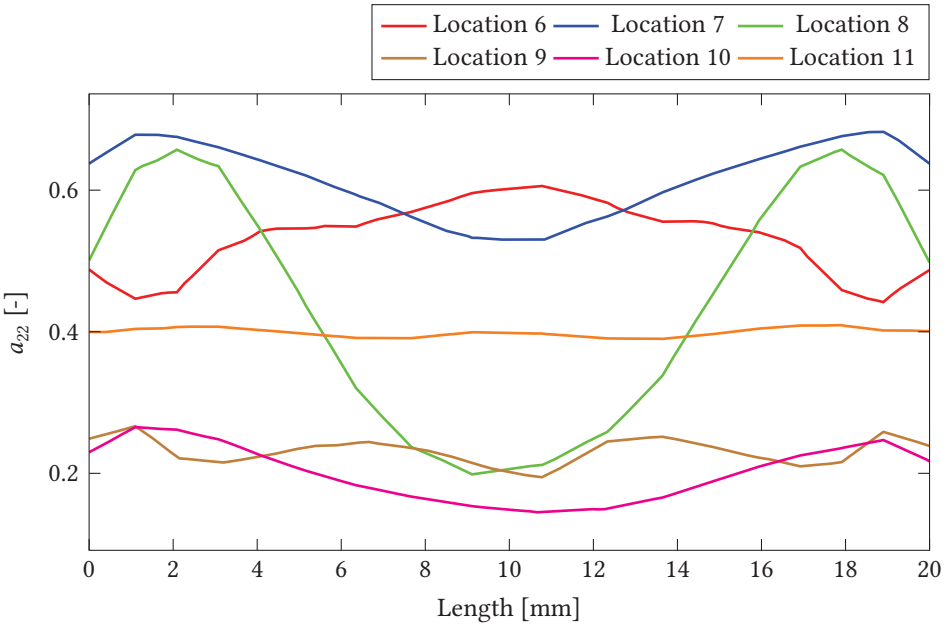

Figure 3.25: Tensor Component a_{22} Through Thickness at Location 6-11

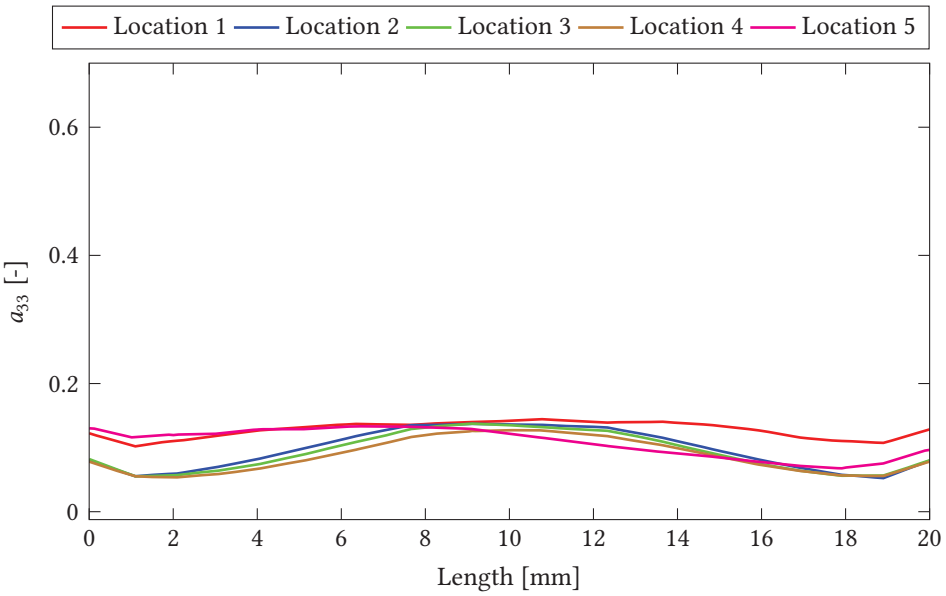

Figure 3.26: Tensor Component a_{33} Through Thickness at Location 1-5

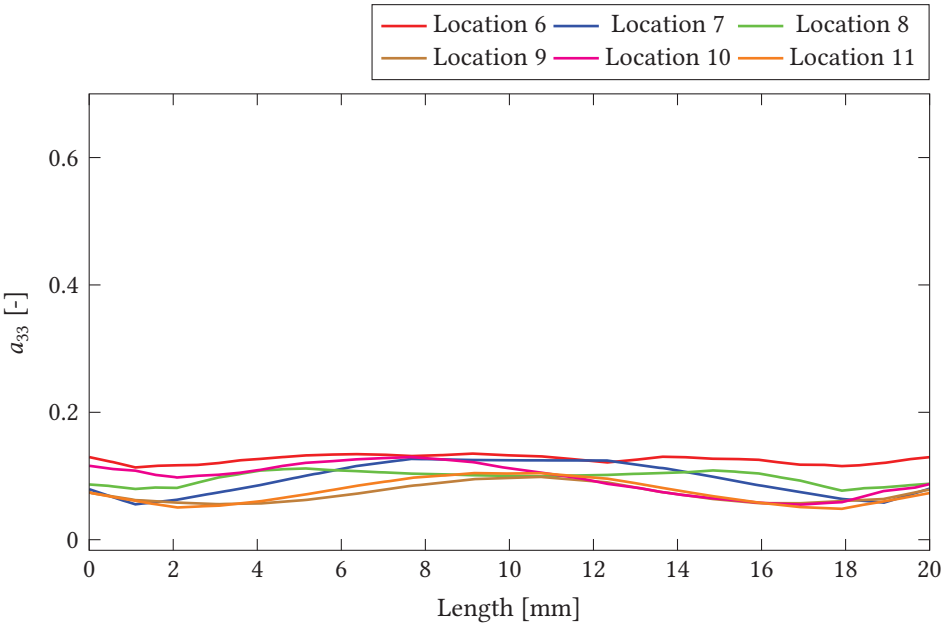

Figure 3.27: Tensor Component a_{33} Through Thickness at Location 6-11

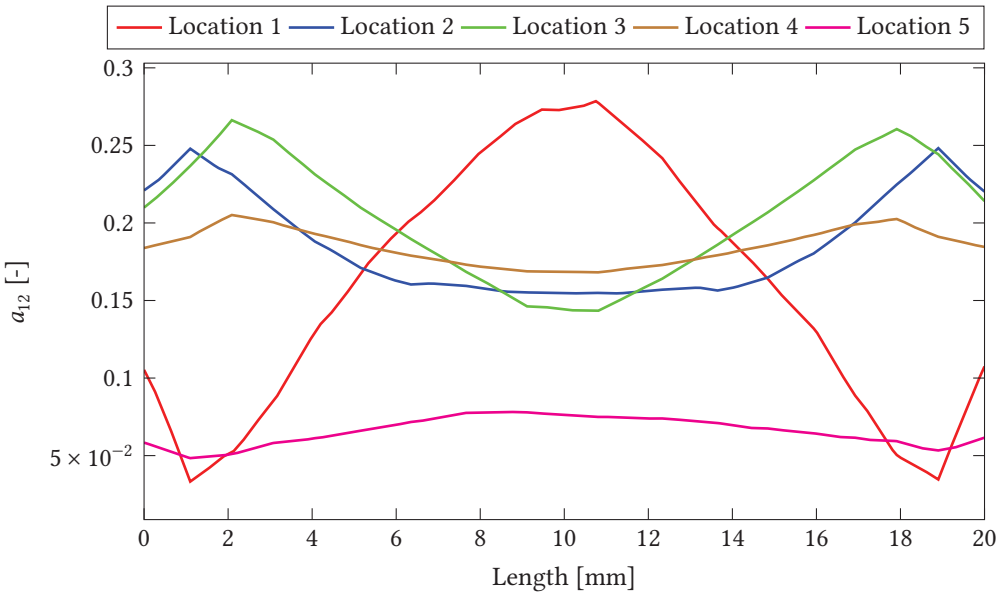

Figure 3.28: Tensor Component a_{12} Through Thickness at Location 1-5

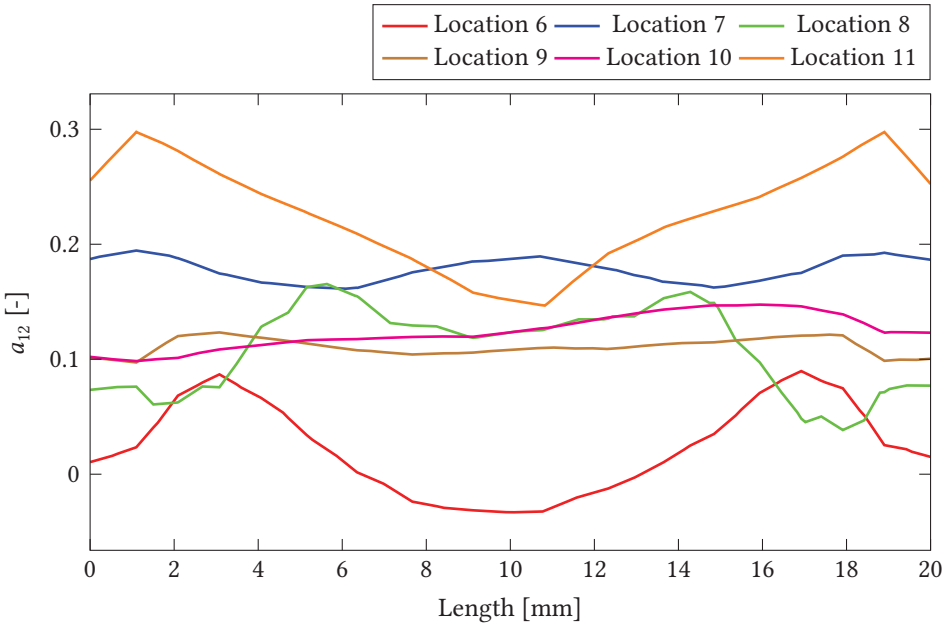

Figure 3.29: Tensor Component a_{12} Through Thickness at Location 6-11

Chapter 4

Finite Element Analysis

4.1 Lower Arm Finite Element Analysis Modelling

4.1.1 FEA modelling using Abaqus®

When using the FEM to do stress analysis in solid mechanics, specialty computer software is usually used to solve the equilibrium equations. There are several different kinds of FEA software that can be used, both in academia and in industry. The method used to define a FEA model can be different in these software tools, but most of them are quite similar because they are all based on same theory. In this research, Abaqus® will be chosen as the FEA software to finish the lower arm modelling. To build a FEA model using Abaqus®, the following items must be specified:

- The geometry of the part. This is the first step and the basis of a FEA model in which the part of interest will be described using a set of coordinates that are defined by the software. In Abaqus®, the user can draw the part from scratch, or import the part from many other CAD software packages.
- The behaviour of the material. There are many different classifications to define the material properties in Abaqus®. For a basic static analysis using a linear material model, the elasticity is the only property needed. In this case, the properties are defined by Young's modulus and Poisson's ratio. For a more complex case or different analysis type, the density, plasticity, damage definition, thermal properties, or user-defined material properties can also be assigned to the material behaviour. Choosing suitable material behaviour is key to obtaining a correct solution.
- The assembly setup is the means by which the user describes the relative position of parts that have been defined in the first step. It is an important step, where the user will place the part in a suitable location and define the proper connector behaviour. In this way, aspects of the problem such as interactions, loading, and boundary conditions can be easily defined.
- The interaction definition. If two or more parts are connected to each other during the simulation, the interaction properties are the key to ensure the proper connection behaviour.

In some cases, two or more parts will be attached and moving together. In this case, a proper constraint between the two surfaces must be defined, which is also implemented through the definition of an interaction. Another useful example of using interaction definition is when a single node and surface need to be constrained together (also called coupling motion). This type of constraint was implemented in the lower arm modelling, which will be discussed later in more detail.

- The loading and boundary conditions. This is one of the most important (but often overlooked) portions of a FEA model. Properly defined loading and boundary conditions are necessary to make the model properly generate a realistic solution. At same time, it can influence the convergence properties and solution time of analysis.
- The type of analysis, indicated by defining a step in the modelling process. There are two types of steps in Abaqus®: 1. The initial step is created automatically by the software. It indicates the very beginning of the analysis sequence. In this initial step, the prescribed boundary conditions and interactions should be defined. 2. The analysis steps are followed after the initial step, which are associated with an analysis type (e.g. static, dynamic, linear perturbation, buckling, etc.). Multiple analysis steps can be assigned in the model. The predefined initial conditions in the initial step will be propagated through every analysis step. Another important feature in the analysis step is to confirm if large displacement and nonlinear geometry should be anticipated in the model, due to the nonlinear definition either in material or boundary conditions. If this is the case, the 'Nlgeom' option must be indicated in the step setting, in order to properly account for the nonlinear behaviours during the simulation. In the step configuration, the user also needs to define the parameters for controlling the analysis progression, i.e., the total time period of the simulation, the initial time increment size, the minimum time increment size, and the maximum number of increments allowed during the simulation. These parameters will influence the speed of the solution computations, especially in a nonlinear analysis.
- The last and arguably the most important item: the mesh definition of the model. This mesh is the foundation that supports the FEM. Selecting the proper element shape and type along with a good mesh quality, will result in more accurate results during simulation. Usually, the user can define the mesh automatically by using a robust algorithm offered by Abaqus®, even when the part geometry of interest is relatively complicated. However, careful checking is important, as edits might be needed when these automatic elements have been generated. A mesh optimization process and mesh size sensitivity study is commonly required to ensure a reliable solution is achieved.

The steps listed above are the general procedure used to complete a FEA model. There are more complex steps associated with the case of the composite suspension lower control arm tested in this research; a more specific process will be discussed later.

4.1.2 Element Choice and Meshing

As mentioned before, the most important step during FEA modelling is to generate the mesh. Of course, the basic idea of FEM is to divide the targeted body into small pieces, solve each individual piece, and then combine the solutions together to get the final solution for the whole body. So, as one might anticipate, a smaller or finer meshing size will generally make the model more closely approximate the real case, and offer more accurate results in general. Based on this principle, the solution of a FEA simulation will be highly mesh dependent. However, a finer mesh can dramatically increase the computation time, often by an order of magnitude or more. The ultimate objective of FEA is to obtain reasonably accurate results with an acceptable computational cost. Clearly, the mesh generation, the element type and shape selection, and the way in which the FEA software will react to different element types needs to be clearly understood. The solution process will differ, based on the element shape, the choice of interpolation method, and the number of integration points. In the following, a brief summary related to these three topics, detailed in the Abaqus® online help documents[53] will be provided.

Element Shape

Abaqus® offers a powerful element library for solving different types of problems. One can characterize the element behaviour by different geometry types, which are shown in Figure 4.1. The black points indicate the possible node locations in that type of element. From this list of elements, the solid and shell element are commonly used for parts with of 3D geometry, where the result in the interior of the part is more complex. The membrane, beam, and truss elements are commonly used in simple structure analysis where the cross-section effect can be ignored. The rigid and connector elements are generally treated as a functional element that will be useful when modelling special behaviour, such as contact or other interaction. The infinity element is commonly used in boundary value problems in which the region of interest is relatively small compared to the surrounding object. Also, among these element types, the solid and shell element will be shape dependent during the solving process. For example, in the composite lower arm model in this research, the simple shell structure modelling wouldn't be capable of including the fibre orientation effect in the three-dimensional space, so the solid element will be the main choice for this research. In addition, in order to properly define the constraints, loads, and boundary conditions, connector and rigid elements could be used as well.

There are three different general shapes in the Abaqus® 3D solid element library, as shown in Figure 4.2. The node and face ordering is labelled with number. The difference between the left side and right side elements is the interpolation function. The left side elements use a first order (linear) interpolation method and the right side elements use the second-order (quadratic) interpolation method. Choosing a different interpolation function will influence what the final deformed shape of the element could be during the simulation. More detail will be introduced in the next part.

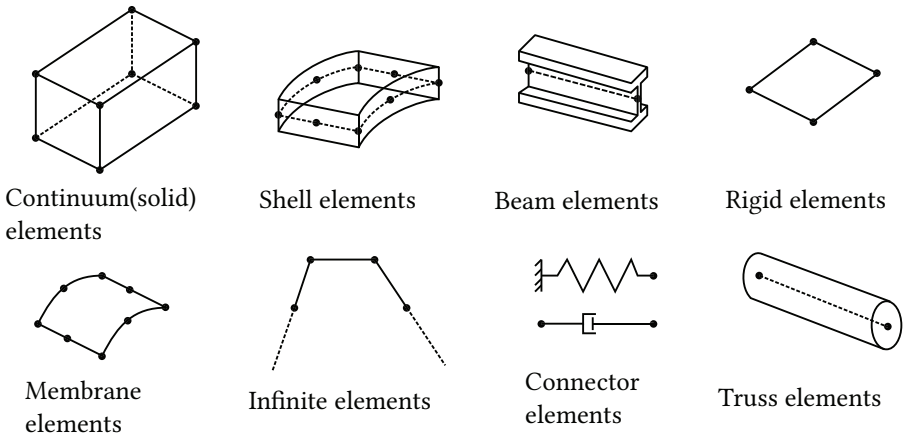

Figure 4.1: Commonly used element type (Reproduced from [53])

Brick elements are also referred as isoparametric elements. They are the preferred element type for many cases. Compared to other types of element, they offer less computational cost with equivalent accuracy if the initial element shape is not severely distorted. The brick element also has a better mesh convergence rate than other element types. But in some cases, it is hard to mesh the geometry with this type of element without causing a poor initial shape, if the geometry is complicated. Abaqus® also offers tetrahedral elements and wedge elements to use in this circumstance. Tetrahedral elements and wedge elements are well-suited for complex geometry and are commonly used in many automatic meshing algorithms. In Abaqus®, it is very convenient to mesh a complex shape with tetrahedral elements. The tetrahedral elements are less sensitive to initial element shape, whereas the brick element will perform better if initial element shape is approximately rectangular. However, first-order tetrahedral elements and wedge elements are usually overly stiff. When using this type of element, extremely fine meshes are required to obtain accurate results, and a mesh sensitivity study should be performed to check the accuracy of results. In most of the cases, the use should attempt to use well-shaped brick elements in regions of interest if possible. In cases where the tetrahedral element must be used to finish the mesh, Abaqus® suggests using second order tetrahedral elements. Due to the complex shape of the lower control arm, it is difficult to mesh the geometry well using brick elements, so automatic meshing with tetrahedral elements was the choice in this research. A mesh sensitivity study will be conducted to keep the results accurate.

Interpolation Functions

The interpolation function is used for calculating the displacement field $\boldsymbol{u}$ at an arbitrary location inside an element from the defined nodal displacement values. For example, consider a 2D

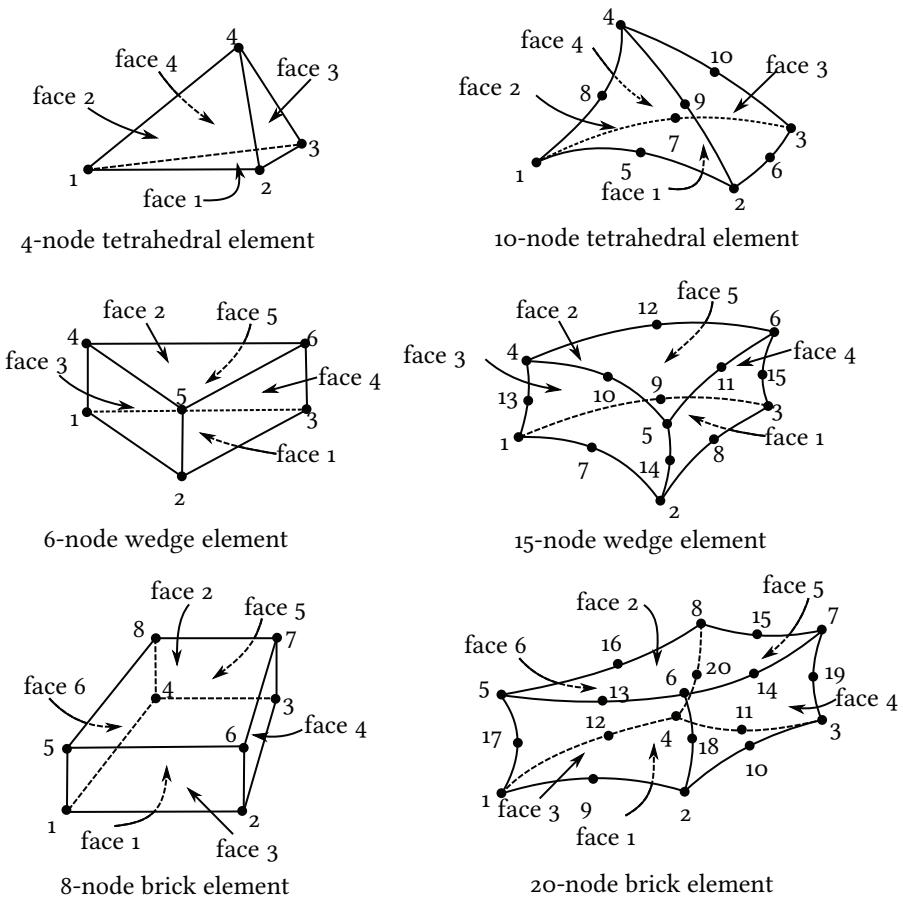

Figure 4.2: Commonly used 3D continuum(solid) element: nodes and faces ordering (Reproduced from [53])

rectangular 4-node element, as shown in Figure 4.3. Assume $({u_x}^{(a)},{u_y}^{(a)})$, $({u_x}^{(b)},{u_y}^{(b)})$, $({u_x}^{(c)},{u_y}^{(c)})$ and $({u_x}^{(d)},{u_y}^{(d)})$ are the displacement values at nodes a, b, c, d, respectively. The displacement at an arbitrary point within the element can be interpolated using the nodal displacement value by:

$$u_x = (1-\xi)(1-\eta){u_x}^{(a)} + \xi(1-\eta){u_x}^{(b)} + \xi\eta{u_x}^{(c)} + (1-\xi)\eta{u_x}^{(d)} \tag{4.1}$$

$$u_y = (1-\xi)(1-\eta){u_y}^{(a)} + \xi(1-\eta){u_y}^{(b)} + \xi\eta{u_y}^{(c)} + (1-\xi)\eta{u_y}^{(d)} \tag{4.2}$$

Where ξ is expressed as:

$$\xi = X/W, \quad \eta = Y/H$$

where X will be the x coordinate of an arbitrary point inside the element, W will be the initial element width, Y will be the y coordinate of an arbitrary point inside the element and H will be

the initial element height.

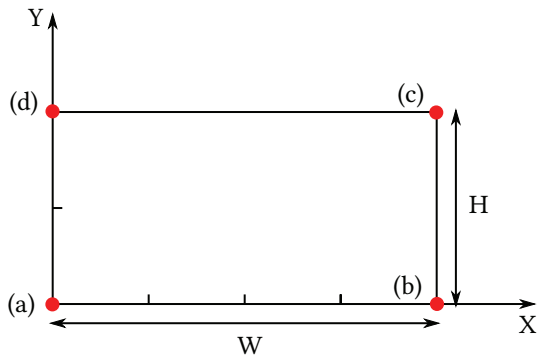

Figure 4.3: Linear 4-node rectangular element interpolation: initial state (Reproduced from [53])

For example, suppose: ${u_x}^{(a)} = 0.5, {u_y}^{(a)} = -0.5, {u_x}^{(b)} = 0.5, {u_y}^{(b)} = 0.5, {u_x}^{(c)} = -0.5, {u_y}^{(c)} = -0.5, {u_x}^{(d)} = -0.5, {u_y}^{(d)} = 0.5$. By using the above equations, the arbitrary point location inside the element and the final element shape is shown in Figure 4.4.

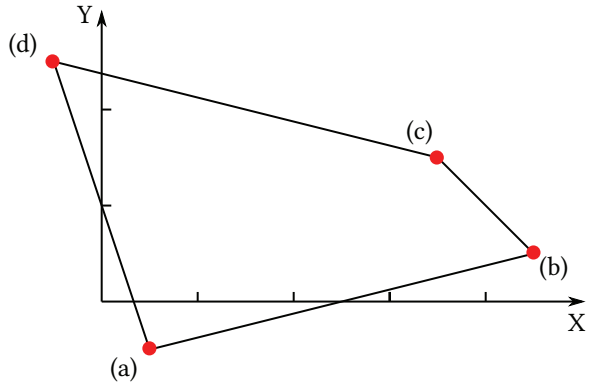

Figure 4.4: Linear 4-node rectangular element interpolation: final state (Reproduced from [53])

Because the linear interpolation function has been used for this calculation, the displacements

evidently vary linearly with position within the element. If the second-order (quadratic) interpolation function is chosen to represent the displacement, the curved element border will be present, as shown on the right side of Figure 4.2. Second-order elements provide higher accuracy than first-order elements for the problems that do not involve huge element distortions. They capture stress concentrations more effectively and are better for modelling geometric features, such as fillets or curved surface boundaries in the geometry, but they will increase the computational cost. In this research, due to the relatively large and complex geometry of lower arm, the model required a large number of elements. The first order tetrahedral elements were the attmped, but both first order and second order tetrahedral elements were in the mesh sensitivity study, in order to see influence on the final result.

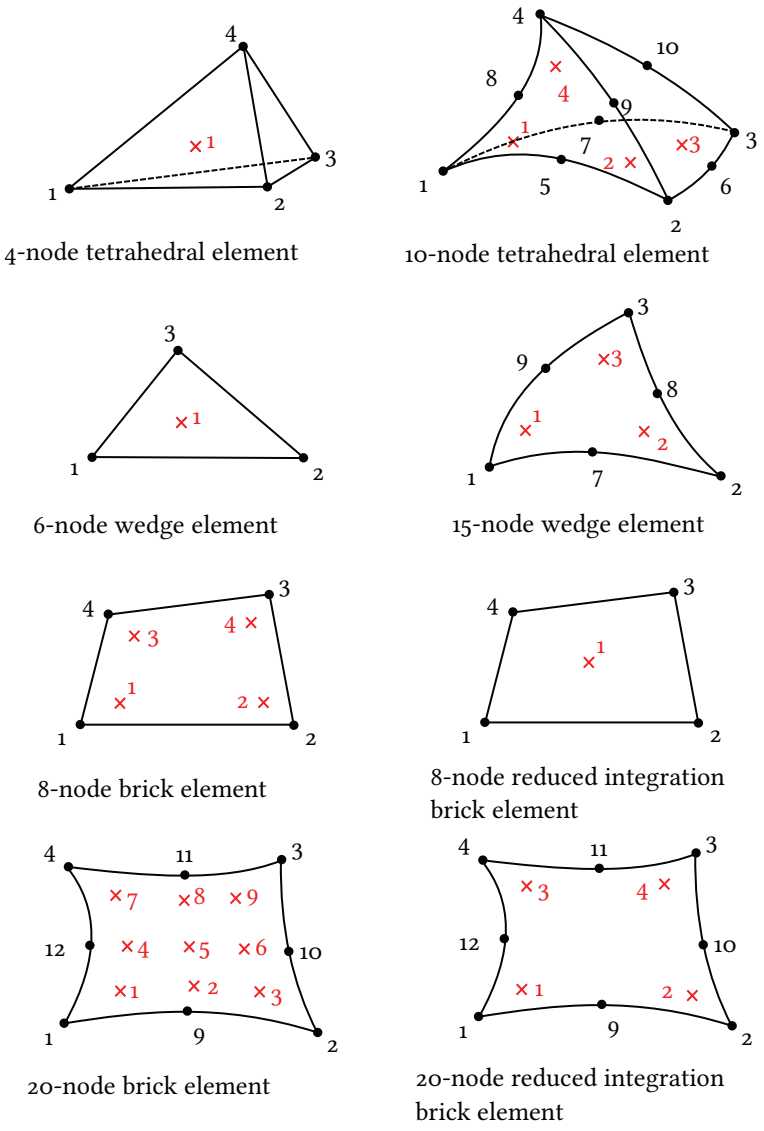

Figure 4.5: Commonly used 3D continuum (solid) element: integration points (Reproduced from [53])

Integration Schemes

One objective of a FEA is solving the stress distribution within a solid. This is done by following steps. First, the displacements at each node are computed according to the external force and stiffness matrix. Second, the element interpolation functions are used to define the displacement at arbitrary points within the element. Then, the displacement field can be differentiated to determine the strains. Once the strains are known, the stress—strain relations for the element are used to compute the stresses.

In principle, this process could be used to determine the stress at any point within an element. However, it has been proven that some points are more representative of the element stress than others[53]. The specific points within an element where stresses are computed are known as *integration points*. The FEA software treats these stresses as samples to evaluate certain volume and area integrals. The detailed locations of the integration points within different 3D elements have are in Figure 4.5. The '×' sign, followed by a number in the figure indicates the location and ordering of the integration points within an element.

There are reduced integration schemes applied on 8-node and 20-node brick elements. The major difference between the full and reduced integration scheme is the accuracy. The reduced integration scheme decreases the simulation time, especially in three dimensions problems, but may lead to inaccurate results. Using first-order reduced integration brick elements causes a problem called *hourglass* behaviour. Since the elements have only one integration point, it is possible for them to distort in such a way that the strains calculated at the integration point are all zero, which leads to the element to deform in an 'hourglass' shape, and causes the total energy to be unbalanced. When using first order reduced integration brick elements, hourglass control should be turned on and finer meshing should be involved. However, using full integration schemes also causes a problem called *volume locking*, which happens when the material is nearly incompressible. In this case, artificial pressure stresses are introduced at the integration points, which cause the element to become artificially stiffer when the deformation should cause no volume change. This is more noticeable when second-order, fully integrated brick elements are used. To compensate for this shortage, in Abaqus®, the first-order, fully integrated brick elements use a selectively reduced integration scheme[53] that prevents *volume locking* when the material is nearly incompressible. In addition, Abaqus® also offera hybrid elements that are intended for use with incompressible and almost incompressible materials.

In this research, the lower arm mesh used tetrahedral elements without a reduced integration scheme for both the first-order and second-order element type. However, for the solid rubber bushing model in Section 4.2, the first-order, fully integrated, hybrid brick element will be used, because of the behabviour of the rubber material in the bushing joint.

4.1.3 Modelling Considerations of the Composite Lower Arm

The reasoning behind the construction of the composite lower arm FEA model is to follow the steps in Section 4.1.1. First, the geometry of the main part (lower control arm) needed to be modelled. The lower control arm geometry should be the same that used in the Moldflow® simulation model. In this way, the shape of the lower arm was consistent in the different simulation software tools, and the mapping process was better able to capture the correct fibre orientation information. The CAD drawing of the lower control arm from Solidworks® was imported into the FEA model. After that, the question was to determine if there was any other parts involved in the model. This step was also related to the question about how to define the boundary condition and load in the FEA model. Consider the loading situation of a lower control arm attached to a MacPherson suspension system, there are four connecting locations that should be defined in the FEA model. To properly define the behaviour of these connecting locations, two strategies could be used: 1. An individual part could be modelled that is attached to the main lower arm part. These attached parts will become a medium to transmit the load between themselves and the lower arm, so a proper contact definition must be defined between these parts and the lower arm. In most cases, this won't be the best choice, because the stress results in these attached parts are less important and this contact will usually make the model more complicated. 2. Another better way to deal with these connecting locations is to define either some kind of boundary condition or load to properly constrain the model. These four connecting locations in the lower arm model will be located at the front bushing and rear bushing joints, the anti-roll bar connecting point, and the ball joint connecting location. Each of them will be discussed in the following content.

As mentioned in Chapter 2, the forces from the lower arm ball joint were used as the main source to test the strength of the composite lower arm, so a load was defined on the ball joint location in the model. To simplify the model, the actual ball joint and the related connecting knuckle weren't modelled. To approximately represent a ball joint connection, the forces transmited from the ball joint were assumed to be uniformly distributed over the inner surface of the connecting hole of the lower arm. A coupling motion constraint was defined at the centre point of the hole of the ball joint connecting location. The motion of this point was coupled with the inner surface of the hole. Then, the force combinations obtained from the multibody dynamics simulations were applied at this point. In this way, the force was properly transferred to the lower arm through the coupling motion constraint between the point and the inner hole surface.

In the multibody dynamic simulation, the anti-roll bar is connected to the lower arm through a drop link. At the upper end of the drop link, there is a compliant ball joint that connects to the anti-roll bar. At the lower end, there is a compliant universal joint connected to the lower arm through a bracket. As the vehicle moves, the lower arm is treated as a linkage between the chassis and wheel. Different motions of the vehicle place the lower arm under different loading conditions, caused by the anti-roll bar stiffness. The load in the anti-roll bar is transferred to the lower arm through the bracket which is attached to the lower arm top surface. To simplify the

model, the actual anti-roll bar wasn't modelled. Instead, the forces and moments transferred from the anti-roll bar were extracted from the multibody dynamics simulation. Similarly, these forces and moments acted on the centre point of the hole located on the bracket, and the motion of this point was coupled with the inner surface of the hole. In this way, the actual solid bracket needed to be modelled in Abaqus® and attached to the lower arm with a proper interaction definition. For the conventional metal lower arm, the bracket would usually be fastened onto the lower arm using bolts or rivets. Considering the composite lower arm, if the bracket was still made from metal, this might not be the ideal solution for the connection between the lower arm and the bracket. Because the connecting bolts and bracket are much stiffer than the composite material, the composite lower arm will be weakened at these bolt connecting locations. In practice, some sort of adhesive might be applied to deal with the connection in order to keep the strength in the connection area, or another solution could be to injection mould the bracket and lower arm as one body during the manufacturing process. This point could considerably broaden the research topic if more consider means of connecting the bracket are explored, so it was not considered in this research. A simplification was made by using a tie constraint between the bracket and the lower arm. This tie constraint forced the bottom surface of the bracket and the contact surface on the top of the lower arm to move and deform together. This definition could cause some stress concentrations between the lower arm and the bracket around the interaction surface due to the stiffer steel material used when modelling the solid bracket part. The geometry of the solid bracket was created in Abaqus® using the part generation tool. As shown in Figure 4.6, the geometry was designed according to the universal joint setting in the multibody dynamics simulation and the geometry of the lower arm body. In this way, the extracted forces and moments from the multibody dynamics simulation can be applied in the correct directions.

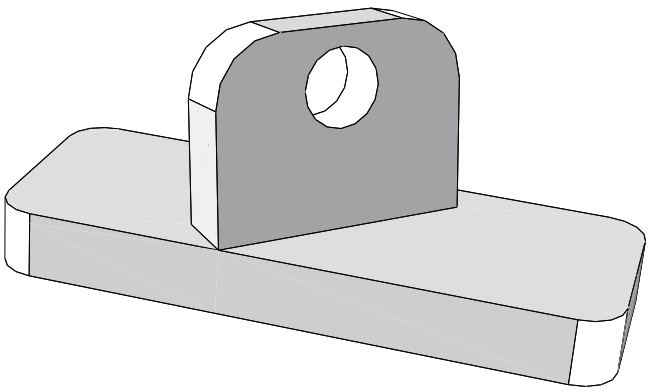

Figure 4.6: Bracket geometry in FEA

For the bushing connecting locations, a rubber sleeve that filled the gap between the inner surface of the hole and a centre shaft was modelled. For a better modelling strategy on this type

of connection, a tentative setup was tested. The solid rubber was modelled using a hyperelastic material definition. In this case, the solid centre shaft was modelled as made of steel. Tie constraints between the lower arm, the rubber, and the centre shaft were defined as well. The centre shafts of both bushings were constrained in all six degrees of freedom in the boundary condition setting. Due to this modelling setup, the analysis step needed to consider the non-linear geometry effect in order to capture the proper rubber material behaviour. This change increased the difficulty in reaching convergence for the simulation when large deformation happened in the rubber material, and dramatic element failure occurred in the composite lower arm. Also, this change made the lower arm finite element model more complicated due to the tie constraint definition and increased the computational cost.

Considering that the rubber bushing modelling is not the main focus in this research, a simplified modelling strategy for the bushing connection was implemented. In Abaqus®, a connector element can be defined using a wire feature that connects two nodes or reference points in the model. The connector element can be signed with different types of connector sections that define how many degrees of freedom are allowed between the two nodes or reference points. To mimic the solid rubber bushing connection in the lower arm, the bushing type connector section was chosen to allow six degrees of freedom. To better represent the contact between the rubber and the lower arm, the following settings were included in the model. These settings were applied to both the front and rear bushings. Two reference points with identical coordinate, located at the centre point of the bushing assembly hole, were defined. A wire feature was generated to connect these two reference points. Then, the bushing type connector element with six degrees of freedom was assigned to this wire feature. For each degree of freedom, either a linear, non-linear, or rigid stiffness definition can be defined to properly represent the stiffness of the rubber. The rubber bushing connector stiffness values used in this research were verified through a confirmation process based on a series of FEA simulations on the solid rubber bushing model in isolation. More details on this model will be introduced later. The front bushing torsional stiffness and the rear bushing conical stiffness were set to extremely large values to prevent the large rotation that occurred during the simulation. The reason for this is that the ball joint output forces are defined in a local reference frame attached to the arm in the multibody dynamics simulations. Under the static analysis in Abaqus®, a large rotation will misalign the force direction of the two simulations. After the bushing stiffness had been defined, proper constraint needed to be set on these two reference points. One of the reference points was treated as the centre shaft the for rubber bushing joint, which was marked as the 'constrained point'. Simultaneously, the other reference point was treated as the 'connecting point', and used to transfer the force and moment to the lower arm. A fully fixed boundary condition in all six degrees of freedom was applied to the constrained point in order to mimic the fixed centre shaft in the rubber bushing connection. A coupling motion constraint was applied between the connecting point and the inner surface of the hole on lower arm. This type of constraint is discussed earlier in the ball joint and anti-roll bar connection definition. It allowed the force and moment caused by the bushing stiffness to be uniformly distributed on

the inner surface of the hole. In this way, this simplified bushing modelling closely approximated the case where a solid rubber is modelled together in the lower arm. The computational cost was dramatically reduced with this arrangement. Based on all the settings discussed in the previous content about the four different connection locations in the model, Figure 4.7 shows the schematic of the composite lower arm FEA model.

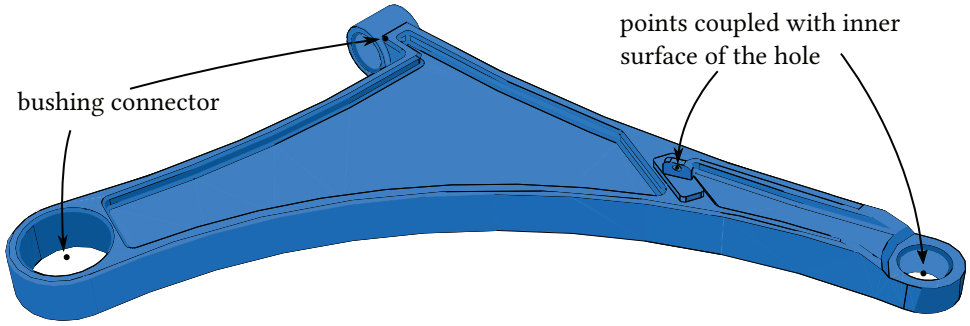

Figure 4.7: Schematic of Lower Arm Assembly Setting in FEA. Both of the bushings were modelled using equivalent stiffness, and the external forces were applied on the bracket and the ball joint.

As mentioned in Chapter 3, the dynamic load effect can be neglected compared to the forces that act on the lower arm ball joint, so the model was built using a static analysis scheme. The major procedure of this type of analysis is to compute the displacement field within a solid subjected to sum of external forces ($\sum F = ku$). At the element level, this means that finding the correct displacement value under the sum of external forces for each single node in an element, based on the calculated stiffness from the material constitutive properties. After finding these displacement values for all the nodes in a element, the stress and strain values for this element can be calculated using the integration method. To initiate a proper static analysis scheme in Abaqus®, a static analysis step must be created in the step definition module. In this definition module, several parameters can be defined, such as the total time period of the simulation, the incrementation strategy, the non-linear geometry effect, the linear equation solver type, and the non-linear solution technique. For the linear equation solver type and the non-linear solution technique, the default setting was chosen (Direct method for solving linear equations and Full Newton method for solving non-linear problems, more details can be found in [53]). The default time period was chosen to vary from 0 to 1 second, because there were no time dependent variables in this model. This time period will be treated as a reference for the incrementation strategy to calculate each time step of the increment.

As introduced in Section 3.4, the material properties of the composite material were defined through the mapping process. In order to check the plastic behaviour and rupture status of the composite lower arm in the Abaqus® output, the field output value of Dependent State Variable (SDV) needed to be added in the field output request. The corresponding meaning of some featured SDV terms are shown in Table 4.1.

Table 4.1: Dependent State Variables. Note that in order to determine the rupture status of the elements when using composite materials, the SDV are required.

State Dependent Variable	Description
SDV1	Gauss point degradation status (1 = Not Ruptured, 2 = Ruptured)
SDV3	Local matrix 11 stress
SDV4	Local matrix 22 stress
SDV5	Local matrix 33 stress
SDV6	Local matrix 12 stress
SDV7	Local matrix 13 stress
SDV8	Local matrix 23 stress
SDV9	Matrix tangent modulus
SDV10	Matrix effective plastic strain
SDV11	Matrix effective stress
SDV13	Matrix failure criterion index. (When SDV13 = 0.0, the matrix stress state is zero. When SDV13 = 1.0, the matrix stress state has initiated failure. SDV13 is computed as the left hand side of Eqn. 3.47.

The mesh of the lower arm was generated using a first-order tetrahedral element shape with an element size of 2.5 mm. The mesh of the bracket was generated using first-order tetrahedral element shape with an element size of 3 mm. The mesh sensitivity study of the lower arm body will be discussed in Section 4.3. As discussed previously, the basic structure of the finite element model for the static composite lower arm analysis can be built in the Abaqus® software. The bushing stiffness properties needed to be defined through a series of solid rubber bushing model tests. The details of this procedure will be discussed in the following section.

4.2 Bushing Stiffness Determination

Solid rubber bushing FEA modelling is not the main focus in this research. However, the high fidelity of the bushing model will define the bushing stiffness values within a reasonable range, in order to make the final lower arm strength prediction more reliable. A rubber-like hyper-elastic material constitutive model was used in Abaqus® to build the solid rubber bushing model. It is based on the strain energy potentials formula. In general, to accurately represent rubber behaviour in Abaqus®, one could provide physical test data on the target rubber material, and the software will analyze the data to determine the optimal strain energy potential parameters automatically. However, due to a lack of experimental data on rubber material from the actual rubber bushing joint, the parameters of strain energy potential formula were chosen to approximate the rubber material behaviour. These parameters were calculated according to the literature[54] and[55]. In

Wang et al[54], the linear elastic stiffness measurements on a series of varying geometry rubber bushings are available. A verification process was made to test the accuracy of the hyper-elastic model in Abaqus®, by generating a solid rubber bushing model with the same geometry as in the literature, and comparing the numerical stiffness prediction with the physical measurement. Because the physical stiffness measurements are in the linear elastic range of the bushing deflection, this verification process was unable to compare the stiffness values in the large deformation range. Considering the loading situation of the bushing joint in a suspension system, large deformation could happen during aggressive vehicle manoeuvers. The numerical solid bushing model in FEA used different orders of the strain energy potential formula to account for the non-linear rubber behaviour. There are no exact physical measurement stiffnesses to compare with this large deformation stiffness prediction in FEA. As a conclusion, it is assumed that the higher order of strain energy potential formula will give an acceptable result. The details of this verification process will be discussed in the following contents along with some basic concepts of the strain energy potential formula.

4.2.1 Hyper-elastic Material Model

The hyper-elastic material model in Abaqus® is suitable for cases where the material is isotropic and non-linear. It is valid for capturing behaviours from the instantaneous elastic response up to large strain deformation. Geometric nonlinearity will be considered during the analysis step[53]. This model has a good representation for rubber or any other type of elastomeric material. One of the big concerns of rubber-like material is the compressibility. Most of the rubber-like materials have small compressibility compared to the shear flexibility. To assess the compressibility of a material, one can get the ratio of initial bulk modulus K_0 to the initial shear modulusμ_0. This ratio can be also related to the Poisson's ratio, by following equation:

$$\nu = \frac{3K_0/\mu_0 - 2}{6K_0/\mu_0 + 2} \tag{4.3}$$

Table 4.2 provides some representative values. A larger Poisson's ratio indicates smaller compressibility:

Table 4.2: Representative Values of Compressibility

K_0/μ_0	ν
10	0.452
20	0.475
50	0.490
100	0.495
1000	0.4995
10000	0.49995

For the solid rubber bushing model, the Poisson's ratio of the rubber was set to a typical value of 0.4999 in this research. Due to this high Poisson's ratio value, the rubber behaved as nearly incompressible, so the solid continuum hybrid elements were chosen when generating the mesh on the rubber part to avoid potential convergence problems. According to Eqn. 4.3, using the known value of initial shear modulus offered by Wang et al[54] and this typical Poisson's ratio 0.4999, the corresponding bulk modulus could be calculated.

Abaqus® describes the hyper-elastic model in terms of the strain energy potential that relates to the initial shear modulus and initial bulk modulus with the following equation:

$$U = \sum_{i+j=1}^{N} C_{ij}(\bar{I}_1 - 3)^i(\bar{I}_2 - 3)^j + \sum_{i=1}^{N} \frac{1}{D_i}(J_{el} - 1)^{2i} \tag{4.4}$$

This equation defines the strain energy stored in the material per unit of reference volume (volume in the initial configuration) as a function of the strain at that point in the material. It is called the general polynomial form of the strain energy function. The $\bar{I}_1$ and $\bar{I}_2$ are the first and second invariants of the deviatoric strain tensor, respectively. The parameter N can be a value varied from 1 to 6. However, values of $N > 2$ are rarely used when both the first and second invariants are taken into account[53]. The C_{ij} and D_i are temperature-dependent material parameters that will be given by user or determined from experimental data by the software. The elastic volume strain J_{el} is calculated from the total volume strain J and the thermal volume strain J_{th} using the equation: $J_{el} = J/J_{th}$. The J_{th} is in terms of the linear thermal expansion ε_{th} as: $J_{th} = (1 + \varepsilon_{th})^3$, where ε_{th} will be defined by the temperature and the isotropic thermal expansion coefficient offered by the user. For this research, the temperature effect wasn't considered during the simulation. The initial shear modulus and the initial bulk modulus depended only on the material parameters when $N = 1$, as in the following expressions:

$$\mu_0 = 2(C_{10} + C_{01}) \tag{4.5}$$

$$K_0 = \frac{2}{D_1} \tag{4.6}$$

In addition to the general polynomial form, Yeoh[56] proposes a justification on the general polynomial form of the strain energy potential by omitting the dependence on the second invariant $\bar{I}_2$ term. Through observations, the sensitivity of the strain energy function to changes in the second invariant is generally much smaller than the sensitivity to first invariant. Also, second invariant is usually difficult to measure, so it might be preferable to neglect it rather than to calculate it based on potentially inaccurate measurements. A reduced polynomial form of strain energy potential called the Yeoh form is generated by assuming the all C_{ij} with $j \neq 0$ are zero and using parameter $N = 3$:

$$U = \sum_{i+j=1}^{3} C_{i0}(\bar{I}_1 - 3)^i + \sum_{i=1}^{3} \frac{1}{D_i}(J_{el} - 1)^{2i} \tag{4.7}$$

where C_{10}, C_{20}, C_{30}, D_1, D_2 and D_3 are parameters that need to be set by the user.

If the reduced polynomial strain energy function is simplified further by setting $N = 1$, then the neo-Hookean form is obtained. This is the simplest hyper-elastic model and often serves as a prototype for elastomeric materials in the absence of accurate material data[53]:

$$U = C_{10}(\bar{I}_1 - 3) + \frac{1}{D_1}(J_{el} - 1)^2 \tag{4.8}$$

where C_{10} and D_1 are parameters that need to be set by the user.

The C_{10} and D_1 values could be calculated through Eqns. 4.5 and 4.5. The C_{20} and C_{30} terms used values offered in the literature[55], and D_2 and D_3 were assumed to be zero. Both the Yeoh and neo-Hookean strain energy potential form were used in the verification process, in order to determine the difference. Because the higher order expression in Yeoh form, it was expected to predict the large deformation behaviour better than the simple neo-Hookean form.

4.2.2 Testing of The Solid Rubber Bushing Model

Based on the bushing geometries provided by Wang et al[54], nine different geometries of solid rubber bushing model have been built in the Abaqus®. The outside ring and inner shaft are modelled using linear aluminum and steel material definition respectively. The rubber sleeve in between is modelled using a hyper-elastic material model (Yeoh and neo-Hookean) as mentioned in the previous section. All six degrees of freedom were constrained on the outer ring. Surface tie constraints were applied on the connection surface between the rubber and the metal part in the model. For each model, four different directions of displacement/rotation type loads were applied on the inner shaft in order to test all four types of stiffness (radial, axial, conical, and torsional). The load magnitude was set to a relatively large value in order to capture the behaviour from small to large strain. The radial direction displacement was 2 mm, and the axial direction displacement was 5 mm. The conical direction rotation was 0.25 rad, and the torsional direction rotation was 0.5 rad. The same magnitude of load was applied for all the different geometry bushing models. A static analysis step was used in the simulation with total 1 second time period and 0.01 second for each increment. A relatively coarse mesh size (4 mm) was used for the metal part with first-order reduced integration 3D brick elements. A finer meshing size (1 mm) was used for the rubber part with first-order reduced integration hybrid 3D brick elements.

The parameters of nine different bushing models are shown in Table 4.3, where L is the height of the bushing, and a and b are the outer radius and inner radius of the rubber sleeve, respectively. As an example, the schematic of 3D model for No.1 and No.6 bushing is shown in Figure 4.8.

Table 4.3: Rubber Bushing Parameters used in FEA

				unit: [MPa]			unit: [MPa^{-1}]		
No.	L [mm]	a [mm]	b [mm]	C_{10}	C_{20}	C_{30}	D_1	D_2	D_3
1	6.35	12.9	6.22	0.1795	0.0232	-3×10^{-4}	1.11×10^{-3}	0	0
2	12.7	12.9	6.22	0.2265	0.0232	-3×10^{-4}	8.83×10^{-4}	0	0
3	19.05	12.9	6.22	0.1687	0.0232	-3×10^{-4}	1.19×10^{-3}	0	0
4	25.4	12.9	6.22	0.2197	0.0232	-3×10^{-4}	9.11×10^{-4}	0	0
5	31.75	12.9	6.22	0.1677	0.0232	-3×10^{-4}	1.19×10^{-3}	0	0
6	38.1	12.9	6.22	0.1814	0.0232	-3×10^{-4}	1.1×10^{-3}	0	0
7	44.45	12.9	6.22	0.1623	0.0232	-3×10^{-4}	1.23×10^{-3}	0	0
8	50.8	12.9	6.22	0.1809	0.0232	-3×10^{-4}	1.11×10^{-3}	0	0
9	96.5	33.35	7.15	0.2334	0.0232	-3×10^{-4}	8.57×10^{-4}	0	0

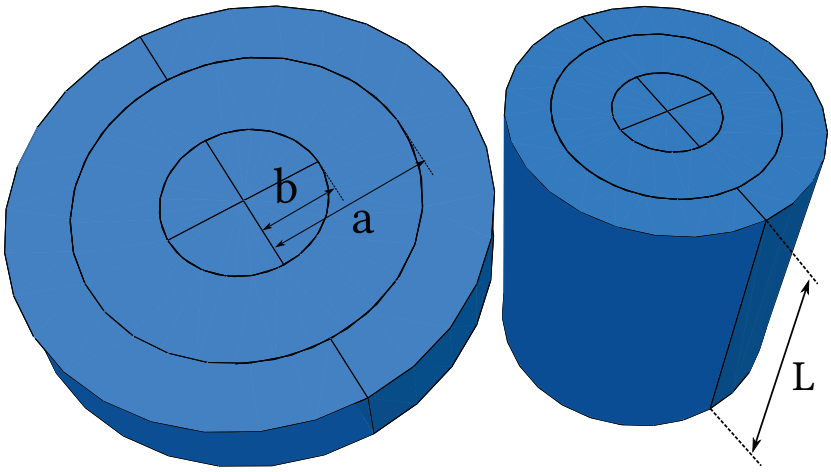

Figure 4.8: Examples of the 3D solid bushing model, Left: No.1 Right: No.6. The model was used to produce stiffnesses in the radial, axial, conical, and torsional directions for nine different bushing geometries.

The bushing stiffnesses of each model for four different directions were calculated using the output reaction force/moment value divided by the input displacement/rotation value in each increment. As an example, the No.1 bushing numerical radial, conical, axial, and torsional stiffness calculation (Yeoh and neo-Hookean) vs the physical measurement are shown in Figure 4.9, respectively. The reaction force/moment change along with the displacement/rotation angle are plotted in for four different directions. Due to the fact that the experimental measurement is given by only one stiffness value, the measured stiffness are plotted as lines (in green). One should compare the results by mainly focusing on the linear range of the curves. By comparing the linear range of four figures, the neo-Hookean model shows better alignment in the radial and axial cases and the Yeoh model has slightly better alignment in the conical and torsional cases. Overall, for linear rubber behaviour prediction, both the neo-Hookean and Yeoh models gave reasonable values compared to the physical measurements. However, the curves in neo-Hooken model were almost linear, even when large displacements/rotations were introduced in the model. In a real bushing joint,

one should expect the reaction force would become larger when larger displacements/rotations occur. The stiffness prediction values from the neo-Hooken model could result in inaccurate behaviour when applied to the lower arm FEA model. Due to the limitation of a lack of stiffness measurements in the large deformation case, it was assumed that the Yeoh model provided a better representation for the real bushing joint. In order to obtain more accurate stiffness values of the rubber bushing, physical tests on the target rubber material would be required; the physical testing results could be provided as the data for the hyper-elastic model in Abaqus®. Considering that the approximate bushing stiffness values were in a reasonable range and will not influence the strength prediction significantly, these physical tests were not conducted in this research.

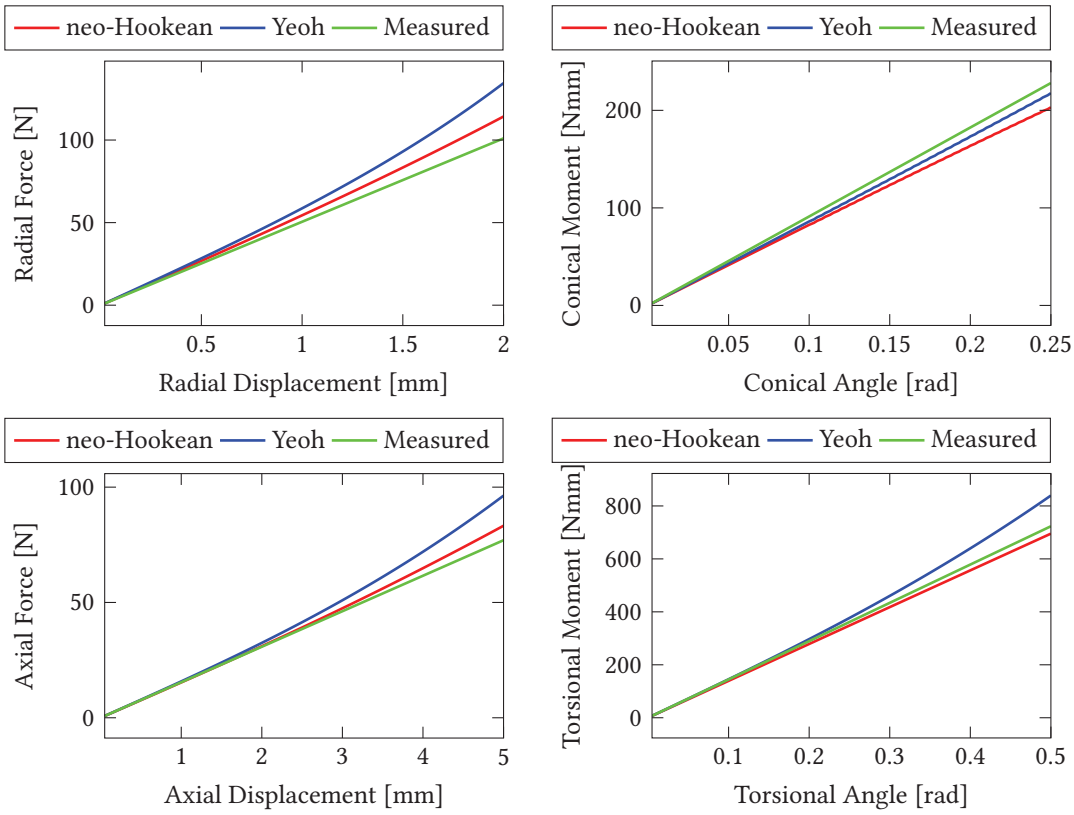

Figure 4.9: Bushing No.1 numerical stiffness calculation (Yeoh and neo-Hookean) vs physical measurement[54]

Additionally, it is worthwhile to show how the numerical stiffness predictions for bushings of differing geometry agree with the published experimental data. In order to do this, the calculated stiffness values from the linear range and the measured stiffness values, which are changing with the bushing number, are plotted in Figure 4.10 for all four stiffness directions. As shown in the figure, the calculated stiffness values shows very good alignment when compared to the physical measurements with different bushing geometry, for both neo-Hookean and Yeoh models. There was a slight underestimation of axial stiffness in bushing Nos. 4 and 6 when using both models, but the differences were not significant. There was a large overestimation of radial stiffness shown

in bushing Nos. 6, 7, and 8 when the Yeoh model was used. The bushing aspect ratio value can be calculated as $l/(a-b)$. From bushing No. 1 to bushing No. 9, the approximate aspect ratio values change from 0.95 to 7.6. Using the target bushing geometry, the aspect ratio values were calculated for both the front and rear bushings. The aspect ratio values were 6.67 and 0.56 for the front bushing and rear bushing, respectively. When these values are compared with the bushing aspect ratio values in the literature, it was anticipated that using the Yeoh model could cause an overestimation in the radial stiffness for the target front bushing, especially in the linear range. However, as mentioned before, the Yeoh model will capture stiffness changes more efficiently than the neo-Hookean model when large deflections occur. The Yeoh model was assumed to be better in overall stiffness prediction, and it was used in the following confirmation process to get the approximate bushing stiffness on the target bushing geometry. More accurate bushing modelling is recommended for future work.

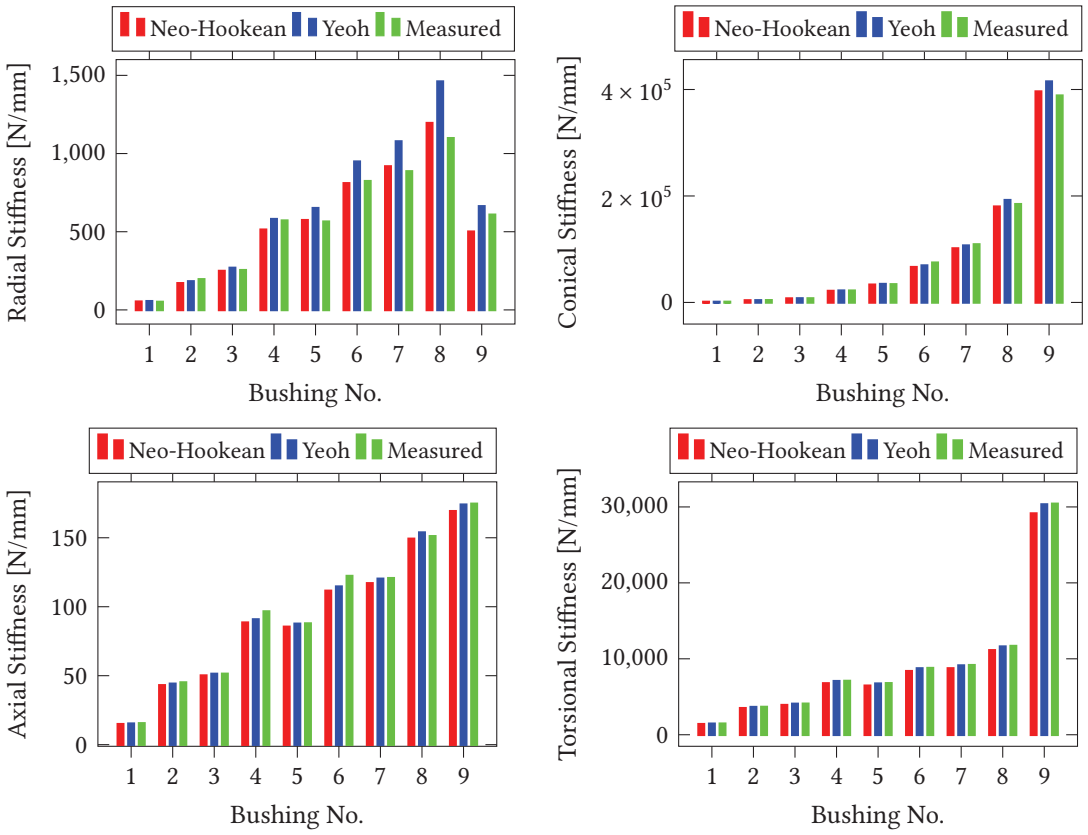

Figure 4.10: Bushing No.1-9 numerical stiffness calculation (Yeoh and neo-Hookean) vs. physical measurement

4.2.3 Meshing Size effect on Predicted Bushing Stiffness

Based on the confirmed parameters of the hyper-elastic material model in the previous section, the stiffness of the target rubber bushing in this research could be predicted by generating the relevant solid rubber bushing model using the geometry from the lower arm sample. The models

were generated using the same settings in the previous section. Each model had four different loading scenarios in order to predict the stiffness in radial, conical, axial and torsional directions. Additionally, three different meshing sizes were used to check the meshing sensitivity of these models. For the front bushing, the tested meshing sizes were 1 mm, 0.5 mm, and 0.3 mm. For the rear bushing, the tested meshing sizes were 4 mm, 1 mm and 0.5 mm. The same element type and meshing size control scheme were used for all different size models. The predicted stiffness values were calculated using the reaction force/moment divided by the input displacement/rotation. The stiffness values from the first three increments of the simulations for the front bushing radial motion and rear bushing conical motion are compared in Tables 4.4 and 4.5. The comparison for the other cases can be found in Appendix B.3. As shown in the tables, the meshing size did have an influence on the predicted stiffness value. However, the deviation became smaller as the meshing size decreased. For example, in the front bushing radial motion, the deviation in value was negligible when the meshing size changed from 0.5 mm to 0.3 mm. Similar results were also found in the other motion types. The front bushing model with 0.5 mm meshing size was selected to give a reasonable stiffness prediction. Likewise, for the rear bushing model, 1 mm meshing size yielded good predictions on the bushing stiffness. These meshing size values were used in the following process to predict the stiffness of the target rubber bushings.

Table 4.4: Front Bushing Radial Motion Mesh Sensitivity Results

Displacement [mm]	Force [N] Size 0.3	Deviation	Force [N] Size 0.5	Deviation	Force [N] Size 1
0.0225	43.5289	0.98%	43.9555	2.47%	45.0417
0.045	87.0608	0.98%	87.9113	2.48%	90.0904
0.0675	130.596	0.97%	131.859	2.49%	135.145

Table 4.5: Rear Bushing Conical Motion Mesh Sensitivity Results

Rotation [rad]	Moment [Nmm] Size 0.5	Deviation	Moment [Nmm] Size 1	Deviation	Moment [Nmm] Size 4
0.005	205.123	0.416%	205.977	3.951%	214.115
0.010	410.253	0.419%	411.971	3.964%	428.3
0.015	615.382	0.422%	617.977	3.979%	642.567

4.2.4 Predicted Rubber Bushing Stiffness

Using the Yeoh model and the confirmed meshing size from previous section, the final solid rubber bushing models, using geometry measured from to the lower arm sample, were built in the Abaqus®. The front and rear bushing stiffness values for four different motions are calculated and plotted in Figures 4.11 and 4.12. The data from these curves was used in both the full car multibody dynamic simulations and the Abaqus® FEA simulations for the relative bushing stiffness property settings.

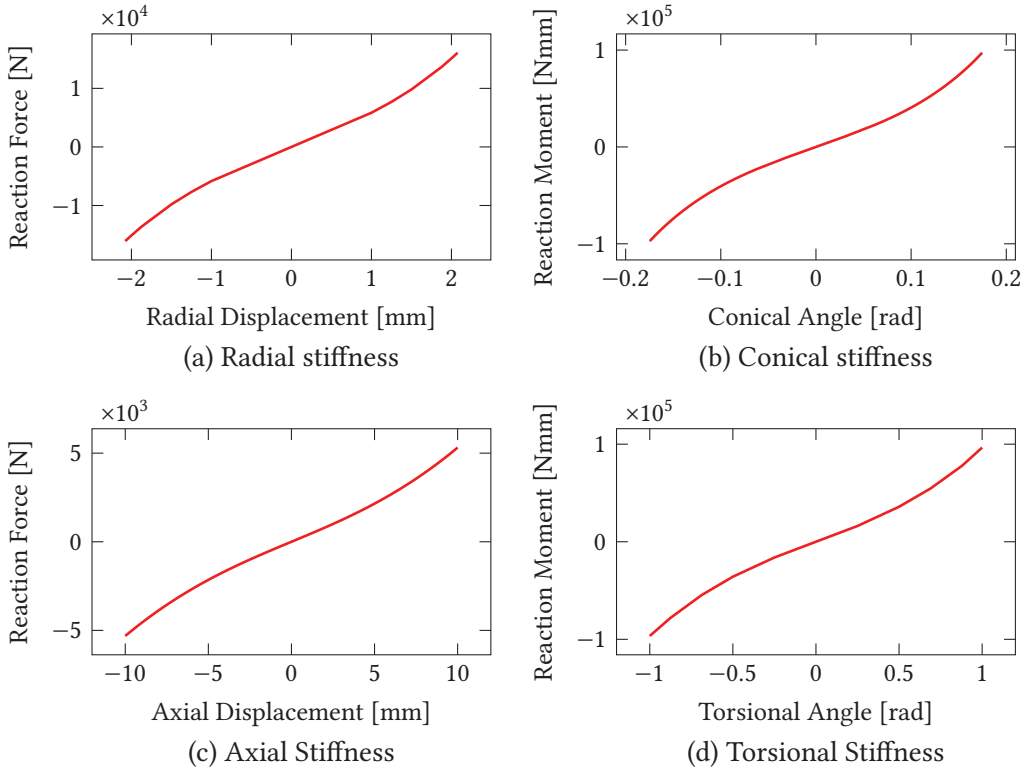

Figure 4.11: Front Bushing Predicted Stiffness Values Using Yeoh Model

4.3 Element Type and Size Influence on Lower Arm Finite Element Analysis

Considering that the FEA results are mesh dependent, and that the tetrahedral element type was chosen for the lower arm meshing, the element size and order were expected to influence the results on the final strength prediction of the lower arm. Before the final stress analysis was completed, a mesh sensitivity study needed to be done in order to ensure that the simulation results are reliable. The objective was to find the proper element size that gave relative accurate results while keeping the simulation run time in the reasonable range as well. As discussed in Section 4.1.2, the tetrahedral element has two order choices: a first-order linear element with 4 nodes denoted as 'C3D4', and second-order non-linear element with 10 nodes denoted as 'C3D10'. Both linear and non-linear type element were tested in the following process. The reduced integration scheme was not considered in either case. In order to test the mesh size effect, different element meshing schemes were used to make the mesh size smaller. In the automatic mesh algorithm, there were two major factors that influence the mesh size: the global mesh size setting and the curvature control factor that influenced the element size on the curved edges in the lower arm body. The strategy used was to build the lower arm model with the same material proprieties and boundary condition settings, so that changes were made to one of the mesh algorithm factors while the other was held fixed.

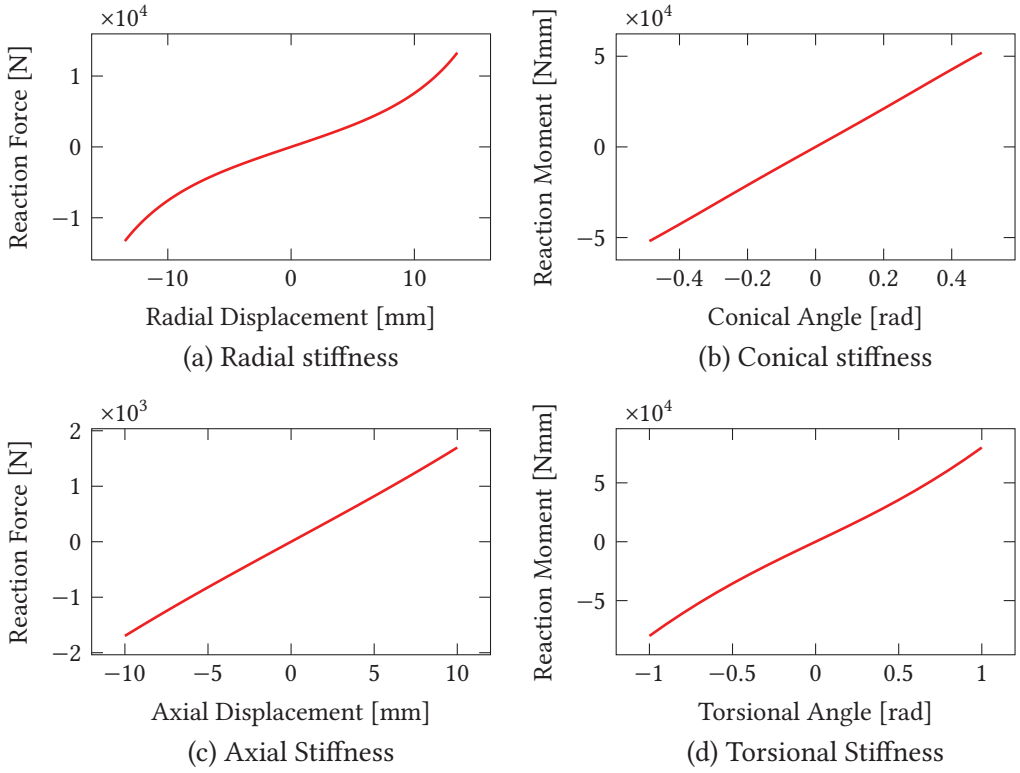

Figure 4.12: Rear Bushing Predicted Stiffness Values Using Yeoh Model

The simulation time and results were also influenced by considering the non-linear geometry effect (denoted as Nlgeom ON or Nlgeom OFF). The following mesh sensitivity study used both cases in order to explore which settings are appropriate for the lower arm. According to the recommendations from the literature[57], a mesh sensitivity study should be used to check if the model overestimates or underestimates the stiffness. One issue must be considered during this kind of study: if the model is load-controlled, one should evaluate displacement or strain values to check for mesh convergence. If it is displacement-controlled, one should evaluate force or stress values instead. The stiffness value is related to the forces and displacements, so to check for stiffness, one needs to check both stress and strain values. In the following mesh sensitivity study, the model was load-controlled, the strain values were the main outputs used to check and compare. Also, estimated stiffness values, which were calculated using maximum principle stress divided by maximum principle strain, were compared as well. This value will give a rough estimate on the system response in the linear range.

4.3.1 Non-linear Geometry Effects

In this section, all models were built with the setting for non-linear geometry effects toggled to 'ON'. The first-order linear element was tested with different global element sizes. The global element sizes tested were 5 mm, 3 mm, 2.5 mm, 2 mm and 1.5 mm. For all simulations, the element

number on local fillet curved edges was set to 4. To compare the simulation results, both linear and non-linear behaviours were checked. For linear behaviour, the following output values were compared at the time step immediately before failure occurred: the maximum principle stress, maximum principle strain, and effective matrix stress. For non-linear behaviour, the effective matrix plastic strain under 10000 N load, and the external force value when failure occurred were compared. The total simulation running time was compared as well. For convenience, different cases will be denoted as follows: S for the global element size, F for the fillet element numbers, followed by the order of the element, i.e., 1st for first order, 2nd for second order. For example, the first order element with 2 mm global size and 20 fillet elements will be denoted as 'S2 F20 1st'. Table 4.6 shows the comparison results of the five different global element sizes. As shown in the table, the maximum principle stress, maximum principle strain, effective matrix stress and effective matrix plastic strain values all increased as the element size decreased. At the same time, failure was detected earlier, i.e., under a smaller load, for element sizes 2 mm and 5 mm. However, the difference became smaller as the element size reduce. As discussed in the previous section, when using the linear tetrahedral element type for the mesh, FEA models can behave stiffer than the real case unless a relatively small element size is used. As expected, for the case with an element size of 5 mm, 3 mm and 2.5 mm, the estimated stiffness value decreased as element size shrank. However, when the element size reached 2 mm and 1.5 mm, the estimated stiffness value began to increase. The reason for this could be that the larger difference between the global element size and the fillet curve element size introduced an artificial stiffness to the boundary of the two different size elements. The estimated stiffness value was anticipated to have some error, because it was calculated from the maximum principle stress and maximum principle strain. As shown in the table, the estimated stiffness values in the case of 2 mm and 1.5 mm are still lower than the case for 3 mm and 5 mm. This indicates that smaller element sizes are needed for linear tetrahedral element in order to reduce the artificial stiffness.

It should also be mentioned that if one considers the non-linear geometry effect in the model, the simulation will end with a non-convergence problem when large plastic strain and failure are detected. This is caused by the plasticity model and rupture model reducing the stiffness value of the failed elements to nearly zero. When this happens, the solver has difficulty in finding the appropriate displacement field to represent the geometric deformation in the output. This non-convergence issue increases the analysis running time, especially in the time step where the large deformation or failure occurred. It can result in the total simulation running time randomly increasing or decreasing when some specific element sizes are used, because in these particular cases, the solver will take longer or less time to confirm that the model is divergent and terminate the simulation. For example, this can be seen in the case with element size of 3 mm. If this case is ignored, the total simulation running time continued to increase when the element size shrank. The simulation time has a significant increase when an element size of 1.5 mm was used. If one considers these five cases by comparing the simulation running time, an element size around 2 mm seems well suited for better analysis results with reasonable computational effort.

Table 4.6: Lower Arm Mesh Sensitivity (Global Size Change, Nlgeom ON)

	Size, Fillet Element Number and Order				
Output	S5 F4 1st	S3 F4 1st	S2.5 F4 1st	S2 F4 1st	S1.5 F4 1st
Max Principle Stress [MPa]	36.22	39.28	39.53	43.54	43.75
Max Principle Strain	5.93×10^{-3}	6.68×10^{-3}	6.9×10^{-3}	7.36×10^{-3}	7.34×10^{-3}
Estimate Stiffness [MPa]	6,107.05	5,881.07	5,726.24	5,919.73	5,963.26
Effective Matrix Stress [MPa]	7.2	7.92	7.94	8.42	8.45
Effective Matrix Plastic strain*	6.3×10^{-4}	1.33×10^{-3}	1.31×10^{-3}	1.86×10^{-3}	1.94×10^{-3}
Failure Happen Under Load [N]	14,000	14,000	14,000	14,000	12,000
Running Time [second]	1,675	13,796	3,601	3,815	16,891

* Under 10000 Newton Force

Because the element size converged around a size of 2 mm in the previous global element size study, in the fillet curve element size study, the models were created with a global element size of 2.5 mm, and with an increased element number on the fillet curve (F10, F20 and F40). The results are compared in Table 4.7. As shown in the table, the fillet curve element size did have an influence on the analysis results as well. Checking the stress and strain values individually, both grew as the fillet curve element size shrank. However, the estimated stiffness values showed little difference. Similarly to the previous global element size study, the estimated stiffness values increased a little. Again, this effect is expected because of the large difference between the global element size and local fillet curve element size. For the failure prediction, failure was detected at same time step with same external force. To be noticed, the S2.5 F10 case gave almost the same result when compared to the S2 F4 case. This indicated that the global element size and local fillet element size should be close to the same in order to avoid artificial stiffness being generated on the element boundary. For the simulation time comparison, decreasing the fillet curve element size did not increase the simulation time very much, with the exception of the S2.5 F40 case. A shorter simulation time was reported in this case due to a non-convergence issue that terminated the simulation early. Overall, the fillet curve element size does not have as significant an influence on the simulation results as the global element size. The model using 10 elements on the fillet curve with a 2.5 mm global element size was selected with the expectation that it would produce an optimal balance between solution accuracy and simulation run time.

As a comparison, it is also worthwhile to show how the second-order tetrahedral element behaved on the composite lower arm model with different global element size and fillet curve element size. In order to check if using second order elements would be a better choice in this research, four different models were created using following setup: a global element size of 4 mm with 10 elements on the fillet curve, a global element size of 4 mm with 20 elements on the fillet curve, global element size of 3.5 mm with 20 elements on the fillet curve, and a global element size of 2.5 mm with 20 elements on the fillet curve. The results are compared in Table 4.8. As shown in the table, consistent results are reported in all the cases. This indicated that the second-order element had quicker convergence compared to the first-order element, and that larger element

Table 4.7: Lower Arm Mesh Sensitivity (Fillet Size Change, Nlgeom ON)

Output	Size, Fillet Element Number and Order S2.5 F10 1st	S2.5 F20 1st	S2.5 F40 1st
Max Principle Stress [MPa]	44.02	50.95	53.14
Max Principle Strain	7.41×10^{-3}	8.53×10^{-3}	8.71×10^{-3}
Estimate Stiffness [MPa]	5,942.94	5,973.27	6,097.28
Effective Matrix Stress [MPa]	8.45	9.77	10.12
Effective Matrix Plastic strain*	2.01×10^{-3}	3.78×10^{-3}	4.73×10^{-3}
Failure Happen Under Load [N]	12,000	12,000	12,000
Running Time [second]	4,225	7,324	6,351

∗ Under 10000 Newton Force

sizes could be used to yield the same results as in the first-order element case. However, the total simulation time increased significantly, even in the case S4 F10 2nd. Comparing this case with the case S2.5 F10 1st, almost the same results are shown, with only one third of the simulation running time. As mentioned before, first-order tetrahedral elements are not recommended except with very fine mesh size. This effect was been observed in this mesh sensitivity study. However, for this particular research on the composite lower arm strength prediction, it was decided that using the second-order tetrahedral elements would not be feasible in terms of simulation running times, considering the number of proposed simulations. According to results shown in Tables 4.6, 4.7, and 4.8, the best choice was using a first-order element with global size 2.5 mm and 10 elements on the fillet curve. This arrangement gave acceptable results with relatively short simulation times.

So far, all the models described were built with the feature that non-linear geometry effects are considered during the analysis. Usually, this feature should be considered if the total strain exceeds 5% during the simulation. However, due to the plasticity and rupture assumptions in the composite material model, and recognizing that this feature will increase the simulation running time and potentially cause non-convergence issues, it was decided to explore the model behaviour without considering this feature, in order to explore potential time saving strategies. In next section, a mesh sensitivity study was performed without considering the non-linear geometry effect in the model.

Table 4.8: Lower Arm Mesh Sensitivity (2nd order element, Nlgeom ON)

Output	Size, Fillet Element Number and Order S4 F10 2nd	S4 F20 2nd	S3.5 F20 2nd	S2.5 F20 2nd
Max Principle Stress [MPa]	44.11	44.15	44.12	46.05
Max Principle Strain	7.83×10^{-3}	7.68×10^{-3}	7.69×10^{-3}	7.83×10^{-3}
Estimate Stiffness [MPa]	5,632.08	5,746.3	5,736.76	5,882.53
Effective Matrix Stress [MPa]	9.11	9.05	9.02	9.28
Effective Matrix Plastic strain*	3.38×10^{-3}	3.23×10^{-3}	3.2×10^{-3}	4.33×10^{-3}
Failure Happen Under Load [N]	13,000	12,000	12,500	12,000
Running Time [second]	12,029	8,277	45,442	68,593

∗ Under 10000 Newton Force

4.3.2 Without Non-linear Geometry Effect

The exact same set of models were created with the global element size and fillet curve element size which were used in the previous mesh sensitivity study. The only difference is that all models did not consider the non-linear geometry effect during the simulation. The results with different global element size are compared in Table 4.9. As shown in the table, the output values for the linear range were quite similar when compared to Table 4.6. The model behaved a somewhat stiffer when comparing the estimated stiffness values; however, the differences were very minor. The difference was noticeable for the non-linear range outputs, e.g., the effective matrix plastic strain under 10000 N was smaller compared to the values in Table 4.6. This lead to the failure happening later, i.e., with larger external force. This result makes sense because the non-linear geometry effect will mainly influence the non-linear behaviours, such as plastic deformation and failure initialization. This could pose a problem because the final strength analysis was expected to give reasonable failure prediction. For a safer design, one should expect the model to detect the failure earlier, with smaller external force. In order to achieve the same failure prediction results, a smaller element size needed to be used if the models were built without using the non-linear geometry solver. For the simulation time comparison, the time for each case was shorter compared to the time in Table 4.6. This indicated that a smaller element size could potentially be used for the model without the non-linear geometry effect. By not considering the non-linear geometry effect, the model wouldn't have non-convergence issues, even when severe deformations happened during the analysis. However, the output values of stress and strain after the time step where failure occurred were unrealistic, due to the stiffness of the failed elements being set to nearly zero. The stress-strain evaluation using a linear geometry relationship on the zero stiffness element made the deformation of the element become extremely large. Considering that the objective of this research is to focus on predicting the strength at initial failure occurrence, rather than the damage evolution status after the failure, the unrealistic stress and strain output after the failure will not influence the final results. Because every analysis was converged right away, the total simulation running time for each case showed a continual increase as the elements shrank. The judgment of which size case had better accuracy and less running time became more apparent. The next step was to show the influence of the fillet curve element size.

Table 4.9: Lower Arm Mesh Sensitivity (Global Size Change, Nlgeom OFF)

	Size, Fillet Element Number and Order				
Output	S5 F4 1st	S3 F4 1st	S2.5 F4 1st	S2 F4 1st	S1.5 F4 1st
Max Principle Stress [MPa]	35.31	38.2	38.51	42.51	42.55
Max Principle Strain	5.67×10^{-3}	6.31×10^{-3}	6.52×10^{-3}	7.03×10^{-3}	7×10^{-3}
Estimate Stiffness [MPa]	6,222.38	6,058.6	5,910.59	6,047.78	6,081.46
Effective Matrix Stress [MPa]	6.82	7.39	7.28	8	7.99
Effective Matrix Plastic strain*	1.75×10^{-4}	4.31×10^{-4}	4.38×10^{-4}	7.45×10^{-4}	7.4×10^{-4}
Failure Happen Under Load [N]	16,000	14,000	14,000	14,000	14,000
Running Time [second]	927	2,215	3,404	5,001	14,497

∗ Under 10000 Newton Force

The results for different fillet curve element size are compared in Table 4.10. If this table is compared with Table 4.7, a similar conclusion can be reached as with the effect of the global element size. The difference in linear range outputs were not significant. The effective matrix plastic strains were still smaller when compared to the values in Table 4.7, but the difference became smaller when 20 elements or 40 elements were used on the fillet curves. These two cases had almost the same values as the case where non-linear geometry effect are considered during the simulation for both the linear and non-linear outputs. The most important point is that the predicted failure load were the same. As in the previous mesh sensitivity study, the S2.5 F40 case had a relative large estimated stiffness value, so that combination was not considered as an appropriate element size choice. The S2.5 F20 case was the best choice among all the cases in Tables 4.9 and 4.7.

Table 4.10: Lower Arm Mesh Sensitivity (Fillet Size Change, Nlgeom OFF)

	Size, Fillet Element Number and Order		
Output	S2.5 F10 1st	S2.5 F20 1st	S2.5 F40 1st
Max Principle Stress [MPa]	42.77	49.73	51.72
Max Principle Strain	7.07×10^{-3}	8.17×10^{-3}	8.34×10^{-3}
Estimate Stiffness [MPa]	6,051.49	6,083.97	6,201
Effective Matrix Stress [MPa]	8	9.19	9.57
Effective Matrix Plastic strain*	7.91×10^{-4}	1.94×10^{-3}	2.39×10^{-3}
Failure Happen Under Load [N]	14,000	12,000	12,000
Running Time [second]	3,832	6,241	8,838

∗ Under 10000 Newton Force

Finally, it also worthwhile to show how the second-order element behaved when non-linear geometry effects were not considered. The results are shown in Table 4.11. Unsurprisingly, the output values are quite consistent even as element size is reduced. The estimated stiffness values were smaller compared to the first-order element, but the differences were not severe. However, simulation running times were significantly increased. A similar output was obtained by using the S2.5 F20 setup with first-order elements, which took much less time to run. There is another shortcoming for the second-order elements: the predicted failure loads were substantially larger when compared to the values from the first-order element case. This could lead to potentially unsafe designs if this kind of elements was used in the final strength prediction, even though the model will behave as if it is was softer. Considering the longer running time and larger failure load prediction, the second-order elements were not a good choice when non-linear geometry effects were not considered.

Overall, the models without the non-linear geometry effect did not show much difference on the output values, especially when first-order elements and appropriate fillet curve element sizes were used, and the running times were shorter than models with the non-linear geometry effect. As a conclusion, building the model without the non-linear geometry effect was a better choice in this composite lower arm analysis. According to this mesh sensitivity study, the final decision for

Table 4.11: Lower Arm Mesh Sensitivity (2nd order element, Nlgeom OFF)

Output	Size, Fillet Element Number and Order			
	S4 F10 2nd	S4 F20 2nd	S3.5 F20 2nd	S2.5 F20 2nd
Max Principle Stress [MPa]	42.9	42.92	42.4	44.79
Max Principle Strain	7.46×10^{-3}	7.32×10^{-3}	7.31×10^{-3}	7.48×10^{-3}
Estimate Stiffness [MPa]	5,753.84	5,864.24	5,803.78	5,987.38
Effective Matrix Stress [MPa]	8.6	8.53	8.37	8.77
Effective Matrix Plastic strain*	1.5×10^{-3}	1.42×10^{-3}	1.39×10^{-3}	2.07×10^{-3}
Failure Happen Under Load [N]	16,000	16,000	16,000	16,000
Running Time [second]	9,455	13,330	22,052	60,984

∗ Under 10000 Newton Force

the element size and type choice was a first order element with global element size of 2.5 mm and 20 elements on the fillet curves. The simulation ran without considering the non-linear geometry effect.

4.4 Finite Element Analysis results on Lower Arm

Based on all the parameters and settings decided from the previous sections and chapters, the final composite lower arm finite element models were generated. The summarized maximum force combinations from levels 5, 6, 7 random roads were used as the external loads to test the strength of the composite lower arm through a static analysis. For each level, there were fourteen different force combination cases. The first eight cases will be the maximum force combinations from each octant in the Cartesian coordinate system. According to the sign of force in each axis, they will be denoted as (+,+,+), (-,-,-), (-,+,+), (+,-,-), (-,-,+), (+,+,-), (+,-,+) and (-,+,-). The last six cases will be the maximum force combinations which have maximum values in each individual axis for both positive and negative direction. They will be denoted as maximum $+x$, maximum $-x$, maximum $+y$, maximum $-y$, maximum $+z$ and maximum $-z$. In addition, for each force combination case, there were four different models that were generated according to the four different injection locations (ball joint side, front bushing side, rear bushing side and middle location of the arm). In total there will be 56 different models for each level of road. It is not necessary to show each individual output from all models. There were two ultimate goals in running all of these different models: 1. To find which force combinations might cause failure or large plastic deformation. 2. To explore the influence of different injection locations on the composite lower arm strength. To achieve these two goals, the values of SDV1 (element failure status) and SDV9 (tangent stiffness) were the main outputs used to check and compare between different models. Recall that the SDV definitions are shown in Table 4.1. In the following contents, the compared and summarized SDV1 and SDV9 outputs will be shown for each level of road separately.

4.4.1 Level 5 Road

For all maximum force combination cases, only a small local failure and plastic deformation were detected in the outputs. The different injection locations did not have significant influence on prevention of failure or plastic deformation. The rear bushing side injection case will be shown as an example in most of the following figures. Local surface element failure was reported in cases (+,+,+), (+,-,+) and maximum $+z$. These three cases corresponded to three different driving scenarios: straight braking, cornering and braking, and constant speed cornering. The failure status (SDV1) output for these three cases is shown in Figures 4.13, 4.14, and 4.15. As shown in the figures, the failures happened on the elements that are located near the connecting surface between the bracket and lower arm. For the (+,-,+) and maximum $+z$ cases, only a single element failed. These local failures could have been caused by a stress concentration introduced by the tie constraint between the steel bracket and the lower arm. Some potential improvements could be made achieved by designing a better bracket connection and model, or by making the bracket integral with the lower arm. In this way, these failure could be avoided. As for this cases, these local rupture weren't considered as a failure for the composite lower arm. However, certain plastic deformation has also been detected in these cases. The output of the tangent stiffness (SDV9) for the plastic behaviour is shown in Figure 4.16, 4.17, and 4.18. The tangent stiffness values from elements indicate the amount of plastic deformation caused by the external force. The original tangent stiffness value was 1.568×10^3 MPa, which indicates that no plastic behaviour was found in the element. Smaller values indicate larger plastic deformation. As shown in Figure 4.16, relatively large plastic behaviour was detected in the elements that are located around the bracket connection region. Although there might not have been critical damage to the majority of the lower arm body, this plastic behaviour is not acceptable when considering the safety issue of using this kind of composite material. As mentioned before, this plastic deformation might be avoided by using softer material on the bracket or an improved design for the connection method. However, further study is needed to prove any potential improvements. Considering the driving scenarios for these three cases, the hard braking and cornering motion was the main reason to cause the plastic deformation. Comparing the rupture status outputs in the other injection location cases, the same location of failure was still detected in the model, except the maximum $+z$ case with ball joint side injection location. In this case, the single element failure near the bracket did not occur. This difference could be caused by the fact that the ball joint side injection location is close to the bracket connection region, which increased the fibre alignment in this region. Also, for the middle side and ball joint side injection location cases, the failures happened in an earlier time step. The rear bushing side and front bushing side injection location cases showed a slight advantage in increasing the strength of the lower arm in the local bracket connection area.

There are six cases that did not indicate that failure occurred, but that did detect plastic deformation. They are the (-,-,-), (-,-,+), maximum $-x$, (+,+,-), maximum $+y$, and maximum $+x$ cases. For the (-,-,-), maximum $-x$, and (-,-,+) cases, only negligible plastic deformation was reported, similar

to the situations shown in Figure 4.18. For the (+,+,-), maximum $+y$, and maximum $+x$ cases, relatively large plastic deformation was detected, similar to the situations shown in Figure 4.16. The other four cases that are not mentioned ((-,+,+), (+,-,-), (-,+,-), maximum $-y$, and maximum $-z$) are the safe cases in which the composite lower arm was strong enough to bear the corresponding maximum forces from the level 5 road.

Overall, based on all the results, the composite lower arm performance under level 5 road roughness barely meets the strength requirements. It is only reliable under low speed diving scenarios without hard braking or cornering. However, some improvements could potentially make the composite lower arm strong enough under a level 5 road without a dramatic change in the lower arm geometry.

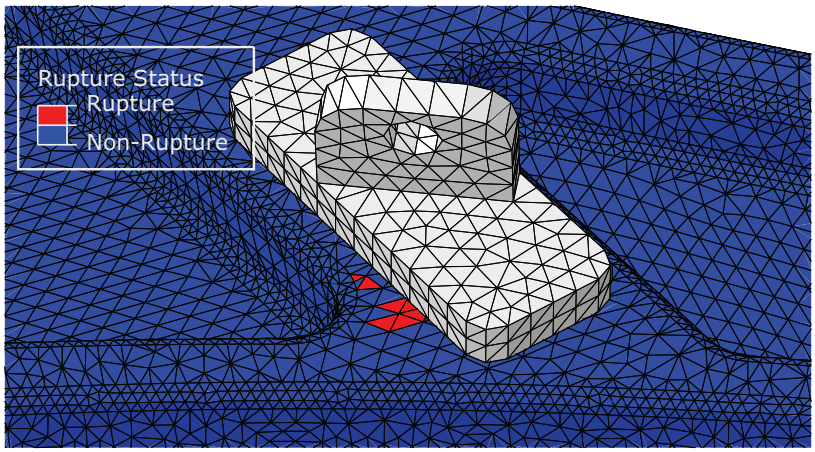

Figure 4.13: Level 5 Road (+,+,+) Rear Bushing Injection Case Element Rupture Status. A few surface elements were predicted to rupture near the location where the steel bracket and composite lower arm are connected.

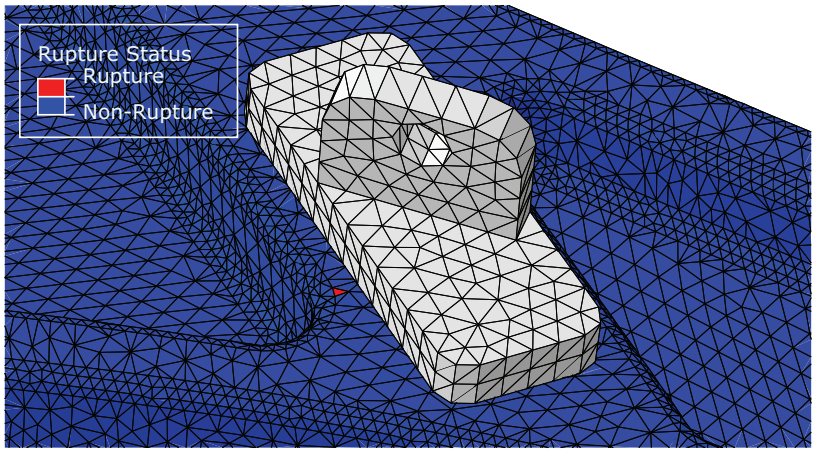

Figure 4.14: Level 5 Road (+,-,+) Rear Bushing Injection Case Element Rupture Status. Only a single element was predicted to rupture, also near the surface where the steel bracket and composite lower arm are connected.

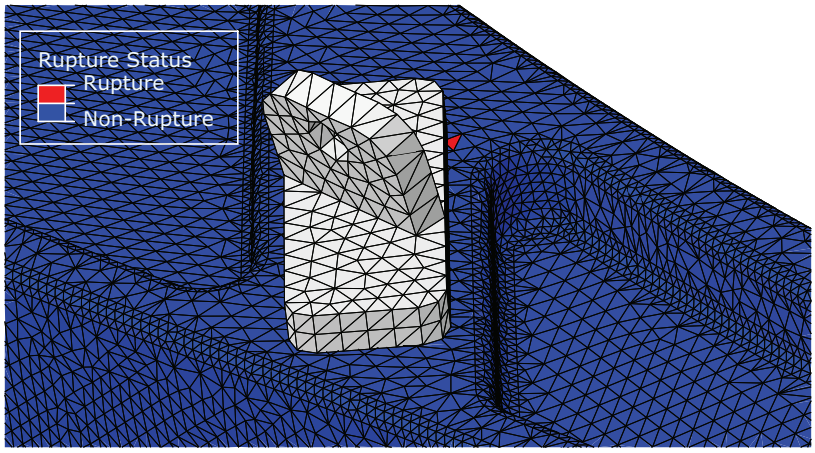

Figure 4.15: Level 5 Road maximum $+z$ Case Element Rupture Status. Again, only a single element was predicted to rupture, also near the surface where the steel bracket and composite lower arm are connected.

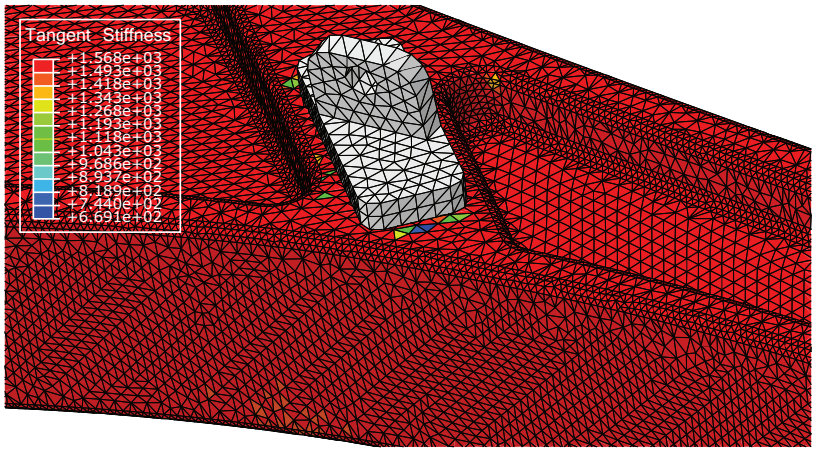

Figure 4.16: Level 5 Road (+,+,+) Rear Bushing Injection Case Plastic Behaviour. Relatively large plastic deformation was predicted near the location where steel bracket and composite lower arm are connected.

4.4.2 Level 6 Road

Further to the results above, the composite lower arm was also tested under loads that represent a level 6 road roughness. Knowing that the force summary results were much larger when compared to the level 5 road, more aggressive failure and plastic deformation were expected in the level 6 road cases. Based on the output values from all cases in level 6, the following summary was obtained: A similar local surface element failure near the bracket connection area was again found in the same cases as in level 5 ((+,+,+), (+,-,+) and maximum $+z$). Additionally, the maximum $-x$ case under the level 6 road also showed the local bracket connection area failure. Further, in these four cases, more elements were detected as ruptured, and larger plastic deformation was shown compared to the level 5 road case. Similarly to the level 5 road simulations, there were eight cases

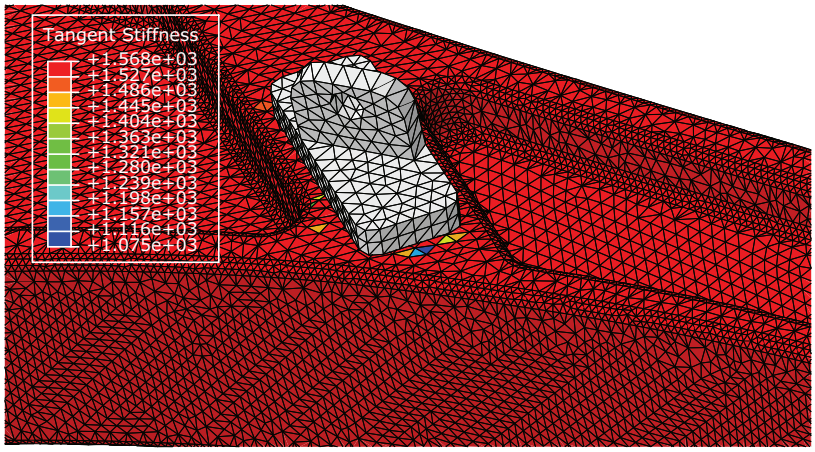

Figure 4.17: Level 5 Road (+,-,+) Rear Bushing Injection Case Plastic Behaviour. Relatively small plastic deformation was predicted near the location where steel bracket and composite lower arm are connected.

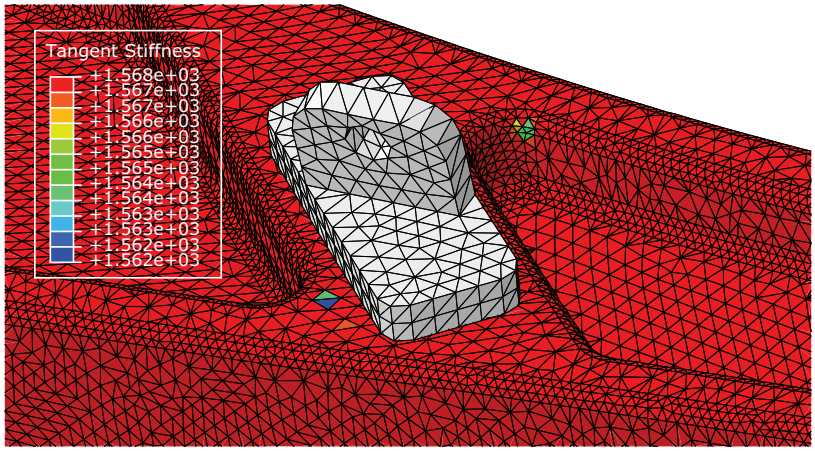

Figure 4.18: Level 5 Road maximum $+z$ Rear Bushing Injection Case Plastic Behaviour. Negligible plastic deformation was reported in this case.

showing plastic deformation only, without any element rupture. They were the (-,-,-), (-,+,+), (-,-,+), (-,+,-), maximum $-y$, maximum $-z$, (+,+,-) and maximum $+y$ cases. Among these cases, only negligible plastic deformation was reported in the (-,-,-), (-,+,+), (-,-,+), (-,+,-), maximum $-y$ and maximum $-z$ cases. Relatively large plastic deformation was shown in the (+,+,-) and maximum $+y$ cases. The only safe case without failure or plastic deformation was the (+,-,-) case.

A crack style failure that is not local to the bracket connection area was found in the maximum $+x$ case. By checking the corresponding driving scenarios for all cases, the following conclusion could be reached: The constant high speed driving and straight accelerating cases are relatively safe with causing failure or large plastic deformation. The braking and cornering cases are the major challenge to the composite lower arm. These cases showed larger plastic deformation and serious failure, especially in the braking during high speed straight driving case. Different injection

locations did have a certain influence on the failure or plastic behaviour. Each injection location will be discussed separately below.

For the rear bushing injection location case, the following behaviour could be summarized through the observation of SDV1 and SDV9 contour outputs (This behaviour also happened in other injection location cases): In the (+,+,+), (+,-,+), maximum $+z$, and maximum $-x$ cases, element failure was only reported around the bracket connection area. The maximum $-x$ case is a new case in which failure was reported compared to the level 5 road. For the (+,+,+) and maximum $+z$ cases, more failure elements were found and the failure happened in an earlier time step. Plastic deformation was also larger compared to the level 5 road. The rupture status in (+,-,+) case was quite similar to the level 5 road. The maximum $+x$ case shows a crack style failure on the fillet edge that is located close the front bushing side. This was the first case in which failure was detected away from the bracket connection area. The force combination that caused this failure came from the braking during straight driving case. The failure was mainly caused by hard braking force during high speed driving that acts to bend the lower arm in the rearward longitudinal direction. If the surface element failure around the bracket connection area is not considered critical, this crack style failure would be the first formal failure that resulted from insufficient lower arm strength. Also, the plastic deformation in the maximum $+x$ case was quite substantial when compared to the (+,+,+), (+,-,+), maximum $+z$, and maximum $-x$ cases. To avoid repetition, only the SDV1 and SDV9 contour plots for maximum $+x$ case will be shown as an example in Figures 4.19 and 4.20 for the level 6 road.

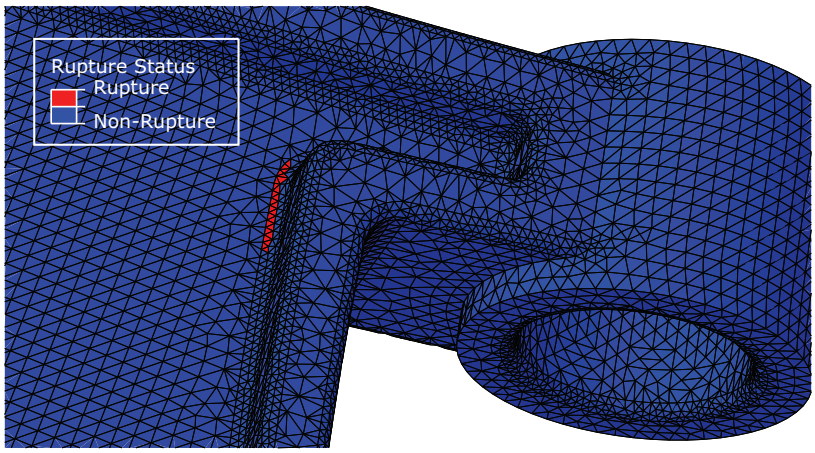

Figure 4.19: Level 6 Road maximum $+x$ Rear Bushing Injection Case Element Rupture Status. A crack style failure was reported on the fillet edge near the front bushing side.

For the ball joint injection location case, the failure occuring in the maximum $-x$ case was prevented. Similarly to the level 5 road case, this is because choosing the injection location closer to the ball joint side resulted in better fibre alignment in the local bracket connection area. In the (+,+,+) and (+,-,+) cases, element rupture was found at an earlier time step when compared to the rear bushing injection location case. In the maximum $+z$ case, fewer elements were ruptured

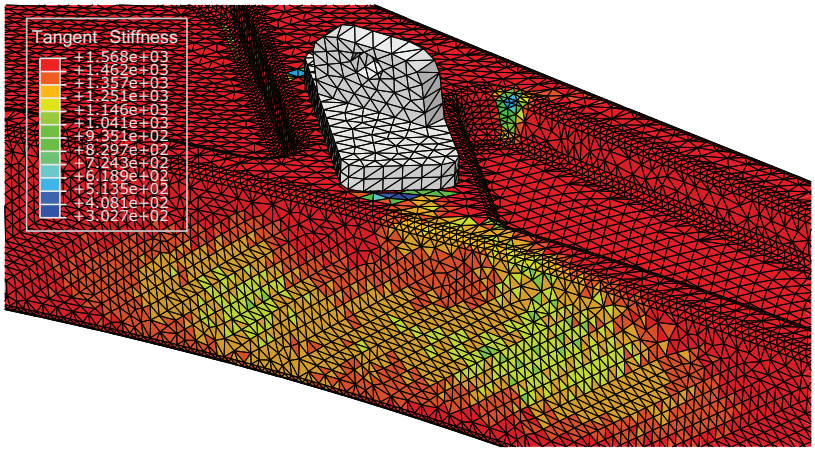

Figure 4.20: Level 6 Road maximum $+x$ Rear Bushing Injection Case Plastic Behaviour. Severe plastic deformation was reported near the bracket connection area.

compared to rear bushing injection location. The crack failure still occurred in the maximum $+x$ case, with slightly fewer failed elements.

For the front bushing injection location case, the failures occurring in both the maximum $-x$ and maximum $+x$ cases were prevented. Similar results were shown in the (+,+,+) and (+,-,+) cases when compared to the rear bushing injection location case. In the maximum $+z$ case, performance was slightly better when compared to the rear bushing injection location case, but the performance wass worse when compared to the ball joint injection location.

For the middle injection location case, the rupture status was worse in the (+,+,+) and (+,-,+) cases when compared to the rear bushing injection location case. However, it also prevented the crack failure from occurring in the maximum $+x$ case. The rupture status in the maximum $-x$ and maximum $+z$ cases was very similar to the rear bushing injection location case.

Overall, based on all results from the level 6 road simulations, the best choice of injection location was the front bushing side. It prevented the crack failure and reduced the severity of the local bracket connection failure in most of the cases. However, the ball joint side injection location could offer better performance in the bracket connection area for the maximum $+z$ and maximum $-x$ cases. As mentioned, the local failure around the bracket connection area could be prevented by finding an improved method of connecting the lower arm and bracket or by manufacturing them as a single body. Preventing the crack failure was considered as more important to improve the strength of the composite lower arm. Based on this, the ball joint side injection location was not as good as the front bushing injection location. The middle injection location also prevented the crack failure but resulted in much worse performance for the local failure in the bracket connection area compared to the front bushing injection location. Thus, the middle injection location could be considered as a potential choice, but further study and testing are needed.

Considering the overall performance on the level 6 road, the injection moulded composite lower arm was found to be not safe to be used in most circumstances. Dramatic geometry change and redesign or improved material properties are needed to make the composite lower arm strong enough under these loads. From the current results, there will not be any devastating damage in the main body of the lower arm, but plastic deformation and small crack failure would likely continue growing to become serious damage if these loads were repeated. Further studies are needed on the damage evolution models in order to predict the final failure status accurately.

4.4.3 Level 7 Road

Because the failure situation are still not critical in the level 6 road simulations, simulations under level 7 road were also conducted. Serious damages was expected during these simulations. Based on the failure and plastic behaviour in all cases, the output situations can be classified into five categories.

1. No failed elements and only minor plastic deformation was shown in the (-,-,-) and maximum -z cases.
2. No failed elements and relatively large plastic deformation was shown in the (+,-,-) and maximum -x cases.
3. Small local bracket connection area failure was shown along with large plastic deformation in the maximum +z case.
4. Large crack style failure on the fillet edge or front bushing ring are with large plastic deformation was shown in the (-,+,+), (-,-,+), (+,-,+), (-,+,-), maximum +y and maximum -y cases.
5. Significant damage and multiple crack failures were shown in the (+,+,+), (+,+,-) and maximum +x cases.

Among all significant damage cases, the (+,+,-) case showed the worst failure. As an example, the rupture status contour plots for the (+,+,-) case with rear bushing injection location will are shown in Figures 4.21 and 4.22. In this (+,+,-) case, the composite lower arm was completely broken due to severe external force. By checking the force summary results in the level 7 road, these severe force combinations mostly result from high speed (100 km/h) straight driving under extremely aggressive road surface conditions. Unlike the level 5 and level 6 cases, the main source of the large forces was the high roughness road surface. Different injection locations did have influence for rupture and plastic deformation; however, it had limited influence, mainly on local elements close to the injection location. The serious damage was not prevented by selection of the injection location, because the failure happened at multiple locations on the lower arm body. Some featured local strength improvement from each individual injection locations will be discussed. For rear bushing injection location case, the failure status and plastic behaviours are as described in the previous list.

In the ball joint injection location case, the element rupture at bracket connection area was prevented in the (-,+,+) and maximum $+z$ case. For other cases, there were no noticeable improvements.

In the front bushing injection location case, the crack failure on the front bushing connection ring was prevented in (+,-,+) and (-,+,+) case. However, a new crack failure on the ball joint connection ring was introduced in the (-,+,+) and (+,+,-) case. There are no obvious changes found in the other cases.

In the middle side injection location case, the best performance was found in the (-,-,+) case. It prevented the rear bushing connection ring crack failure, and it had a smaller crack failure on the ball joint connection ring. However, it could not prevent the rear bushing connection ring crack failure in the (+,+,-) case.

Even though some crack failures were prevented in the previous cases, the overall damage and plastic deformation were still quite large in these cases. This proves that the local element strength close to the injection location can be improved through better aligned fibre orientation in this particular region, but the element performance near the end of the injection flow might may be compromised due to the circular ring shape filling. The filling of the ring resulted in colliding flow fronts that give highly randomized fiber orientation locally to the ring. The optimal injection location is difficult to determine, as it depends on the loading situation and the critical failure location in lower arm body. According to the simulations which were conducted, the critical failure location in this particular lower arm geometry were mainly located near the front bushing side and bracket connection location. Based on this, the front bushing side injection location could be the best choice to offer highest performance in most of the cases. However, more different injection locations and loading situations are still needed for testing in order to fully prove this result.

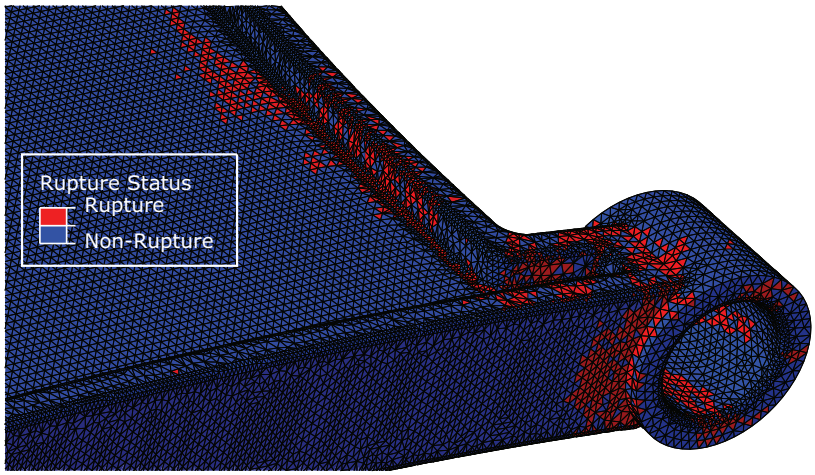

Figure 4.21: Level 7 Road (+,+,-) Rear Bushing Injection Case Element Rupture Status 1. Serious damage occurred near the front bushing joint.

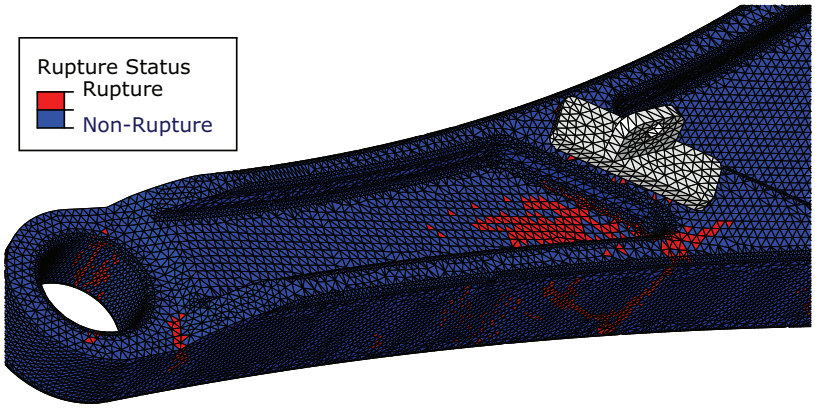

Figure 4.22: Level 7 Road (+,+,-) Rear Bushing Injection Case Element Rupture Status 2. Serious damage occurred near the bracket connection location.

It is important to note that the level 7 road condition is extremely rough compared to regular driving that a normal commuter would experience in daily life. It is not surprising that the composite lower arm would be completely broken in this case. As a comparison, the performance of the standard aluminum lower arm under this condition was also explored. A linear static analysis using the maximum force combination from the PPN case on the aluminum lower arm with the same geometry was conducted. The contour plot of the von Mises stress is shown in Figure 4.23. The material properties of a typical aluminum alloy (6061 T6) were used, and are shown in Table 4.12 as a benchmark. If one compares the value of yield strength σ_Y with the maximum von Mises stress in the contour plot, it is clear that the aluminum lower arm is close to the yield point, showing that level 7 road conditions are critical indeed. It also illustrates that the composite lower arm falls far short from fulfilling the requirements under this type of road condition when compared to its aluminum counterpart.

Table 4.12: Aluminum Alloy 6061 T6 Material Properties Benchmark

Aluminum Alloy	Temper	E [GPa]	G [GPa]	σ_Y [MPa]	σ_u [MPa]
6061	T6	68.9	26.2	241	290

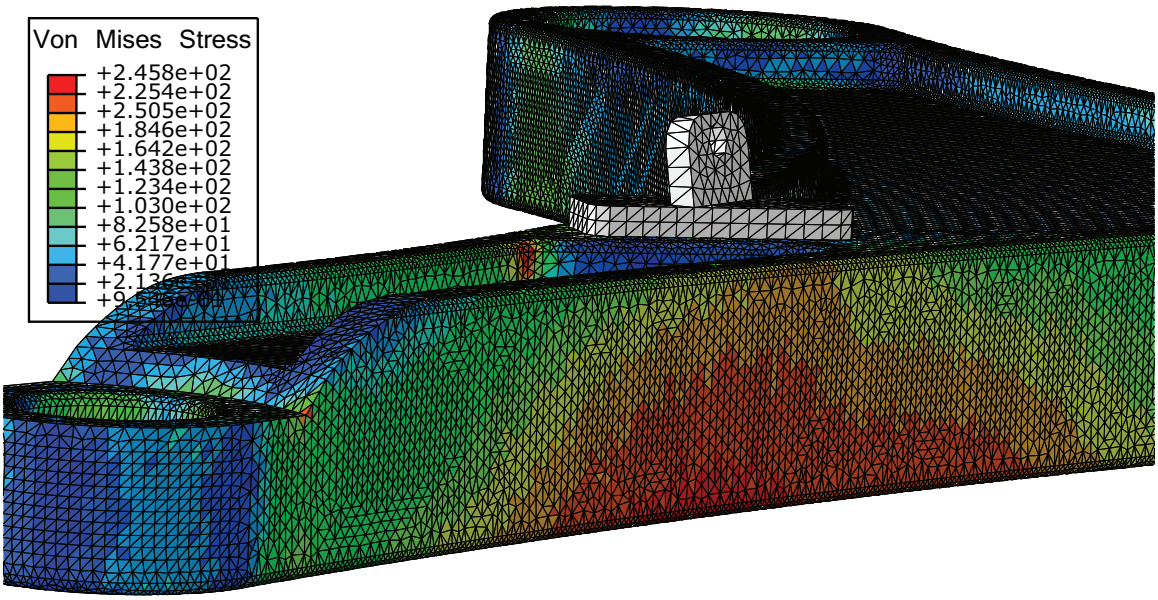

Figure 4.23: Level 7 Road (+,+,-) Case Aluminum Lower Arm: The contour plot of von Mises stress shows large stress are present near the bracket connection location.

Chapter 5

Conclusions and Recommendations

5.1 Conclusions

Following the procedures in the previous chapters, the performance of an injection moulded composite suspension lower arm was predicted through a static finite element analysis using different maximum load combinations that were obtained from three different random roads of increasing roughness (levels 5, 6 and 7). To better understand the results, the condition of each level of road roughness can be described as follows: a level 5 road can be treated as regular road surface for usual daily driving, but not one that would be suitable for a highway. A level 6 road will be a relatively bumpy road surface that could still be experienced for daily driving when the road condition is rough or in particularly bad maintenance status. A level 7 road will be an aggressive road surface that is not usually travelled during daily driving, such as some off-road style terrain. The objective of this whole process is to explore the possibility of replacing the conventional aluminum with injection moulded composite material in the suspension lower arm with the same geometry. Based on the simulation results from each road level, the following conclusions can be stated:

1. The overall performance for level 5 road shows that the replacement of conventional metal materials are not 100% reliable, even in this mild road condition. Some small failures and plastic deformations were shown in the bracket connection location. Some redesigned bracket connection method and an appropriate injection location selection would be needed to ensure no failure or plastic behaviour occurred in a level 5 road.

2. With the level 6 road, some large failure and plastic deformations are detected. There is still no serious damage where the lower arm was completely broken. However, it is definitely not safe to use a composite lower arm under this kind of situation, because the damage evolution and the influence of plastic deformation on the lower arm is unknown. This indicates that there is potential to replace conventional metal materials with composite material in level 6 road conditions, but additional study and research is needed to fulfill this goal.

3. For the level 7 roads, the composite lower arm is completely broken in some cases. Comparing to the aluminum lower arm performance under the same load condition shows that the composite lower arm performance is still far away from requirements. Major changes on the geometry, improved composite material properties, or even a completely different manufacturing method are needed to make the lower arm much stronger.

4. According to the previous points, with currently available material properties, using composite material on a lower suspension arm without dramatic geometry change results in a component that is only suitable for mild road condition and lower speed situation.

5. Based on the density of aluminum alloy 6061 T6 (2.7 g/cm^3) and the selected composite material (1.36 g/cm^3) in this research, the approximate weight reduction obtained from switching materials is approximately 49.6%. This indicates the possibility of potential strength improvements with composite materials. After a redesign of the composite lower arm geometry to meet the strength requirements, the final product could still conceivably result in weight reductions compared to the aluminum lower arm.

6. The most critical cases that challenge the strength of the composite lower arm happen during high speed driving under aggressive road conditions. The road condition appears to be more important than the driving manoeuvre in assessing the load severity. The performance is borderline acceptable under regular driving scenarios such as braking, accelerating, and cornering, on mild road conditions.

7. The location of the injection point has a quantifiable but not dramatic effect on the lower arm strength. This point may be more important in components where the directions of the external loads do not show as much change when in operation as in the suspension lower arm. This will be further discussed below.

8. Attaching brackets or other similar external components poses a challenge if the bracket is a metal or other dissimilar material with high stiffness properties, due to potential local stress concentrations.

9. The procedure of the simulation in this research has established a method for numerical performance prediction of composite material replacements. With this procedure, the strength of the target component can be estimated without manufacturing the actual part. Only testing specimens are needed.

5.2 Limitations

As described above, these conclusions are based on the establishment of multiple numerical models. There are some assumptions and limitations for each kind of simulation model. First, the thrust of the research is exploring and designing a methodology of replacing the conventional metal material with a proposed composite material in general load bearing suspension component.

During this process, no specific lower arm geometry, car model, composite material properties, or bushing properties are targeted. Every parameter or property needed in the modelling process was chosen from a sample or from the literature. The objective was to build the models applicable in the general case. The final strength prediction depends on the accuracy of each model.

For the multibody dynamics model, even though a wide range of driving scenarios have been included in the tests, there are still many situations not covered in these cases. The summarized maximum force combinations from each level of road are limited to these proposed situations. Additionally, the force summary process assumes that the maximum magnitude value of the lower ball joint force in each octant could sufficiently represent the maximum force case from the whole time history of force results. This might not be true in certain circumstances. Also, due to the method of 3D random road generation, the road roughness will be in the correct level according to the ISO standard road roughness classification. However, for each randomly generated 3D road surface, it might not cover all the possible situations, precisely because the road data are randomly generated. A failure or non-failure situation that is obtained in the final FEA simulation only represents a general situation for that particular road surface.

For the injection moulding process simulation, there are many processing parameters used with the software suggested values, including the heating temperature, moulding pressure, initial fibre orientation status at the injection inlet, the cooling process parameters, etc. The influence of these parameters to the final fibre orientation prediction could be notable. However, these impacts will be treated as beyond the scope of this research and won't be explored and discussed. These default values are assumed to be acceptable in the final fibre orientation prediction. The final fibre length and breakable prediction is not considered during the simulation. The residual strain and warping during the cooling process are also not considered in the fibre orientation mapping process. Even though the mapped fibre orientation that was used in the FEA model was confirmed according the physical tensile test in the literature, the accuracy of the composite material properties in finite element model are still at the numerical level. No actual injection moulded lower arm was available for physical testing to validate the results.

For the finite element model, the mesh size influence on the simulation results was avoided as much as possible through the meshing sensitivity study. However, it is always possible to use a more refined mesh size in order to increase the accuracy of the simulation results if a more powerful computer is available. Only a static analysis was conducted in the final strength prediction. This assumes the dynamic force effect was small compared to the individual applied forces. In general, the strength under static load is a major concern when designing a part or component. However, considering the nature of a suspension component, it always suffers cyclic forces due to travel of the suspension. Fatigue strength is another important factor that needs to be considered during the design, especially for composite materials. One of the shortfalls in this research is that the fatigue analysis is not considered. Due to the fact that the composite lower arm was not strong enough even under static load for level 6 and level 7 road cases, a fatigue analysis would not be

meaningful. However, this should be the major concern if one was to redesign the composite lower arm to fulfill the strength requirements.

To simplify the model, several simplified boundary conditions are implemented in the model. The connector elements and coupling motion constraints are used for both bushing connecting point and ball joint connecting point to mimic the behaviours of actual solid part connection. This is usually sufficient when the model response is in linear range or only small failures occur. When the model carries a severe external load, the inner hole surface elements start to fail, which might not happen in the real case, especially in the pulling direction. Also, the surface tie constraint used between the bracket and the lower arm does not fully represent the actual connection between two parts. These settings are assumed to not have significant influence the overall strength prediction. For more accurate damage evaluation, better boundary condition settings are needed.

5.3 Design Recommendation

The purpose of this research was to establish and explore a systematized methodology of replacing metal materials with lightweight materials in a load bearing component by using multiple numerical simulations. The procedure and the simulation process that are introduced in the dissertation will be a useful reference in any future study of a similar topic. According to the generating process of each type of simulation and the final strength prediction, the following recommendations can be summarized:

5.3.1 Consistency Between Models

Three powerful software tools are used for generating each simulation model to fulfill final strength prediction. However, deeper understanding of each single parameter setting in the software is key to forming a successful numerical model for any particular research. The other important matter is the consistency between the different types of simulations (Dynamics simulation, Injection moulding, Finite element analysis). This is key to building the connections between all numerical models and to make the final strength prediction meaningful. The connection from the dynamic simulation to the stress analysis is the force outputs. Each connection joint on the lower arm will contribute forces to the FEA model. Special care is needed to make sure the forces are recorded in a reference coordinate system that is in the same direction as the FEA model. Considering that the finite element model will be running with static analysis, the local reference frame attached to the lower arm body must be chosen for the force outputs on ball joint. Similarly, the force and moment outputs on the bracket connection point also need to be in the local reference frame. The corresponding applied external forces in the FEA model need to be set in the correct direction according to the output directions in the dynamics model. Also, the bushing properties need to be matched in both the dynamics model and the FEA model. The connection between the manufacturing simulation and finite element model will be the mesh size suitability. Both simulations will use the finite element method to obtain the analysis results. Of course, all the geometry

must be same in the two models, but the mesh size must also be at a similar level. This will make sure the transfer of the fibre orientation data is as close as possible to the situations shown in the manufacturing simulation results.

5.3.2 Injection Location Selection

According to the performance prediction of each injection location in the FEA model, the following points can be stated. These statements are based on the limit of testing of only four general injection locations.

1. Changing the injection location does not have such a significant effect that it is likely to prevent failures from happening under severe load.
2. However, different injection locations do influence the strength in the local area of the lower arm. Better performance is shown in the area close to the injection point.
3. In most of the cases, the force direction in lower arm will be in the xy-plane, so the injection locations are better located at or close to the point that makes the injection flow follow the main shape of the arm without too many diversions.
4. Generally, the injection location should be close the location where the failure is predicted, in order to have better fibre alignment and to the increase the local area strength.

5.3.3 Potential Geometry Changes

Initial plastic deformations were predicted with locations on or near the fillet curves. This is due to the stress concentrations that are usually present in these locations. The same situation occurs in the conventional metal lower arm, but there is another related factor that influences composite materials. Traditional part design often uses wider cross sections near the periphery of planar parts to maximize the cross-section area moment of inertia properties, in order to maximize resistance to bending. These changes in section thickness can complicate the local flow in a way that results in misaligned fibres near the change in section thickness. These misaligned fibres may serve to reduce the overall strength of the part, precisely in the area where the strength is needed. The changes in section thickness may need have more generous fillets than in a metal part to help smooth the flow into the thicker sections.

Severe failures were mainly shown at the anti-roll bar bracket and the front bushing connection area. Better treatments and designs are required on these locations to achieve better performance. For a composite lower arm, some kind of softer isolation material could be placed between the bracket and arm connection. This will decrease the impact of the bracket direct contact on the composite lower arm body.

The weakest portion of this particular composite lower arm is located at the front bushing side. Instead of making the whole arm thicker, a thicker and bigger cross-section area for the front

bushing ring and connecting neck are the preferred changes to try. The second preferable location for geometry change would be near the ball joint connection. According to the current results, failures were rarely shown in the rear bushing side, so the geometry of this portion could keep the original shape.

5.4 Future works

From the limitations of this research, there are several tasks that can be done in the future to make the performance prediction more reliable:

- More systematic driving scenario selections that will cover more critical cases in different levels of random road roughness. This ensures the strength analysis end up with more confidence results.
- If suitable equipment is available, manufacture an actual composite lower arm using an injection moulding process and validate the fibre orientation prediction results. This reduces the possibility of an inaccurate material model leading to overestimating the performance.
- Testing the actual rubber material in the targeted bushing joint to define a more accurate hyperelastic material model for a better representation of the bushing behaviour in the FEA model.
- Consider the fatigue strength analysis in the FEA model.
- Explore the possibility of more accurate damage evolution prediction to better represent the failure status under severe load.
- Redesign the geometry of lower arm to meet the strength requirements and explore the resulting weight savings, and any other potential improvements that can be achieved.

References

[1] P. Brady and M. Brady. "Automotive composites: which way are we going?" In: *Reinforced Plastics* 51.10 (2007), pp. 32–35. DOI: 10.1016/S0034-3617(07)70349-1.

[2] M. S. Sarfraz, H. Hong, and S. S. Kim. "Recent developments in the manufacturing technologies of composite components and their cost-effectiveness in the automotive industry: A review study". In: *Composite Structures* 266 (June 2021), p. 113864. DOI: 10.1016/j.compstruct.2021.113864.

[3] S. Das. *The Cost of Automotive Polymer Composites: A Review and Assessment of DOE's Lightweight Materials Composites Research*. DOI: 10.2172/777656.

[4] R. Stewart. "Rebounding automotive industry welcome news for FRP". In: *Reinforced Plastics* 55.1 (Jan. 2011), pp. 38–44. DOI: 10.1016/s0034-3617(11)70036-4.

[5] A. A. Shabana. *Computational dynamics*. John Wiley & Sons, 2009.

[6] M. J. Owen, V. Middleton, and I. A. Jones. *Integrated design and manufacture using fibre-reinforced polymeric composites*. Woodhead Publishing, 2000.

[7] P. Mallick. *Fiber-reinforced composites: materials, manufacturing, and design*. CRC press, 2007.

[8] S. G. Advani and C. L. Tucker III. "The Use of Tensors to Describe and Predict Fiber Orientation in Short Fiber Composites". In: *Journal of Rheology* 31.8 (Nov. 1987), pp. 751–784. DOI: 10.1122/1.549945.

[9] O. C. Zienkiewicz, R. L. Taylor, and J. Zhu. *The Finite Element Method: Its Basis and Fundamentals*. Butterworth-Heinemann, 2005. ISBN: 0750663200. URL: https://www.amazon.com/Finite-Element-Method-Basis-Fundamentals/dp/0750663200?SubscriptionId=AKIAIOBINVZYXZQZ2U3A&tag=chimbori05-20&linkCode=xm2&camp=2025&creative=165953&creativeASIN=0750663200.

[10] E. Mahdi, O. Alkoles, A. Hamouda, B. Sahari, R. Yonus, and G. Goudah. "Light composite elliptic springs for vehicle suspension". In: *Composite Structures* 75.1 (2006). Thirteenth International Conference on Composite Structures, pp. 24–28. ISSN: 0263-8223. DOI: https://doi.org/10.1016/j.compstruct.2006.04.082. URL: https://www.sciencedirect.com/science/article/pii/S0263822306001139.

[11] D. Scuccimarra. "Vehicle lightening with composite materials: Objective performance comparison of material-systems for structural applications". MA thesis. University of Windsor, 2012.

[12] M. Doody. "Design and development of a composite automotive anti-roll bar". MA thesis. University of Windsor, 2013.

[13] H. N. Honickman. "Development of hybrid composite co-pultruded structural members". PhD thesis. University of Windsor, 2013.

[14] D. Kim, D. Choi, and H. Kim. "Design optimization of a carbon fiber reinforced composite automotive lower arm". In: *Composites Part B: Engineering* 58 (Mar. 2014), pp. 400–407. DOI: 10.1016/j.compositesb.2013.10.067.

[15] Q. Liu, Y. Lin, Z. Zong, G. Sun, and Q. Li. "Lightweight design of carbon twill weave fabric composite body structure for electric vehicle". In: *Composite Structures* 97 (2013), pp. 231–238. ISSN: 0263-8223. DOI: https://doi.org/10.1016/j.compstruct.2012.09.052. URL: https://www.sciencedirect.com/science/article/pii/S0263822312005119.

[16] G. R. Chavhan and L. N. Wankhade. "Experimental analysis of E-glass fiber/epoxy composite material leaf spring used in automotive". In: *Materials Today: Proceedings* 26 (2020). 10th International Conference of Materials Processing and Characterization, pp. 373–377. ISSN: 2214-7853. DOI: https://doi.org/10.1016/j.matpr.2019.12.058. URL: https://www.sciencedirect.com/science/article/pii/S2214785319340696.

[17] P. Anandakumar, M. V. Timmaraju, and R. Velmurugan. "Development of efficient short-/continuous fiber thermoplastic composite automobile suspension upper control arm". In: *Materials Today: Proceedings* 39 (2021). 2nd International Conference on Recent Trends in Metallurgy, Materials Science and Manufacturing, pp. 1187–1191. ISSN: 2214-7853. DOI: https://doi.org/10.1016/j.matpr.2020.03.543. URL: https://www.sciencedirect.com/science/article/pii/S2214785320323245.

[18] G. J. Heydinger, R. A. Bixel, W. R. Garrott, M. Pyne, J. G. Howe, and D. A. Guenther. *Measured Vehicle Inertial Parameters-NHTSA's Data Through November 1998*. DOI: 10.4271/1999-01-1336.

[19] *MF-Tyre/MF-Swift 6.2 Help Manual*. TNO. 2013.

[20] B. Minaker. *Fundamentals of Vehicle Dynamics and Modelling: A Textbook for Engineers With Illustrations and Examples*. Automotive Series. Wiley, 2019. ISBN: 9781118980095. URL: https://books.google.ca/books?id=a4rKsgEACAAJ.

[21] M. Agostinacchio, D. Ciampa, and S. Olita. "The vibrations induced by surface irregularities in road pavements – a Matlab® approach". In: *European Transport Research Review* 6.3 (Dec. 2013), pp. 267–275. DOI: 10.1007/s12544-013-0127-8.

[22] M. Yeh and L. Lin. "Evaluating the Control Variable of Economic Growth by Using Extenics Theoretical Analysis". In: *Journal of Testing and Evaluation* 44.5 (Oct. 2015), p. 20140493. DOI: 10.1520/jte20140493.

[23] *OpenCRG® User Manual*. VIRES Simulationstechnologie GmbH. June 2017.

[24] A. Botzer, O. Musicant, and Y. Mama. "Relationship between hazard-perception-test scores and proportion of hard-braking events during on-road driving – An investigation using a range of thresholds for hard-braking". In: *Accident Analysis & Prevention* 132 (Nov. 2019), p. 105267. DOI: 10.1016/j.aap.2019.105267.

[25] P. Bosetti, M. D. Lio, and A. Saroldi. "On the human control of vehicles: an experimental study of acceleration". In: *European Transport Research Review* 6.2 (Sept. 2013), pp. 157–170. DOI: 10.1007/s12544-013-0120-2.

[26] J. Fu and Y. Ma. "A method to predict early-ejected plastic part air-cooling behavior towards quality mold design and less molding cycle time". In: *Robotics and Computer-Integrated Manufacturing* 56 (2019), pp. 66–74. ISSN: 0736-5845. DOI: https://doi.org/10.1016/j.rcim.2018.08.004. URL: https://www.sciencedirect.com/science/article/pii/S0736584517300868.

[27] L. T. Sin, W. Rahman, A. Rahmat, T. Tee, S. T. Bee, and L. Chong-Yu. "Computer aided injection moulding process analysis of polyvinyl alcohol–starch green biodegradable polymer compound". In: *Journal of Manufacturing Processes* 14.1 (2012), pp. 8–19. ISSN: 1526-6125. DOI: https://doi.org/10.1016/j.jmapro.2011.06.001. URL: https://www.sciencedirect.com/science/article/pii/S1526612511000132.

[28] F. Szabó, A. Suplicz, and J. G. Kovács. "Development of injection molding simulation algorithms that take into account segregation". In: *Powder Technology* 389 (2021), pp. 368–375. ISSN: 0032-5910. DOI: https://doi.org/10.1016/j.powtec.2021.05.053. URL: https://www.sciencedirect.com/science/article/pii/S0032591021004605.

[29] G. B. Jeffery and L. N. G. Filon. "The motion of ellipsoidal particles immersed in a viscous fluid". In: *Proceedings of the Royal Society of London. Series A, Containing Papers of a Mathematical and Physical Character* 102.715 (1922), pp. 161–179. DOI: 10.1098/rspa.1922.0078. eprint: https://royalsocietypublishing.org/doi/pdf/10.1098/rspa.1922.0078. URL: https://royalsocietypublishing.org/doi/abs/10.1098/rspa.1922.0078.

[30] F. Folgar and C. L. Tucker III. "Orientation Behavior of Fibers in Concentrated Suspensions". In: *Journal of Reinforced Plastics and Composites* 3.2 (1984), pp. 98–119. DOI: 10.1177/073168448400300201. eprint: https://doi.org/10.1177/073168448400300201. URL: https://doi.org/10.1177/073168448400300201.

[31] R. S. Bay. "Fiber orientation in injection-molded composites: a comparison of theory and experiment". PhD thesis. University of Illinois at Urbana-Champaign, 1991, p. 233. URL: https://www.proquest.com/dissertations-theses/fiber-orientation-injection-molded-composites/docview/303941981/se-2?accountid=14789.

[32] N. Phan-Thien, X. Fan, R. Tanner, and R. Zheng. "Folgar–Tucker constant for a fibre suspension in a Newtonian fluid". In: *Journal of Non-Newtonian Fluid Mechanics* 103.2 (2002), pp. 251–260. ISSN: 0377-0257. DOI: https://doi.org/10.1016/S0377-0257(02)00006-X. URL: https://www.sciencedirect.com/science/article/pii/S037702570200006X.

[33] J. Wang, J. F. O'Gara, and C. L. Tucker III. "An objective model for slow orientation kinetics in concentrated fiber suspensions: Theory and rheological evidence". In: *Journal of Rheology* 52.5 (2008), pp. 1179–1200. DOI: 10.1122/1.2946437. URL: https://doi.org/10.1122/1.2946437.

[34] J. Wang. "Improved fiber orientation predictions for injection molded composites". English. Copyright - Database copyright ProQuest LLC; ProQuest does not claim copyright in the

individual underlying works; Last updated - 2020-12-03. PhD thesis. 2007, p. 145. ISBN: 978-0-549-46362-7. URL: https://www.proquest.com/dissertations-theses/improved-fiber-orientation-predictions-injection/docview/304858233/se-2?accountid=14789.

[35] J. Wang, B. Nguyen, R. Mathur, B. Sharma, M. Sangid, F. Costa, X. Jin, C. L. Tucker III, and L. Fifield. "Fiber Orientation in Injection Molded Long Carbon Fiber Thermoplastic Composites". In: Mar. 2015.

[36] A. J. Favaloro and C. L. Tucker III. "Analysis of anisotropic rotary diffusion models for fiber orientation". In: *Composites Part A: Applied Science and Manufacturing* 126 (2019), p. 105605. ISSN: 1359-835X. DOI: https://doi.org/10.1016/j.compositesa.2019.105605. URL: https://www.sciencedirect.com/science/article/pii/S1359835X19303549.

[37] J. H. Phelps and C. L. Tucker III. "An anisotropic rotary diffusion model for fiber orientation in short- and long-fiber thermoplastics". In: *Journal of Non-Newtonian Fluid Mechanics* 156.3 (Feb. 2009), pp. 165–176. DOI: 10.1016/j.jnnfm.2008.08.002.

[38] A. Bakharev, H. Yu, S. Ray, R. Speight, and J. Wang. "Using new anisotropic rotational diffusion model to improve prediction of short fibers in thermoplastic injection molding". In: *Proceedings of the Society of Plastics Engineers (SPE) Annual Technical Conference (ANTEC), Orlando, FL, USA*. 2018, pp. 7–10.

[39] G. L. Hand. "A theory of anisotropic fluids". In: *Journal of Fluid Mechanics* 13.1 (1962), pp. 33–46. DOI: 10.1017/S0022112062000476.

[40] E. J. Hinch and L. G. Leal. "Constitutive equations in suspension mechanics. Part 2. Approximate forms for a suspension of rigid particles affected by Brownian rotations". In: *Journal of Fluid Mechanics* 76.1 (1976), pp. 187–208. DOI: 10.1017/S0022112076003200.

[41] S. G. Advani and C. L. Tucker III. "Closure approximations for three-dimensional structure tensors". In: *Journal of Rheology* 34.3 (1990), pp. 367–386. DOI: 10.1122/1.550133. URL: https://doi.org/10.1122/1.550133.

[42] J. S. Cintra and C. L. Tucker III. "Orthotropic closure approximations for flow induced fiber orientation". In: *Journal of Rheology* 39.6 (1995), pp. 1095–1122. DOI: 10.1122/1.550630. URL: https://doi.org/10.1122/1.550630.

[43] B. E. VerWeyst. "Numerical predictions of flow induced fiber orientation in three dimensional geometries". English. Copyright - Database copyright ProQuest LLC; ProQuest does not claim copyright in the individual underlying works; Last updated - 2021-04-02. PhD thesis. 1998, p. 230. ISBN: 978-0-599-10728-1. URL: https://www.proquest.com/dissertations-theses/numerical-predictions-flow-induced-fiber/docview/304440327/se-2?accountid=14789.

[44] *Fiber orientation prediction theory references*. Autodesk® Knowledge Network. 2019. URL: https://help.autodesk.com/view/MFIA/2019/ENU/?guid=GUID-BD0CFAC8-D8A9-42E7-8838-7DD2E67829B1.

[45] P. H. Holmström, O. S. Hopperstad, and A. H. Clausen. "Anisotropic tensile behaviour of short glass fibre reinforced polyamide-6". In: *Composites Part C: Open Access* 2 (2020), pp. 10–

0019. ISSN: 2666-6820. DOI: https://doi.org/10.1016/j.jcomc.2020.100019. URL: https://www.sciencedirect.com/science/article/pii/S2666682020300190.

[46] *Moldflow's fiber orientation models*. Autodesk® Knowledge Network. 2019. URL: https://help.autodesk.com/view/MFIA/2019/ENU/?guid=GUID-6B3A7386-DE57-450E-BF94-B10BD629EC9B.

[47] C. W. Camacho, C. L. Tucker III, S. Yalvaç, and R. L. McGee. "Stiffness and thermal expansion predictions for hybrid short fiber composites". In: *Polymer Composites* 11.4 (1990), pp. 229–239. DOI: https://doi.org/10.1002/pc.750110406. eprint: https://onlinelibrary.wiley.com/doi/pdf/10.1002/pc.750110406. URL: https://onlinelibrary.wiley.com/doi/abs/10.1002/pc.750110406.

[48] Y. Benveniste. "A new approach to the application of Mori-Tanaka's theory in composite materials". In: *Mechanics of Materials* 6 (1987), pp. 147–157.

[49] *Theory Manual*. Autodesk® Knowledge Network. 2019. URL: https://help.autodesk.com/view/ACMPAN/2016/ENU/?guid=GUID-D60A05C0-DD63-47B6-B1CD-248F2BDF1A9D.

[50] F. Meraghni and M. Benzeggagh. "Micromechanical modelling of matrix degradation in randomly oriented discontinuous-fibre composites". In: *Composites Science and Technology* 55.2 (1995), pp. 171–186. ISSN: 0266-3538. DOI: https://doi.org/10.1016/0266-3538(95)00096-8. URL: https://www.sciencedirect.com/science/article/pii/0266353895000968.

[51] B. N. Nguyen, S. K. Bapanapalli, V. Kunc, J. H. Phelps, and C. L. Tucker III. "Prediction of the Elastic Plastic Stress/Strain Response for Injection Molded Long Fiber Thermoplastics". In: *Journal of Composite Materials* 43.3 (Dec. 2008), pp. 217–246. DOI: 10.1177/0021998308099219.

[52] W. Ramberg and W. R. Osgood. "Description of stress-strain curves by three parameters". In: (1943).

[53] M. Smith. "ABAQUS 6.14 Online Documentation". In: *Dassault Systemes* (2014).

[54] J. E. Adkins and A. N. Gent. "Load-deflexion relations of rubber bush mountings". In: *British Journal of Applied Physics* 5.10 (Oct. 1954), pp. 354–358. DOI: 10.1088/0508-3443/5/10/305.

[55] K. Hofstetter, C. Grohs, J. Eberhardsteiner, and H. Mang. "Sliding behaviour of simplified tire tread patterns investigated by means of FEM". In: *Computers & Structures* 84.17-18 (June 2006), pp. 1151–1163. DOI: 10.1016/j.compstruc.2006.01.010.

[56] O. H. Yeoh. "Some Forms of the Strain Energy Function for Rubber". In: *Rubber Chemistry and Technology* 66 (1993), pp. 754–771.

[57] M. Bäker. "How to get meaningful and correct results from your finite element model". In: *ArXiv* abs/1811.05753 (2018).

Appendix A

Code List

A.1 2D Random Road Generation

random_road.m

```
function [x,z1]=random_road(varargin)

class=3;
L=100; % max wavelength [m], also equals road length
B=0.1; % shortest wavelength [m]

switch(nargin)
  case 1
    class=varargin{1};
  case 2
    class=varargin{1};
    L=varargin{2};
  case 3
    class=varargin{1};
    L=varargin{2};
    B=varargin{3};
end

% class is an integer from 3 - 9, where class=3 is an A-B road (smooth), class=9 is G-
    H road (rough)

if(class<3)
  class=3;
  disp('Warning: class out of range, resetting to minimum value (3)');
end

if(class>9)
  class=9;
  disp('Warning: class out of range, resetting to maximum value (9)');
end

N=L/B; % number of frequencies
```

```
deltan=1/L; % spatial frequency interval

n=(deltan:deltan:N*deltan); % frequency span

phi1=rand(1,N)*2*pi; % random phase lag for each frequency
% phi2=rand(1,N)*2*pi; % random phase lag for each frequency

a=sqrt(deltan)*(2^class)*1e-3*(0.1./n); % amplitude of each frequency, based on psd
    content

x=(0:B/10:L)'; % road coordinate
% y=(0:B/10:3)';

z1=zeros(length(x),1); % road vertical

for i=1:length(n) % sum for each frequency included
  z1=z1+a(i)*cos(2*pi*n(i)*x+phi1(i));
end

end %% Leave
```

A.2 3D Random Road Generation

random_3D_road_surface.m

```
function [data,x,z1,y,z2]=random_3D_road_surface(varargin)

level=6; %random road level
L=30; %longitudinal length [m]
W=30; %lateral length [m]
B=0.1; %shortest wavelength [m]

switch(nargin)
  case 1
    level=varargin{1};
  case 2
    level=varargin{1};
    L=varargin{2};
  case 3
    level=varargin{1};
    L=varargin{2};
    W=varargin{3};
  case 4
    level=varargin{1};
    L=varargin{2};
    W=varargin{3};
    B=varargin{4};
end

close all;

filename = sprintf('3D_random_road_surface_level%d.crg',level); %output crg file name

[x,z1]=random_road(level,L,B);
[y,z2]=random_road(level,W,B); %create two 2D random road

data = struct;

for i=1:length(z1)
  for j=1:length(z2)          %combine two Z value
    data.z(i,j)=z1(i)+z2(j); %form elevation matrix
  end
end

%data.p=zeros(1,L*(1/(B/10)));              %
%for i=1:length(data.p)                     %
% data.p(i)=(x(i)-45)/30;                   %
% if data.p(i)<0                            %
%   data.p(i)=0;                            % define heading angle
% end                                       %
```

```
% if data.p(i)>pi                          %
%   data.p(i)=-((2*pi)-data.p(i));         %
% end                                      %
%end                                       %

data.u=L; %define rfline longitudinal parameter
%data.head.xbeg=-L/2; %define the rfline start position in local xyz coordinate
data.v=[-10 20]; %define rfline lateral parameter

data=crg_check(crg_single(data)); %check data

data.head.zbeg=-data.z(1,1);
data.head.zend=-data.z(1,1); %make out of range road elevation equal zero

if isfield(data, 'ok') %check if the data is correct
  data.ct{1} = 'create random road surface';%write the comment at beginning
  crg_write(data, filename); %generate 3D random road file
  %crg_show(crg); %visualize road
  %crg=crg_show_road_surface(crg); %visualize road
else
  error('check of DATA was not completely successful') %if the data is not correct,
      return error
end

end
```

A.3 CRG road xy to z evaluation

crg_eval_xy2z.m

```
function [pz, data] = crg_eval_xy2z(data, pxy)
%CRG__EVAL_XY2Z CRG evaluate z at position xy.
%   [PZ, DATA] = CRG_EVAL_XY2Z(DATA, PXY) evaluates z at grid positions
%   given in xy coordinate system. This function combines the calls of
%   CRG_EVAL_XY2UV and CRG_EVAL_UV2Z.
%
%   inputs:
%       DATA    struct array as defined in CRG_INTRO.
%       PXY     (np, 2) array of points in xy system
%
%   outputs:
%       PZ      (np) vector of z values
%       DATA    struct array as defined in CRG_INTRO, with history added
%
%   Examples:
%   [pz, data] = crg_eval_xy2z(data, pxy) evaluates z at grid positions
%   given in xy coordinate system.
%
%   See also CRG_EVAL_XY2UV, CRG_EVAL_UV2Z, CRG_INTRO.

%   Copyright 2005-2008 OpenCRG - Daimler AG - Jochen Rauh
%
%   Licensed under the Apache License, Version 2.0 (the "License");
%   you may not use this file except in compliance with the License.
%   You may obtain a copy of the License at
%
%       http://www.apache.org/licenses/LICENSE-2.0
%
%   Unless required by applicable law or agreed to in writing, software
%   distributed under the License is distributed on an "AS IS" BASIS,
%   WITHOUT WARRANTIES OR CONDITIONS OF ANY KIND, either express or implied.
%   See the License for the specific language governing permissions and
%   limitations under the License.
%
%   More Information on OpenCRG open file formats and tools can be found at
%
%       http://www.opencrg.org
%
%   $Id: crg_eval_xy2z.m 184 2010-09-22 07:41:39Z jorauh $
%% just do it
[puv, data] = crg_eval_xy2uv(data, pxy);
[pz , data] = crg_eval_uv2z (data, puv);
end
```

crg_eval_xy2uv.m

```
function [puv, data] = crg_eval_xy2uv(data, pxy)
%CRG_EVAL_XY2UV CRG tranform point in xy to uv.
%   [PUV, DATA] = CRG_EVAL_XY2UV(DATA, PXY) transforms points given in
%   xy coordinate system to uv coordinate system. IF available, history of
%   a previous evaluations is used to start the search approprieately.
%
%   inputs:
%       DATA    struct array as defined in CRG_INTRO.
%       PXY     (np, 2) array of points in xy system
%
%   outputs:
%       PUV     (np, 2) array of points in uv system
%       DATA    struct array as defined in CRG_INTRO, with history added
%
%   Examples:
%   [puv, data] = crg_eval_xy2uv(data, pxy) transforms pxy points to puv
%   History information is updated in data on return from function.
%   [puv, data] = crg_eval_xy2uv(data, pxy) transforms pxy points to puv
%   History information is updated in data on return from function.
%
%   See also CRG_INTRO.

%   Copyright 2005-2009 OpenCRG - Daimler AG - Jochen Rauh
%
%   Licensed under the Apache License, Version 2.0 (the "License");
%   you may not use this file except in compliance with the License.
%   You may obtain a copy of the License at
%
%       http://www.apache.org/licenses/LICENSE-2.0
%
%   Unless required by applicable law or agreed to in writing, software
%   distributed under the License is distributed on an "AS IS" BASIS,
%   WITHOUT WARRANTIES OR CONDITIONS OF ANY KIND, either express or implied.
%   See the License for the specific language governing permissions and
%   limitations under the License.
%
%   More Information on OpenCRG open file formats and tools can be found at
%
%       http://www.opencrg.org
%
%   $Id: crg_eval_xy2uv.m 184 2010-09-22 07:41:39Z jorauh $

%% check if already succesfully checked

if ~isfield(data, 'ok')
  data = crg_check(data);
  if ~isfield(data, 'ok')
```

```
48      error('CRG:checkError', 'check of DATA was not completely successful')
49    end
50  end
51
52  %% pre-allocate output
53
54  np = size(pxy, 1);
55  puv = zeros(np, 2);
56
57  %% simplify data access 1
58
59  px = pxy(:, 1);
60  py = pxy(:, 2);
61
62  ubeg = data.head.ubeg;
63
64  xbeg = data.head.xbeg;
65  ybeg = data.head.ybeg;
66
67  pbec = data.dved.pbec;
68  pbes = data.dved.pbes;
69
70  %% straight reference line: simple transformation only
71
72  if ~isfield(data, 'rx')
73    dx = px - xbeg;
74    dy = py - ybeg;
75
76    puv(:, 1) = ubeg + pbec*dx + pbes*dy;
77    puv(:, 2) =      - pbes*dx + pbec*dy;
78
79    return
80  end
81
82  %% simplify data access
83
84  uend = data.head.uend;
85  uinc = data.head.uinc;
86
87  xend = data.head.xend;
88  yend = data.head.yend;
89
90  penc = data.dved.penc;
91  pens = data.dved.pens;
92
93  rx = data.rx;
94  ry = data.ry;
95  nu = length(rx);
```

```
96
97  %%  use history
98
99  mhisto = data.hist.m;
100 ohisto = data.hist.o;
101 chisto = data.hist.c;
102 fhisto = data.hist.f;
103 nhisto = data.hist.n;
104 ihisto = data.hist.i;
105 xhisto = data.hist.x;
106 yhisto = data.hist.y;
107
108 %TODO: preload/reset history with reference point, with special function, etc.
109 switch ohisto
110   case -1 % forget history, restart search from beginning
111     ohisto = 0;
112     nhisto = 1;
113     ihisto(1) = 1;
114     xhisto(1) = rx(1);
115     yhisto(1) = ry(1);
116   case -2 % forget history, restart search from end
117     ohisto = 0;
118     nhisto = 1;
119     ihisto(1) = nu;
120     xhisto(1) = rx(nu);
121     yhisto(1) = ry(nu);
122 end
123
124 iu = 0;
125 if ohisto > 0
126   if nhisto > 0
127     error('CRG:evalError', 'mixing of history seach and explicit history point no. not
          allowed')
128   end
129   if ohisto > mhisto
130     error('CRG:evalError', 'history size of %d insufficient to store history point no
          .=%d', mhisto, ohisto)
131   end
132   if ihisto(ohisto) > 0
133     jhisto = ohisto;
134     iu = ihisto(ohisto);
135   end
136 end
137
138 if iu == 0
139   % look for search start interval in history
140   dclose = realmax;
141   iclose = 0;
```

```
142   % TODO: search might be formulated more efficiently in MATLAB
143   % using vector operations instead of loops
144   for i = 1:nhisto
145     hd = (pxy(1,1)-xhisto(i))^2 + (pxy(1,2)-yhisto(i))^2;
146     if hd < chisto
147       % first choice: closer than CHISTO to history points
148       % (fast)
149       dclose = hd;
150       iclose = i;
151       break;
152     end
153     if hd < dclose
154       % second choice: find closest point in history
155       % (still fairly fast)
156       dclose = hd;
157       iclose = i;
158     end
159   end
160
161   if dclose < fhisto
162     % we got a useful history point
163     jhisto = iclose;
164     iu = ihisto(iclose);
165   else
166     % best history point too far away, global search necessary
167     dclose = realmax;
168     iclose = 0;
169     for i = 1:round(nu/1000):nu
170       hd = (pxy(1,1)-rx(i))^2 +  (pxy(1,2)-ry(i))^2;
171       if hd < dclose
172         dclose = hd;
173         iclose = i;
174       end
175     end
176     jhisto = nhisto + 1;
177     iu = iclose + 1;
178   end
179 end
180
181 iu = min(max(2, iu), nu-1);
182
183 %% work on all points
184
185 % FIXME: watch for multiple points too far away - only for the first point
186 % of each call a history search/update is done.
187
188 for ip = 1:np
189
```

```
% TODO: look if interval number IU could be made more close to what is
% expected by reading the theory doc.

% search for relevant reference line interval iu
%  looking at some points
%  P0: iu0 = iu - 2: (X0, Y0)
%  P1: iu1 = iu - 1: (X1, Y1)
%  P2: iu2 = iu    : (X2, Y2)
%  P3: iu3 = iu + 1: (X3, Y3)
%  P :               (X , Y ) (current input from function call)
x = px(ip);
y = py(ip);

forward search

t_hd = 0; % check uend/ubeg closer to (x,y) than ubeg/uend

while 1
  ium1 =     iu - 1     ;
  iup1 = min(iu + 1, nu);

  x1 = rx(ium1);
  y1 = ry(ium1);
  x2 = rx(iu  );
  y2 = ry(iu  );
  x3 = rx(iup1);
  y3 = ry(iup1);

  % evaluate dot product (P -P2).(P3-P1):
  % - unnormalized projection of (P -P2) on (P3-P1)
  % - hd is negative for P "left"  of normal on P3-P1 through P2
  % - hd is positive for P "right" of normal on P3-P1 through P2
  hdf = (x -x2)*(x3-x1) + (y -y2)*(y3-y1);

  % look if P belongs to current interval iu:
  %  update interval upwards as long as necessary/possible
  %  to make hd negative
  if hdf > 0
    if iu < nu
      iu = iu + 1;
    elseif data.dved.ulex~=0

      t_hd = (x-rx(1))*(rx(2)-rx(1)) + (y-ry(1))*(ry(2)-ry(1));

      if t_hd <= 0, break; end % ubeg may be closer
      iu = 2;
    else
      break
```

```
    end
  else
    break
  end
end

backward search

while 1
  ium2 = max(1, iu-2);
  ium1 =        iu-1 ;

  x0 = rx(ium2);
  y0 = ry(ium2);
  x1 = rx(ium1);
  y1 = ry(ium1);
  x2 = rx(iu  );
  y2 = ry(iu  );

  % evaluate dot product (P -P1).(P2- P0)
  % - unnormalized projection of (P -P1) on (P2-P0)
  % - hd is negative for P "left"  of normal on P2-P0 through P1
  % - hd is positive for P "right" of normal on P2-P0 through P1
  xxx1 = x -x1;
  x2x0 = x2-x0;
  yyy1 = y -y1;
  y2y0 = y2-y0;
  hdb = xxx1*x2x0 + yyy1*y2y0;

  % look if P belongs to current interval:
  %  update interval downwards as long as necessary/possible
  %  to make hd positive
  if hdb < 0
    if iu > 2
      iu = iu - 1;
    elseif data.dved.ulex~=0

      if t_hd~=0, break; end % uend already checked

      t_hd = (x-rx(nu))*(rx(nu)-rx(nu-1))+(y-ry(nu))*(ry(nu)-ry(nu-1));
      if t_hd >= 0, break; end % uend may be closer

      iu = nu;
    else
      break
    end
  else
    break
```

```
286     end
287   end
288
289   at this point we have got the right interval
290
291   if ip == 1 % store interval of first PXY for history
292     iuhist = iu;
293   end
294
295   evaluate result
296
297   if hdb < 0 % extrapolation beyond ubeg: simple transformation
298     dx = x - xbeg;
299     dy = y - ybeg;
300
301     puv(ip, 1) = ubeg + pbec*dx + pbes*dy;
302     puv(ip, 2) =      - pbes*dx + pbec*dy;
303
304     if data.opts.rflc && data.dved.ulex~=0
305       if puv(ip,1) < data.dved.ubex || ...
306           (puv(ip,1) > data.head.uend && puv(ip,1) < data.dved.uenx)
307         dx = x - xend;
308         dy = y - yend;
309
310         puv(ip, 1) = uend + penc*dx + pens*dy;
311         puv(ip, 2) =      - pens*dx + penc*dy;
312       end
313     end
314
315     continue
316   end
317
318   if hdf > 0 % extrapolation beyond uend: simple transformation
319     dx = x - xend;
320     dy = y - yend;
321
322     puv(ip, 1) = uend + penc*dx + pens*dy;
323     puv(ip, 2) =      - pens*dx + penc*dy;
324
325     if data.opts.rflc && data.dved.ulex~=0
326       if puv(ip,1) > data.dved.uenx
327
328         dx = x - xbeg;
329         dy = y - ybeg;
330
331         puv(ip, 1) = ubeg + pbec*dx + pbes*dy;
332         puv(ip, 2) =      - pbes*dx + pbec*dy;
333       end
```

```
334     end
335
336     continue
337   end
338
339   % evaluate v as distance between P and line trough P2-P1
340   % by calculating the normalized cross product
341   % (P2-P1)x(P-P1) / |P2-P1|
342   x2x1 = x2-x1;
343   y2y1 = y2-y1;
344   %
345   v = (x2x1*yyy1-y2y1*xxx1)/sqrt(x2x1^2+y2y1^2);
346
347   % TODO: here we could check distance related to curvature:
348   %  warn  if not closer than max/min curvature
349   %  abort if not closer than current curvature
350
351   % now we need a line parallel to P2-P1 through P,
352   % cut this line with the normal on P2-P0 through P1 in A
353   % cut this line with the normal on P3-P1 through P2 in B
354   % evaluate
355   %  du = |P-A|/|B-A|*|P2-P1|
356   % which is (after some vector calculus) identical to
357   %  du = ta/(ta+tb) * |P2-P1| with
358   %  ta = ((P2-P0).(P -P1))/((P2-P0).(P2-P1))
359   %  tb = ((P3-P1).(P2-P ))/((P3-P1).(P2-P1))
360   iup1 = min(iu+1, nu);
361
362   x3 = rx(iup1);
363   y3 = ry(iup1);
364
365   x3x1 = x3-x1;
366   y3y1 = y3-y1;
367
368   x2xx = x2-x;
369   y2yy = y2-y;
370
371   %ta= (x2x0*xxx1+y2y0*yyy1)/(x2x0*x2x1+y2y0*y2y1)
372   ta = hdb                   /(x2x0*x2x1+y2y0*y2y1);
373   tb = (x3x1*x2xx+y3y1*y2yy)/(x3x1*x2x1+y3y1*y2y1);
374
375   puv(ip, 1) = ubeg + (iu-2 + ta/(ta+tb))*uinc;
376   puv(ip, 2) = v;
377
378 end
379
380 %% update history
381
```

```
% save point in history, use result of pxy(1, :) search
if ohisto > 0
  % save current point
  ihisto(ohisto  ) = iuhist;
  xhisto(ohisto  ) = pxy(1            , 1);
  yhisto(ohisto  ) = pxy(1            , 2);
else
  jhisto = min(jhisto, mhisto);
  nhisto = max(jhisto, nhisto);
  % shift history
  ihisto(2:jhisto) = ihisto(1:jhisto-1);
  xhisto(2:jhisto) = xhisto(1:jhisto-1);
  yhisto(2:jhisto) = yhisto(1:jhisto-1);
  % insert current point
  ihisto(1       ) = iuhist;
  xhisto(1       ) = pxy(1            , 1);
  yhisto(1       ) = pxy(1            , 2);
end

%% save history in DATA

data.hist.o = ohisto;
data.hist.n = nhisto;
data.hist.i = ihisto;
data.hist.x = xhisto;
data.hist.y = yhisto;

end
```

crg_eval_uv2z.m

```
function [pz, data] = crg_eval_uv2z(data, puv)
%CRG_EVAL_UV2Z CRG evaluate  z at grid position uv.
%   [PZ, DATA] = CRG_EVAL_UV2Z(DATA, PUV) evaluates z at grid positions
%   given in uv coordinate system.
%
%   Inputs:
%       DATA    struct array as defined in CRG_INTRO.
%       PUV     (np, 2) array of points in uv system
%
%   Outputs:
%       PZ      (np) vector of z values
%       DATA    struct array as defined in CRG_INTRO.
%
%   Examples:
%   pz = crg_eval_uv2z(data, puv) evaluates z at grid positions given by
%   puv points in uv coordinate system.
%
%   See also CRG_INTRO.

%   Copyright 2005-2011 OpenCRG - Daimler AG - Jochen Rauh
%
%   Licensed under the Apache License, Version 2.0 (the "License");
%   you may not use this file except in compliance with the License.
%   You may obtain a copy of the License at
%
%       http://www.apache.org/licenses/LICENSE-2.0
%
%   Unless required by applicable law or agreed to in writing, software
%   distributed under the License is distributed on an "AS IS" BASIS,
%   WITHOUT WARRANTIES OR CONDITIONS OF ANY KIND, either express or implied.
%   See the License for the specific language governing permissions and
%   limitations under the License.
%
%   More Information on OpenCRG open file formats and tools can be found at
%
%       http://www.opencrg.org
%
%   $Id: crg_eval_uv2z.m 216 2011-02-05 21:59:55Z jorauh $

%% check if already succesfully checked

if ~isfield(data, 'ok')
  data = crg_check(data);
  if ~isfield(data, 'ok')
    error('CRG:checkError', 'check of DATA was not completely successful')
  end
end
```

```
48
49 %% for closed refline: map u values to valid interval
50
51 if data.opts.rflc==1 && data.dved.ulex~=0
52   puv(:,1) = mod(puv(:,1)-data.dved.ubex, data.dved.ulex) + data.dved.ubex;
53 end
54
55 %% simplify data access
56
57 np = size(puv, 1);
58
59 bdmu = data.opts.bdmu;
60 bdmv = data.opts.bdmv;
61 bdou = data.opts.bdou;
62 bdov = data.opts.bdov;
63 bdss = data.opts.bdss;
64 bdse = data.opts.bdse;
65
66 ubeg = data.head.ubeg;
67 uend = data.head.uend;
68 uinc = data.head.uinc;
69 ulen = uend - ubeg;
70 ule2 = ulen * 2;
71
72 vmin = data.head.vmin;
73 vmax = data.head.vmax;
74 if isfield(data.head, 'vinc')
75   vinc = data.head.vinc;
76 else
77   vinc = 0;
78   v = data.v;
79 end
80 vwid = vmax - vmin;
81 vwi2 = vwid * 2;
82
83 zbeg = data.head.zbeg;
84 zend = data.head.zend;
85 sbeg = data.head.sbeg;
86 bbeg = data.head.bbeg;
87
88 z = data.z;
89 [nu nv] = size(z);
90 nvm1 = nv - 1;
91
92 if isfield(data, 'rz')
93   rz = data.rz;
94   nrz = length(rz);
95 else
```

```
  nrz = 0;
end

if isfield(data, 'b')
  b = data.b;
  nb = length(b);
else
  nb = 0;
end

%% pre-allocate output

pz = zeros(np, 1);

%% work on all points

for ip = 1 : np
  pui = puv(ip, 1);
  pvi = puv(ip, 2);

  % repeat/reflect border mode maps u value into [ubeg uend] interval
  switch bdmu % border_mode_u
    case 3 % repeat
      pui = mod(pui-ubeg, ulen) + ubeg;
    case 4 % reflect
      pui = mod(pui-ubeg, ule2);
      if pui > ulen, pui = ule2 - pui; end
      pui = pui + ubeg;
  end

  % repeat/reflect border mode maps v value into [vmin vmax] interval
  switch bdmv % border_mode_v
    case 3 % repeat
      pvi = mod(pvi-vmin, vwid) + vmin;
    case 4 % reflect
      pvi = mod(pvi-vmin, vwi2);
      if pvi > vwid, pvi = vwi2 - pvi; end
      pvi = pvi + vmin;
  end

  % find u interval in constantly spaced u axis
  ui = (pui - ubeg) / uinc;
  iu = min(max(0, floor(ui)), nu-2); % find u interval
  du = ui-iu;
  ui = min(max(0, du), 1); % limit to [0 1] border interval
  iu = iu + 1; % MATLAB counts from 1

  if vinc ~= 0
```

```
144     % find v interval in constanty spaced v axis
145     vi = (pvi - vmin) / vinc;
146     iv = min(max(0, floor(vi)), nv-2); % find v interval
147     dv = vi-iv;
148     vi = min(max(0, dv), 1); % limit to [0 1] border interval
149     iv = iv + 1; % MATLAB counts from 1
150   else
151     % find v interval in variably spaced v axis
152     i0 = nvm1;
153     iv = 0;
154     while 1
155       im = floor((iv+i0)/2);
156       if im > iv
157         if pvi <  v(im+1)
158           i0 = im;
159         else
160           iv = im;
161         end
162       else
163         break
164       end
165     end
166     iv = iv + 1; % MATLAB counts from 1
167     dv = (pvi-v(iv))/(v(iv+1)-v(iv));
168     vi = min(max(0, dv), 1);
169   end
170
171   % evaluate z(u, v) by bilinear interpolation
172   z00 = double(z(iu  , iv  ));
173   z10 = double(z(iu+1, iv  )) - z00;
174   z01 = double(z(iu  , iv+1));
175   z11 = double(z(iu+1, iv+1)) - (z10 + z01);
176   z01 = z01 - z00;
177   piz = (z11*vi + z10)*ui + z01*vi + z00;
178
179   % add slope
180   if nrz > 0
181     piz = piz + rz(iu) + ui*(rz(iu+1)-rz(iu));
182   else
183     piz = piz + zbeg + (min(max(ubeg, pui), uend)-ubeg)*sbeg;
184   end
185
186   % add banking
187   if nb > 1
188     pib = b(iu) + ui*(b(iu+1)-b(iu));
189   else
190     pib = bbeg;
191   end
```

```
192   piz = piz + min(max(vmin, pvi), vmax)*pib;
193
194   % extrapolating border mode in u direction
195   if ui ~= du % ui was limited to [0 1] border interval
196     switch bdmu % border_mode_u
197       case 1 % set zero
198         piz = bdou;
199       case 2 % keep last
200         piz = piz + bdou;
201     end
202   end
203
204   % extrapolating border mode in v direction
205   if vi ~= dv % vi was limited to [0 1] border interval
206     switch bdmv % border_mode_v
207       case 1 % set zero
208         piz = bdov;
209       case 2 % keep last
210         piz = piz + bdov;
211     end
212   end
213
214   % smoothing zone at start
215   urel = max(0, pui-ubeg);
216   if bdss>urel % inside smooting zone
217     piz = urel/bdss*(piz-zbeg) + zbeg;
218   end
219
220   % smoothing zone at end
221   urel = max(0, uend-pui);
222   if bdse>urel % inside smooting zone
223     piz = urel/bdse*(piz-zend) + zend;
224   end
225
226   if (bdmu==0 && ui~=du) || (bdmv==0 && vi~=dv) % NaN border mode and ui or vi was
          outside [0 1] border interval
227     pz(ip) = NaN;
228   else
229     pz(ip) = piz;
230   end
231 end
232
233 end
```

A.4 PSD Curve Plotting

PSD_single.m

```
% compute the psd of the random road
% should be a straight line in log space, down to wl_min
sf=1/0.005;     % sampling frequency
N1=length(pz)-1;    % number of samples % pz is the contact patch location data in z
    axis
xdft1=fft(pz);% fast Fourier transform
xdft1=xdft1(1:N1/2+1);     % take only half results (symmetric)
psdx1=(1/(sf*N1))*abs(xdft1).^2;   % compute power
psdx1(2:end-1)=2*psdx1(2:end-1);   % other half
freq1=(0:sf/N1:sf/2)';% compute frequencies
loglog(freq1,psdx1)     %plot the curve in log-log space
xlabel('Freq [cycles/m]')
ylabel('Power/Frequency [m^2*m/cycle]')
psdplot=[freq1 psdx1];
dlmwrite('PSD_circle.txt',psdplot) %write output file for pgfplot
```

A.5 Lower Control Arm Ball Joint Force Summary 1

pick_max_force.m

```
filePattern = fullfile('./', '*.csv');
files = dir(filePattern);
for i=1:length(files)

  F = importdata(files(i).name);
  numdata=length(F)/6;
  t=F(1:numdata,1);
  F = F(:,2);
  xyz=zeros(numdata,6);

  for j=1:6
    xyz(:,j)=F(((j-1)*numdata)+1:j*numdata,1);
  end

  xyz= [xyz(:,1) -xyz(:,2) xyz(:,3) xyz(:,4) xyz(:,5) xyz(:,6)];

  ppplt=[0 0 0];
  pppl=[0 0 0];
  npplt=[0 0 0];
  nppl=[0 0 0];
  pnplt=[0 0 0];
  pnpl=[0 0 0];
  ppnlt=[0 0 0];
  ppnl=[0 0 0];
  nnplt=[0 0 0];
```

```
nnpl=[0 0 0];
npnlt=[0 0 0];
npnl=[0 0 0];
pnnlt=[0 0 0];
pnnl=[0 0 0];
nnnlt=[0 0 0];
nnnl=[0 0 0];

ppprt=[0 0 0];
pppr=[0 0 0];
npprt=[0 0 0];
nppr=[0 0 0];
pnprt=[0 0 0];
pnpr=[0 0 0];
ppnrt=[0 0 0];
ppnr=[0 0 0];
nnprt=[0 0 0];
nnpr=[0 0 0];
npnrt=[0 0 0];
npnr=[0 0 0];
pnnrt=[0 0 0];
pnnr=[0 0 0];
nnnrt=[0 0 0];
nnnr=[0 0 0];

for k=1:length(xyz)
  if xyz(k,1) > 0 && xyz(k,2)>0 && xyz(k,3)>0
    if k > 1
      if ppplt(1) == 0 && ppplt(2) == 0 && ppplt(3) == 0
        ppplt= [xyz(k,1) xyz(k,2) xyz(k,3)];
      else
        ppplt= [ppplt;xyz(k,1) xyz(k,2) xyz(k,3)];
      end
      if xyz(k,1)^2+xyz(k,2)^2+xyz(k,3)^2 > pppl(1)^2+pppl(2)^2+pppl(3)^2
        pppl=[xyz(k,1) xyz(k,2) xyz(k,3)];
        tpppl=t(k);
      end
    else
      pppl=[xyz(k,1) xyz(k,2) xyz(k,3)];
      tpppl=t(k);
      ppplt= [xyz(k,1) xyz(k,2) xyz(k,3)];
    end
  elseif xyz(k,1) < 0 && xyz(k,2)>0 && xyz(k,3)>0
    if k > 1
      if npplt(1) == 0 && npplt(2) == 0 && npplt(3) == 0
        npplt= [xyz(k,1) xyz(k,2) xyz(k,3)];
      else
        npplt= [npplt;xyz(k,1) xyz(k,2) xyz(k,3)];
```

```
74          end
75          if xyz(k,1)^2+xyz(k,2)^2+xyz(k,3)^2 > nppl(1)^2+nppl(2)^2+nppl(3)^2
76            nppl=[xyz(k,1) xyz(k,2) xyz(k,3)];
77            tnppl=t(k);
78          end
79        else
80          nppl=[xyz(k,1) xyz(k,2) xyz(k,3)];
81          tnppl=t(k);
82          npplt= [xyz(k,1) xyz(k,2) xyz(k,3)];
83        end
84      elseif xyz(k,1) > 0 && xyz(k,2)<0 && xyz(k,3)>0
85        if k > 1
86          if pnplt(1) == 0 && pnplt(2) == 0 && pnplt(3) == 0
87            pnplt= [xyz(k,1) xyz(k,2) xyz(k,3)];
88          else
89            pnplt= [pnplt;xyz(k,1) xyz(k,2) xyz(k,3)];
90          end
91          if xyz(k,1)^2+xyz(k,2)^2+xyz(k,3)^2 > pnpl(1)^2+pnpl(2)^2+pnpl(3)^2
92            pnpl=[xyz(k,1) xyz(k,2) xyz(k,3)];
93            tpnpl=t(k);
94          end
95        else
96          pnpl=[xyz(k,1) xyz(k,2) xyz(k,3)];
97          tpnpl=t(k);
98          pnplt= [xyz(k,1) xyz(k,2) xyz(k,3)];
99        end
100     elseif xyz(k,1) > 0 && xyz(k,2)>0 && xyz(k,3)<0
101       if k > 1
102         if ppnlt(1) == 0 && ppnlt(2) == 0 && ppnlt(3) == 0
103           ppnlt= [xyz(k,1) xyz(k,2) xyz(k,3)];
104         else
105           ppnlt= [ppnlt;xyz(k,1) xyz(k,2) xyz(k,3)];
106         end
107         if xyz(k,1)^2+xyz(k,2)^2+xyz(k,3)^2 > ppnl(1)^2+ppnl(2)^2+ppnl(3)^2
108           ppnl=[xyz(k,1) xyz(k,2) xyz(k,3)];
109           tppnl=t(k);
110         end
111       else
112         ppnl=[xyz(k,1) xyz(k,2) xyz(k,3)];
113         tppnl=t(k);
114         ppnlt= [xyz(k,1) xyz(k,2) xyz(k,3)];
115       end
116     elseif xyz(k,1) < 0 && xyz(k,2)<0 && xyz(k,3)>0
117       if k > 1
118         if nnplt(1) == 0 && nnplt(2) == 0 && nnplt(3) == 0
119           nnplt= [xyz(k,1) xyz(k,2) xyz(k,3)];
120         else
121           nnplt= [nnplt;xyz(k,1) xyz(k,2) xyz(k,3)];
```

```
122         end
123         if xyz(k,1)^2+xyz(k,2)^2+xyz(k,3)^2 > nnpl(1)^2+nnpl(2)^2+nnpl(3)^2
124           nnpl=[xyz(k,1) xyz(k,2) xyz(k,3)];
125           tnnpl=t(k);
126         end
127       else
128         nnpl=[xyz(k,1) xyz(k,2) xyz(k,3)];
129         tnnpl=t(k);
130         nnplt= [xyz(k,1) xyz(k,2) xyz(k,3)];
131       end
132     elseif xyz(k,1) < 0 && xyz(k,2)>0 && xyz(k,3)<0
133       if k > 1
134         if npnlt(1) == 0 && npnlt(2) == 0 && npnlt(3) == 0
135           npnlt= [xyz(k,1) xyz(k,2) xyz(k,3)];
136         else
137           npnlt= [npnlt;xyz(k,1) xyz(k,2) xyz(k,3)];
138         end
139         if xyz(k,1)^2+xyz(k,2)^2+xyz(k,3)^2 > npnl(1)^2+npnl(2)^2+npnl(3)^2
140           npnl=[xyz(k,1) xyz(k,2) xyz(k,3)];
141           tnpnl=t(k);
142         end
143       else
144         npnl=[xyz(k,1) xyz(k,2) xyz(k,3)];
145         tnpnl=t(k);
146         npnlt= [xyz(k,1) xyz(k,2) xyz(k,3)];
147       end
148     elseif xyz(k,1) > 0 && xyz(k,2)<0 && xyz(k,3)<0
149       if k > 1
150         if pnnlt(1) == 0 && pnnlt(2) == 0 && pnnlt(3) == 0
151           pnnlt= [xyz(k,1) xyz(k,2) xyz(k,3)];
152         else
153           pnnlt= [pnnlt;xyz(k,1) xyz(k,2) xyz(k,3)];
154         end
155         if xyz(k,1)^2+xyz(k,2)^2+xyz(k,3)^2 > pnnl(1)^2+pnnl(2)^2+pnnl(3)^2
156           pnnl=[xyz(k,1) xyz(k,2) xyz(k,3)];
157           tpnnl=t(k);
158         end
159       else
160         pnnl=[xyz(k,1) xyz(k,2) xyz(k,3)];
161         tpnnl=t(k);
162         pnnlt= [xyz(k,1) xyz(k,2) xyz(k,3)];
163       end
164     elseif xyz(k,1) < 0 && xyz(k,2)<0 && xyz(k,3)<0
165       if k > 1
166         if nnnlt(1) == 0 && nnnlt(2) == 0 && nnnlt(3) == 0
167           nnnlt= [xyz(k,1) xyz(k,2) xyz(k,3)];
168         else
169           nnnlt= [nnnlt;xyz(k,1) xyz(k,2) xyz(k,3)];
```

```
170       end
171       if xyz(k,1)^2+xyz(k,2)^2+xyz(k,3)^2 > nnnl(1)^2+nnnl(2)^2+nnnl(3)^2
172         nnnl=[xyz(k,1) xyz(k,2) xyz(k,3)];
173         tnnnl=t(k);
174       end
175     else
176       nnnl=[xyz(k,1) xyz(k,2) xyz(k,3)];
177       tnnnl=t(k);
178       nnnlt= [xyz(k,1) xyz(k,2) xyz(k,3)];
179     end
180   end
181 end
182
183 for k=1:length(xyz)
184   if xyz(k,4) > 0 && xyz(k,5)>0 && xyz(k,6)>0
185     if k > 1
186       if ppprt(1) == 0 && ppprt(2) == 0 && ppprt(3) == 0
187         ppprt= [xyz(k,4) xyz(k,5) xyz(k,6)];
188       else
189         ppprt= [ppprt;xyz(k,4) xyz(k,5) xyz(k,6)];
190       end
191       if xyz(k,4)^2+xyz(k,5)^2+xyz(k,6)^2 > pppr(1)^2+pppr(2)^2+pppr(3)^2
192         pppr=[xyz(k,4) xyz(k,5) xyz(k,6)];
193         tpppr=t(k);
194       end
195     else
196       pppr=[xyz(k,4) xyz(k,5) xyz(k,6)];
197       tpppr=t(k);
198       ppprt= [xyz(k,4) xyz(k,5) xyz(k,6)];
199     end
200   elseif xyz(k,4) < 0 && xyz(k,5)>0 && xyz(k,6)>0
201     if k > 1
202       if npprt(1) == 0 && npprt(2) == 0 && npprt(3) == 0
203         npprt= [xyz(k,4) xyz(k,5) xyz(k,6)];
204       else
205         npprt= [npprt;xyz(k,4) xyz(k,5) xyz(k,6)];
206       end
207       if xyz(k,4)^2+xyz(k,5)^2+xyz(k,6)^2 > nppr(1)^2+nppr(2)^2+nppr(3)^2
208         nppr=[xyz(k,4) xyz(k,5) xyz(k,6)];
209         tnppr=t(k);
210       end
211     else
212       nppr=[xyz(k,4) xyz(k,5) xyz(k,6)];
213       tnppr=t(k);
214       npprt= [xyz(k,4) xyz(k,5) xyz(k,6)];
215     end
216   elseif xyz(k,4) > 0 && xyz(k,5)<0 && xyz(k,6)>0
217     if k > 1
```

```
218         if pnprt(1) == 0 && pnprt(2) == 0 && pnprt(3) == 0
219           pnprt= [xyz(k,4) xyz(k,5) xyz(k,6)];
220         else
221           pnprt= [pnprt;xyz(k,4) xyz(k,5) xyz(k,6)];
222         end
223         if xyz(k,4)^2+xyz(k,5)^2+xyz(k,6)^2 > pnpr(1)^2+pnpr(2)^2+pnpr(3)^2
224           pnpr=[xyz(k,4) xyz(k,5) xyz(k,6)];
225           tpnpr=t(k);
226         end
227       else
228         pnpr=[xyz(k,4) xyz(k,5) xyz(k,6)];
229         tpnpr=t(k);
230         pnprt= [xyz(k,4) xyz(k,5) xyz(k,6)];
231       end
232     elseif xyz(k,4) > 0 && xyz(k,5)>0 && xyz(k,6)<0
233       if k > 1
234         if ppnrt(1) == 0 && ppnrt(2) == 0 && ppnrt(3) == 0
235           ppnrt= [xyz(k,4) xyz(k,5) xyz(k,6)];
236         else
237           ppnrt= [ppnrt;xyz(k,4) xyz(k,5) xyz(k,6)];
238         end
239         if xyz(k,4)^2+xyz(k,5)^2+xyz(k,6)^2 > ppnr(1)^2+ppnr(2)^2+ppnr(3)^2
240           ppnr=[xyz(k,4) xyz(k,5) xyz(k,6)];
241           tppnr=t(k);
242         end
243       else
244         ppnr=[xyz(k,4) xyz(k,5) xyz(k,6)];
245         tppnr=t(k);
246         ppnrt= [xyz(k,4) xyz(k,5) xyz(k,6)];
247       end
248     elseif xyz(k,4) < 0 && xyz(k,5)<0 && xyz(k,6)>0
249       if k > 1
250         if nnprt(1) == 0 && nnprt(2) == 0 && nnprt(3) == 0
251           nnprt= [xyz(k,4) xyz(k,5) xyz(k,6)];
252         else
253           nnprt= [nnprt;xyz(k,4) xyz(k,5) xyz(k,6)];
254         end
255         if xyz(k,4)^2+xyz(k,5)^2+xyz(k,6)^2 > nnpr(1)^2+nnpr(2)^2+nnpr(3)^2
256           nnpr=[xyz(k,4) xyz(k,5) xyz(k,6)];
257           tnnpr=t(k);
258         end
259       else
260         nnpr=[xyz(k,4) xyz(k,5) xyz(k,6)];
261         tnnpr=t(k);
262         nnprt= [xyz(k,4) xyz(k,5) xyz(k,6)];
263       end
264     elseif xyz(k,4) < 0 && xyz(k,5)>0 && xyz(k,6)<0
265       if k > 1
```

```
266         if npnrt(1) == 0 && npnrt(2) == 0 && npnrt(3) == 0
267           npnrt= [xyz(k,4) xyz(k,5) xyz(k,6)];
268         else
269           npnrt= [npnrt;xyz(k,4) xyz(k,5) xyz(k,6)];
270         end
271         if xyz(k,4)^2+xyz(k,5)^2+xyz(k,6)^2 > npnr(1)^2+npnr(2)^2+npnr(3)^2
272           npnr=[xyz(k,4) xyz(k,5) xyz(k,6)];
273           tnpnr=t(k);
274         end
275       else
276         npnr=[xyz(k,4) xyz(k,5) xyz(k,6)];
277         tnpnr=t(k);
278         npnrt= [xyz(k,4) xyz(k,5) xyz(k,6)];
279       end
280     elseif xyz(k,4) > 0 && xyz(k,5)<0 && xyz(k,6)<0
281       if k > 1
282         if pnnrt(1) == 0 && pnnrt(2) == 0 && pnnrt(3) == 0
283           pnnrt= [xyz(k,4) xyz(k,5) xyz(k,6)];
284         else
285           pnnrt= [pnnrt;xyz(k,4) xyz(k,5) xyz(k,6)];
286         end
287         if xyz(k,4)^2+xyz(k,5)^2+xyz(k,6)^2 > pnnr(1)^2+pnnr(2)^2+pnnr(3)^2
288           pnnr=[xyz(k,4) xyz(k,5) xyz(k,6)];
289           tpnnr=t(k);
290         end
291       else
292         pnnr=[xyz(k,4) xyz(k,5) xyz(k,6)];
293         tpnnr=t(k);
294         pnnrt= [xyz(k,4) xyz(k,5) xyz(k,6)];
295       end
296     elseif xyz(k,4) < 0 && xyz(k,5)<0 && xyz(k,6)<0
297       if k > 1
298         if nnnrt(1) == 0 && nnnrt(2) == 0 && nnnrt(3) == 0
299           nnnrt= [xyz(k,4) xyz(k,5) xyz(k,6)];
300         else
301           nnnrt= [nnnrt;xyz(k,4) xyz(k,5) xyz(k,6)];
302         end
303         if xyz(k,4)^2+xyz(k,5)^2+xyz(k,6)^2 > nnnr(1)^2+nnnr(2)^2+nnnr(3)^2
304           nnnr=[xyz(k,4) xyz(k,5) xyz(k,6)];
305           tnnnr=t(k);
306         end
307       else
308         nnnr=[xyz(k,4) xyz(k,5) xyz(k,6)];
309         tnnnr=t(k);
310         nnnrt= [xyz(k,4) xyz(k,5) xyz(k,6)];
311       end
312     end
313   end
```

```
314
315 if pppl(1)^2+pppl(2)^2+pppl(3)^2 > pppr(1)^2+pppr(2)^2+pppr(3)^2
316   ppp=[pppl(1) pppl(2) pppl(3)];
317   tppp=tpppl;
318   pppside='Left';
319 else
320   ppp=pppr;
321   tppp=tpppr;
322   pppside='Right';
323 end
324
325 if ppnl(1)^2+ppnl(2)^2+ppnl(3)^2 > ppnr(1)^2+ppnr(2)^2+ppnr(3)^2
326   ppn=[ppnl(1) ppnl(2) ppnl(3)];
327   tppn=tppnl;
328   ppnside='Left';
329 else
330   ppn=ppnr;
331   tppn=tppnr;
332   ppnside='Right';
333 end
334
335 if pnpl(1)^2+pnpl(2)^2+pnpl(3)^2 > pnpr(1)^2+pnpr(2)^2+pnpr(3)^2
336   pnp=[pnpl(1) pnpl(2) pnpl(3)];
337   tpnp=tpnpl;
338   pnpside='Left';
339 else
340   pnp=pnpr;
341   tpnp=tpnpr;
342   pnpside='Right';
343 end
344
345 if pnnl(1)^2+pnnl(2)^2+pnnl(3)^2 > pnnr(1)^2+pnnr(2)^2+pnnr(3)^2
346   pnn=[pnnl(1) pnnl(2) pnnl(3)];
347   tpnn=tpnnl;
348   pnnside='Left';
349 else
350   pnn=pnnr;
351   tpnn=tpnnr;
352   pnnside='Right';
353 end
354
355 if nppl(1)^2+nppl(2)^2+nppl(3)^2 > nppr(1)^2+nppr(2)^2+nppr(3)^2
356   npp=[nppl(1) nppl(2) nppl(3)];
357   tnpp=tnppl;
358   nppside='Left';
359 else
360   npp=nppr;
361   tnpp=tnppr;
```

```
362     nppside='Right';
363   end
364
365   if npnl(1)^2+npnl(2)^2+npnl(3)^2 > npnr(1)^2+npnr(2)^2+npnr(3)^2
366     npn=[npnl(1) npnl(2) npnl(3)];
367     tnpn=tnpnl;
368     npnside='Left';
369   else
370     npn=npnr;
371     tnpn=tnpnr;
372     npnside='Right';
373   end
374
375   if nnpl(1)^2+nnpl(2)^2+nnpl(3)^2 > nnpr(1)^2+nnpr(2)^2+nnpr(3)^2
376     nnp=[nnpl(1) nnpl(2) nnpl(3)];
377     tnnp=tnnpl;
378     nnpside='Left';
379   else
380     nnp=nnpr;
381     tnnp=tnnpr;
382     nnpside='Right';
383   end
384
385   if nnnl(1)^2+nnnl(2)^2+nnnl(3)^2 > nnnr(1)^2+nnnr(2)^2+nnnr(3)^2
386     nnn=[nnnl(1) nnnl(2) nnnl(3)];
387     tnnn=tnnnl;
388     nnnside='Left';
389   else
390     nnn=nnnr;
391     tnnn=tnnnr;
392     nnnside='Right';
393   end
394
395   max=max(xyz);
396   max_l=[max(1) max(2) max(3)];
397   max_r=[max(4) max(5) max(6)];
398   min=min(xyz);
399   min_l=[min(1) min(2) min(3)];
400   min_r=[min(4) min(5) min(6)];
401
402   for l=1:length(xyz)
403     if xyz(l,1) == max_l(1)
404       max_x_l=[xyz(l,1) xyz(l,2) xyz(l,3)];
405       tmax_x_l=t(l);
406     end
407   end
408
409   for l=1:length(xyz)
```

```
410     if xyz(l,2) == max_l(2)
411       max_y_l=[xyz(l,1) xyz(l,2) xyz(l,3)];
412       tmax_y_l=t(l);
413     end
414   end
415
416   for l=1:length(xyz)
417     if xyz(l,3) == max_l(3)
418       max_z_l=[xyz(l,1) xyz(l,2) xyz(l,3)];
419       tmax_z_l=t(l);
420     end
421   end
422
423   for l=1:length(xyz)
424     if xyz(l,4) == max_r(1)
425       max_x_r=[xyz(l,4) xyz(l,5) xyz(l,6)];
426       tmax_x_r=t(l);
427     end
428   end
429
430   for l=1:length(xyz)
431     if xyz(l,5) == max_r(2)
432       max_y_r=[xyz(l,4) xyz(l,5) xyz(l,6)];
433       tmax_y_r=t(l);
434     end
435   end
436
437   for l=1:length(xyz)
438     if xyz(l,6) == max_r(3)
439       max_z_r=[xyz(l,4) xyz(l,5) xyz(l,6)];
440       tmax_z_r=t(l);
441     end
442   end
443
444   for l=1:length(xyz)
445     if xyz(l,1) == min_l(1)
446       min_x_l=[xyz(l,1) xyz(l,2) xyz(l,3)];
447       tmin_x_l=t(l);
448     end
449   end
450
451   for l=1:length(xyz)
452     if xyz(l,2) == min_l(2)
453       min_y_l=[xyz(l,1) xyz(l,2) xyz(l,3)];
454       tmin_y_l=t(l);
455     end
456   end
457
```

```
458  for l=1:length(xyz)
459    if xyz(l,3) == min_l(3)
460      min_z_l=[xyz(l,1) xyz(l,2) xyz(l,3)];
461      tmin_z_l=t(l);
462    end
463  end
464
465  for l=1:length(xyz)
466    if xyz(l,4) == min_r(1)
467      min_x_r=[xyz(l,4) xyz(l,5) xyz(l,6)];
468      tmin_x_r=t(l);
469    end
470  end
471
472  for l=1:length(xyz)
473    if xyz(l,5) == min_r(2)
474      min_y_r=[xyz(l,4) xyz(l,5) xyz(l,6)];
475      tmin_y_r=t(l);
476    end
477  end
478
479  for l=1:length(xyz)
480    if xyz(l,6) == min_r(3)
481      min_z_r=[xyz(l,4) xyz(l,5) xyz(l,6)];
482      tmin_z_r=t(l);
483    end
484  end
485
486  if max_x_l(1) > max_x_r(1)
487    max_x=max_x_l;
488    tmax_x=tmax_x_l;
489    max_xside='Left';
490  else
491    max_x=max_x_r;
492    tmax_x=tmax_x_r;
493    max_xside='Right';
494  end
495
496  if max_y_l(2) > max_y_r(2)
497    max_y=max_y_l;
498    tmax_y=tmax_y_l;
499    max_yside='Left';
500  else
501    max_y=max_y_r;
502    tmax_y=tmax_y_r;
503    max_yside='Right';
504  end
505
```

```
506  if max_z_l(3) > max_z_r(3)
507    max_z=max_z_l;
508    tmax_z=tmax_z_l;
509    max_zside='Left';
510  else
511    max_z=max_z_r;
512    tmax_z=tmax_z_r;
513    max_zside='Right';
514  end
515
516  if min_x_l(1) < min_x_r(1)
517    min_x=min_x_l;
518    tmin_x=tmin_x_l;
519    min_xside='Left';
520  else
521    min_x=min_x_r;
522    tmin_x=tmin_x_r;
523    min_xside='Right';
524  end
525
526  if min_y_l(2) < min_y_r(2)
527    min_y=min_y_l;
528    tmin_y=tmin_y_l;
529    min_yside='Left';
530  else
531    min_y=min_y_r;
532    tmin_y=tmin_y_r;
533    min_yside='Right';
534  end
535
536  if min_z_l(3) < min_z_r(3)
537    min_z=min_z_l;
538    tmin_z=tmin_z_l;
539    min_zside='Left';
540  else
541    min_z=min_z_r;
542    tmin_z=tmin_z_r;
543    min_zside='Right';
544  end
545
546  force=[ppp;nnn;npp;pnn;nnp;ppn;pnp;npn;max_x;max_y;max_z;min_x;min_y;min_z];
547  side={pppside;nnnside;nppside;pnnside;nnpside;ppnside;pnpside;npnside;max_xside;
         max_yside;max_zside;min_xside;min_yside;min_zside};
548  time=[tppp;tnnn;tnpp;tpnn;tnnp;tppn;tpnp;tnpn;tmax_x;tmax_y;tmax_z;tmin_x;tmin_y;
         tmin_z];
549  Description = {'{$(+,+,+)$}';'{$(-,-,-)$}';'{$(-,+,+)$}';'{$(+,-,-)$}';'{$(-,-,+)$}'
         ;'{$(+,+,-)$}';'{$(+,-,+)$}';'{$(-,+,-)$}';'maximum $+x$';'maximum $+y$';'
         maximum $+z$';'maximum $-x$';'maximum $-y$';'maximum $-z$'};
```

```
550
551   T = table(Description,side,time,force);
552   name=files(i).name;
553   Nchar=length(files(i).name)-4;
554   newname = [name(1:Nchar) '_force_summary.txt'];
555   newdataname = [name(1:Nchar) '_force_summary'];
556
557   writetable(T,newname)
558   save(newdataname)
559
560 end
```

A.6 Lower Control Arm Ball Joint Force Summary 2

abaqus_force.m

```
clc;
clear all;
filePattern = fullfile('./', '*.txt');
files = dir(filePattern);
v=zeros(7,15);

for i=1:length(files)
    fileID = fopen(files(i).name, 'r');
    [F,pos] = textscan(fileID,'%*12c %s %f %f %f %f','HeaderLines',1,'Delimiter',',');
    fclose(fileID);
    n=str2double(files(i).name(1));

    for j=1:length(F{3})+1
        if j==1
            v(i,j)=n;
        elseif j > 1 && j < 10
            v(i,j)=(F{1,3}(j-1))^2+(F{1,4}(j-1))^2+(F{1,5}(j-1))^2;
        elseif j == 10
            v(i,j)=F{1,3}(j-1);
        elseif j == 11
            v(i,j)=F{1,4}(j-1);
        elseif j == 12
            v(i,j)=F{1,5}(j-1);
        elseif j == 13
            v(i,j)=abs(F{1,3}(j-1));
        elseif j == 14
            v(i,j)=abs(F{1,4}(j-1));
        elseif j == 15
            v(i,j)=abs(F{1,5}(j-1));
        end
    end
end

[M,I]=max(v);
I=I(2:15);
x=zeros(14,1);
y=zeros(14,1);
z=zeros(14,1);
Sc=cell(14,1);
Description = {'{$(+,+,+)$}';'{$(-,-,-)$}';'{$(-,+,+)$}';'{$(+,-,-)$}';'{$(-,-,+)$}';'
    {$(+,+,-)$}';'{$(+,-,+)$}';'{$(-,+,-)$}';'maximum $+x$';'maximum $+y$';'maximum
    $+z$';'maximum $-x$';'maximum $-y$';'maximum $-z$'};
for k=1:length(I)
        fileID = fopen(files(I(k)).name, 'r');
```

```
43          [F,pos] = textscan(fileID,'%*12c %s %f %f %f %f','HeaderLines',1,'Delimiter',','
                ,');
44          fclose(fileID);
45          Sc{k}=files(I(k)).name(9:end-18);
46          x(k)=F{1,3}(k);
47          y(k)=F{1,4}(k);
48          z(k)=F{1,5}(k);
49  end
50
51  T = table(Description,Sc,x,y,z);
52  writetable(T,'level6_force.txt')
```

A.7 Python Script to Extract The Strain And Stress Data

10W20T.py

```
from abaqus import *
from abaqusConstants import *
import winsound

angle=['00','15','30','45','60','75','90']
# angle=['00','45','90']
for a in angle:
  odb = session.openOdb('specimen_final_10W20T_map_'+a+'.odb')
  path = odb.name
  main = 'TrueS_VS_TrueE_'
  case1 = path[52:58]+'_'
  case2 = path[63:65]+'_'
  case3 = 'MCT'
  case4 = ''
  name = main+case1+case2+case3+case4

  rst = open(name+'.txt', 'w')
  rst.write('Te'+a+case4+','+'Ts'+a+case4+'\n')

  TopNodeLabel = 195
  BottomNodeLabel = 388
  LeftNodeLabel = 420
  RightNodeLabel = 398
  DownNodeLabel = 409

  AllFrames = odb.steps[odb.steps.keys()[-1]].frames
  Part = odb.rootAssembly.instances['SPECIMEN_FINAL_MODIFY-1']
  TopNode = Part.getNodeFromLabel(TopNodeLabel)
  BottomNode = Part.getNodeFromLabel(BottomNodeLabel)
  LeftNode = Part.getNodeFromLabel(LeftNodeLabel)
  RightNode = Part.getNodeFromLabel(RightNodeLabel)
  DownNode = Part.getNodeFromLabel(DownNodeLabel)
  LoadNode = odb.rootAssembly.nodeSets['LOAD_NODE']

  for f1 in AllFrames:
    SDV1=f1.fieldOutputs['SDV1'].values
    Rupture=0
    for r in SDV1:
      if r.data == 2:
        Rupture =  1
    if Rupture == 0:
      RuptureFrame = f1.frameValue + 1

  for f in AllFrames:
    if f.frameValue < RuptureFrame:
```

```
46      U1Top = f.fieldOutputs['U'].getSubset(region=TopNode).values[0].data[0]
47      U1Bottom = f.fieldOutputs['U'].getSubset(region=BottomNode).values[0].data[0]
48      U2Left = f.fieldOutputs['U'].getSubset(region=LeftNode).values[0].data[1]
49      U2Right = f.fieldOutputs['U'].getSubset(region=RightNode).values[0].data[1]
50      U3Up = f.fieldOutputs['U'].getSubset(region=RightNode).values[0].data[2]
51      U3Down = f.fieldOutputs['U'].getSubset(region=DownNode).values[0].data[2]
52      RF = f.fieldOutputs['RF'].getSubset(region=LoadNode).values[0].data[0]
53      U1 = U1Top - U1Bottom
54      U2 = U2Left - U2Right
55      U3 = U3Up - U3Down
56      E = log(1 + (U1 / 15))
57      S = RF / (30 * (1 + (U2 / 10)) * (1 + (U3 / 3)))
58      rst.write('%(Strain)e, %(Stress)e\n' % {'Strain':E, 'Stress':S})
59
60  odb.close()
61  rst.close()
62 winsound.MessageBeep(winsound.MB_ICONEXCLAMATION)
```

Appendix B

Supplemental Tables

B.1 Tables for Force Summary Results

Table B.1: Maximum Forces of Constant Speed Cornering on Level 6 Road

Direction	Side	Time [s]	F_x [N]	F_y [N]	F_z [N]
$(+,+,+)$	Left	14.86	6.09×10^2	8.10×10^3	1.85×10^1
$(-,-,-)$	Right	19.9	-3.73×10^2	-6.88×10^3	-3.11×10^1
$(-,+,+)$	Left	12.17	-2.80×10^2	7.63×10^3	3.62×10^1
$(+,-,-)$	Right	11.29	4.64×10^1	-4.39×10^3	-8.38×10^1
$(-,-,+)$	Right	15.28	-3.99×10^3	-8.02×10^3	2.90×10^2
$(+,+,-)$	Left	12.97	1.08×10^2	1.04×10^4	-3.23×10^2
$(+,-,+)$	Right	19.01	2.12×10^2	-4.99×10^3	3.18×10^2
$(-,+,-)$	Left	12.96	-2.96×10^2	8.47×10^3	-4.22×10^2
maximum $+x$	Left	10.79	2.64×10^3	9.82×10^3	-2.61×10^2
maximum $+y$	Left	12.97	1.08×10^2	1.04×10^4	-3.23×10^2
maximum $+z$	Right	12.86	-1.90×10^3	-1.34×10^3	1.41×10^3
maximum $-x$	Left	14.64	-4.17×10^3	-2.97×10^3	-1.51×10^2
maximum $-y$	Right	14.64	-1.79×10^3	-8.12×10^3	2.15×10^2
maximum $-z$	Left	17.06	-1.27×10^2	6.18×10^2	-1.02×10^3

Table B.2: Maximum Forces of Straight Accelerating on Level 6 Road

Direction	Side	Time [s]	F_x [N]	F_y [N]	F_z [N]
$(+,+,+)$	Left	14.67	2.49×10^{1}	4.19×10^{3}	2.25×10^{2}
$(-,-,-)$	Left	10.62	-3.51×10^{3}	-8.06×10^{3}	-5.57×10^{1}
$(-,+,+)$	Right	11.93	-4.43×10^{3}	4.20×10^{3}	7.21×10^{1}
$(+,-,-)$	Right	11.61	3.91×10^{2}	-6.45×10^{3}	-1.64×10^{2}
$(-,-,+)$	Left	10.63	-3.03×10^{3}	-1.33×10^{4}	1.04×10^{2}
$(+,+,-)$	Right	5.8	9.65×10^{1}	2.22×10^{3}	-6.82×10^{1}
$(+,-,+)$	Right	19.01	0.00×10^{0}	0.00×10^{0}	0.00×10^{0}
$(-,+,-)$	Left	12.11	-2.77×10^{3}	8.86×10^{3}	-2.40×10^{2}
maximum $+x$	Right	14.54	6.95×10^{2}	4.75×10^{2}	7.79×10^{1}
maximum $+y$	Left	12.11	-2.77×10^{3}	8.86×10^{3}	-2.40×10^{2}
maximum $+z$	Right	11.84	-4.13×10^{3}	-1.19×10^{4}	4.60×10^{2}
maximum $-x$	Right	5.75	-6.67×10^{3}	-5.00×10^{3}	1.46×10^{2}
maximum $-y$	Left	10.63	-3.03×10^{3}	-1.33×10^{4}	1.04×10^{2}
maximum $-z$	Right	11.58	-1.06×10^{3}	8.63×10^{3}	-5.42×10^{2}

Table B.3: Maximum Forces of Straight Braking on Level 6 Road

Direction	Side	Time [s]	F_x [N]	F_y [N]	F_z [N]
$(+,+,+)$	Right	15.89	7.67×10^{3}	7.69×10^{3}	6.64×10^{0}
$(-,-,-)$	Right	13.29	-5.58×10^{3}	-3.58×10^{3}	-2.04×10^{1}
$(-,+,+)$	Left	13.52	-9.10×10^{2}	6.00×10^{3}	1.83×10^{2}
$(+,-,-)$	Left	16.18	3.85×10^{3}	-3.67×10^{2}	-6.76×10^{1}
$(-,-,+)$	Left	13.3	-6.19×10^{3}	-7.26×10^{3}	1.01×10^{2}
$(+,+,-)$	Left	16.52	8.45×10^{3}	8.30×10^{3}	-2.80×10^{1}
$(+,-,+)$	Left	17.01	2.75×10^{3}	-9.52×10^{2}	1.16×10^{2}
$(-,+,-)$	Right	12.8	-1.83×10^{2}	3.26×10^{3}	-5.18×10^{1}
maximum $+x$	Left	16.52	8.45×10^{3}	8.30×10^{3}	-2.80×10^{1}
maximum $+y$	Right	16.52	7.53×10^{3}	8.35×10^{3}	-5.77×10^{1}
maximum $+z$	Right	10.97	-2.51×10^{3}	-3.93×10^{2}	3.57×10^{2}
maximum $-x$	Right	13.35	-6.71×10^{3}	-3.59×10^{3}	1.50×10^{2}
maximum $-y$	Left	13.3	-6.19×10^{3}	-7.26×10^{3}	1.01×10^{2}
maximum $-z$	Right	13.68	-1.35×10^{2}	1.24×10^{3}	-3.58×10^{2}

Table B.4: Maximum Forces of Straight Constant Speed [60km/h] on Level 6 Road

Direction	Side	Time [s]	F_x [N]	F_y [N]	F_z [N]
$(+,+,+)$	Left	18.47	9.75×10^2	5.40×10^3	1.87×10^2
$(-,-,-)$	Left	9	-2.98×10^3	-1.96×10^3	-8.49×10^1
$(-,+,+)$	Right	11.98	-1.57×10^2	4.81×10^3	1.79×10^2
$(+,-,-)$	Left	11.68	8.28×10^2	-8.44×10^2	-1.66×10^2
$(-,-,+)$	Left	13.58	-3.65×10^3	-9.24×10^2	1.16×10^2
$(+,+,-)$	Left	15.02	6.03×10^2	3.02×10^3	-3.76×10^1
$(+,-,+)$	Right	16.8	0.00×10^0	0.00×10^0	0.00×10^0
$(-,+,-)$	Right	17.35	-3.00×10^2	3.35×10^3	-7.88×10^{-1}
maximum $+x$	Right	9.66	1.95×10^3	2.74×10^3	1.24×10^2
maximum $+y$	Left	18.47	9.75×10^2	5.40×10^3	1.87×10^2
maximum $+z$	Left	11.94	-3.33×10^3	1.36×10^3	2.77×10^2
maximum $-x$	Left	13.58	-3.65×10^3	-9.24×10^2	1.16×10^2
maximum $-y$	Left	9	-2.98×10^3	-1.96×10^3	-8.49×10^1
maximum $-z$	Right	11.66	-8.40×10^1	8.16×10^2	-3.71×10^2

Table B.5: Maximum Forces of Straight Constant Speed [80km/h] on Level 6 Road

Direction	Side	Time [s]	F_x [N]	F_y [N]	F_z [N]
$(+,+,+)$	Left	13.4	2.77×10^3	6.52×10^3	7.07×10^1
$(-,-,-)$	Right	13.29	-5.58×10^3	-3.58×10^3	-2.04×10^1
$(-,+,+)$	Left	13.52	-9.10×10^2	6.00×10^3	1.83×10^2
$(+,-,-)$	Left	13.12	2.25×10^2	-1.48×10^3	-1.93×10^2
$(-,-,+)$	Left	13.3	-6.19×10^3	-7.26×10^3	1.01×10^2
$(+,+,-)$	Right	16.76	5.40×10^1	3.91×10^3	-3.36×10^1
$(+,-,+)$	Right	12.12	7.56×10^2	-6.76×10^1	1.29×10^2
$(-,+,-)$	Right	15.24	-3.70×10^2	3.29×10^3	-5.02×10^1
maximum $+x$	Left	13.39	3.26×10^3	6.26×10^3	5.63×10^1
maximum $+y$	Left	13.4	2.77×10^3	6.52×10^3	7.07×10^1
maximum $+z$	Left	16.71	-3.39×10^3	2.44×10^3	3.69×10^2
maximum $-x$	Right	13.35	-6.71×10^3	-3.59×10^3	1.50×10^2
maximum $-y$	Left	13.3	-6.19×10^3	-7.26×10^3	1.01×10^2
maximum $-z$	Left	17.68	-1.83×10^2	1.21×10^3	-3.67×10^2

Table B.6: Maximum Forces of Straight Constant Speed [100km/h] on Level 6 Road

Direction	Side	Time [s]	F_x [N]	F_y [N]	F_z [N]
$(+,+,+)$	Left	17.6	6.46×10^{1}	4.99×10^{3}	2.48×10^{2}
$(-,-,-)$	Left	14.9	-3.06×10^{3}	-4.95×10^{3}	-2.50×10^{1}
$(-,+,+)$	Left	16.91	-2.82×10^{3}	7.55×10^{3}	3.01×10^{2}
$(+,-,-)$	Left	14.85	1.10×10^{2}	-1.54×10^{3}	-1.96×10^{2}
$(-,-,+)$	Right	13.35	-1.60×10^{3}	-1.49×10^{3}	7.30×10^{1}
$(+,+,-)$	Right	15.25	1.01×10^{2}	2.65×10^{3}	-2.04×10^{1}
$(+,-,+)$	Right	16.8	2.25×10^{2}	-1.52×10^{3}	2.08×10^{2}
$(-,+,-)$	Left	13.88	-4.03×10^{2}	3.32×10^{3}	-3.22×10^{1}
maximum $+x$	Left	16.36	1.15×10^{3}	3.75×10^{3}	1.50×10^{2}
maximum $+y$	Left	16.91	-2.82×10^{3}	7.55×10^{3}	3.01×10^{2}
maximum $+z$	Left	17.57	-4.03×10^{3}	4.33×10^{3}	4.41×10^{2}
maximum $-x$	Right	17.57	-4.16×10^{3}	4.17×10^{3}	4.13×10^{2}
maximum $-y$	Left	14.9	-3.06×10^{3}	-4.95×10^{3}	-2.50×10^{1}
maximum $-z$	Left	13.48	-4.37×10^{2}	2.34×10^{3}	-3.55×10^{2}

Table B.7: Maximum Forces of Constant Speed Cornering on Level 7 Road

Direction	Side	Time [s]	F_x [N]	F_y [N]	F_z [N]
$(+,+,+)$	Left	9.25	3.32×10^{3}	1.78×10^{4}	2.85×10^{2}
$(-,-,-)$	Right	12.54	-2.00×10^{2}	-9.61×10^{3}	-3.74×10^{2}
$(-,+,+)$	Right	10.72	-1.97×10^{2}	1.68×10^{4}	6.72×10^{2}
$(+,-,-)$	Right	16.78	4.47×10^{2}	-9.68×10^{3}	-1.79×10^{2}
$(-,-,+)$	Right	18.71	-9.69×10^{2}	-1.14×10^{4}	1.06×10^{3}
$(+,+,-)$	Left	9.27	3.53×10^{3}	1.57×10^{4}	-2.61×10^{2}
$(+,-,+)$	Right	17.07	1.08×10^{3}	-9.87×10^{3}	7.43×10^{2}
$(-,+,-)$	Left	13.92	-5.15×10^{1}	1.22×10^{4}	-3.73×10^{2}
maximum $+x$	Right	11.36	7.08×10^{3}	1.30×10^{4}	8.52×10^{2}
maximum $+y$	Left	9.25	3.32×10^{3}	1.78×10^{4}	2.85×10^{2}
maximum $+z$	Right	17.66	-1.16×10^{3}	1.88×10^{3}	1.66×10^{3}
maximum $-x$	Left	14.58	-6.88×10^{3}	4.02×10^{3}	6.64×10^{2}
maximum $-y$	Right	18.71	-9.69×10^{2}	-1.14×10^{4}	1.06×10^{3}
maximum $-z$	Left	13.23	5.35×10^{1}	-3.21×10^{2}	-1.37×10^{3}

Table B.8: Maximum Forces of Braking During Cornering on Level 7 Road

Direction	Side	Time [s]	F_x [N]	F_y [N]	F_z [N]
$(+,+,+)$	Right	8.66	9.47×10^3	1.50×10^4	4.31×10^2
$(-,-,-)$	Right	6.54	-1.70×10^3	-6.93×10^3	-1.10×10^1
$(-,+,+)$	Left	5.35	-3.71×10^2	1.35×10^4	4.08×10^1
$(+,-,-)$	Right	8.83	6.54×10^3	-5.36×10^2	-2.55×10^2
$(-,-,+)$	Right	5.84	-5.82×10^3	-9.68×10^3	4.04×10^2
$(+,+,-)$	Left	9.22	7.59×10^3	1.38×10^4	-9.38×10^1
$(+,-,+)$	Right	8.3	5.24×10^3	-6.02×10^3	4.00×10^2
$(-,+,-)$	Left	4.66	-3.61×10^2	7.85×10^3	-1.64×10^2
maximum $+x$	Right	8.66	9.47×10^3	1.50×10^4	4.31×10^2
maximum $+y$	Left	2.5	6.68×10^2	1.63×10^4	1.52×10^2
maximum $+z$	Right	5.88	-2.78×10^3	-4.94×10^3	1.18×10^3
maximum $-x$	Left	3.06	-6.39×10^3	-7.28×10^3	6.21×10^1
maximum $-y$	Right	5.84	-5.82×10^3	-9.68×10^3	4.04×10^2
maximum $-z$	Left	8.17	2.36×10^2	1.09×10^3	-1.11×10^3

Table B.9: Maximum Forces of Straight Accelerating on Level 7 Road

Direction	Side	Time [s]	F_x [N]	F_y [N]	F_z [N]
$(+,+,+)$	Left	14.01	8.17×10^2	1.21×10^3	2.73×10^2
$(-,-,-)$	Left	9.43	-3.94×10^3	-1.05×10^4	-6.22×10^1
$(-,+,+)$	Left	14.66	-5.74×10^3	1.64×10^4	5.31×10^2
$(+,-,-)$	Left	12.76	9.52×10^2	-1.08×10^4	-1.14×10^1
$(-,-,+)$	Right	13.72	-4.35×10^2	-4.34×10^4	1.38×10^3
$(+,+,-)$	Right	11.29	6.51×10^1	3.57×10^3	-1.94×10^2
$(+,-,+)$	Left	12.58	4.11×10^1	-1.37×10^4	8.15×10^2
$(-,+,-)$	Right	12.71	-4.48×10^3	2.71×10^4	-5.36×10^2
maximum $+x$	Right	13.74	1.05×10^3	-8.04×10^3	4.73×10^2
maximum $+y$	Right	12.71	-4.48×10^3	2.71×10^4	-5.36×10^2
maximum $+z$	Right	13.72	-4.35×10^2	-4.34×10^4	1.38×10^3
maximum $-x$	Left	14.67	-7.46×10^3	7.81×10^3	4.46×10^2
maximum $-y$	Right	13.72	-4.35×10^2	-4.34×10^4	1.38×10^3
maximum $-z$	Right	11.97	-1.48×10^3	1.22×10^4	-8.07×10^2

Table B.10: Maximum Forces of Straight Braking on Level 7 Road

Direction	Side	Time [s]	F_x [N]	F_y [N]	F_z [N]
$(+,+,+)$	Left	15.22	1.39×10^4	2.67×10^4	1.93×10^2
$(-,-,-)$	Right	13.52	-6.41×10^3	-3.31×10^3	-1.49×10^2
$(-,+,+)$	Right	11.96	-1.60×10^3	1.91×10^4	2.92×10^2
$(+,-,-)$	Right	17.51	6.79×10^3	-1.75×10^1	-6.08×10^2
$(-,-,+)$	Right	19.29	-5.25×10^2	-4.33×10^3	2.54×10^2
$(+,+,-)$	Left	15.24	1.28×10^4	2.40×10^4	-1.71×10^2
$(+,-,+)$	Left	14.54	2.16×10^3	-4.32×10^3	2.77×10^1
$(-,+,-)$	Right	12.62	-8.83×10^2	9.79×10^3	-3.33×10^1
maximum $+x$	Right	15.22	1.56×10^4	2.34×10^4	8.18×10^2
maximum $+y$	Left	15.22	1.39×10^4	2.67×10^4	1.93×10^2
maximum $+z$	Right	16.77	8.57×10^3	4.27×10^3	1.20×10^3
maximum $-x$	Left	11.99	-6.44×10^3	1.69×10^3	3.04×10^2
maximum $-y$	Right	14.53	2.47×10^3	-4.55×10^3	-1.45×10^1
maximum $-z$	Left	17.38	3.50×10^3	1.05×10^3	-1.19×10^3

Table B.11: Maximum Forces of Straight Constant Speed [60km/h] on Level 7 Road

Direction	Side	Time [s]	F_x [N]	F_y [N]	F_z [N]
$(+,+,+)$	Left	15.52	6.12×10^3	1.93×10^4	3.21×10^1
$(-,-,-)$	Right	13.58	-5.17×10^3	-4.82×10^3	-2.68×10^1
$(-,+,+)$	Left	14.84	-4.13×10^3	1.23×10^4	6.87×10^2
$(+,-,-)$	Right	16.67	2.81×10^2	-2.32×10^3	-2.47×10^2
$(-,-,+)$	Right	14.7	-4.11×10^3	-6.42×10^3	5.81×10^2
$(+,+,-)$	Left	15.53	6.20×10^3	1.88×10^4	-9.02×10^1
$(+,-,+)$	Right	15.4	1.33×10^3	-1.60×10^3	1.80×10^2
$(-,+,-)$	Left	15.65	-1.57×10^2	4.13×10^3	-4.25×10^1
maximum $+x$	Right	15.51	8.49×10^3	9.25×10^3	2.28×10^2
maximum $+y$	Left	15.52	6.12×10^3	1.93×10^4	3.21×10^1
maximum $+z$	Right	14.83	1.53×10^3	7.70×10^3	7.32×10^2
maximum $-x$	Left	10.77	-7.89×10^3	3.53×10^3	5.56×10^2
maximum $-y$	Right	14.7	-4.11×10^3	-6.42×10^3	5.81×10^2
maximum $-z$	Left	14.97	5.33×10^0	7.48×10^2	-4.65×10^2

Table B.12: Maximum Forces of Straight Constant Speed [80km/h] on Level 7 Road

Direction	Side	Time [s]	F_x [N]	F_y [N]	F_z [N]
$(+,+,+)$	Left	11.93	5.60×10^3	1.97×10^4	6.70×10^1
$(-,-,-)$	Left	16.04	-6.95×10^3	-7.47×10^3	-6.20×10^1
$(-,+,+)$	Right	11.96	-1.60×10^3	1.91×10^4	2.92×10^2
$(+,-,-)$	Right	16.74	2.17×10^2	-2.51×10^3	-4.54×10^1
$(-,-,+)$	Left	15.2	-4.50×10^3	-1.13×10^4	3.12×10^2
$(+,+,-)$	Left	12.02	1.26×10^3	4.79×10^3	-1.48×10^2
$(+,-,+)$	Left	16.75	3.43×10^2	-2.29×10^3	9.83×10^0
$(-,+,-)$	Right	12.62	-8.83×10^2	9.79×10^3	-3.33×10^1
maximum $+x$	Right	11.93	6.20×10^3	1.92×10^4	1.92×10^1
maximum $+y$	Left	11.93	5.60×10^3	1.97×10^4	6.70×10^1
maximum $+z$	Right	15.33	-5.58×10^3	2.16×10^3	9.88×10^2
maximum $-x$	Left	15.3	-1.05×10^4	-6.12×10^2	6.95×10^2
maximum $-y$	Left	15.2	-4.50×10^3	-1.13×10^4	3.12×10^2
maximum $-z$	Right	16.72	-3.90×10^2	1.85×10^3	-5.23×10^2

Table B.13: Maximum Forces of Straight Constant Speed [100km/h] on Level 7 Road

Direction	Side	Time [s]	F_x [N]	F_y [N]	F_z [N]
$(+,+,+)$	Right	16.7	6.59×10^3	2.92×10^4	1.21×10^2
$(-,-,-)$	Right	17.75	-9.01×10^1	-1.59×10^4	-2.34×10^2
$(-,+,+)$	Left	17.74	-2.54×10^3	3.05×10^4	2.74×10^2
$(+,-,-)$	Left	18.89	3.62×10^3	-2.50×10^4	-8.17×10^1
$(-,-,+)$	Right	18.52	-1.44×10^2	-2.19×10^4	8.90×10^2
$(+,+,-)$	Right	16.69	1.78×10^4	3.27×10^4	-1.55×10^2
$(+,-,+)$	Left	18.07	5.01×10^3	-3.57×10^4	5.35×10^2
$(-,+,-)$	Right	18.08	-6.31×10^3	3.83×10^4	-1.19×10^3
maximum $+x$	Left	16.68	1.87×10^4	2.01×10^4	1.90×10^1
maximum $+y$	Right	18.08	-6.31×10^3	3.83×10^4	-1.19×10^3
maximum $+z$	Right	17.65	5.00×10^3	3.21×10^3	1.97×10^3
maximum $-x$	Left	18.57	-6.51×10^3	2.22×10^4	-5.45×10^2
maximum $-y$	Left	18.07	5.01×10^3	-3.57×10^4	5.35×10^2
maximum $-z$	Left	17.64	-1.59×10^3	1.17×10^4	-1.54×10^3

Table B.14: Maximum Forces of Constant Speed Cornering on Level 8 Road

Direction	Side	Time [s]	F_x [N]	F_y [N]	F_z [N]
$(+,+,+)$	Right	7.31	9.90×10^3	3.18×10^4	1.81×10^3
$(-,-,-)$	Right	3.98	-8.53×10^3	-9.54×10^3	-1.42×10^1
$(-,+,+)$	Right	7.32	-1.18×10^4	2.37×10^4	2.13×10^3
$(+,-,-)$	Left	7.22	9.94×10^2	-5.66×10^3	-2.01×10^2
$(-,-,+)$	Left	17.92	-1.50×10^4	-1.90×10^4	1.41×10^3
$(+,+,-)$	Right	16.98	1.46×10^4	5.42×10^4	-3.55×10^2
$(+,-,+)$	Right	18.55	2.25×10^3	-1.81×10^4	1.39×10^3
$(-,+,-)$	Right	17.88	-9.09×10^3	8.54×10^3	-6.82×10^1
maximum $+x$	Right	5.69	1.88×10^4	2.25×10^4	3.25×10^2
maximum $+y$	Right	16.98	1.46×10^4	5.42×10^4	-3.55×10^2
maximum $+z$	Right	7.33	-1.55×10^4	-1.45×10^4	3.29×10^3
maximum $-x$	Left	17.91	-1.73×10^4	-1.65×10^4	1.78×10^3
maximum $-y$	Left	17.92	-1.50×10^4	-1.90×10^4	1.41×10^3
maximum $-z$	Left	7.29	4.41×10^1	7.25×10^2	-1.79×10^3

Table B.15: Maximum Forces of Braking During Cornering on Level 8 Road

Direction	Side	Time [s]	F_x [N]	F_y [N]	F_z [N]
$(+,+,+)$	Right	7.31	9.90×10^3	3.18×10^4	1.81×10^3
$(-,-,-)$	Right	3.98	-8.53×10^3	-9.54×10^3	-1.42×10^1
$(-,+,+)$	Right	7.32	-1.18×10^4	2.37×10^4	2.13×10^3
$(+,-,-)$	Right	10.85	5.93×10^3	-4.96×10^2	-3.03×10^1
$(-,-,+)$	Right	7.33	-1.55×10^4	-1.45×10^4	3.29×10^3
$(+,+,-)$	Left	6.53	1.44×10^4	2.99×10^4	-5.47×10^2
$(+,-,+)$	Right	10.76	9.67×10^3	-1.10×10^3	4.17×10^2
$(-,+,-)$	Left	7.33	-1.76×10^3	8.06×10^3	-1.23×10^3
maximum $+x$	Right	10.61	2.12×10^4	2.24×10^4	6.00×10^2
maximum $+y$	Right	7.31	9.90×10^3	3.18×10^4	1.81×10^3
maximum $+z$	Right	7.33	-1.55×10^4	-1.45×10^4	3.29×10^3
maximum $-x$	Right	7.33	-1.55×10^4	-1.45×10^4	3.29×10^3
maximum $-y$	Right	7.34	-1.07×10^4	-1.54×10^4	1.70×10^3
maximum $-z$	Left	7.29	4.41×10^1	7.25×10^2	-1.79×10^3

Table B.16: Maximum Forces of Straight Accelerating on Level 8 Road

Direction	Side	Time [s]	F_x [N]	F_y [N]	F_z [N]
$(+,+,+)$	Left	16.8	7.72×10^3	6.86×10^4	1.45×10^2
$(-,-,-)$	Right	11.05	-1.37×10^3	-2.45×10^4	-1.35×10^2
$(-,+,+)$	Right	14.08	-1.81×10^4	4.98×10^4	3.66×10^2
$(+,-,-)$	Left	14.83	4.03×10^3	-3.86×10^4	-1.91×10^2
$(-,-,+)$	Left	16.73	-4.20×10^3	-7.64×10^4	2.04×10^3
$(+,+,-)$	Left	16.81	8.30×10^3	7.44×10^4	-7.21×10^2
$(+,-,+)$	Left	16.72	2.60×10^3	-1.20×10^5	2.97×10^3
$(-,+,-)$	Left	16.91	-1.07×10^4	8.72×10^4	-1.72×10^3
maximum $+x$	Right	15.65	3.40×10^4	5.68×10^4	-5.97×10^2
maximum $+y$	Left	16.91	-1.07×10^4	8.72×10^4	-1.72×10^3
maximum $+z$	Left	16.72	2.60×10^3	-1.20×10^5	2.97×10^3
maximum $-x$	Right	14.08	-1.81×10^4	4.98×10^4	3.66×10^2
maximum $-y$	Left	16.72	2.60×10^3	-1.20×10^5	2.97×10^3
maximum $-z$	Left	16.93	-1.12×10^4	6.80×10^4	-2.21×10^3

Table B.17: Maximum Forces of Straight Braking on Level 8 Road

Direction	Side	Time [s]	F_x [N]	F_y [N]	F_z [N]
$(+,+,+)$	Left	16.75	6.16×10^4	2.16×10^4	1.49×10^2
$(-,-,-)$	Left	15.77	-1.11×10^4	-5.34×10^3	-3.93×10^2
$(-,+,+)$	Right	12.01	-2.19×10^3	1.93×10^4	4.29×10^2
$(+,-,-)$	Right	15.05	5.51×10^3	-1.14×10^4	-2.95×10^2
$(-,-,+)$	Right	15.79	-2.52×10^4	-2.19×10^4	3.33×10^3
$(+,+,-)$	Left	16.76	4.32×10^4	3.08×10^4	-4.00×10^2
$(+,-,+)$	Left	16.71	5.56×10^4	-9.04×10^3	1.61×10^3
$(-,+,-)$	Left	11.94	-3.35×10^2	1.30×10^4	-2.84×10^1
maximum $+x$	Left	16.75	6.16×10^4	2.16×10^4	1.49×10^2
maximum $+y$	Right	14.88	4.17×10^4	4.93×10^4	6.50×10^1
maximum $+z$	Right	15.79	-2.52×10^4	-2.19×10^4	3.33×10^3
maximum $-x$	Right	15.79	-2.52×10^4	-2.19×10^4	3.33×10^3
maximum $-y$	Right	15.79	-2.52×10^4	-2.19×10^4	3.33×10^3
maximum $-z$	Right	16.72	4.59×10^3	1.36×10^4	-1.75×10^3

Table B.18: Maximum Forces of Straight Constant Speed [60km/h] on Level 8 Road

Direction	Side	Time [s]	F_x [N]	F_y [N]	F_z [N]
$(+,+,+)$	Left	17.32	4.48×10^3	9.23×10^4	6.36×10^2
$(-,-,-)$	Left	18.55	-5.22×10^2	-1.43×10^4	-4.75×10^0
$(-,+,+)$	Right	18.76	-6.22×10^3	6.28×10^4	1.05×10^2
$(+,-,-)$	Left	17.88	6.46×10^3	-4.94×10^4	-2.40×10^1
$(-,-,+)$	Right	17.27	-5.68×10^3	-1.36×10^5	3.71×10^3
$(+,+,-)$	Left	17.3	6.69×10^1	9.67×10^4	-1.02×10^3
$(+,-,+)$	Right	17.23	7.18×10^2	-8.43×10^4	3.62×10^3
$(-,+,-)$	Left	17.26	-1.70×10^4	1.22×10^5	-2.85×10^3
maximum $+x$	Left	17.33	1.78×10^4	8.18×10^4	1.28×10^3
maximum $+y$	Left	17.26	-1.70×10^4	1.22×10^5	-2.85×10^3
maximum $+z$	Right	17.26	-1.53×10^3	-1.09×10^5	4.17×10^3
maximum $-x$	Left	17.26	-1.70×10^4	1.22×10^5	-2.85×10^3
maximum $-y$	Right	17.27	-5.68×10^3	-1.36×10^5	3.71×10^3
maximum $-z$	Left	17.25	-1.30×10^4	1.02×10^5	-3.01×10^3

Table B.19: Maximum Forces of Straight Constant Speed [80km/h] on Level 8 Road

Direction	Side	Time [s]	F_x [N]	F_y [N]	F_z [N]
$(+,+,+)$	Right	17.23	1.76×10^5	1.59×10^5	1.78×10^1
$(-,-,-)$	Left	14.91	-5.28×10^3	-3.24×10^4	-2.83×10^2
$(-,+,+)$	Right	14.92	-2.38×10^3	5.47×10^4	7.01×10^2
$(+,-,-)$	Right	19.37	3.33×10^3	-4.24×10^4	-7.98×10^1
$(-,-,+)$	Right	16.15	-8.27×10^3	-1.06×10^5	2.36×10^3
$(+,+,-)$	Right	17.24	1.98×10^5	9.83×10^4	-3.05×10^3
$(+,-,+)$	Right	18.29	1.80×10^4	-1.43×10^5	2.44×10^3
$(-,+,-)$	Left	18.29	-2.56×10^4	1.50×10^5	-4.15×10^3
maximum $+x$	Right	17.24	1.98×10^5	9.83×10^4	-3.05×10^3
maximum $+y$	Right	17.23	1.76×10^5	1.59×10^5	1.78×10^1
maximum $+z$	Left	18.6	-6.38×10^3	-8.50×10^4	4.78×10^3
maximum $-x$	Right	18.75	-2.99×10^4	9.93×10^4	-4.50×10^3
maximum $-y$	Right	18.29	1.80×10^4	-1.43×10^5	2.44×10^3
maximum $-z$	Right	17.25	9.54×10^4	1.21×10^5	-8.02×10^3

Table B.20: Maximum Forces of Straight Constant Speed [100km/h] on Level 8 Road

Direction	Side	Time [s]	F_x [N]	F_y [N]	F_z [N]
$(+,+,+)$	Left	17.04	5.97×10^3	3.28×10^4	2.18×10^2
$(-,-,-)$	Right	17.18	-1.44×10^3	-1.32×10^4	-3.41×10^2
$(-,+,+)$	Right	13.37	-5.26×10^2	2.12×10^4	5.16×10^2
$(+,-,-)$	Left	18.54	1.52×10^3	-1.15×10^4	-1.66×10^0
$(-,-,+)$	Left	16.05	-1.16×10^4	-1.09×10^4	8.09×10^2
$(+,+,-)$	Left	17.1	2.05×10^4	6.49×10^4	-7.46×10^1
$(+,-,+)$	Left	17.14	1.56×10^2	-1.86×10^4	9.48×10^2
$(-,+,-)$	Right	17.15	-1.70×10^3	1.41×10^4	-1.34×10^3
maximum $+x$	Left	17.09	3.29×10^4	4.83×10^4	-4.42×10^1
maximum $+y$	Left	17.1	2.05×10^4	6.49×10^4	-7.46×10^1
maximum $+z$	Left	16	-2.35×10^3	8.91×10^3	1.32×10^3
maximum $-x$	Left	16.05	-1.16×10^4	-1.09×10^4	8.09×10^2
maximum $-y$	Left	17.14	1.56×10^2	-1.86×10^4	9.48×10^2
maximum $-z$	Right	17.15	-1.70×10^3	1.41×10^4	-1.34×10^3

Table B.21: Maximum Forces of Constant Speed Cornering on Level 5 Road

Direction	Side	Time [s]	F_x [N]	F_y [N]	F_z [N]
$(+,+,+)$	Left	5.22	4.39×10^2	3.11×10^3	1.14×10^1
$(-,-,-)$	Right	18.89	-1.17×10^3	-4.49×10^3	-6.29×10^1
$(-,+,+)$	Left	5.23	-8.58×10^0	2.90×10^3	1.65×10^1
$(+,-,-)$	Right	10.91	2.92×10^0	-2.29×10^3	-7.35×10^1
$(-,-,+)$	Right	10.41	-1.02×10^3	-5.30×10^3	4.22×10^2
$(+,+,-)$	Left	19.28	5.26×10^2	5.67×10^3	-3.94×10^2
$(+,-,+)$	Right	17.8	1.63×10^2	-3.77×10^3	3.11×10^2
$(-,+,-)$	Left	11.23	-3.92×10^2	6.25×10^3	-2.62×10^2
maximum $+x$	Left	17.9	5.53×10^2	4.51×10^3	-2.61×10^2
maximum $+y$	Left	11.23	-3.92×10^2	6.25×10^3	-2.62×10^2
maximum $+z$	Right	10.54	-1.97×10^3	-1.83×10^3	1.02×10^3
maximum $-x$	Right	19.16	-2.24×10^3	-8.67×10^2	7.33×10^2
maximum $-y$	Right	10.41	-1.02×10^3	-5.30×10^3	4.22×10^2
maximum $-z$	Left	8.99	-3.95×10^2	1.49×10^3	-8.45×10^2

Table B.22: Maximum Forces of Braking During Cornering on Level 5 Road

Direction	Side	Time [s]	F_x [N]	F_y [N]	F_z [N]
$(+,+,+)$	Right	9.86	5.40×10^{3}	2.21×10^{3}	5.54×10^{1}
$(-,-,-)$	Right	10.5	0.00×10^{0}	0.00×10^{0}	0.00×10^{0}
$(-,+,+)$	Left	5.23	-8.58×10^{0}	2.90×10^{3}	1.65×10^{1}
$(+,-,-)$	Right	17.01	0.00×10^{0}	0.00×10^{0}	0.00×10^{0}
$(-,-,+)$	Right	6.95	-1.23×10^{3}	-4.77×10^{3}	3.91×10^{2}
$(+,+,-)$	Left	8.68	6.60×10^{3}	6.67×10^{3}	-2.71×10^{2}
$(+,-,+)$	Right	9.03	6.16×10^{3}	-1.71×10^{3}	3.09×10^{2}
$(-,+,-)$	Left	7.08	-3.89×10^{2}	4.24×10^{3}	-4.88×10^{2}
maximum $+x$	Left	9.98	7.01×10^{3}	3.99×10^{3}	-4.02×10^{1}
maximum $+y$	Left	8.68	6.60×10^{3}	6.67×10^{3}	-2.71×10^{2}
maximum $+z$	Right	5.96	-4.63×10^{2}	-2.08×10^{3}	6.64×10^{2}
maximum $-x$	Right	5.9	-2.12×10^{3}	-2.07×10^{3}	6.37×10^{2}
maximum $-y$	Right	6.95	-1.23×10^{3}	-4.77×10^{3}	3.91×10^{2}
maximum $-z$	Left	6.83	-2.52×10^{2}	7.30×10^{2}	-6.83×10^{2}

Table B.23: Maximum Forces of Straight Accelerating on Level 5 Road

Direction	Side	Time [s]	F_x [N]	F_y [N]	F_z [N]
$(+,+,+)$	Left	12.46	6.58×10^{1}	2.37×10^{3}	1.90×10^{1}
$(-,-,-)$	Left	9.39	-4.99×10^{3}	-4.49×10^{3}	-2.83×10^{1}
$(-,+,+)$	Left	13.92	-6.82×10^{1}	2.41×10^{3}	4.03×10^{1}
$(+,-,-)$	Right	10.91	0.00×10^{0}	0.00×10^{0}	0.00×10^{0}
$(-,-,+)$	Left	10.1	-5.13×10^{3}	-4.35×10^{3}	6.90×10^{0}
$(+,+,-)$	Right	12.46	6.72×10^{1}	2.37×10^{3}	-6.22×10^{1}
$(+,-,+)$	Right	17.8	0.00×10^{0}	0.00×10^{0}	0.00×10^{0}
$(-,+,-)$	Left	11.36	-1.57×10^{2}	2.59×10^{3}	-4.17×10^{1}
maximum $+x$	Right	10.57	5.23×10^{2}	2.06×10^{3}	-1.15×10^{2}
maximum $+y$	Left	11.36	-1.57×10^{2}	2.59×10^{3}	-4.17×10^{1}
maximum $+z$	Right	14.5	-1.73×10^{3}	1.71×10^{2}	1.26×10^{2}
maximum $-x$	Left	10.1	-5.13×10^{3}	-4.35×10^{3}	6.90×10^{0}
maximum $-y$	Left	10.02	-4.66×10^{3}	-4.73×10^{3}	-7.11×10^{1}
maximum $-z$	Right	13.69	-3.87×10^{2}	1.50×10^{3}	-2.64×10^{2}

Table B.24: Maximum Forces of Straight Braking on Level 5 Road

Direction	Side	Time [s]	F_x [N]	F_y [N]	F_z [N]
$(+,+,+)$	Right	15.79	6.57×10^3	4.26×10^3	1.54×10^1
$(-,-,-)$	Left	10.5	-2.96×10^3	-1.94×10^3	-8.61×10^1
$(-,+,+)$	Left	11.96	-5.65×10^2	2.43×10^3	7.54×10^1
$(+,-,-)$	Right	10.91	0.00×10^0	0.00×10^0	0.00×10^0
$(-,-,+)$	Left	11.36	-2.50×10^3	-5.04×10^1	5.47×10^1
$(+,+,-)$	Left	14.75	6.76×10^3	3.71×10^3	-1.60×10^1
$(+,-,+)$	Right	17.8	0.00×10^0	0.00×10^0	0.00×10^0
$(-,+,-)$	Right	11.36	-2.42×10^3	4.69×10^1	-5.57×10^0
maximum $+x$	Left	14.86	6.92×10^3	3.19×10^3	2.31×10^1
maximum $+y$	Left	14.48	5.76×10^3	4.98×10^3	3.43×10^1
maximum $+z$	Left	11.92	-5.28×10^2	1.71×10^3	1.05×10^2
maximum $-x$	Right	10.54	-3.02×10^3	-1.44×10^3	-1.05×10^2
maximum $-y$	Left	10.5	-2.96×10^3	-1.94×10^3	-8.61×10^1
maximum $-z$	Right	14.11	3.38×10^0	1.22×10^3	-1.74×10^2

Table B.25: Maximum Forces of Straight Constant Speed [60km/h] on Level 5 Road

Direction	Side	Time [s]	F_x [N]	F_y [N]	F_z [N]
$(+,+,+)$	Left	18.58	4.20×10^2	3.41×10^3	7.02×10^1
$(-,-,-)$	Left	9	-2.98×10^3	-1.96×10^3	-8.49×10^1
$(-,+,+)$	Left	17.83	-1.89×10^2	3.27×10^3	7.81×10^1
$(+,-,-)$	Right	17.01	0.00×10^0	0.00×10^0	0.00×10^0
$(-,-,+)$	Left	10.15	-2.48×10^3	-1.96×10^2	1.09×10^2
$(+,+,-)$	Right	11.49	1.46×10^2	2.99×10^3	-5.46×10^0
$(+,-,+)$	Right	14.28	0.00×10^0	0.00×10^0	0.00×10^0
$(-,+,-)$	Right	11.5	-1.45×10^2	2.68×10^3	-2.51×10^1
maximum $+x$	Left	9.19	8.96×10^2	2.63×10^3	-1.21×10^2
maximum $+y$	Left	18.58	4.20×10^2	3.41×10^3	7.02×10^1
maximum $+z$	Right	17.8	-1.39×10^3	1.02×10^3	1.37×10^2
maximum $-x$	Right	9	-3.01×10^3	-1.71×10^3	-1.01×10^2
maximum $-y$	Left	9	-2.98×10^3	-1.96×10^3	-8.49×10^1
maximum $-z$	Right	17.49	-2.47×10^2	7.34×10^2	-2.69×10^2

Table B.26: Maximum Forces of Straight Constant Speed [80km/h] on Level 5 Road

Direction	Side	Time [s]	F_x [N]	F_y [N]	F_z [N]
$(+,+,+)$	Left	17.69	5.77×10^{0}	2.61×10^{3}	5.06×10^{1}
$(-,-,-)$	Left	10.5	-2.96×10^{3}	-1.94×10^{3}	-8.61×10^{1}
$(-,+,+)$	Left	14.48	-2.56×10^{1}	2.99×10^{3}	7.47×10^{1}
$(+,-,-)$	Right	17.01	0.00×10^{0}	0.00×10^{0}	0.00×10^{0}
$(-,-,+)$	Left	11.36	-2.50×10^{3}	-5.04×10^{1}	5.47×10^{1}
$(+,+,-)$	Left	16.45	1.03×10^{2}	2.15×10^{3}	-1.53×10^{1}
$(+,-,+)$	Right	14.28	0.00×10^{0}	0.00×10^{0}	0.00×10^{0}
$(-,+,-)$	Left	15.07	-1.11×10^{2}	2.50×10^{3}	-1.10×10^{1}
maximum $+x$	Left	10.58	4.51×10^{2}	2.07×10^{3}	-1.17×10^{2}
maximum $+y$	Left	14.48	-2.56×10^{1}	2.99×10^{3}	7.47×10^{1}
maximum $+z$	Right	14.43	-5.20×10^{2}	2.34×10^{3}	1.20×10^{2}
maximum $-x$	Right	10.54	-3.02×10^{3}	-1.44×10^{3}	-1.05×10^{2}
maximum $-y$	Left	10.5	-2.96×10^{3}	-1.94×10^{3}	-8.61×10^{1}
maximum $-z$	Left	14.69	-3.25×10^{2}	1.28×10^{3}	-2.45×10^{2}

Table B.27: Maximum Forces of Straight Constant Speed [100km/h] on Level 5 Road

Direction	Side	Time [s]	F_x [N]	F_y [N]	F_z [N]
$(+,+,+)$	Right	14.52	3.17×10^{1}	2.83×10^{3}	1.56×10^{1}
$(-,-,-)$	Left	11.9	-2.95×10^{3}	-1.94×10^{3}	-8.69×10^{1}
$(-,+,+)$	Left	15.1	-3.03×10^{2}	3.77×10^{3}	1.64×10^{2}
$(+,-,-)$	Right	17.01	5.90×10^{1}	-3.04×10^{2}	-1.04×10^{2}
$(-,-,+)$	Left	13.73	-2.15×10^{3}	-1.03×10^{2}	6.20×10^{1}
$(+,+,-)$	Left	15.94	2.48×10^{1}	2.11×10^{3}	-3.07×10^{1}
$(+,-,+)$	Right	14.28	3.74×10^{2}	-3.17×10^{0}	6.09×10^{1}
$(-,+,-)$	Left	14.53	-1.45×10^{2}	2.93×10^{3}	-1.09×10^{0}
maximum $+x$	Right	14.28	3.74×10^{2}	-3.17×10^{0}	6.09×10^{1}
maximum $+y$	Left	15.1	-3.03×10^{2}	3.77×10^{3}	1.64×10^{2}
maximum $+z$	Left	15.09	-7.96×10^{1}	3.76×10^{3}	1.78×10^{2}
maximum $-x$	Right	11.9	-2.99×10^{3}	-1.69×10^{3}	-1.00×10^{2}
maximum $-y$	Left	11.9	-2.95×10^{3}	-1.94×10^{3}	-8.69×10^{1}
maximum $-z$	Right	16.98	-4.26×10^{2}	1.97×10^{3}	-2.98×10^{2}

B.2 Tables for Anti-roll Bar Forces and Moments Summary Results

Table B.28: Anti-roll Bar Forces and Moments Summary of Level 6 Road

Case	F_x [N]	F_y [N]	F_z [N]	M_x [Nmm]	M_y [Nmm]	M_z [Nmm]
$(+,+,+)$	1.69×10^3	-2.31×10^2	-2.01×10^3	-3.32×10^4	1.76×10^4	-2.87×10^4
$(-,-,-)$	-7.60×10^2	4.57×10^2	1.05×10^3	-1.67×10^4	-1.10×10^4	-1.31×10^4
$(-,+,+)$	-2.40×10^1	-2.62×10^2	9.76×10^2	-5.85×10^4	6.63×10^3	1.42×10^4
$(+,-,-)$	-6.64×10^2	4.08×10^2	8.81×10^2	5.04×10^3	1.21×10^4	1.44×10^4
$(-,-,+)$	-5.25×10^2	3.11×10^2	7.97×10^2	-1.76×10^4	-5.19×10^3	-8.04×10^3
$(+,+,-)$	4.14×10^2	3.29×10^2	-1.06×10^3	2.68×10^4	2.80×10^2	5.40×10^3
$(+,-,+)$	9.83×10^2	-1.96×10^2	-1.66×10^3	-5.26×10^4	2.24×10^3	-1.02×10^4
$(-,+,-)$	-8.16×10^2	1.74×10^2	1.07×10^3	-2.29×10^4	-8.85×10^3	-1.29×10^4
maximum $+x$	1.71×10^3	-2.89×10^2	-2.30×10^3	4.74×10^4	-1.74×10^4	2.68×10^4
maximum $+z$	-1.70×10^2	-1.68×10^3	1.44×10^3	6.90×10^4	-9.02×10^3	-1.50×10^4
maximum $-x$	-5.99×10^2	1.29×10^2	1.17×10^3	4.39×10^4	5.21×10^2	3.24×10^3
maximum $-z$	-7.40×10^2	1.47×10^3	2.77×10^2	6.03×10^3	-8.83×10^3	-1.29×10^4

Table B.29: Anti-roll Bar Forces and Moments Summary of Level 7 Road

Case	F_x [N]	F_y [N]	F_z [N]	M_x [Nmm]	M_y [Nmm]	M_z [Nmm]
$(+,+,+)$	2.49×10^3	-2.98×10^2	-2.33×10^3	1.82×10^4	-3.34×10^4	4.15×10^4
$(-,-,-)$	3.85×10^2	6.71×10^2	-6.96×10^2	-1.14×10^4	-3.70×10^2	-5.78×10^3
$(-,+,+)$	-4.90×10^2	-7.52×10^2	1.56×10^3	-7.74×10^4	8.08×10^3	8.92×10^3
$(+,-,-)$	-3.38×10^2	7.01×10^2	2.46×10^2	1.60×10^4	-7.52×10^3	-1.20×10^4
$(-,-,+)$	1.80×10^2	-6.30×10^2	4.36×10^2	1.97×10^4	-3.12×10^3	-5.21×10^3
$(+,+,-)$	2.27×10^3	-3.21×10^2	-2.45×10^3	-2.97×10^4	3.15×10^4	-3.99×10^4
$(+,-,+)$	2.95×10^2	-9.21×10^1	-3.84×10^2	3.51×10^4	-1.70×10^3	-6.12×10^3
$(-,+,-)$	-1.58×10^3	9.60×10^2	1.97×10^3	3.00×10^4	2.73×10^4	2.28×10^4
maximum $+x$	2.19×10^3	-4.05×10^2	-2.64×10^3	4.11×10^4	-3.04×10^4	3.80×10^4
maximum $+z$	2.24×10^2	-2.60×10^3	9.68×10^2	5.79×10^4	-6.48×10^3	-3.07×10^4
maximum $-x$	-1.05×10^3	-4.67×10^2	2.83×10^3	-1.21×10^5	1.24×10^4	3.31×10^3
maximum $-z$	-7.22×10^2	1.94×10^3	-3.10×10^2	1.39×10^4	-5.78×10^3	-1.07×10^4

B.3 Tables for Mesh Sensitivity Study of Solid Bushing Model

Table B.30: Front Bushing Conical Motion Mesh Sensitivity Results

Rotation [rad]	Moment [Nmm] Size 0.3	Deviation	Moment [Nmm] Size 0.5	Deviation	Moment [Nmm] Size 1
0.0015	199.492	0.901%	201.29	2.463%	206.247
0.003	399.002	0.903%	402.605	2.469%	412.545
0.0045	598.531	0.905%	603.946	2.476%	618.9

Table B.31: Front Bushing Axial Motion Mesh Sensitivity Results

Displacement [mm]	Force [N] Size 0.3	Deviation	Force [N] Size 0.5	Deviation	Force [N] Size 1
0.05	7.58452	0.153%	7.59616	0.470%	7.63186
0.1	15.1692	0.154%	15.1925	0.471%	15.264
0.15	22.7541	0.154%	22.7891	0.471%	22.8964

Table B.32: Front Bushing Torsional Motion Mesh Sensitivity Results

Rotation [rad]	Moment [Nmm] Size 0.3	Deviation	Moment [Nmm] Size 0.5	Deviation	Moment [Nmm] Size 1
0.005	119.637	0.653%	120.418	0.173%	120.21
0.010	239.275	0.653%	240.837	0.169%	240.431
0.015	358.916	0.651%	361.253	0.163%	360.664

Table B.33: Rear Bushing Radial Motion Mesh Sensitivity Results

Displacement [mm]	Force [N] Size 0.5	Deviation	Force [N] Size 1	Deviation	Force [N] Size 4
0.1	22.8702	0.45%	22.9727	5.01%	24.1236
0.2	45.7421	0.45%	45.9479	4.99%	48.2412
0.3	68.6163	0.45%	68.9264	4.97%	72.3536

Table B.34: Rear Bushing Axial Motion Mesh Sensitivity Results

Displacement [mm]	Force [N] Size 0.5	Deviation	Force [N] Size 1	Deviation	Force [N] Size 4
0.05	3.19462	0.323%	3.20493	2.855%	3.29643
0.1	6.38927	0.323%	6.40991	2.856%	6.59295
0.15	9.58395	0.323%	9.61494	2.856%	9.88956

Table B.35: Rear Bushing Torsional Motion Mesh Sensitivity Results

Rotation [rad]	Moment [Nmm] Size 0.5	Deviation	Moment [Nmm] Size 1	Deviation	Moment [Nmm] Size 4
0.005	132.78	0.124%	132.945	3.125%	137.1
0.010	265.561	0.125%	265.893	3.129%	274.214
0.015	398.343	0.126%	398.844	3.131%	411.333

Appendix C

Supplemental Figures

C.1 Figures For Stress-Strain Prediction Confirmation

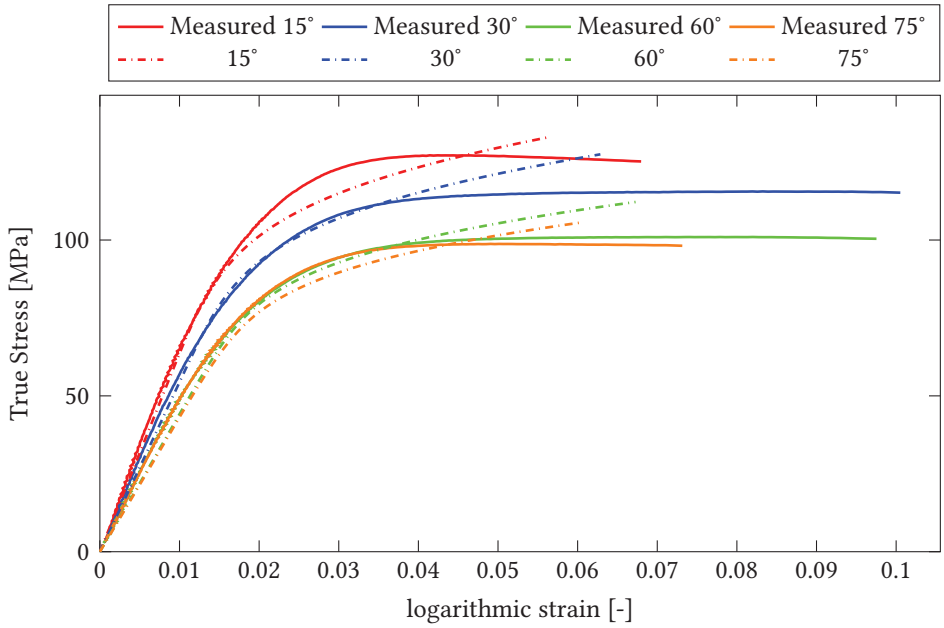

Figure C.1: Numerical Test With Standard Meshing Size vs Physical Test in 15°, 30°, 60°, 75°

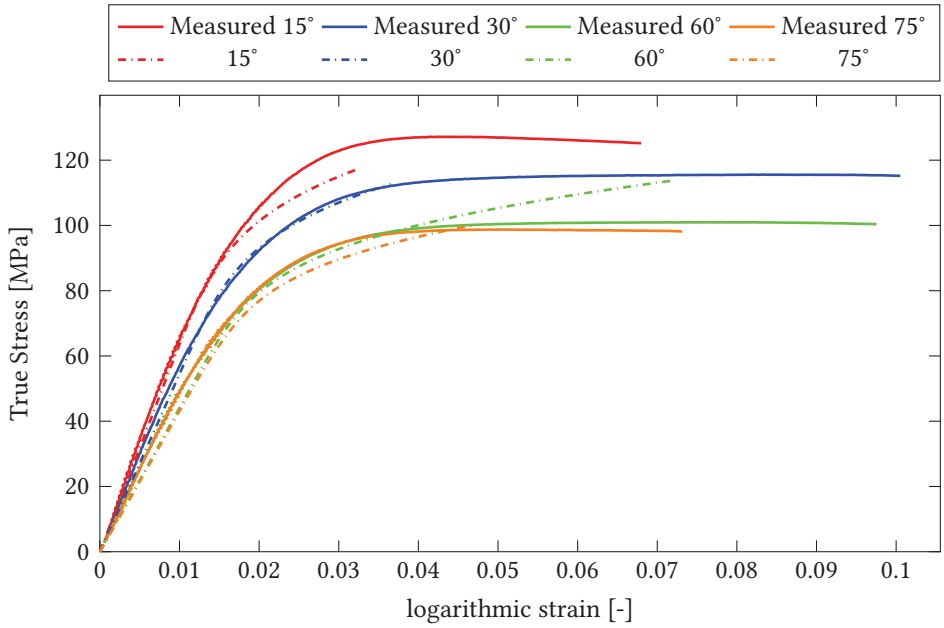

Figure C.2: Numerical Test With 1/2 Meshing Size vs Physical Test in 15°, 30°, 60°, 75°

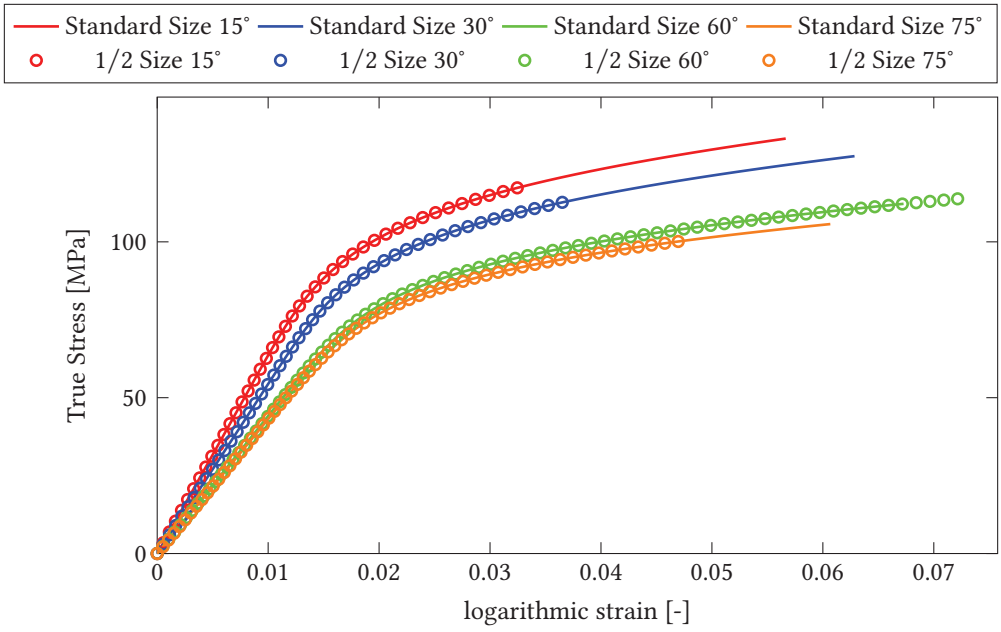

Figure C.3: 1/2 Meshing Size vs Standard Meshing Size in 15°, 30°, 60°,75°

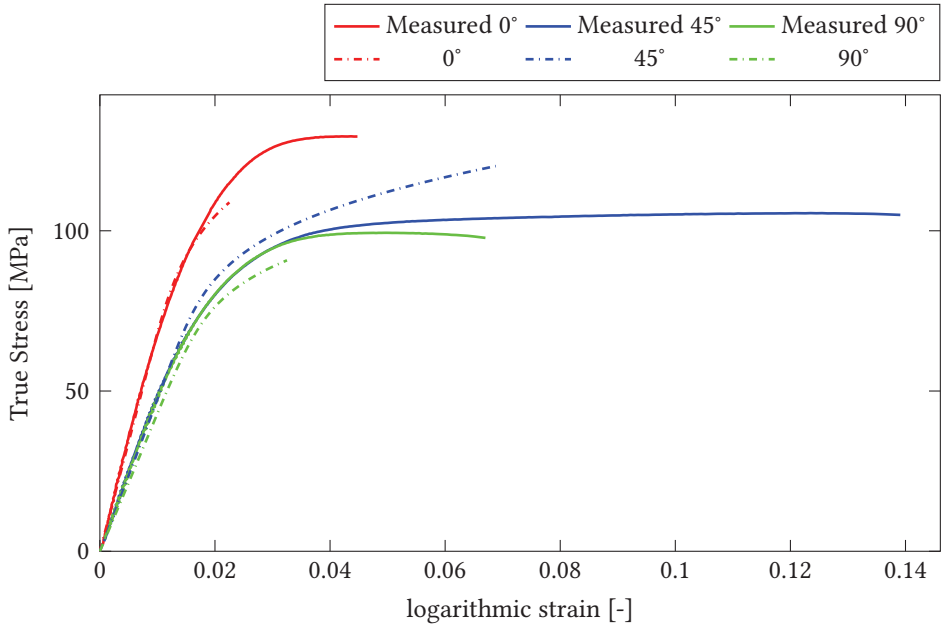

Figure C.4: Numerical Test With 1/3 Meshing Size vs Physical Test in 0°, 45°, 90°

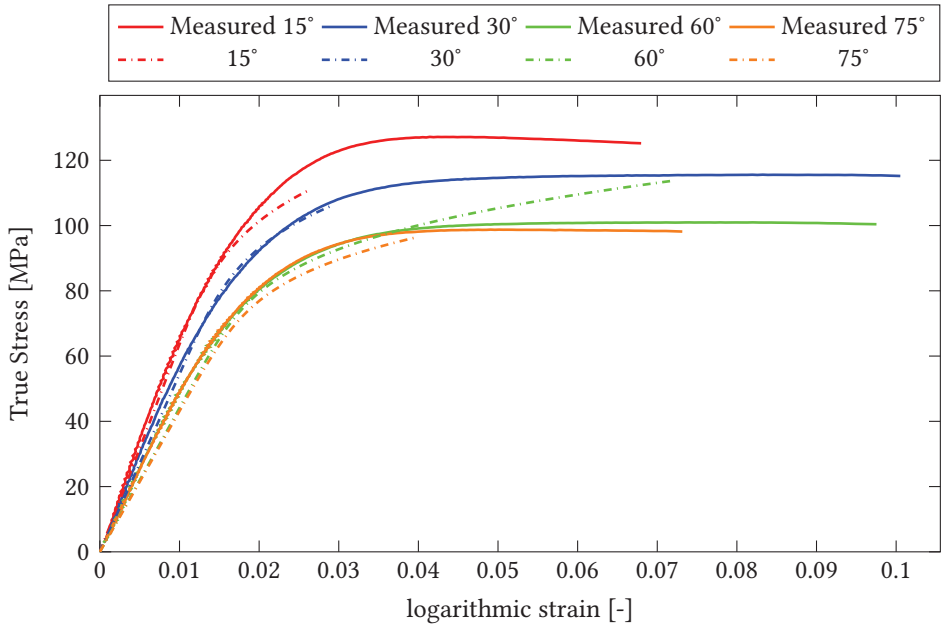

Figure C.5: Numerical Test With 1/3 Meshing Size vs Physical Test in 15°, 30°, 60°, 75°

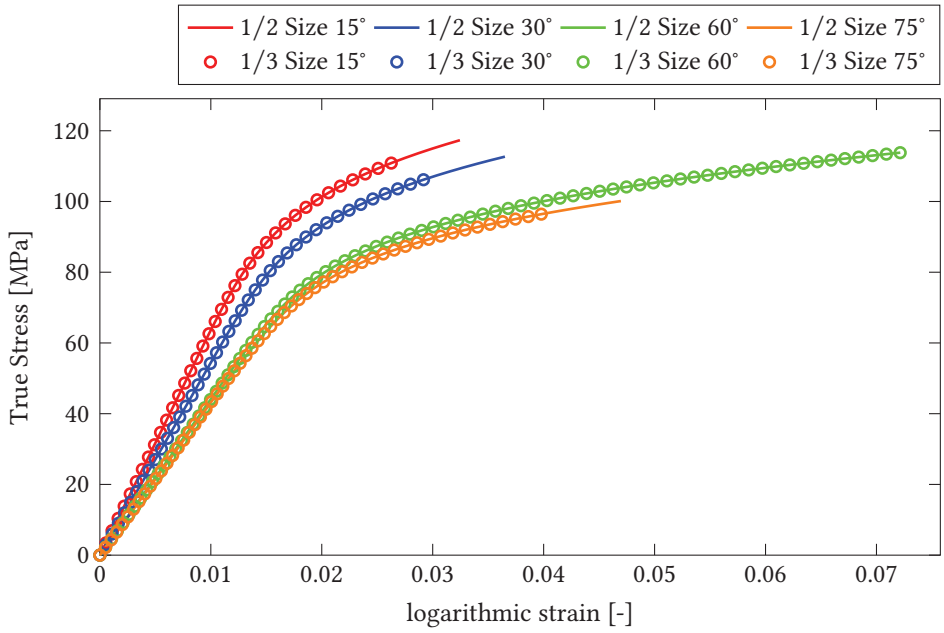

Figure C.6: 1/3 Meshing Size vs 1/2 Meshing Size in 15˚, 30˚, 60˚,75˚

C.2 Figures For FEA Tensile Test Strain Contour Plots

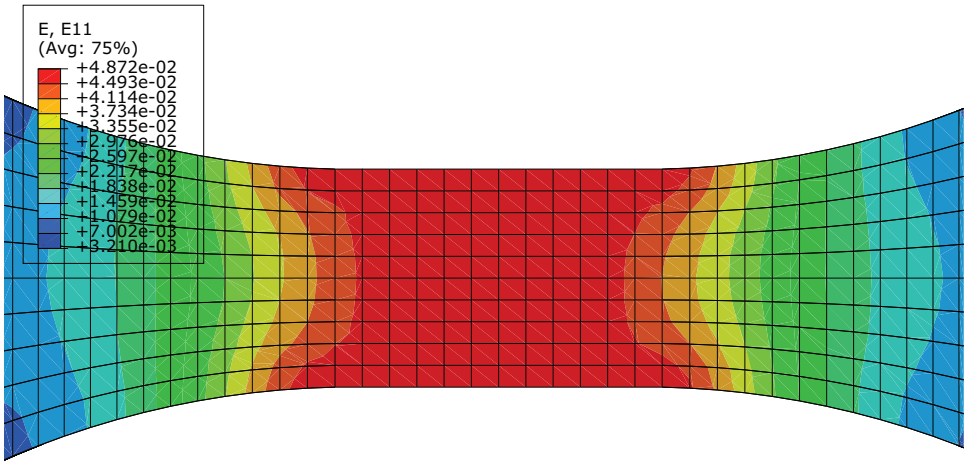

Figure C.7: Strain ε_{11} (along the pull direction) Contour Plots for 0°

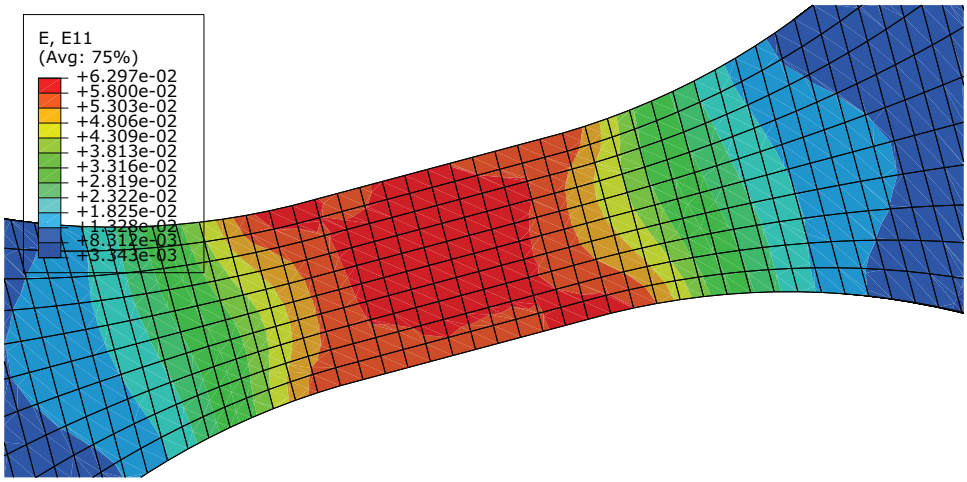

Figure C.8: Strain ε_{11} (along the pull direction) Contour Plots for 15°

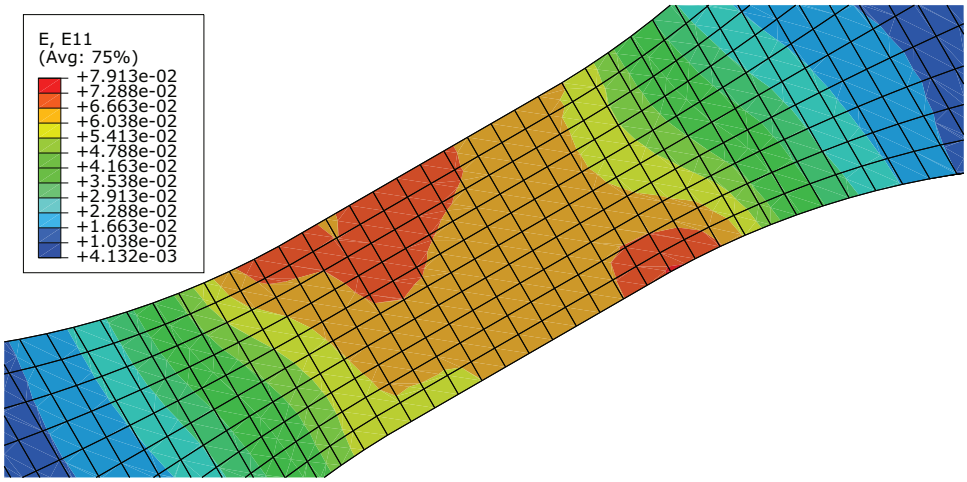

Figure C.9: Strain ε_{11} (along the pull direction) Contour Plots for 30°

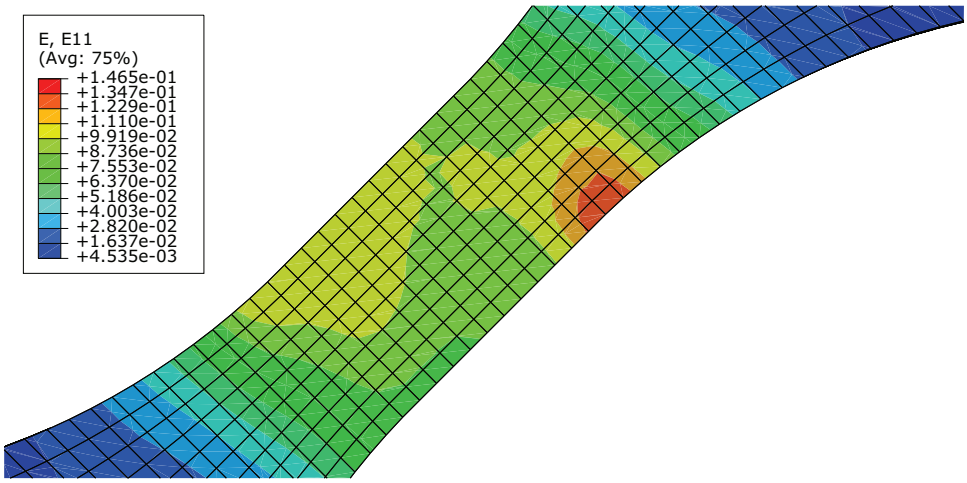

Figure C.10: Strain ε_{11} (along the pull direction) Contour Plots for 45°

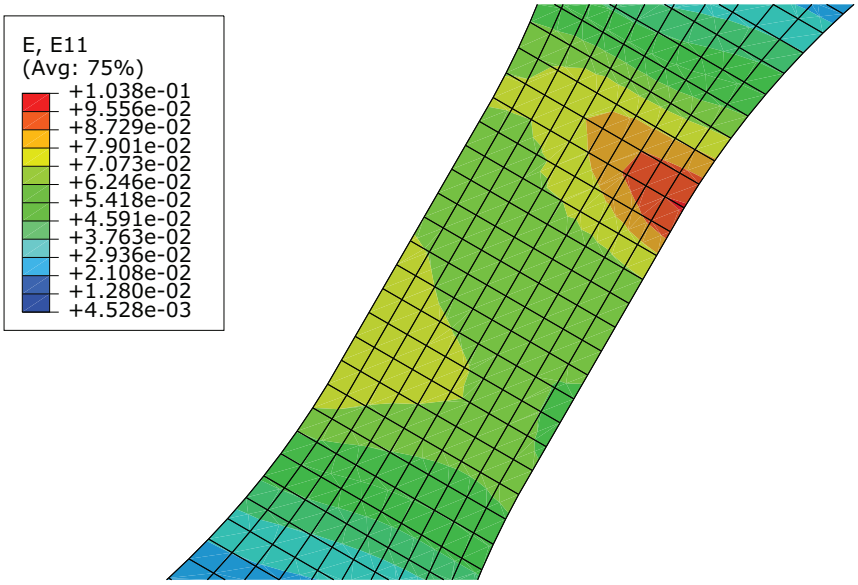

Figure C.11: Strain ε_{11} (along the pull direction) Contour Plots for 60˚

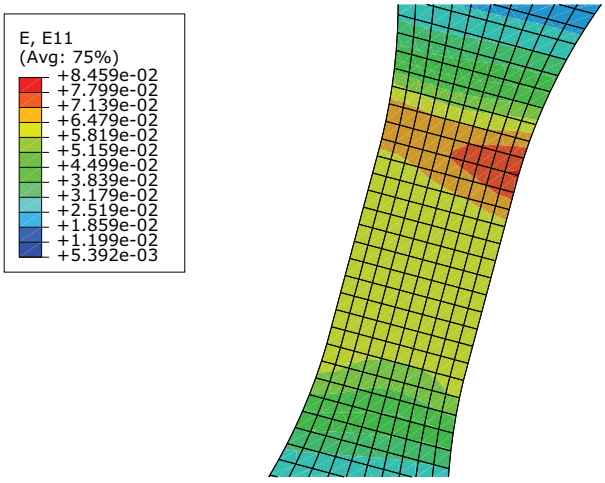

Figure C.12: Strain ε_{11} (along the pull direction) Contour Plots for 75˚

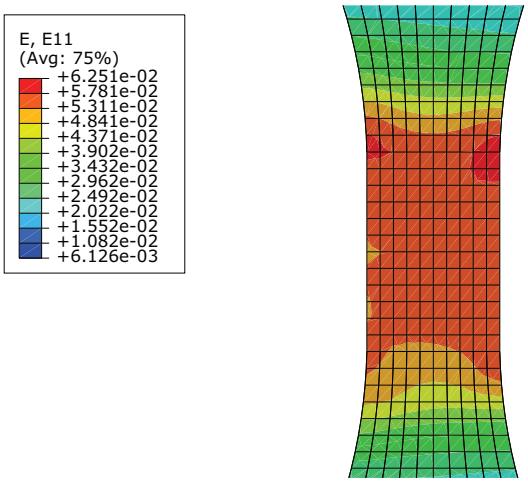

Figure C.13: Strain ε_{11} (along the pull direction) Contour Plots for 90°

C.3 Figures For Fibre Orientation Distribution Contour Plot

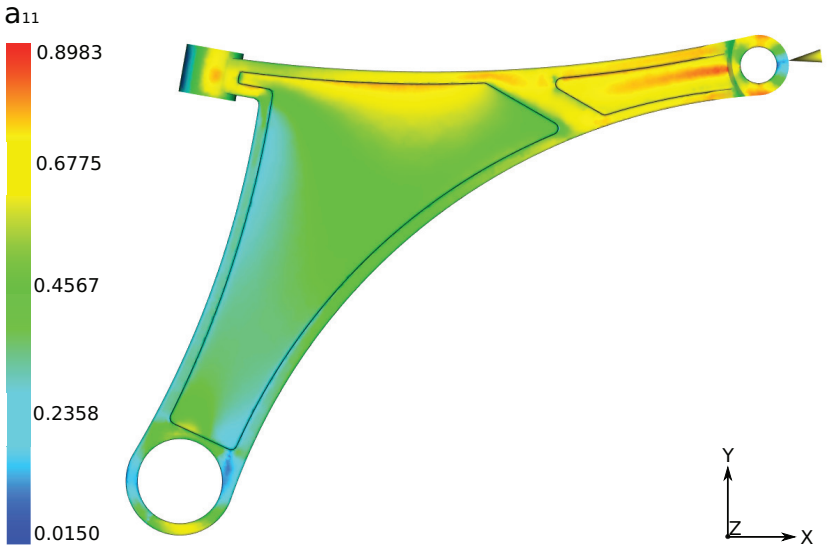

Figure C.14: Fibre Orientation Result a_{11} Injection Point Locate at Ball joint Side

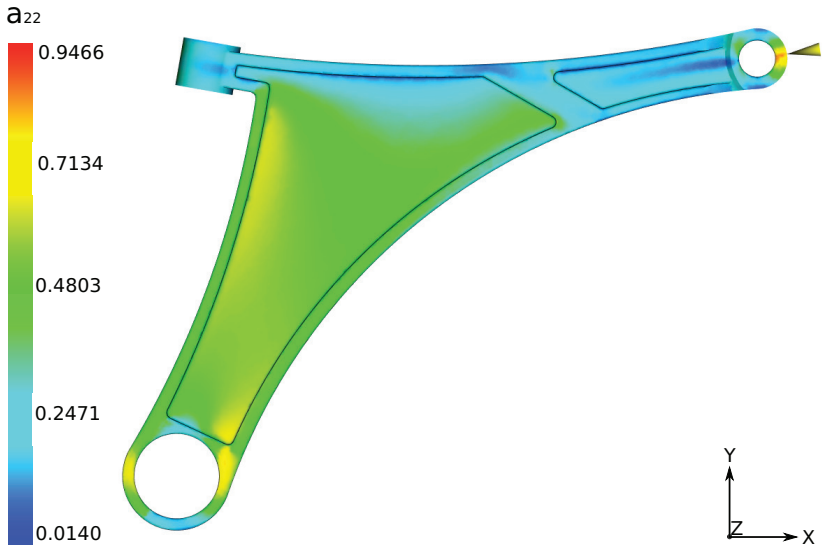

Figure C.15: Fibre Orientation Result a_{22} Injection Point Locate at Ball joint Side

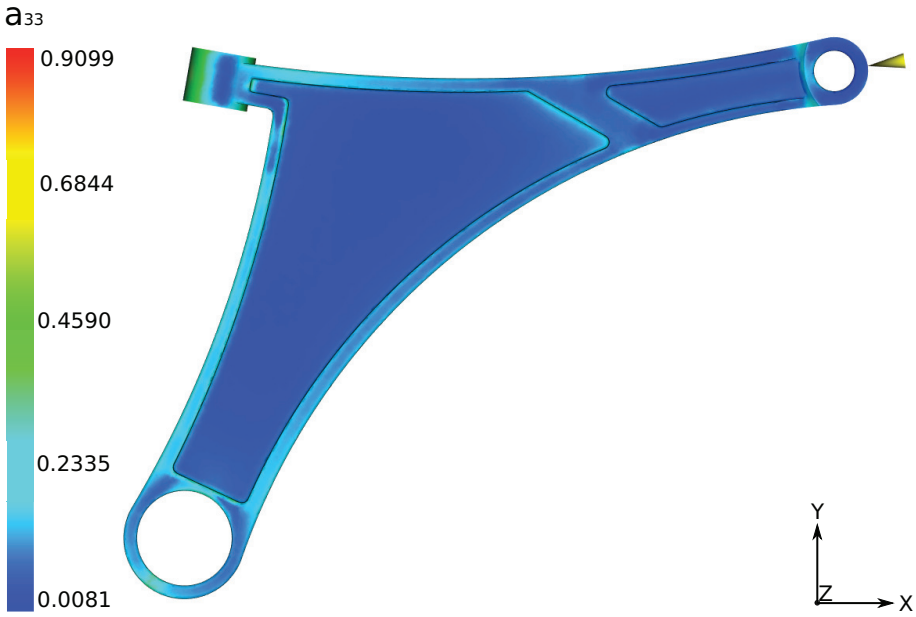

Figure C.16: Fibre Orientation Result a_{33} Injection Point Locate at Ball joint Side

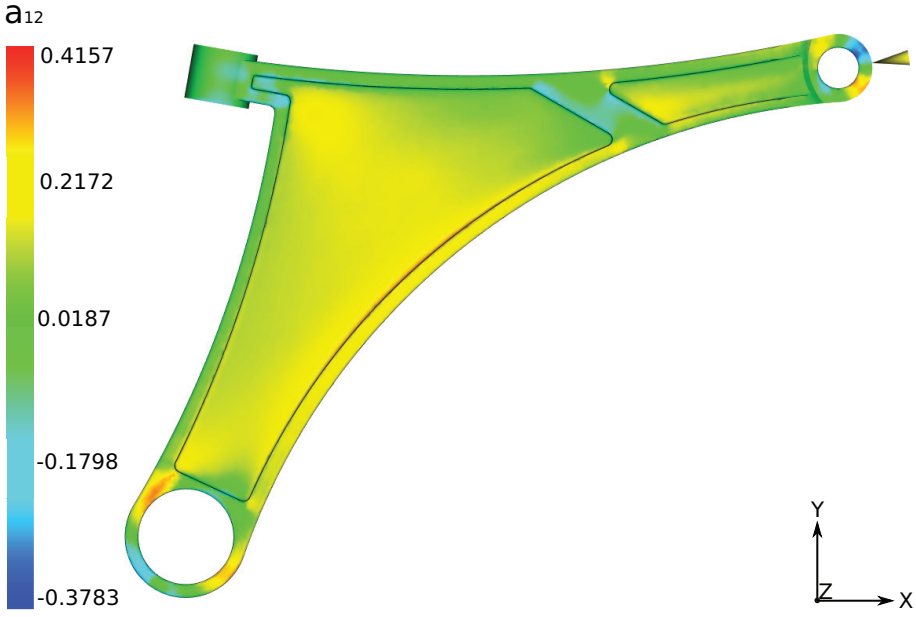

Figure C.17: Fibre Orientation Result a_{12} Injection Point Locate at Ball joint Side

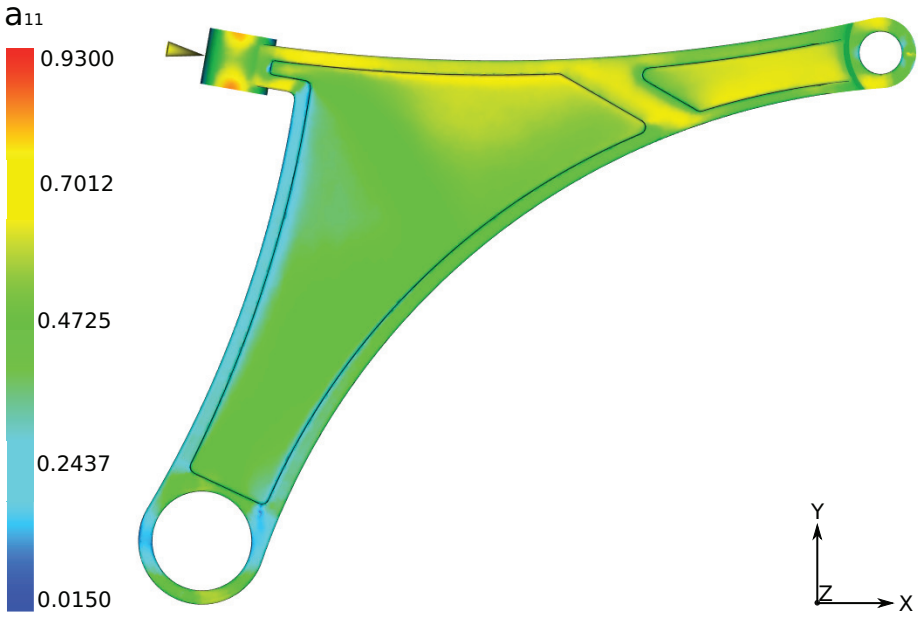

Figure C.18: Fibre Orientation Result a_{11} Injection Point Locate at Front Bushing Side

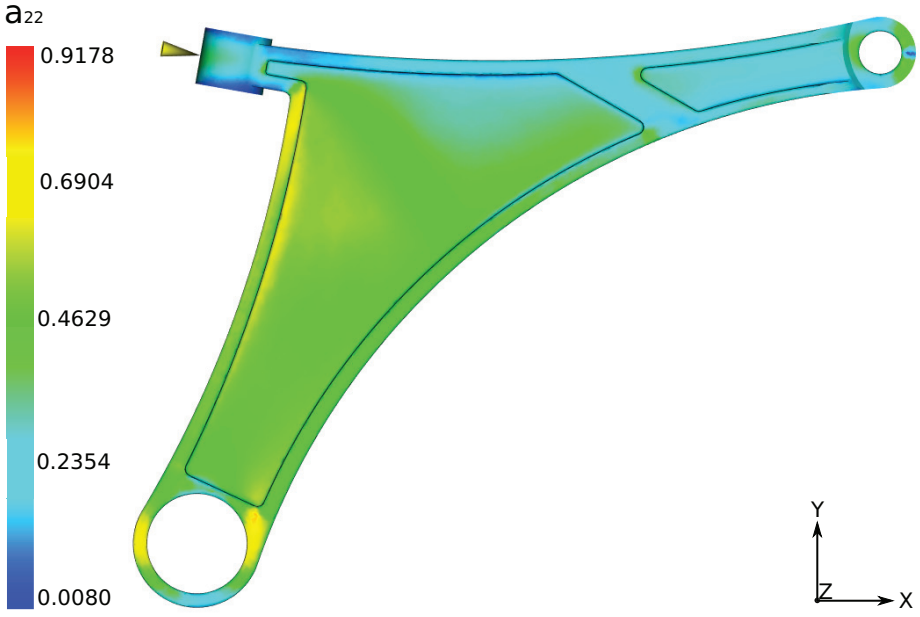

Figure C.19: Fibre Orientation Result a_{22} Injection Point Locate at Front Bushing Side

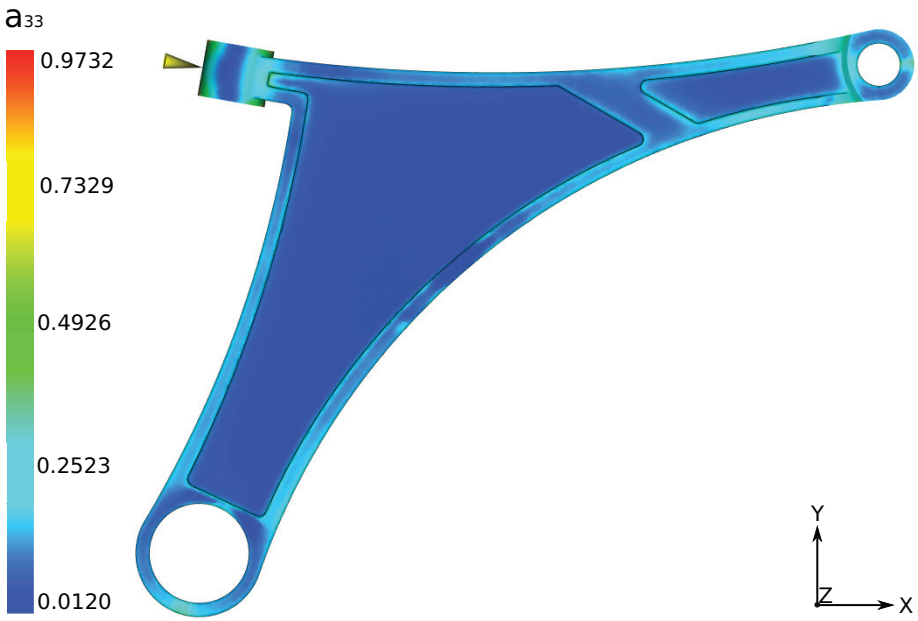

Figure C.20: Fibre Orientation Result a_{33} Injection Point Locate at Front Bushing Side

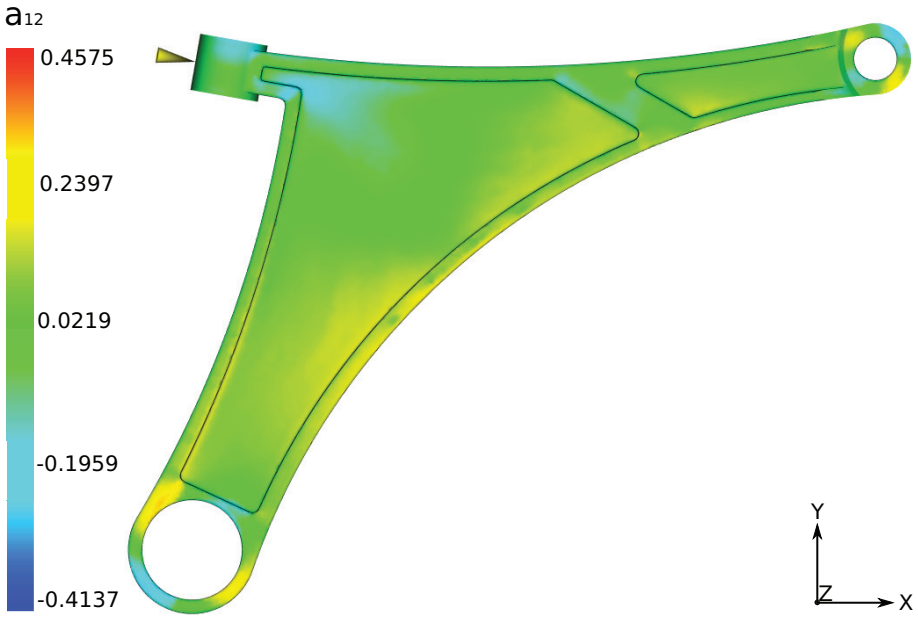

Figure C.21: Fibre Orientation Result a_{12} Injection Point Locate at Front Bushing Side

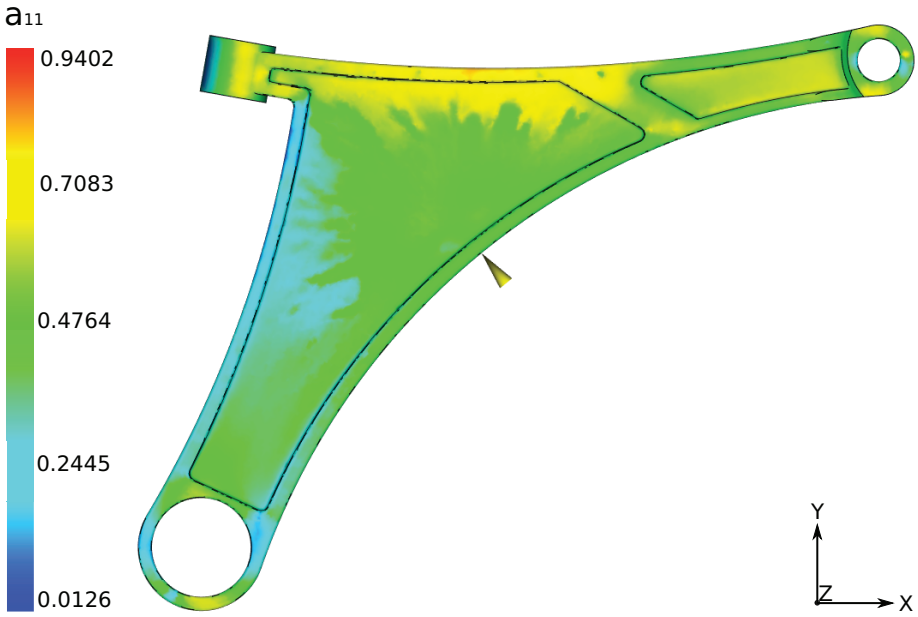

Figure C.22: Fibre Orientation Result a_{11} Injection Point Locate at Middle Region

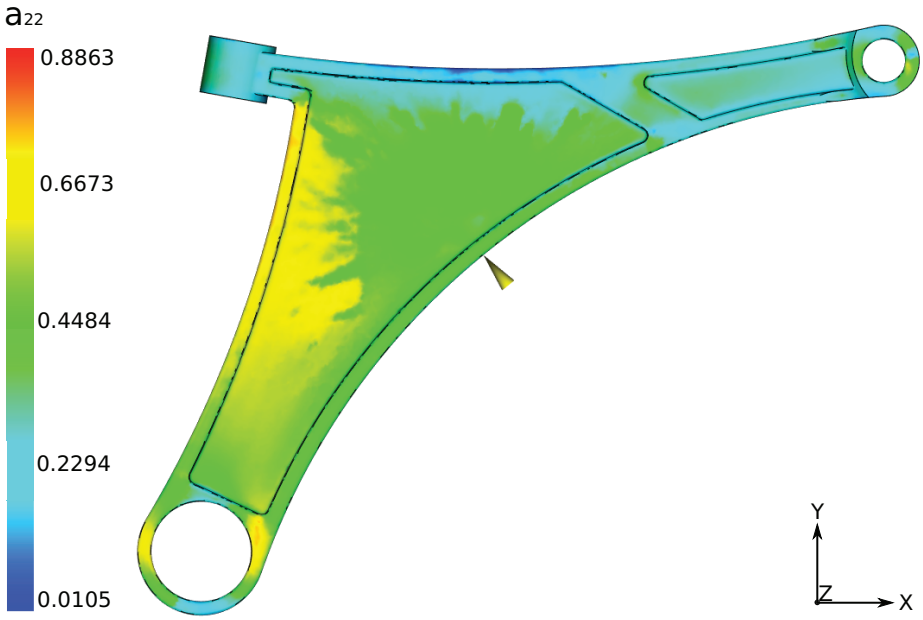

Figure C.23: Fibre Orientation Result a_{22} Injection Point Locate at Middle Region

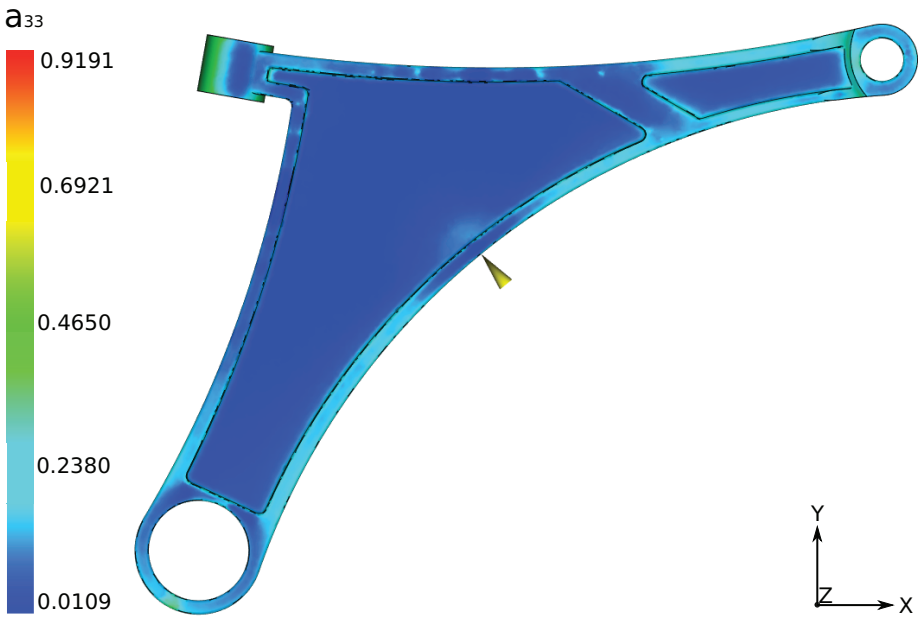

Figure C.24: Fibre Orientation Result a_{33} Injection Point Locate at Middle Region

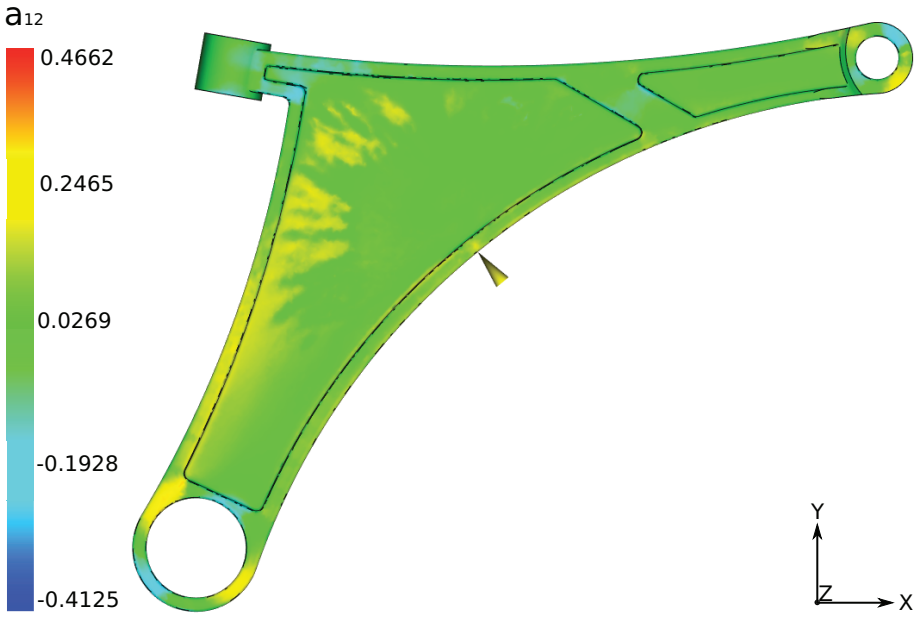

Figure C.25: Fibre Orientation Result a_{12} Injection Point Locate at Middle Region

Vita Auctoris

Zhe (Tom) Ma was born in Beijing, China in 1988. He graduated from the Beijing No.15 High School in 2007. He then attended Beijing Forestry University, where he earned a Bachelor's Degree of Mechanical Engineering and Automatization in 2011. He came to Canada to study in Meng program in 2011. Then he transferred to Master of Applied Science program at the University of Windsor in 2013 and since that time, he worked with Dr. Bruce Minaker. He transferred to PhD program to continue his research in 2015. He is presently a candidate for PhD Degree in Mechanical Engineering at University of Windsor, and is scheduled to graduate in 2022.